Development of Nanosalt and Heat Transfer Optimization for Solar Energy Storage

Afrah Turki Awad

Submitted in accordance with the requirements for the degree of
Doctor of Philosophy

The University of Leeds
School of Mechanical Engineering

August, 2018

The candidate confirms that the work submitted is her own, except where work which has formed part of jointly authored publications has been included. The contribution of the candidate and the other authors to this work has been explicitly indicated below. The candidate confirms that appropriate credit has been given within the thesis where reference has been made to the work of others.

Publications

[1] AWAD, A., BURNS, A., WALEED, M., AL-YASIRI, M. & WEN, D. 2018a. Latent and sensible energy storage enhancement of nano-nitrate molten salt. Solar Energy. 172, pp.191-197.

[2] AWAD, A., NAVARRO, H., DING, Y. & WEN, D. 2018b. Thermal-physical properties of nanoparticle-seeded nitrate molten salts. Renewable Energy, 120, 275-288.

[3] LUO, Y., DU, X., AWAD, A. & WEN, D. 2017. Thermal energy storage enhancement of a binary molten salt via in-situ produced nanoparticles. International Journal of Heat and Mass Transfer, 104, 658-664.

Conferences- Oral presentations:

[1] AWAD, A. & WEN, D. 2016. Thermal energy storage enhancement of dispersing nanoparticles in a phase change material. UK Energy Storage Conference (UKES2016) conference, University of Birmingham, Birmingham, UK.

[2] AWAD, A. & WEN, D. 2017. Latent and Sensible Energy Storage Enhancement of Nano-Nitrate Molten Salt. AEM2017 conference, University of Surrey, Guilford, UK.

Conferences- Poster:

[1] AWAD, A. & WEN, D. 2017. Latent and sensible energy storage enhancement of nitrate salt with same size of two different types of nanoparticles. ICHEME conference, UK Particle Technology Forum 2017. University of Birmingham, Birmingham, UK. Poster.

[2] Training in Universitat Jaume I, Castellon, Spain (nanouptake event#1).

Acknowledgements

First of all, I owe my success and the courage to complete my thesis to my Gracious God who gave me all the strength and determination to finish my research study.

I would like to extend the warm thanks to my supervisors, Prof. Dongsheng Wen and Dr. Alan Burns, for their help and their valuable comments and recommendations during my research work.

I gratefully acknowledge to my sponsor (Higher Committee for Education Development in Iraq, HCED) for their finical support during my PhD study.

I want to express my thanks to my colleagues in Prof Wen's research group, my friends Ehsan Omaraa, Hasan Al-Asadi, and all of my other friends. I very thankful for all the technicians in the energy building specifically I obliged to Mr Ed Woodhouse, Mr Gurdev Bhogal, Mr Samuel Burdon and Mr Kevin Dyer and the electrical workshop technicians especially Mr Tarsem Hunjan and Mr Matthew Buckley for their support and help during my experimental rig setup.

I would like to give my appreciations to my husband for all the support he gave and still giving to me through my research without any complaints, I cannot imagine how it will be without your support.

My thanks and appreciation for my family, my parents, sisters and brothers, for all the continuous support and encouragements from them overseas.

Abstract

This thesis is concerned with solar energy storage systems in terms of storage materials and storage systems for high temperature applications. The main focus has been given to either improve the thermophysical properties of the storage medium or to improve the design of the storage medium by optimizing the solar energy storage system. Nitrate salts have been chosen as the phase change material with nanoparticles as additive materials. Different types or concentrations of nanoparticles and different types of nitrate salt have been selected and studied.

There are different objectives, starting from a few grams (up to 5 g) to kilograms (up to 3 kg), that have been considered through this research. In the first objective, nanosalts, which are nanoparticles seeded in the nitrate salts, have been prepared by two different methods, either the 2-step method or the 1-step method. Nanosalt prepared by the 2-step method showed higher specific heat capacity (cp) than the base salt by 10.5% with higher thermal conductivity (k) values up to 60%. Up to 6% increments in total thermal energy storage have been observed for nanosalt (iron oxide (Fe_2O_3) nanoparticles and binary nitrate salt). Additionally, the 1-step method was used to prepare copper oxide (CuO) nanoparticles directly inside the nitrate salt, which showed improvements in cp in comparison to base nitrate salt.

In the second objective, alongside with the thermophysical properties measurements, material characterizations have been considered using different devices to show the morphology of the surface area of salts and nanosalts samples.

In the third objective, an experimental rig has been designed and built to study heat transfer of salts and nanosalts. Temperature measurements have been made at different axial, radial and azimuthal locations. Both charging and cooling of the salt (or nanosalt) were studied, showing that improvements in the charging process are related to the type or concentration of the nanoparticles material. Overall, heat transfer is improved in the case of nanosalt compared to salt alone. Two different types of salt were tested in this experiment rig which was single salt (sodium nitrate) and binary solar salt (sodium nitrate: potassium nitrate by 60:40 molar ratio) with different additives materials such as CuO (by 0.5 wt. %) and Fe_2O_3 (by 0.1 wt. %, 0.5 wt. % and 1 wt. %).

In the fourth objective, Computational Fluid Dynamics software has been used to solve the charging process of salt and nanosalt. A validation for the ANSYS CFX code (version

17.0) is conducted by comparing the experimental data with the simulation data. A good agreement is obtained for both cases of salt or nanosalt.

In the fifth objective, an optimization for the solar energy storage system has been conducted. Different designs for the storage system employing finned structures were studied. The new combination effect of both nanosalt and fins system has been studied using the validated CFX code, showing a promising improvement in the charging process in comparison to salt alone, nanosalt alone or salt-fins system alone.

As a result, our overall aim is to improve the thermal properties of nitrate salts and optimize the thermal energy storage system.

Table of Contents

Contents

List of Tables

List of Figures

Abbreviations

Symbol	**Definition**
DSS	Direct Storage System
HTF	Heat Transfer Fluid
DSG	Direct Steam Generation
MW	Megawatt
PCM	Phase Change Material
$NaNO_3$	Sodium nitrate salt
CO_2	Carbon dioxide gas
CO	Carbon monoxide gas
N_2	Nitrogen gas
vol.	Volume fraction
DSC	Differential scanning calorimetry
LFA	Laser flash analysis
DSC/TGA	Thermogravimetric analyser device
Nano/NP	Nanoparticles/ nanoscale
SiO_2	Silica
wt.%	Weigh percentage concentration
ml	Millilitre
min	Minutes
KNO_3	Potassium nitrate salt
$Ca(NO_3)_2$	Calcium nitrate salt
$LiNO_3$	Lithium nitrate salt
$BaCl_2$	Barium chloride salt
NaCl	Sodium chloride salt
$CaCl_2$	Calcium chloride salt.
LiCl	Lithium chloride salt
KCl	Potassium chloride salt
Li_2CO_3	Lithium carbonate salt.
K_2CO_3	Potassium carbonate salt
MWCNT	Multi walled carbon nanotube
SDS	Sodium dodecyl sulfate
mg	Milligram
m^3	Cubic meter
Al_2O_3	Alumina
$NaNO_2$	Sodium nitrite salt
rpm	Revolution per minute
$CuSO_4.5H_2O$	Copper sulphate
CuC_2O_4	Copper oxalate
$TiOSO_4$	Titanium(IV) oxysulfate solution
SWCNT	Single walled carbon nanotube.
CNT	Carbon nanotube.
C60	Fullerene
SDBS, $C_{18}H_{29}NaO_3S$	Sodium dodecyl benzene sulfonate
MgO	Magnesium oxide
CuO	Copper oxide
TiO_2	Titanium dioxide
$\emptyset_{\mathrm{np}}$	Volume fraction of nanoparticles
$\emptyset_{\mathrm{f}}$	Volume fraction of base fluid (salt).
$\emptyset_{\mathrm{c}}$	Volume fraction of compressed layer (interfacial layer).
Cu	Copper
Al	Aluminium
Au	Gold

ZnO	Zinc oxide
W	Watt unit
m	Meter unit
g	Gram unit
2-D	Two dimension
Nu	Nusselt number
φ_n	Fraction of nanoparticles
Pe	Peclet number which is the ratio of heat transported by convection to that transports by conduction.
Re	Reynold number
Pr	Prandtl number
nano-PCM	Nanophase change material
β	Liquid fraction
S	Source term
e	Constant
CFD	Computational Fluid Dynamic
VOF	Volume Of Fluid
Fe_2O_3	Iron oxide nanoparticles.
SEM	Scanning Electron Microscopy
TEM	Transmission Electron Microscopy
DLS	Dynamic Light Scattering
2-step	Two step method
DW	Distilled water
s.s	Solar salt, or binary nitrate salt
1-step	One step method
SO_3	Sulfur trioxide
EDX	Energy Dispersive X-ray Spectroscopy
TES	Total thermal energy storage
Ra	Rayleigh number
PCMs	Phase Change Materials
β_{liq}	Liquid mass fraction
β_{sol}	Solid mass fraction
K	Kelvin
kJ	Kilo Joule
kg	kilogram
nm	Nanometre
C	Constant
^{n}	Constant parameter

Nomenclature

Symbol	**Definition**
cp	Specific heat capacity, J/ (g. K)
ΔT or dT	Temperature differences, K
$q_{sensible}$	Sensible heat, (J/kg)
T	Temperature, K
k	Thermal conductivity, W/(m. K)
L	Latent heat, (J/g)
d_p	Diameter of nanoparticles, nm.
$c_{p,nf}$	Specific heat capacity of nanosalt or nanofluid, (J/g. K)
$c_{p,np}$	Specific heat capacity of nanoparticles, (J/g. K)
$c_{p,f}$	Specific heat capacity of base fluid, (J/g. K)
cp_{salt}	Specific heat capacity of salt, J/(g. K)
cp_c	Specific heat capacity of compressed layer, J/(g. K)
ρ	Density, kg/ m^3
ρ_{np}	Density of nanoparticles, kg/m^3
ρ_f	Density of base fluid, kg/m^3
ρ_{salt}	Density of salt, kg/ m^3
ρ_c	Density of compressed layer, kg/ m^3
$\rho_{nanosalt}$	Density of nanosalt, kg/ m^3
dT/dx	Thermal gradient, K/m.
q	Heat flow, W
H	Enthalpy, J/g
$\vec{\vartheta}$	Fluid velocity, m/sec.
A or K*	Mushy zone constant, kg/(m^3. sec)
cp_{eff}	Effective specific heat capacity, J/g. K
T_{melt}	Melting temperature, K
a	Thermal diffusivity m^2/s
g	Gravity, m/sec^2
α_T	Thermal expansion coefficient (K^{-1})
Lc	Characteristic length, m.
$q_{storage}$	Storage energy, J/kg
q_{latent}	Latent energy, J/kg
T_{ambent}	Ambient temperature, K
T_{melt}	Melting temperature, K
T_{liquid}	Liquid phase temperature, K
$T_{max.}$	Maximum temperature, K
$q_{sensible\ in\ solid\ phase}$	Sensible energy of solid phase, J/kg
$q_{sensible\ in\ liquid\ phase}$	Sensible energy of liquid phase, J/kg
T_{onset}	Onset temperature, K
µ	Dynamic viscosity, mPa. sec.
h	Heat transfer coefficient, W/m^2. K
z	Length in axial direction, mm
ri	Inner radius, mm
ro	Outer radius, mm
r	Length in radial direction, mm.
C^S_w	specific heat capacity of the solid phase, J/g. ^0C
C^L_w	specific heat capacity of the liquid phase, J/g. ^0C
R	Resistance coefficient, kg/ m^3.sec.
Fz	Gravity force in z direction, N
T_f	Film temperature, ^0C
$\mu_{nanosalt}$	Viscosity of nanosalt, kg/ m.sec

Chapter 1 Introduction

1.1 Background

In today's world, energy demand is on the increase for most applications in our daily lives, therefore, energy needs to be widely produced from renewable source i.e. solar energy plants instead of non-renewable ones e.g. oil plants (Manzano-Agugliaro et al., 2013). Solar energy is totally free with an endless source of heat from the sun and it is environmentally friendly compared to the limitation of non-renewable energies sources (Thirugnanasambandam et al., 2010). Additionally, the radiation from the sun equals 7500 times the annual consumption of energy in the world (Thirugnanasambandam et al., 2010).

The first use of solar energy was in 1866 to produce steam by Auguste Mouchout while the first operational solar thermal plant was built in 1968, Sant'llario, Italy by Professor Giovanni Francia (aalborgcsp, 2015). Solar thermal power plants and photovoltaic technology are the common types of solar energy. The main difference between these two is, photovoltaic cells directly convert solar energy to electricity while concentrated solar thermal plants convert solar energy to thermal power by producing steam, which is able to produce electricity with the aid of turbines and generators.

Solar concentrated thermal energy plants can be subdivided into four main plants which are parabolic trough solar plant, solar tower power plant, liner Fresnel solar plant and parabolic dish solar thermal system. Furthermore, the parabolic trough plant is the most common commercial solar thermal plant and it has been installed in the real world for more than 25 years (Vasquez Padilla, 2011). These plants consist of some components such as solar field and power block. The solar field includes the collector and the receiver. The collector collects the sun radiation while the receiver, which contains the heat transfer fluid (HTF), receives the solar energy that is reflected by the collector. The power block contains turbines and generators to produce the electricity and condenser to feedback the HTF to a collector and repeat the cycle. However, this type of plant would work only during the daytime with the availability of Sun while it is off during the cloudy weather or night. In order to solve this limitation, energy storage systems have been integrated into solar thermal plants to store the energy and permit heat retrieval after some time ensuring reproducibility of power under users' requests, during the night or on cloudy days.

1.2 Solar energy storage systems

Solar energy storage systems can be classified into four different types according to their arrangements, as shown in Figure (1-1). For the direct storage system (DSS), one type of fluid is used to store and transfer the heat in the concentrated solar thermal power plant such as salt, oil, etc., as shown in Figure (1-2). Contrary to DSS, the heat transfer fluid (HTF) is different from the storage medium in the indirect storage system and an additional heat exchanger is needed in this type, as shown in Figure (1-3). Molten salt can be used either as a HTF or storage medium, as explained in the next section. Using molten salt as HTF would require higher temperatures compared with the indirect tank resulting in higher turbine efficiency. However, the salt should always be in the liquid phase to avoid any solidification in the HTF pipes and this adds extra cost to the plants.

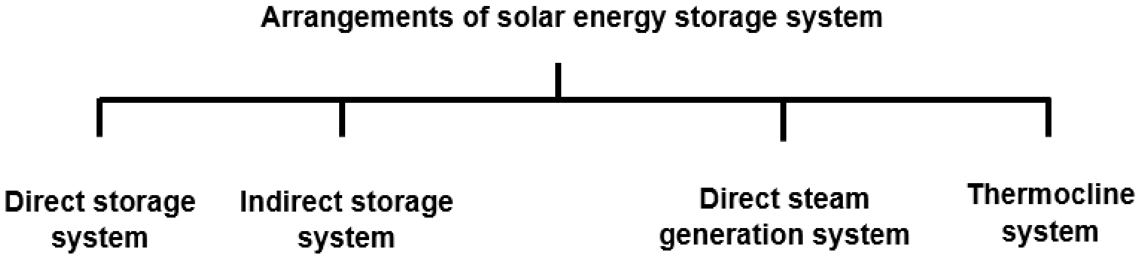

Figure 1-1 Shows the different arrangements of storage system.

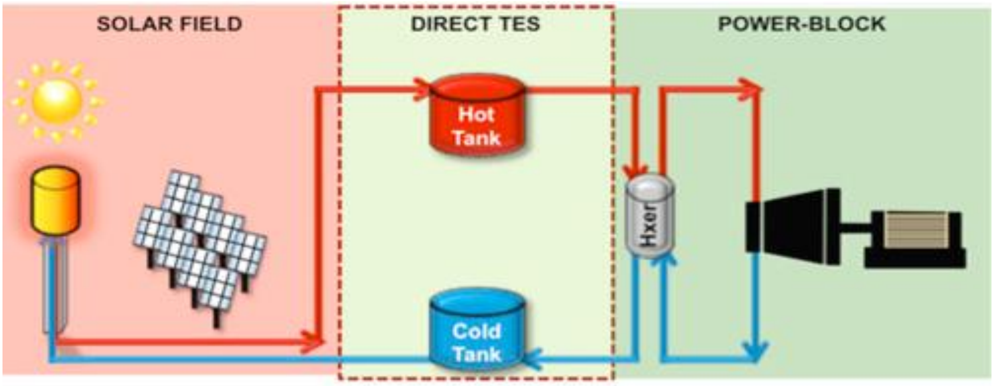

Figure 1-2 Simplified scheme of a solar power plant with direct storage system (Liu et al., 2016).

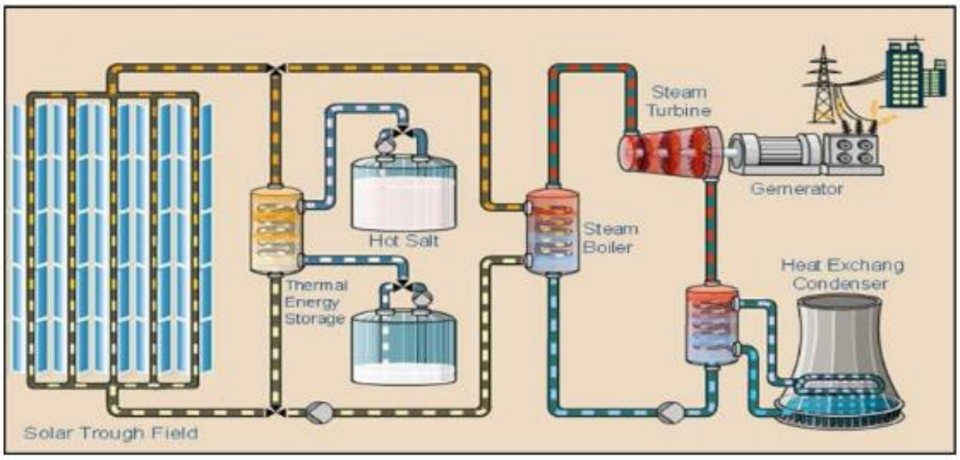

Figure 1-3 Simplified scheme of a trough power plant with indirect storage system (Rohit et al., 2017).

The use of oil or other different types of fluid as HTF will add an extra heat exchanger in the power block compared with the use of steam as HTF in the direct steam generation (DSG). In DSG, there is no need for a heat exchanger in the power block where steam will directly use to generate electricity via turbine and generator and part of the steam will be used in the storage system block to charge the storage medium, as shown in Figure (1-4).

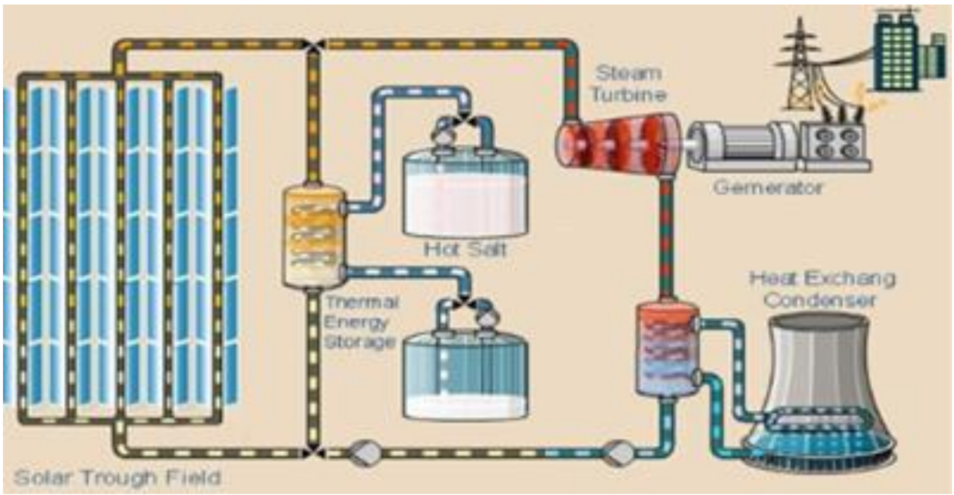

Figure 1-4 Shows the schematic of parabolic trough power plant with direct steam generation (DSG).

The use of steam in DSG parabolic trough plants delivers higher efficiency than the use of oil as HTF by 7% of annual efficiency and reduces the cost of the plant by 9%. These values were tested for a small collector field of 10 MW where the expectation for a larger plant is better (Price et al., 2002). According to Price et al. (2002), DSG was tested and used safely under 100 bar with LS-3 trough plant. They also recommended to use the phase change material (PCM) as a storage material in the DSG-parabolic trough plant, PCM will be explained in the next section (section 1.3). Furthermore, the effect of the HTF on the plant plays an important role depending on the maximum working temperature of the HTF type. For instance, Feldhoff et al. (2012) did a comparison between the use of oil or steam as HTF. According to their work, DSG plant has the gross efficiency of 6% compared to oil as HTF in the parabolic plant. The use of steam as HTF needs certain conditions such as high pressure (i.e. 150 bar) and high temperature (i.e. 550 ^{0}C) therefore the pipe of the plant needs to withstand these conditions. As a result, Eck et al. (2008b) proposed thickening the wall of the receiver tube to eliminate the effect of high pressure (150 bar) and controlling high temperature (550 ^{0}C) by the use of the coating. DSG is a promising technique which can be used to produce solar energy at higher levels of temperatures up to 500 ^{0}C Feldhoff et al. (2010).

There is another type of the storage system which is the thermocline system. In thermocline systems, the energy could be stored in one tank instead of using two storage tanks (hot and cold tanks). This type depends on the heat gradient where the hot fluid is located at the top and cold fluid is located in the bottom of the same tank, as shown in Figure (1-5).

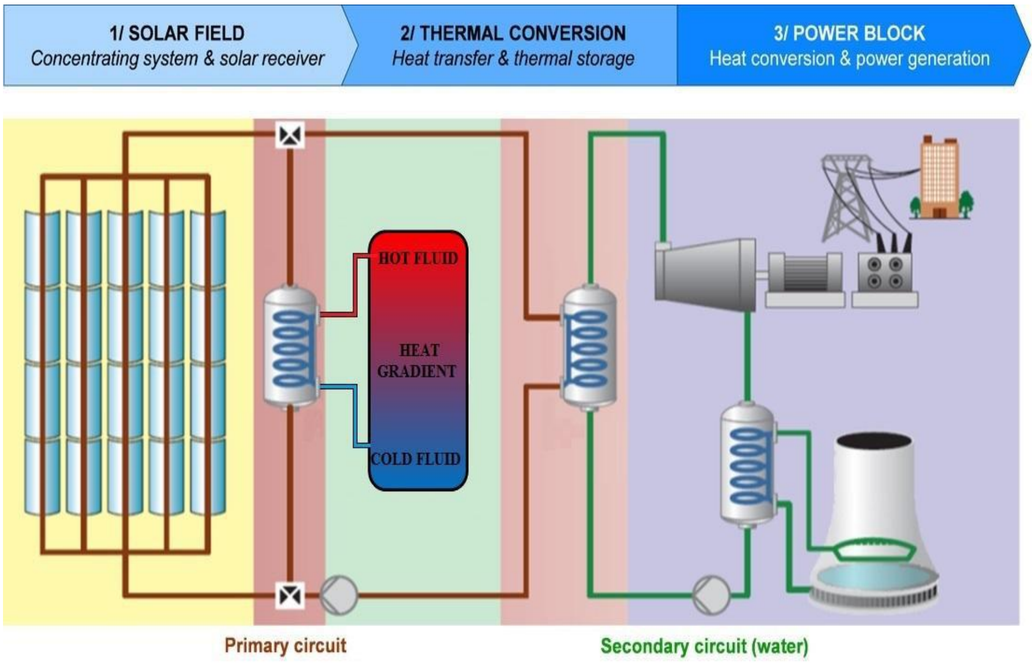

Figure 1-5 Shows the simplified scheme of a trough power plant with thermocline storage system (Lasfargues, 2014).

In storage tanks, there are three different reversible methods to store the energy, namely two physical processes like the sensible, or latent heat, and the chemical process named the thermochemical method. Sensible heat indicates the increase of material temperature due to heat transferred from HTF to the storage medium (Mehling and Cabeza, 2008). Specific heat capacity (cp) is represented by the ratio of the energy stored ($q_{sensible}$) to the temperature difference (ΔT), as shown in Equation (1-1).

$$\mathrm{cp} = \mathrm{q}_{\mathrm{sensible}} / (\mathrm{mass.}\ \Delta\mathrm{T}) \qquad \textbf{Equation 1-1}$$

Sensible heat storage is very common in storing the energy of solids or liquids. However, this method requires an increase in the volume of the storage tank due to its lower energy density.

Furthermore, the second type is the latent heat storage method which depends on the phase change of the storage material called PCM. This has much higher energy density than sensible heat storage due to the large value of the latent heat. Full details are given in the next section. The application of both sensible and latent heat was reported by Feldhoff et al. (2012) who suggested a design of the storage system using both three sensible tanks and one latent tank in DSG in a parabolic trough plant. Their design of plant was under 112 bar (T condensate is 320 ^{0}C) and 500 ^{0}C during charging (storing energy in storage system) and 78 bar (T condensate is 294 ^{0}C) during discharging (releasing energy from storage system). The charging process was as following

- Superheated process firstly by exchanging heat from superheated steam to the hot tank.
- Evaporation process as heat from steam will charge the PCM sodium nitrate ($NaNO_3$) and HTF becomes saturated water.
- Preheating process as the saturated water will charge the cold tank via the buffer tank.

A pressure of 78 bar is used as the condition for discharging process as following

- Cold tank (converts water from liquid state to saturated water) in the preheating process.
- PCM tank (converts water from saturated to steam) in the evaporation process.
- Hot tank (converts from steam state to superheated state) in superheating process.

The buffer tank is used to cover the high volume needed in the cold tank as the difference in temperature is low between the salt in the cold tank and the saturated water during the preheating process.

However, Feldhoff et al. (2012) suggested different arrangements in the storage system by using concrete or salts as a sensible storage medium with PCM. Overall, DSG technology is a promising plant and it is built in the real world in Thai solar energy with 5 MWe with working conditions of 30 bar and 340 ^{0}C. If this plant is integrated with an energy storage system, the type of nitrate salt (with a melting temperature around to 220 ^{0}C) will be a good option to store the energy. The condensation temperature of water at 30 bar equals to 233 ^{0}C and these conditions match with the nitrate solar salt condition.

Additionally, the thermochemical storage method basically depends on breaking the bonds of the storage material and this can provide a large amount of heat and good storage efficiency (Sharma et al. (2009) and Abedin and Rosen (2011)). However, the breaking and recombination of the bonds may result in undesirable products, therefore, a careful understanding of the chemical reaction needs to be taken into account (Schmidt, 2011). Therefore, the complex design of the storage system is needed for this method.

1.3 Phase change material (PCM)

The PCM can be defined as the material that has the ability to change from one phase to another at a known constant value of temperature or over a range of temperatures. Latent heat is the heat required to accomplish the phase change for the material such as solid-solid, solid-liquid, solid-gas, and liquid-gas. For the case of solid-solid, the change of material structure requires a small energy which gives limited energy storage. Furthermore, solid-gas and liquid-gas phase changes are accompanied remarkable changes in volume with a high pressure because of the gas phase. Therefore, the latent heat in these phases is not practical due to the pressure rising in the vapour phase that leads to problems (Mehling and Cabeza, 2008). The most suitable phase change process is from solid to liquid and vice versa due to relatively small changes in pressure and volume with higher energy density. Figure (1-6) shows the schematic for both of melting process, which is phase change from solid to liquid by absorbing energy, and solidification process, which is solidifying from liquid phase to solid phase by releasing energy.

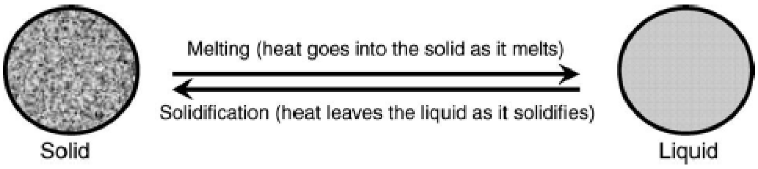

Figure 1-6 Shows the process of the PCM (Mondal, 2008).

According to Mehling and Cabeza (2008), sub-cooling or super-cooling occurs when the material solidifies at a temperature lower than the specified solidification temperature, as shown in Figure (1-7).

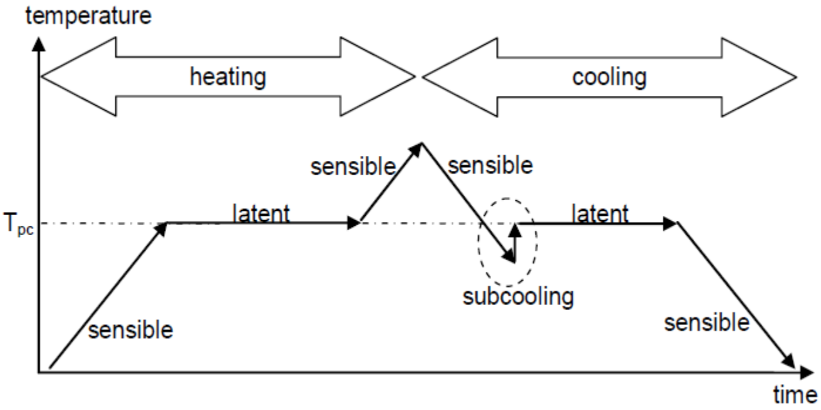

Figure 1-7 Shows the schematic diagram shows the charging and discharging processes with sub-cooling (Mehling and Cabeza, 2008).

Furthermore, PCM can be classified into three different types such as organic, inorganic and metal alloys (Rousse et al., 2009). This classification is according to their thermal and chemical properties such as melting temperature or melting enthalpy. Organic PCM such as paraffin wax has been used in an application at certain temperatures of 0-200 ^{0}C. Organic materials are insoluble in water, have a high energy density, are not corrosive and their compatibility with other materials is good. However, paraffin is considered as a flammable material which limits its use, especially at elevated temperature. Besides, its low melting point, it is not applicable for other applications such as thermal energy storage at a higher temperature above 200 ^{0}C. Moreover, their covalent bonds will not help them to be stable at high temperature (Fleischer (2015) and Mehling and Cabeza (2008)).

On the other hand, inorganic materials have higher melting points which are suitable for applications of high temperature > 200 ^{0}C. An inorganic material such as molten salt is economic, chemically stable, not highly flammable or combustible, high density with changing volume between two phases (solid to liquid) as 10 vol. %, and low vapour pressure (Pfleger et al. (2015a) and Fleischer (2015)). Furthermore, metal alloys have high thermal conductivity (k) while specific heat (cp) and storage density are low (Liu et al., 2012).

Moreover, the type of PCM used to store energy in concentrated solar thermal power plants needs to have the following parameters. First and foremost, the PCM should have suitable phase change temperature for different applications. Secondly, the PCM should have higher values of thermophysical properties such as density, cp and latent heat in order to reduce the size of a storage tank. In addition, a higher value of k will help in absorbing and releasing energy. Thirdly, it must have a low level of changing in volume and pressure. Fourthly, it needs to be chemically stable to avoid toxicity. Additionally, PCM is readily available and at a low price. It seems to be that molten salt is the most appropriate material to be used in the storage tank of the solar thermal plant at high temperature (Pfleger et al. (2015a); Fleischer (2015) and Bradshaw and Siegel (2008)). Moreover, molten salt can store energy in two different forms such as sensible heat (depending on the cp of salt) and latent form depending on the latent heat of salt. The latent heat of salt has higher energy density with a small size of storage tank compared with sensible heat (Fleischer, 2015). However, the main issue of the molten salt is the higher values of its melting temperature and lower values of both k and cp. On the other hand, the decomposition of molten salt should be high enough to meet the requirements of the application they used for, where their decomposition point depends on many factors such as the temperature, and the environmental condition (Pfleger et al. (2015a); Peng et al. (2008) and Bradshaw and Siegel (2008)).

1.4 Problem Statement

The use of molten salts as PCM is economical, widely available and has an appropriate working temperature with lower vapour pressure compared with others like oil. However, their limited thermophysical properties such as thermal conductivity (in a range from 0.1 - 0.6 W/m. K (Kong et al., 2014)) and low specific heat capacity, as well as the high freezing point eliminate their wide applications. Regarding the freezing point, it can be engineered depending on the molar ratios of molten salt used. However, their ability to conduct heat and store energy limit their application due to their lower values of thermophysical properties. Therefore, this research focuses on improving the charging process of nitrate salt (either single nitrate salt or eutectic binary salt) by preparing and analysing new nanosalt materials that possess higher storage energy than salt. Additionally, the new nanosalt material would have a lower melting value which means even wider application use.

1.5 Aim of Project and objectives

This work aims to improve the solar energy storage efficiency via three routes: i) by enhancing the thermophysical properties of molten salts via nanoparticles; ii) by improving the design of the storage tank with the addition of fins; and iii) via the combined effects of both nanoparticles and fin structures in the storage system. Both experimental and numerical work will be conducted, which includes:

i. Synthesis and preparation of nanosalts made up of different types and concentrations of nanoparticles on single salt or binary salt by using two different methods, i.e., 2-step method and 1-step method.

ii. Characterisation of thermophysical properties and morphology of salts/nanosalts using different devices such as DSC, LFA, DLS, TEM, TGA/DSC, and SEM.

iii. Design and fabrication a pilot experimental rig to study for the first time the heat transfer behaviour of different nanosalts up to 350 ^{0}C. A comparison between the salts and nanosalts are obtained during the charging process and cooling at same conditions.

iv. Numerical study of the heat transfer of nanosalts by Ansys-CFX code by using experimentally determined thermophysical properties. The CFX code has been validated against our experimental data in this objective for salt and nanosalt.

v. Design and optimization of the energy storage systems by using validated code of Ansys-CFX software with different fin structures.

1.6 Thesis Organisation

The thesis is organized as follows

1. Chapter 1 is a brief background about the solar energy plants with the main focus on the storage system and PCM used in a storage tank of solar thermal power plants, aims and objectives of this research are mentioned in chapter 1.
2. Chapter 2 is a literature review which considers research works that are related to the subject area in different aspects. Firstly, experimental work is reviewed on how to prepare nanosalt materials without and with surfactants followed by a review of measuring different thermophysical properties such as cp, latent heat and k. Moreover, a review is presented on the experimental side of experimental heat transfer device related to PCM, nano-PCM, and PCM-fin in the storage tank. Then a review is presented mainly focused on the simulation methods used to simulate PCM for energy storage, nano-PCM in a storage system and finned with PCM in storage application. At the end of this chapter, the state of art has highlighted the gap of literature.
3. Chapter 3 presents the small-scale preparation methods of 1-step and 2-step of nanosalts and thermophysical properties measurements for different salts and nanosalts such as cp, latent heat, melting point, decomposition point, thermal diffusivity and thermal conductivity. Furthermore, material characterizations using different devices have been included.
4. Chapter 4 includes the full detail for the experimental setup, the design of the rig, the devices used during the experiments, material preparations, the procedure of the work in the rig, and the results and discussions from the experimental rig for different materials of salts and nanosalts.
5. Chapter 5 includes the validation of the CFX code and a comparison of the results for salt and nanosalt with the experimental data. A sensitivity study of different parameters in the CFX code is included and the charging code has been compared with the literature.
6. Chapter 6 includes the simulation work of melting process using the validated code of CFX in chapter 5 to simulate the storage system with salt, nanosalt, salt and fin or nanosalt with a fin for different fin structure inside a storage system.
7. Chapter 7 is the conclusions and recommendations of the thesis work.

Chapter 2 Literature review

2.1 Introduction

In solar energy storage applications, the low values of thermophysical properties of PCMs based on salts have limited their wide applications. Therefore, different methods have been implemented to improve the storage system in solar thermal power plants which either improve the storage medium or the storage system design. The storage medium (PCM) can be improved by dispersing nanoparticles into the PCM; while the storage system can be improved by many methods such as using finned structures, metal foams, heat pipes and so on. For example, fins could enhance the heat transfer from the hot medium towards the cold medium during the charging process and conversely during the discharging process. All of the mentioned techniques aim to increase the surface area either for PCM or for the storage system surfaces and therefore better charging and discharging by shortening the melting and solidification times.

In the case of improving thermophysical properties of the base material by dispersing nanoparticles, it was investigated for the first time by Chol (1995) that adding smaller particles of dimension (10^{-9} m) into a base fluid termed as ‘’nanofluid’’ would improve their properties. On the other hand, improving the heat transfer in heat exchangers using fins and other methods has been conducted many years ago.

This literature state of the art chapter aims to include reviews for most aspects regarding the storage system and the techniques used to develop the solar energy storage system. Additionally, for medium and high temperatures in solar energy storage system applications, the PCM is molten salt. Therefore, the first two sections in the experimental state of art focus on the molten salt and nanosalt by reviewing both the preparations methods and thermophysical properties measurements. The other main part of this literature review concerns the heat transfer studies of PCM, nano-PCM, and finned-PCM experimentally. Furthermore, simulation studies of heat transfer numerically for the PCM system have been reviewed and this section was subdivided for three parts dealing with the PCM, nano-PCM, and finned-PCM system. Finally, state of art has been included stating the gaps in knowledge found and considered to study for this research.

2.2 Experimental state of art

2.2.1 Nanosalt synthesis methods

This section is mainly about salts (carbonate, nitrate, chloride, etc.), as the PCM with nanoparticles dispersion, prepared by different methods. There are different methods used to prepare nanosalts on a small scale such as 2-step method and 1-step method for high temperature applications. The 2-step method has been widely used for the preparation of nanosalt by many researchers with different procedures. The 2-step method mainly depends on the water dispersion method. Tiznobaik and Shin (2013a), Dudda and Shin (2013) and Tiznobaik and Shin (2012) used the 2-step method to prepare 1 wt.% silica (SiO_2)-nanosalt by mixing the required amount of salt, nanoparticles and 20 ml of water. Including the water in the sample ensures the dissolution of salt and nanoparticles. Then, this mixture is sonicated using a water bath for 200 min to ensure the good mixing of all components; the sonication procedure ensures low agglomeration of nanoparticles. Followed by the evaporation process, the heating step was done using a hot plate set at 200 ^{0}C for 3 hours to evaporate the water. A similar procedure was carried out by Devaradjane and Shin (2012) to prepare nanosalt of 1 wt.% SiO_2 + HITEC XL (49% sodium nitrate ($NaNO_3$), 30% potassium nitrate (KNO_3) and 21% Calcium nitrate ($Ca(NO_3)_2$) by mole) except that the evaporation time was longer for about 8 hours. Shin and Banerjee (2015), Shin and Banerjee (2011b) and Chieruzzi et al. (2015b) on their own used same procedure but the sonication time was 1 hr 40 min using water bath sonicates. Additionally, all of them used the same concentration and the same type of nanoparticle (1 wt. % SiO_2 nanoparticles) with different types of salt such as carbonate eutectics, chloride eutectics, and potassium nitrate, respectively.

Chieruzzi et al. (2013a) used the same procedure except that the nitrate eutectic salt was prepared first then heated at high temperature of 300 ^{0}C to achieve a complete melting and mixing of the two salts components (60 $NaNO_3$: 40 KNO_3). After that, the resultant mixture was cooled to room temperature to obtain a white solid mixture. A similar method was provided by Lu and Huang (2013) using the same type of nitrate eutectic salt but the evaporation was for 12 hours at 90 ^{0}C followed by a melting inside the oven at 300 ^{0}C for 40 min.

Seo and Shin (2014) used the same method for the preparation of nanosalt by mixing the ternary nitrate salt (59.99 mg of lithium nitrate ($LiNO_3$), 29.19 mg of $NaNO_3$ and 10.881 mg of KNO_3) with 1 wt. % SiO_2 nanoparticle then dispersed the mixture with 20 ml of water followed by a sonication to make sure that nanoparticles are fully dispersed into the salt. After that, a hot plate was used to evaporate the water from the mixture at 300 ^{0}C for 60 min. Yang and Banerjee (2012) studied the effect of nanoparticle size (1 wt. % SiO_2 nanoparticles) on two different types of salt which are alkali chloride salt eutectic (68.490 mg of barium chloride ($BaCl_2$), 24.784 mg of sodium chloride (NaCl), 79.206 mg of calcium chloride ($CaCl_2$) and 25.520 mg of lithium chloride (LiCl)) and the second salt of eutectic mixture of alkali carbonate salt (92.25 mg of lithium carbonate (Li_2CO_3) and 105.75 mg of potassium carbonate (K_2CO_3)). They used the same method for the preparation by firstly mixing the nanoparticles, salt and water together followed by a sonication for 100 min, the heating was done using the hot plate at 200 ^{0}C to evaporate the water and obtain the solid state of nanosalt. Furthermore, Banerjee (2011) studied the effect of dispersing 1 wt.% SiO_2 nanoparticles into chloride salt. The chloride salt and SiO_2 were then dissolved into 20 ml of water afterward sonicated for 100 min. The heating was at 150 ^{0}C using a hot plate to evaporate water from the mixture for 180 min followed by another heating at 300 ^{0}C for 120 min to make sure that the sample was dried and contained no moisture at all.

Jung and Banerjee (2011) used a similar protocol to prepare the nanosalt by mixing the mica nanoparticles with water and nitrate salt ($NaNO_3$: KNO_3 by 60:40 molar ratio), although it had a size range from few nanoscales to a few microscales, the authors assumed it behaved as nanoparticles. The sonication was for 180 min then the evaporation of water used a hot plate at 100 ^{0}C.

The use of stabilizer (surfactant) helps the nanosalt sample to become more stable with less sedimentation or agglomerations of nanoparticles in the nanosalt materials. It seems that the only known published work which studied the effect of the addition of surfactant were conducted by (Liu et al. (2013); Tiznobaik and Shin (2013b); Tao et al. (2015a); Jo and Banerjee (2014); Jo and Banerjee (2015) and Niu et al. (2014)). According to Liu et al. (2013) and Niu et al. (2014), the Arabic gum was used as a surfactant and mixed with multi-walled carbon nanotube (MWCNT) and 20 ml of distilled water then the mixture was sonicated for 60 min. After that nitrate salt ($NaNO_3$: KNO_3 with 60:40 molar ratio) was added to the mixture and another sonication was carried out for another 60 min to prevent the agglomeration of the nanoparticles. On the other hand, Tiznobaik and Shin (2013b) studied the effect of adding a small concentration of hydroxide (0.02%) to the nanomaterial and their results shed there is no nanostructure observed. Furthermore, Tao et al. (2015a) used sodium dodecyl sulfate (SDS) as a surface active agent and they tested the different concentrations of the (SDS) as 1 wt. %, 5 wt. % and 10 wt. %. They made a comparison of three different cases. The first one mixed the MWCNT with the carbonate eutectic salt (Li_2CO_3: K_2CO_3 with 62:38 molar ratio). The second case mixed the carbonate eutectic salt with SDS. The third case mixed carbonate eutectic salt with MWCNT and SDS. The concentrations of MWCNT were 0.25%, 0.5%, 1.0% and 2.5% by weight. They concluded that SDS can improve the dispersion of nanoparticles into the molten salt. However; the decomposition of SDS causes a reduction in the thermal properties of the salt. Furthermore, Jo and Banerjee (2014) reported the effect of using Arabic gum used as a surfactant added to nano-binary carbonate salt. They prepared their nanosalt (0.1 wt. % graphite and binary carbonate salt) by firstly mixing the Arabic gum with graphite nanoparticles and distilled water followed by a sonication for 120 min. After that salt was added to the mixture and another sonication was carried out for an additional 180 min to prevent the agglomeration of the nanoparticles. The resulted nanosalt was put on a hot plate to evaporate the water at 100 ^{0}C with the use of two different methods employing either a large beaker or a petri dish.

In addition, carbonate eutectic salt (Li_2CO_3: K_2CO_3 with 62:38 mole ratios) was mixed with MWCNT of different concentrations such as 0.1 wt. %, 0.5 wt. %, 1 wt. % and 5 wt. % (Jo and Banerjee, 2015). The SDS was used as a surfactant to help the nanosalt to be more stable by preventing the agglomerations of the MWCNT. The preparation of nanosalt followed mixing of MWCNT and 1 wt. % of the surfactant then dispersing the mixture into the distilled water and sonicating for 120 min. After that, eutectic carbonate salt was added to the mixture where the second sonication for 180 min was conducted to ensure a good dispersion of the mixture followed by water evaporation from the nanosalt sample. Moreover, Dudda and Shin (2013) prepared their nanosalt material with a same basic method by mixing salt and nanoparticle. The mixture was then dissolved in 20 ml of distilled water. After a sonication of the mixture for 200 min, a hot plate was used to evaporate the water. To evaporate water from the mixture of nanosalt, a hot plate had been used which was put inside a glove box of 100 ^{0}C with an air filtration circulated in order to give a quick evaporation of water from the mixture. Furthermore, Shin and Banerjee (2014), Tiznobaik et al. (2015) and Shin and Banerjee (2011a) followed the same procedure except that sonication was for 100 min and the evaporation took place under a higher temperature of 200 ^{0}C. Andreu-Cabedo et al. (2014a) prepared the nano-binary nitrate salt with the same principles by weighing the required amount of the salt mixture then distilled water was added to the mixture with a ratio of 1:10. Nanoparticles (SiO_2) were also added and evaporation took place for 1 hour at 100 ^{0}C in order to avoid the boiling of water which could cause a loss of nanoparticle from the nanosalt sample.

Schuller et al. (2015) used the same procedure to prepare nanosalt, starting with the mixing of alumina nanoparticles (Al_2O_3) with the eutectic nitrate binary salt followed by adding distilled water and then ultra-sonication for 2 hours. The evaporation of water was done by using a hot plate at 90 ^{0}C. Riazi et al. (2016) also used the same method for preparing nanosalt of eutectic nitrate binary salt with SiO_2 nanoparticles as indicated previously. The only difference is that the volume of water used in the mixing was 3 ml compared to 20 ml that have been widely used. Additionally, Ho and Pan (2014) prepared nanosalt (20 wt. % Al_2O_3+ Hitec salt) using the water dispersion method. First of all, the Al_2O_3-water was sonicated for 100 min then dispersed into Hitec salt (17.9 g of $NaNO_3$, 102.4 g of $NaNO_2$ (sodium nitrite) and 135.7 g of KNO_3). This is followed by melting for one hour by heating the container surroundings of working samples up to 350 ^{0}C as shown in Figure (2-1). This was then stirred for 180 min and the result nanosalt was heated again at 120 ^{0}C for 180 min to ensure there was no moisture remaining in the sample.

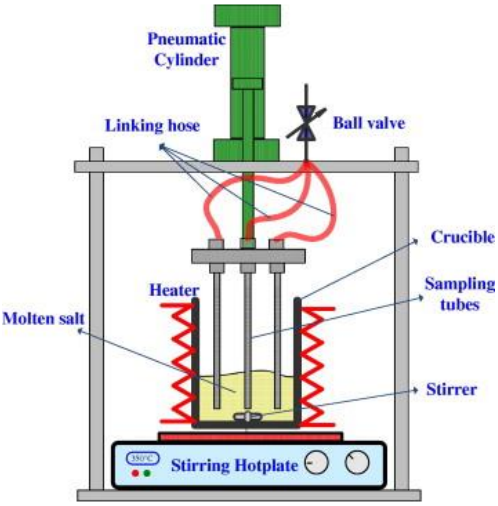

Figure 2-1 shows the schematic diagram of the rig used to prepare the nanosalt by (Ho and Pan, 2014).

In addition, Hu et al. (2017) prepared nanosalt using the water dispersion method. They studied the effect on nanoparticle concentrations (0.5 wt. %, 1 wt. %, 1.5 wt. % and 2 wt. % Al_2O_3-eutectic nitrate salt) on cp values.

On the other hand, Lasfargues et al. (2015) used the mechanical dispersion method to prepare their nano-binary nitrate salt. Their mixture of molten salt and nanoparticles were dried followed by a melting process to prepare well-dispersed nanoparticles inside molten nitrate salt without using water to disperse the nanoparticles. However, they noticed there was an agglomeration of nanoparticles. Additionally, the mechanical mixing of salt and nanoparticles at high temperature had been studied by (Song et al., 2018).

They mixed SiO_2 with a quaternary nitrate ($Ca(NO_3)_2$-$4H_2OKNO_3$-$NaNO_3$-$LiNO_3$) without the addition of water at high temperate of 300 ^{0}C, which is higher than the melting point of this quaternary nitrate salt ($T_{melting}$= 90 ^{0}C). The mixing took place under different times (15 min, 45 min, 90 min, 120 min, and 150 min) and different stirrer speeds (600 rpm, 750 rpm, and 1000 rpm). Chen et al. (2018) did a comparative study of nanosalts prepared by the 2-step method of water dispersion and the mixing at high temperature. The base material was quaternary-mixed nitrate salt ($Ca(NO_3)_2$-KNO_3-$NaNO_3$-$LiNO_3$ (2:6:1:2 in mass ratio)) with a melting point of 85.4 ^{0}C mixed with 1 wt. % SiO_2.

There is a new method used to prepare nanosalt, known as the 1-step method. This method has been studied by few researchers such as (Luo et al., 2017; Lasfargues et al., 2017; Awad et al., 2018a; Lasfargues et al., 2016). The nanoparticles directly prepared in the molten salt depend on the chemical reactions for the precursor used. All of those researchers used the same base material of eutectic nitrate salt. Copper oxide (CuO) nanoparticles have been prepared by the 1-step method by (Awad et al., 2018a; Lasfargues et al., 2017; Luo et al., 2017) using the copper sulphate ($CuSO_4.5H_2O$) or copper oxalate (CuC_2O_4). While Lasfargues et al. (2016) prepared titanium dioxide nanoparticles using titanium (IV) oxysulfate solution ($TiOSO_4$). In this method, there is no need for purchasing nanoparticles in advance or using water to disperse the component of the mixture where nanoparticles are directly prepared inside the molten salt without any preparations in advance.

2.2.2 Thermophysical properties of PCM and nano-PCM

2.2.2.1 Sensible and latent heat measurements

Sensible heat is mainly calculated by the specific heat capacity (cp), as shown in Equation (2-1)

$$\mathrm{q_{sensible}} = \int \mathrm{mass.\,cp.\,dT} \qquad \textbf{Equation 2-1}$$

Where $q_{sensible}$ is sensible heat (J/g. K) and T is temperature (K). Each solid and liquid phases of the PCM has their own $q_{sensible}$ which is depending on their cp and the temperatures range of each phase of the PCM. On the other hand, latent heat (L) depends on the heat absorb or release during the phase change between the solid phase and liquid phase and vice versa.

Moreover, the cp of a material is defined as the amount of heat required to increase the temperature of one gram of the material by 1 ^{0}C. In solar storage application, it is important to increase the cp of the PCM in order to store a large amount of energy which reflects on the efficiency of the solar energy storage system. This can be achieved by adding nanoparticles into the PCM. Table (2-1) shows the literature researches conducted on the solar storage material (salt/nanosalt) for solar energy storage application. The sensible heat and latent heat has been measured using the differential scanning calorimetry (DSC) device that measures heat flow vs the temperature/time. Additionally, there are different types of nanoparticles (with different sizes and concentrations) were dispersed into different types of molten salt (molten salt used as PCM in the storage system to store the solar energy) which are studied extensively by many researchers.

SiO_2 nanoparticles were tested by many researchers such as Shin and Banerjee (2011b) used 1 wt. % SiO_2 nanoparticles, with size in a range of (20-30 nm), dispersed into the chloride eutectics. They concluded an enhancement in cp of nanosalt by 14.5 %. On the other hand, Tiznobaik and Shin (2013a) studied the effect of 1 wt.% SiO_2 nanoparticles size on the carbonate eutectics salt (Li_2CO_3: K_2CO_3, with 62:38 molar ratio). The sizes of the nanoparticles were 5 nm, 10 nm, 30 nm and 60 nm to obtain the optimum diameter that enhanced the cp of nanosalt (Tiznobaik and Shin, 2013a). They found out that improvements in cp of nanosalt by 25 %, 29 %, 23 % and 28 % for 5 nm, 10 nm, 30 nm and 60 nm, respectively. They considered that this improvement in cp of nanosalts relies on the formation of the needle-like structures due to the small surface area of nanoparticles. In their related research work, Tiznobaik and Shin (2012) showed that SiO_2 of 5 nm in size enhanced cp of nanosalt by 20%. This emphasized that there is something during the preparation or cp measurements which needs to be considered carefully because the same researchers even though uses same procedures reported varying enhancement of cp of 20% and 25% in their articles.

However, Shin and Banerjee (2015) used the same concentration of 1 wt. % and the same salt but the size of nanoparticle was 10 nm (10 nm was the manufacturer's specification; 23 nm in diameter was observed experimentally) and the cp enhancement they obtained was in the range of 5-15 %. The enhancements obtained by Tiznobaik and Shin (2013a) are better than those of Shin and Banerjee (2011b) and Shin and Banerjee (2015). Where the base salt used by Tiznobaik and Shin (2013a) is different from that used by Shin and Banerjee (2011b) and this resulted with a remarkable conclusion that carbonate salt can have higher cp compared with chloride etuctics when nanoparticles are added to these salts. In addition, the sonication time during the preparation of nanosalt was 100 minutes for the work done by both Shin and Banerjee (2011b) and Shin and Banerjee (2015) but Tiznobaik and Shin (2013a) used double of the time for sonication. Although the same material was used by (Shin and Banerjee (2015) and Tiznobaik and Shin (2013a)) the increase in cp by the work carried out by Tiznobaik and Shin (2013a) was better due to the good dispersion of nanoparticles ensured by the long time of sonication.

Furthermore, dispersing 2 wt. % of SiO_2 nanoparticles into a binary mixture of chloride salt (LiCl: KCl by 45:55 molar ratio) resulted in an improvement in cp of nanosalt in the solid phase by 12% and 15% in the liquid phase (Sambasivam, 2015). These results ensure the benefits of adding nanoparticles into the molten salt which could be due to the formation of the nanostructure (Sambasivam, 2015). 1 wt.% SiO_2 (with a size of 10 nm) dispersed in eutectic carbonate salt (Li_2CO_3: K_2CO_3 with 62:38 ratio) studied by Tiznobaik et al. (2015), Shin and Banerjee (2011a) and Tiznobaik and Shin (2013b). Tiznobaik et al. (2015) got 26% enhancement in cp value without the addition of surfactant (sodium hydroxide). On the other hand, Shin and Banerjee (2011a) showed 19-24% improvement in cp value which is similar to the Tiznobaik and Shin (2013b) result of 27% enhancement. It, therefore, showed that long-time sonication would enhance cp. In addition, the same salt and nanoparticles with a diameter of the nanoparticle of 10 nm and larger concentration (1.5 wt. %) had been tested. The results showed a higher enhancement in cp by 34% in solid phase and 101 % in liquid phase for the case they used a petri dish as a container for the samples to evaporate the water from the samples compared with using of bottle glass which gave them an enhancement of 22 % in solid phase and 74 % in liquid phase (Shin and Banerjee, 2010). The reason that Shin and Banerjee (2010) got these results is that they removed out the coarse powder from the sample in the petri dish method so there is no agglomerate of nanoparticles compared with the large bottle used which contains the agglomeration. Besides the high temperature used for the evaporation in the method of the large beaker was 100 ^{0}C while for the petri-dish method 60 ^{0}C only used, where increasing the temperature will help the nanoparticles to agglomerate which is clearly noticeable in the result they obtained.

Dudda and Shin (2013) tested the same concentration and range of diameters as Tiznobaik and Shin (2013a) but with the different type of salt which was eutectic nitrate salt ($NaNO_3$: KNO_3 with 60:40 molar ratio). It was concluded that increasing the size of nanoparticles would lead to a better enhancement where the improvements in cp were 8 %, 12 %, 19 % and 27 % for 5 nm, 10 nm, 30 nm and 60 nm, respectively. This shows a linear relationship between the size of nanoparticle and the enhancement of cp which is in contrast to the results got from Tiznobaik and Shin (2013a) where the cp of nanosalt (with nanoparticles diameter equals to 10 nm) was above all the others diameters and the ratio of enhancement in cp were all larger than that the result from (Dudda and Shin, 2013). As seen from the different values of enhancement got from Tiznobaik and Shin (2013a), the use of chloride salt has a better enhancement of its thermal properties when SiO_2 nanoparticles dispersed in it compared with the work carried out by Dudda and Shin (2013) as the same procedure for the preparation of nanosalt and same material were used. The only difference was with the type of salt used.

Chieruzzi et al. (2013a) tested the SiO_2 with the same salt used by Dudda and Shin (2013), the diameter of nanoparticle was 7 nm and concentrations were 0.5 wt.%, 1 wt.%, and 1.5 wt.%. Their results showed that optimum concentration was 1 wt.% which gave the higher enhancement by 14.9 % in the solid phase and 0.8 % in the liquid phase. At the same time, 1.5 wt.% nanosalt showed only 2% enhancement in the solid phase with no enhancement in the liquid phase which is converse to the result obtained by Shin and Banerjee (2010). The results indicate that increasing concentration causes a negative effect of the nanoparticles on thermal properties of the salt which could be due to easier agglomeration hence bringing out a decrease in the cp.

Additionally, Chieruzzi et al. (2015b) tested nitrate single salt (KNO_3) with 1 wt. % SiO_2. The size of SiO_2 was 7 nm. They obtained the result that the cp of nanosalt increased in a range from 5 to 9.5 % in the solid phase which was higher than that obtained by Dudda and Shin (2013). Moreover, the enhancement in cp of the liquid phase was 6% which is less than the 13% obtained by Dudda and Shin (2013). This difference in enhancement of cp values of the nanosalt between these two papers can be related to the lower time of sonication were increasing the sonicated time is a better way to ensure a good dispersion of nanoparticles. Furthermore, a single nitrate salt (KNO_3) was considered by Chieruzzi et al. (2015b) while a mixture nitrate salt ($NaNO_3$: KNO_3 by 60:40 molar ratio) was studied by Dudda and Shin (2013).

Andreu-Cabedo et al. (2014b) tested 12 nm in diameter of SiO_2 dispersed into eutectic nitrate salt ($NaNO_3$: KNO_3 by 60:40 molar ratio) with different nanoparticles concentrations of 0.5 wt.%, 1 wt.%, 1.5 wt. % and 2 wt.%. The optimum concentration was 1 wt.% with an improvement in the values of cp by 25% at a temperature range of 250 ^{0}C – 420 ^{0}C. On the other hand, bigger sizes of SiO_2 nanoparticles (30 nm in diameter) had been tested by dispersing these nanoparticles inside a HITEC XL salt of (49% $NaNO_3$, 30% KNO_3 and 21% Ca $(NO_3)_2$ by mole) (Devaradjane and Shin, 2012). And the increase in the cp was in the range of 14.4 -15 %. The comparison between the work of Andreu-Cabedo et al. (2014b) and Devaradjane and Shin (2012) indicated that the increase in the diameter of nanoparticles will give fewer enhancements in the cp of nanosalt. Furthermore, the salt with many components (e.g. the HITEC XL) will be difficult to control its stability along with the stability consideration of nanoparticle dispersed inside this type of salt. These reasons could be why the enhancement in the cp of the HITEC XL salt is less than what is obtained by the nitrate eutectic.

According to Seo and Shin (2014), the enhancement in cp was 13 % by dispersing SiO_2 into the ternary salt (59.99 mg of $LiNO_3$, 29.19 mg of $NaNO_3$, and 108.81 mg of KNO_3). They attributed this enhancement in cp to the formation of the fractal like nanostructure. Yang and Banerjee (2012) studied the effect of dispersing SiO_2 nanoparticles into two different types of salt such as alkali chloride salt eutectics (68.490 mg of $BaCl_2$, 24.784 mg of NaCl, 79.206 mg of $CaCl_2$ and 25.520 mg of LiCl) and eutectic mixtures of alkali carbonate salts (92.25 mg of Li_2CO_3 and 105.75 mg of K_2CO_3). They observed that cp can enhance if the size distribution is studied rather than assume it has a fixed value. On the other hand, according to Banerjee (2011), the enhancement in cp was 7% for the eutectic mixture (68.490 mg of $BaCl_2$, 79.206 mg of $CaCl_2$, 25.520 mg of LiCl, and 24.784 mg of NaCl) with 1 wt. % of SiO_2. Furthermore, 18 % enhancement in cp of eutectic nitrate salt when SiO_2 nanoparticles are dispersed into it was reported by (Riazi et al., 2016). They discussed that reducing the amount of water to 3 ml needs only 70 ^{0}C to be evaporated which means avoiding agglomeration of nanoparticle where the temperature is low compared with previous work where the evaporation process took place at the temperature more than 100 ^{0}C. Additionally, the amount of water is low (3 ml) which requires less time to evaporate than others (around 20 ml). At the same time, the controlling of the sonication power will help to produce a stable mixture. Furthermore, Chen et al. (2018) found that high temperature mixing preparation method of 1 wt.% SiO_2-nanosalt showed an increment in cp of nanosalt by 16.4% and good stability was shown after 2000 hours.

All the above discussed literature concerned SiO_2 nanoparticles types. Following is the literature regarding the effects of other types of nanoparticles on salts.

Another type of nanoparticle used by researchers is the Al_2O_3 nanoparticle. Lu and Huang (2013) used different concentrations of 0.9, 2.7, and 4.6 vol. % and they tested two different diameters as 13 nm and 90 nm in eutectic nitrate salt as ($NaNO_3$: KNO_3 with 60:40 molar ratio). Their results showed no enhancement in cp of nanosalt. Chieruzzi et al. (2013a) dispersed Al_2O_3 nanoparticle (with a diameter of 13 nm) in eutectic nitrate salt as ($NaNO_3$: KNO_3 with 60:40 molar ratio) with different concentrations of 0.5 wt. %, 1 wt. %, 1.5 wt. %. They concluded that 1 wt. % Al_2O_3–nanosalt showed an increase in the cp of the solid phase by 19.9% and the liquid phase by 5.9% while other concentrations did not show any enhancement. Chieruzzi et al. (2015b) used the same nanoparticle with the same diameter of 13 nm but the base salt was KNO_3 with no enhancement at all in this type of nanoparticles. In contrast to the case of SiO_2 nanoparticles, the eutectic mixture of salt showed enhancement in cp value when Al_2O_3 nanoparticles were added to this salt in comparison to the pure salt (KNO_3). This can be related to the methodology followed for the preparation of Al_2O_3 nanoparticle with nitrate eutectic ($NaNO_3$: KNO_3 by 60:40 molar ratio) where the salt mixture melted to ensure a stable mixture of salt before addition of Al_2O_3 nanoparticles into it. Furthermore, Shin and Banerjee (2014) measured the cp of 1 wt.% Al_2O_3- eutectic carbonate salt (Li_2CO_3: K_2CO_3 with 62:38 by molar ratio). The size of the nanoparticles was 10 nm. Their result showed there was an enhancement in cp value by 32%. Tiznobaik et al. (2015) used the same salt as Shin and Banerjee (2014) with the same diameter and concentration of nanoparticles, and they obtained a similar enhancement of 33 %. The mechanical dispersion method was used to prepare nanosalt (Song et al., 2018). Their results demonstrated that the improvement in cp value was related to the mixing time and stirrer speed during the preparation. They observed a 17% increment in cp of nanosalt at 15 min and 750 rpm preparations parameters of nanosalt.

Furthermore, Schuller et al. (2015) measured the cp of Al_2O_3-nanosalt over a wide range of concentrations of Al_2O_3 such as 0.125 wt. %, 0.25 wt. %, 0.5 wt. %, 0.75 wt. %, 1 wt. %, 1.5 wt. % and 2 wt. %. The size of nanoparticles was 40 nm and the base material was eutectic nitrate salt ($NaNO_3$: KNO_3 by 60:40 mole fraction). Their results show a maximum enhancement in cp of 30.6% at 0.75 wt. %. This increase in cp values by the dispersing of Al_2O_3 nanoparticles showed the benefit of nanoparticles inside salt with an optimum weight concentration. Additionally, one of the reasons behind this improvement in cp values could be due to the fact that the evaporation of water from the dissolved mixture of salt and nanoparticle was at a low temperature equal to 100 ^{0}C and 90 ^{0}C in Shin and Banerjee (2014) and Schuller et al. (2015), respectively. This resulted in less agglomeration of nanoparticles inside the salt. Furthermore, Al_2O_3 nanoparticles were dispersed in Hitec salt (53% KNO_3 + 40% $NaNO_2$ + 7% $NaNO_3$, mol.%) and the cp of the nanosalt was measured by Ho and Pan (2014). The size of nanoparticles was 50 nm and the effect of different concentrations on the cp values was studied. The results showed that optimum concentration was 0.063 wt. % which gives 19.9% enhancement in cp while 2 wt. % of Al_2O_3 nanoparticles represents the worst concentration.

Moreover, MALIK (2010) dispersed Al_2O_3 nanoparticle with different concentrations as 0.1 wt.%, 1 wt.% and 10 wt.% into a Hitec solar salt and their results show that 0.1 wt. % and 1 wt.% did not showed any enhancement in the cp of the nanosalt while the higher concentration as 10 wt.% gave 5.5 % increase in cp of the nanosalt. In addition, Hu et al. (2017) reported that cp of nanosalt increased with the increment in Al_2O_3 concentrations from 0.5 wt.% to 2 wt.% by cp improvement from 1.9% to 8.3%. Furthermore, Muñoz-Sánchez et al. (2017) measured the cp of eutectic nitrate salt and nanosalt (1 wt. % Al_2O_3 + eutectic nitrate salt). The size of Al_2O_3 nanoparticles was 10 nm. They mentioned that the differences between the cp measurements among the researchers are due to the procedure of the preparation of nanosalts and the method used for the measurements. Particularly, the types of crucibles and the sample size are the main factors that affect the cp measurements.

A hybrid nanoparticle of SiO_2 and Al_2O_3 was employed by Chieruzzi et al. (2013a) and Chieruzzi et al. (2015b). In the work of Chieruzzi et al. (2013a), the diameter of the hybrid nanoparticle was in the range of 2 to 200 nm with different concentrations of 0.5 wt. %, 1 wt. %, 1.5 wt.% were dispersed into the eutectic nitrate salt ($NaNO_3$: KNO_3 by 60:40 molar ratio). They got an increase in cp at the solid phase 57.7% at 1 wt. % and 34.8% at 1.5 wt. % and the liquid phase enhanced by 22.5% at 1 wt. % and 1.5% at 1.5 wt. % while no enhancement was observed at 0.5 wt. %. On the other hand, Chieruzzi et al. (2015b) used the same material and size of nanoparticles but changed the salt to KNO_3 and only one concentration was studied (1 wt. %). The cp of the solid phase was enhanced by 4.7%.

In most cases, the results indicated that nanoparticles do not affect in a positive way on the liquid phase while most time the cp of the solid phase is increased with the presence of nanoparticles. This could be due to the higher temperature at a liquid phase which could help the aggregation of nanoparticle that leads to this decreasing in the cp compared with the solid phase temperature of salt.

The third type of nanoparticles which is studied was graphite. Jo and Banerjee (2014) studied graphite nanoparticles with 50 nm in diameter and 0.1 wt. % concentration dispersed into a binary carbonate salt (Li_2CO_3: K_2CO_3 by 62:38 molar ratio) with an improvement in cp at liquid phase by 57% and in the solid phase by 40%. Jo and Banerjee (2011) used molecular dynamics simulation to study the effect of adding graphite nanoparticles on eutectic carbonate molten salt (same molten salt studied by Jo and Banerjee (2014) with a variation in nanoparticle diameter from 0.724 nm to 1.836 nm). Their work presents a simulation study of the effect of disk shape graphite nanoparticles on the interfacial resistance between molten salt and nanoparticles. Even though the concentration was so low there is a noticeable large improvement in cp values (Jo and Banerjee, 2014). In addition, Arabic gum was employed as a surfactant that helps the stability of nanoparticles and the dispersion of them in the base salt with the minimizing of the agglomerations. The surfactant could be one of the reasons that helped graphite to give this good enhancement in the cp of nanosalt. Side by side, the shape of graphite nanoparticle was disc-shaped lamellar with better enhancement in cp in comparison with carbon nanotube (CNT) which has a tube-shape cylindrical structure.

Tao et al. (2015a) studied single-walled carbon nanotubes (SWCNT), MWCNT, Graphene and fullerene (C60) nanoparticles were mixed with carbonate salt (62 mol. % Li_2CO_3: 38 mol. % K_2CO_3) with different concentrations of nanoparticles as 0.25%, 0.5 %, 1 %, 2.5%, 5% and 10%. The effect of surfactant (SDS) was studied where SDS was added to the nanosalt with different mass ratios as 1%, 5%, and 10%. They concluded that graphene has the best enhancement in cp due to its larger surface area followed by SWCNT, MWCNT then C60 and the surface active agent should be added with a minimum concentration to reduce its negative effect on the cp (Tao et al., 2015a). The addition of surface active agent was also considered by this publication and it was found that SDS ($NaC_{12}H_{25}SO_4$) and sodium dodecyl benzene sulfonate (SDBS, $C_{18}H_{29}NaO_3S$) with purity P99%, which are the surface active agent, these added to the nanosalt in order to enhance the dispersion of nanoparticle inside the salt and eliminate the agglomeration. However, the results showed that the surface active agent would minimize the thermal properties of the nanosalt and there is an optimum percentage need to be added to reduce the negative effects of it.

SWCNT, Graphene, and C60 were studied by Tao et al. (2015a) and Jo and Banerjee (2011). The salt used was carbonate salt (62 mol. % Li_2CO_3: 38 mol. % K_2CO_3) with different ranges of nanoparticles concentrations investigated in each paper. Tao et al. (2015b) studied a different range of concentrations as 0.1 wt. %, 0.5 wt. %, 1.0 wt. %, 1.5 wt. %, 2.5 wt. % and the surfactant used was SDS with purity P99%. The diameter of nanoparticles was as follows 5-20 nm, 10 nm-20 nm, 500 nm- 2 micrometer for SWCNT (long cylinder), Graphene (square sheet) and C60 (spherical), respectively. They obtained an enhancement in cp of solid phase using SWCNT by 18.7%. The enhancement in Graphene was 16.8% at 1.5 wt. %, and for C60 it was 16.8% at 2 wt. %. The enhancements of cp in the liquid phase were as follows: using SWCNT by 14.4%, and for Graphene it was 18.57% at 1.5 wt. %, and for C60 it was 12.05% at 2 wt. %. On the other hand, Jo and Banerjee (2011) presented a simulation of nanosalt using molecular dynamic software with the consideration of different shapes as SWCNT with a cylinder, Graphite as disk and C60 as a sphere. They studied the interfacial resistance between salt and nanoparticles with different diameters of the SWCNT with 0.271 nm-

1.356 nm and graphite with 0.724 nm-1.836 nm and C60 with 0.662 nm (Jo and Banerjee, 2011).

Furthermore, Tao et al. (2015b) studied MWCNT with a diameter of 10 nm and 50 nm with an enhancement in cp of 12.4 % and 14.52 % in solid phase and liquid phase respectively. Another study of MWCNT added to eutectic nitrate salt ($NaNO_3$: KNO_3 by 60:40 molar ratio) with different concentrations of 1.5 wt.% and 0.5 wt.% was conducted by Niu et al. (2014) and Liu et al. (2013). Liu et al. (2013) concluded that a smaller concentration of MWCNT is better in the enhancement of cp of the nanosalt. According to Liu et al. (2013), the enhancement of cp of the nanosalt is due to the increase of the interfacial thermal resistance. In contrast, Niu et al. (2014) mentioned that nanoparticles enhanced the value of cp of molten salt with a careful choice of the concentration.

Moreover, MWCNT with diameter range (10-30 nm) and length of 1.5 micrometres was reported by (Jo and Banerjee, 2015). Their results showed an improvement of the cp in the solid phase by about 12% while in the liquid phase approximately 15% in the case of 5 wt. % of the concentrations. They concluded that the enhancement of cp value increases with increase in the concentration. However, some papers mentioned that increasing the concentration will reduce the enhancement of the cp values. The continuous enhancement in the cp values by this work could be due to the use of the surfactant that helps the nanoparticles to be stable and well dispersed into the salt results with this improvement. Furthermore, the type and dimensions of nanoparticles used have large effects on the results also.

Magnesium oxide (MgO) nanoparticles were considered by Tiznobaik et al. (2015) at 1 wt.% concentration and 10 nm in diameter into a carbonate salt (Li_2CO_3: K_2CO_3 at 62:38 molar ratio). They reported that the enhancement in cp was 22%.

The use of Mica nanoparticles with different concentrations (0.5 wt.%, 1 wt.%, and 2 wt.%) gave an enhancement in cp of the nitrate salt of 15 % in solid phase and nearly 19% in the liquid phase (Jung and Banerjee, 2011). They concluded that this improvement in cp is due to the layering formed in the interface between the salt and solid nanoparticles.

Copper oxide (CuO) and titanium dioxide (TiO_2) nanoparticles were considered by Lasfargues et al. (2015) with a concentration of 0.1 wt.%, 0.5 wt.%, 1 wt.%, and 1.5 wt.% and diameter of CuO 29 nm and TiO_2 of 34 nm dispersed into eutectic nitrate salt ($NaNO_3$: KNO_3 with 60:40 molar ratio) resulted with an enhancement of 10.48% at 440 ^{0}C for 0.1 wt. % CuO and 4.95% at 440 ^{0}C for 0.5 wt. % TiO_2. The results indicated that TiO_2 did not affected by the concentration in contrast to the CuO which is affect by the concentration where at lower concentrations values a better enhancement can be obtained. It is reported that nanostructure, which formed between the base material and the added nanoparticles, can be one of the reasons that lead to enhancement for cp of molten salt. This enhancement in the cp of nanosalt could be due to the large surface area of these tiny particles (Chieruzzi et al., 2013b). They conclude that Brownian motion is not responsible of the enhancement in the cp, because the last one is not a transportation property which is not affected by the motion.

Ercole et al. (2017) tried to predict a correlation depending on the literature review for the effect of SiO_2 on different types of molten salt (eutectic nitrate salt and binary eutectic carbonate salt (Li_2CO_3-K_2CO_3)). However, this predicted equation of the cp has limitations in term of concentrations, temperatures, and the size of nanoparticles. For instance, cp of eutectic nitrate salt can be calculated according to Equation (2-2). Equation (2-2) can only be used for a concentration equals 0.01, the temperature range between 150 ^{0}C and 190 ^{0}C and nanoparticles size between 5 nm and 60 nm.

$$\mathrm{cp} = \left(5.980 \text{ x } 10^{-5} - 1.881 \text{ x } 10^{-6}\mathrm{d_p} + 1.853 \text{ x } 10^{-8}\mathrm{d_p^2}\right)\mathrm{d_p T} + 4.228 \text{ x } 10^{-1}\ \mathrm{T}^{0.20477}$$

Equation 2-2

The above equations are for the case of the nitrate salt. Where $\mathrm{d_p}$ represents the diameter of nanoparticles (nm) and T is the temperature (K).

There are some models used to predict the improvement in cp when nanoparticles are added to the molten salt and these models are mentioned by many researchers for example (Seo and Shin, 2014). The classical model of effective specific heat can be given by the Equation (2-3) (Seo and Shin, 2014).

$$\mathrm{c_{p,nf}} = \frac{\rho_{\mathrm{np}}\emptyset_{\mathrm{np}}\mathrm{c_{p,np}} + \rho_{\mathrm{f}}\emptyset_{\mathrm{f}}\mathrm{c_{p,f}}}{\rho_{\mathrm{np}}\emptyset_{\mathrm{np}} + \rho_{\mathrm{f}}\emptyset_{\mathrm{f}}}$$

Equation 2-3

where $\mathrm{c_{p,nf}}$, $\mathrm{c_{p,np}}$ and $\mathrm{c_{p,f}}$ represent cp of nanosalt, nanoparticle and salt (J/g. K). $\emptyset_{\mathrm{np}}$ and $\emptyset_{\mathrm{f}}$ are the volume fraction of nanoparticles and salt. Both of ρ_{np} and ρ_{f} are the density of nanoparticle and salt (kg/m^3). However, this model does not show enhancement in cp unlike the most of the experimental results and this discrepancy is due to the lower value of cp of nanoparticles compared to the salt. At the same time, the concentration is relatively low and this can be the reasons behind the lower value of cp of nanosalt.

Most of the literature researches reported the reason of the increase in cp of the molten salt when nanoparticles dispersed into it due to the following three modes (Chieruzzi et al. (2015b), Shin and Banerjee (2011b), Tiznobaik and Shin (2013a), Lasfargues et al. (2015) and Lu and Huang (2013)). Mode 1 represents that the improvement of cp is due to the higher values of cp of nanoparticles compared with the base material. This is not applied to the case of nanosalt where cp of molten salt is larger than that of the nanoparticles used in the respective work. This model is more relevant to the classical model as shown in Equation (2-3), as explained earlier.

As the concentration of nanoparticles is low, for example, 0.01 by weight, and the value of cp is low for nanoparticles, then Equation (2-3) does not give enhancement in the calculated value of cp of nanosalt. This is in contrast to experiments where a noticeable enhancement can be observed. Therefore, this model needs to be expanded and needs to include more effective factors such as the shape of nanoparticles, the size and the interfacial area formatted at the surface of the nanoparticle and the molten salt molecular structure.

Mode 2 argues that cp of nanosalt increases because the large surface area possessed by the nanoparticles causes an increase in thermal resistance between nanoparticles and the molecular structure of the salt resulting in a rise in the interfacial interaction between them. Mode 3 indicates the influence of the molecular structure of base salt on the surface of nanoparticles as semi-solid layers having larger thermal properties compared with the base salt without nanoparticles. Dudda and Shin (2013) proposed that molten salt molecules formed compressed layers on the surface of nanoparticles, as this layers have higher cp which lead to increase cp of nanosalt. Additionally, the mass fraction of these layers depends on the size and concentrations of nanoparticles. The cp of the interfacial layer has a significant effect on the overall cp of nanosalt as shown in Equation (2-4).

$$c_{p,nf} = \frac{\rho_{np}\emptyset_{np}c_{p,np}+\rho_c\emptyset_c c_{p,c}+\rho_f\emptyset_f c_{p,f}}{\rho_{np}\emptyset_{np}+\rho_c\emptyset_c+\rho_f\emptyset_f}$$ **Equation 2-4**

where $c_{p,c}$, $\emptyset_c$ and ρ_c represent c_p, volume fraction and density of the compressed layer (interfacial layer), respectively. The above mode 2 and mode 3 can be considered as the reasons that enhance cp of the molten salt when nanoparticles are dispersed into it.

Additionally, Chieruzzi et al. (2013a) measured the latent heat of salt/nanosalt. They concluded that almost all their nanosalt increased the latent heat by 15% apart from TiO_2-nanosalt which increased by only 5%. Moreover, Chieruzzi et al. (2015b) measured the latent heat of single potassium salt and nanosalt. They observed that 1 wt.% SiO_2-nanosalt increased the heat of fusion by 12%. They suggested that the agglomerated nanoparticles are the reason behind this increment in the latent heat. Furthermore, the latent heat had been measured of different types of nitrate salt (single salt KNO_3 or binary eutectic nitrate salt) and nanosalts by (Awad et al., 2018b). The increments in latent heat value depend on the concentrations and the types of nanopartricle materials.

2.2.2.2 Thermal conductivity measurements

Basically, thermal conductivity (k) is defined as a material‘s ability to conduct heat while the material does not move (Siva et al., 2010). According to Fourier’s law k represents the ratio of heat flow (q) to thermal gradient (dT⁄dx) (Louie, 2011) as shown in Equation (2-5), where A is the area (m^2).

$$q = -k\,A\,(dT/dx)$$ **Equation 2-5**

There are many different methods used to measure k of the molten salt. The steady state method depends on the heat conduction according to Fourier‘s law either in two parallel plate or concentric cylinders. The method of parallel plates basically heats the top plate and depends on the heat transfer between the top and bottom plates by the fluid in-between these regions. The advantage of parallel plates is that it is a simple design, however, there are issues with this method, for instance, the heat lost by convection from the fluid region lead to inaccurate results and also the insulation needs to be effective or the results will not be accurate. The parallel hot plate method reported by Dasgupta and Umarji (2005) and the working temperature they used was between room temperature and 700 K.

Another method used to measure k of the material is the concentric cylinders steady state method. This method was used to measure k of molten salt by (Gechuanqi et al. (2014); White and Davis (1967); Smirnov et al. (1987); Santini et al. (1984) and Tufeu et al. (1985)).

Omotani and Nagashima (1984), Omotani et al. (1982), McDonald and Davis (1971), Lee et al. (1999) and Nagasaka and Nagashima (1981) reported the measurement of k of molten salt using the transient hot-wire Method. Omotani et al. (1982) tested a pure $NaNO_3$ and eutectic mixture of $NaNO_3$: KNO_3 in range of temperature between 225 ^{0}C and 320 ^{0}C. Their results showed a linear relationship between temperature and k. They stated that the hot wire method failed at high temperature because of the differences between the thermal expansion coefficient of the wire and coating material. In addition, McDonald and Davis (1971) used the transient hot wire method to measure k of the salt at higher temperature of 673 K while Omotani et al. (1982) worked at a temperature of 590 K.

Moreover, Warzoha and Fleischer (2014) used the hot disk method to design a measurement of k for three different types of fluid, i.e. deionized water, copper sulfate, glycerol, and ethylene glycol using the Fluent software. There are few studies conducted on k when nanoparticles are dispersed into the base fluid. For instance, Fox et al. (2013) measured k values and evaluated the effect of many different types of nanoparticles such as SiO_2, Al_2O_3 whiskers, Al_2O_3 spheres, gold (Au), zinc oxide (ZnO), CuO, iron II oxide (Fe_2O_3), MWCNT, SWCNT and carbon black dispersed in ionic liquid of 1-Butyl-2,3-dimethylimidazolium bis trifluoromethylsulfonyl) imide [C4mmim][Tf2N], which is working as a HTF used in solar energy system. Their finding was that nanoparticles' morphology has a big effect on the enhancement of k and the stability of nanoparticles. The whiskers shape is found to improve the thermal conductivity of nanofluids better than nanoparticles with a spherical shape. On the other hand, Lee et al. (1999) reported that the transient hot wire method is not preferred for electrically conductive materials and needs to be avoided especially in the case when metallic nanoparticles (i.e. Cu and Al) are used with the base material. Nanofluids are likely to be electrically conducting because metallic nanoparticles and the suspending fluid such as water are electrically conducting materials, so the ordinary transient hot-wire technique cannot be used. Therefore, Nagasaka and Nagashima's method has been adopted in this experiment. However, the ceramic coated wire can be used to solve the problem of the electrically conducting materials (Nagasaka and Nagashima, 1981).

Thermal conductivity (k) of eutectic nitrate salt with Al_2O_3 nanoparticles was measured using the laser flash analysis (LFA) and it was found that adding nanoparticle to molten salt decreases its k in the temperature range between 65 ^{0}C - 145 ^{0}C (Schuller et al., 2012). In contrast, Shin (2011) used the LFA to measure k of a solid phase of eutectic carbonate salt (Li_2CO_3: K_2CO_3 with 62:38 molar ratio). They observed an increase using disperse 1 wt. % SiO_2 nanoparticles with 37% - 47%.

Additionally, Myers Jr et al. (2016) used LFA to measure k of three different molten salts as $NaNO_3$, KNO_3 and eutectic nitrate salt ($NaNO_3$: KNO_3 with 60:40 molar ratio) with dispersing of CuO nanoparticle with 2 vol. %, 3 vol. % and 4 vol. % and size of 40 nm. Their results demonstrate that adding 2 vol. % of CuO nanoparticles in the molten salt can enhance k values of $NaNO_3$ below 150 ^{0}C while in the case of KNO_3 below 300 ^{0}C where the improvement of k values in the range of working temperature was observed for the case of nano-KNO_3 and nano-eutectic nitrate salt ($NaNO_3$: KNO_3 of 60:40 molar ratio). According to their viewpoint the enhancement is due to the formation of nanostructure between the nanoparticles and the molten salt. In addition, the values of k of nanoparticles are larger than those of the salt which is one of the reasons that causes this improvement in k values of nanosalt.

Table 2-1 the summarized of different types and properties of nanoparticles added into different types of salt

No	Name of authors	Type of nanoparticles	Concentration of nanoparticles	Size of nanoparticles	Type of molten salt used
1	(Shin and Banerjee, 2011b)	SiO_2	1 wt.%	20–30 nm	Chloride eutectics.
2	(Shin and Banerjee, 2010)	SiO_2	1.5 wt.%	~ 10 nm	Lithium carbonate and potassium carbonate.
3	(Lu and Huang, 2013)	Al_2O_3	0.9, 2.7, and 4.6 vol.%,	13 nm, 90 nm	Nitrate molten salt of 60 wt. % of $NaNO_3$ and 40 wt. % of KNO_3.
4	(Tiznobaik and Shin, 2013a)	SiO_2	1 wt.%	5, 10, 30, and 60 nm	Lithium carbonate and potassium carbonate (62:38 by molar ratio).
5	(Dudda and Shin, 2013)	SiO_2	1 wt.%	5 nm, 10 nm, 30 nm, and 60 nm.	Nitrate molten salt of 60 wt. % of NaNO3 and 40 wt. % of KNO3.
6	Chieruzzi et al. (2013a)	SiO_2, Al_2O_3, mix of (SiO_2-Al_2O_3)	0.5, 1.0, and 1.5 wt. %	SiO_2 = 7 nm, AL_2O_3= 13 nm, Hybrid nanoparticles = 2 to 200 nm.	Nitrate molten salt of 60 wt. % of NaNO3 and 40 wt. % of KNO3.

No	Name of authors	Type of nanoparticles	Concentration of nanoparticles	Size of nanoparticles	Type of molten salt used
7	(Jo and Banerjee, 2014)	Graphite	0.1 wt.%	50 nm	Binary carbonate salt mixture with 62:38 molar ratio of lithium carbonate (Li_2CO_3) and potassium carbonate (K_2CO_3), respectively.
8	(Tao et al., 2015b)	SWCNT, MWCNT, Graphene, C60	0.1 wt.%, 0.5 wt.%, 1 wt.%,1.5wt.%, 2.5 wt.%	SWCNT = 5-20 nm, MWCNT = 10-50 nm Graphene =10-20 nm, C60= 500 nm- 2 micro-meter.	Binary carbonate eutectic salts (62 mol. % Li_2CO_3: 38 mol. % K_2CO_3).
9	Chieruzzi et al. (2015b)	SiO_2, Al_2O_3, hybrid of SiO_2-Al_2O_3 (by 86-14 wt. %)	1 wt.%	SiO_2= 7nm, AL_2O_3 =13 nm Hybrid (SiO_2-Al_2O_3) =2-200 nm.	KNO_3
10	(Shin and Banerjee, 2015)	SiO_2	1 wt.%	10 nm manufacturer’s specification; 23 nm in diameter was observed experimentally.	Lithium carbonate and potassium carbonate with (62:38 molar ratio).
11	(Jo and Banerjee, 2011)	SWNT, fullerene (C60), graphite sheet were used to represent different shapes of cylinders, a spheres, and disks, respectively.		Diameters of SWNTs and the graphite particles were varied from to a fixed value of 6.62 Å (=0.662 nm).	Carbonate salt eutectic which consists of lithium carbonate (Li_2CO_3) and potassium carbonate

No	Name of authors	Type of nanoparticles	Concentration of nanoparticles	Size of nanoparticles	Type of molten salt used
					(K_2CO_3) in 62:38 molar ratios, in respective.
12	(Lasfargues et al., 2015)	CuO, TiO_2	0.5 wt.%-1.5 wt.%	CuO= 29 nm, TiO_2= 34 nm	Solar salt (Nitrate salt of 60% $NaNO_3$ and 40% KNO_3).
13	(Shin and Banerjee, 2014)	Al_2O_3	1 wt.%	10 nm	Eutectic of lithium carbonate and potassium carbonate (62:38 by molar ratio).
14	(Devaradjane and Shin, 2012)	SiO_2	1wt. %	10 nm and 30 nm	HITEC XL (49% $NaNO_3$, 30% KNO_3 and 21% Ca $(NO_3)_2$ by mole).
15	(Andreu-Cabedo et al., 2014a)	SiO_2	0.5 wt.%, 1 wt.%, 1.5 wt.%, and 2wt.%	12 nm	Solar salt (Nitrate salt of 60% $NaNO_3$ and 40% KNO_3).
16	(Tiznobaik et al., 2015)	MgO, SiO_2, Al_2O_3	1 wt.%	10 nm	Eutectic salt mixture of Li_2CO_3 and K_2CO_3 by 62:38 molar ratios.

No	Name of authors	Type of nanoparticles	Concentration of nanoparticles	Size of nanoparticles	Type of molten salt used
17	(Shin and Banerjee, 2011a)	SiO_2	1 wt.%	10 nm	Eutectic of lithium carbonate and potassium carbonate (62:38 molar ratio).
18	(Tao et al., 2015a)	SWCNT; MWCNT; graphene; fullerene C60	0.25 wt.%, 0.5wt.%,1 wt.%, 2.5 wt.%, 5 wt.% and 10 wt.%	Sodium dodecyl sulfate (SDS, nano-PCM and a high mass ratio of SDS 10:1).	Eutectic salt mixture of 62 mol.% Li_2CO_3:38 mol.% K_2CO_3.
19	(Schuller et al., 2015)	Al_2O_3	0.125%, 0.25%, 0.5%, 0.75%, 1%, 1.5% and 2%	40 nm	Sodium nitrate and potassium nitrate (60:40 mole fraction).
20	(Tiznobaik and Shin, 2013b)	SiO_2	1 wt.%	10 nm	Eutectic salt mixtures of (Li_2CO_3-K_2CO_3).
21	(Jo and Banerjee, 2015)	CNT	0.1 wt.%, 0.5wt.%, 1 wt.%, 5wt.%	Nanoparticle diameter was in range of (10–30 nm) and 1.5 micrometre in length.	Eutectic salt mixtures of (Li_2CO_3-K_2CO_3) with 62:38 molar ratio.
22	(Ho and Pan, 2014)	Al_2O_3	0.016 wt.%, 0.0625 wt.%, 0.125 wt.%, 0.25 wt.%, 0.5 wt.%, 1wt.%, 2 wt.%,	Less than 50 nm.	Hitec salt by mixing of (17.9 g of $NaNO_3$, 135.7 g of KNO_3 and 102.4 g of $NaNO_2$).

No	Name of authors	Type of nanoparticles	Concentration of nanoparticles	Size of nanoparticles	Type of molten salt used
23	(Niu et al., 2014)	MWCNT, gold	0.5 wt.%, 1.5 wt.%		Solar salt (Nitrate salt of 60% $NaNO_3$ and 40% KNO_3).
24	(Seo and Shin, 2014)	SiO_2	1 wt.%	60 nm	Ternary molten nitrate salt eutectic ($LiNO_3$-$NaNO_3$-KNO_3 with 38:15:47 mole ratios)
25	(Yang and Banerjee, 2012)	SiO_2	1 wt.%	(25.95 nm with chloride salt), (32.6 nm with carbonate salt).	Chloride eutectics (68.490mg of barium chloride, 24.784 mg of sodium chloride, 79.206 mg of calcium chloride and 25.520 mg of lithium chloride) and Eutectic of carbonate salts (92.25 mg of lithium carbonate and 105.75 mg of potassium carbonate).
26	(Banerjee, 2011)	SiO_2	1 wt.%	30 nm	Eutectic $BaCl_2$-$CaCl_2$-LiCl-NaCl with these molar ratios (15.9:34.5:29.1:20.5).
27	(Jung and Banerjee, 2011)	Mica	0.5 wt.%; 1 wt.%; 2wt.%	45 micrometre	Nitrate salt (sodium nitrate and potassium nitrate by 60:40 molar ratios).

No	Name of authors	Type of nanoparticles	Concentration of nanoparticles	Size of nanoparticles	Type of molten salt used
28	(Sambasivam, 2015)	SiO_2	2 wt.%	60 nm	Binary mixture of lithum chloride and potasium cloride (by 45:55 by molar ratio).
29	(MALIK, 2010)	Al_2O_3	0.1wt.%,1wt.%,10 wt.%	10 nm	Hitec-Solar Salt.
30	(Tiznobaik and Shin, 2012)	SiO_2	1 wt.%	5 nm	Mixture of lithium carbonate and potassium carbonate (62:38 by molar ratio).
31	(Riazi et al., 2016)	SiO_2	1 wt.%	Nanosalt A= 116 nm to 173 nm, Nanosalt B= 19 nm to 92 nm, Nanosalt C= Agglomeration large size.	Nitrate salt (sodium nitrate and potassium nitrate by 60:40 molar ratios).
32	(Hu et al., 2017)	Al_2O_3	0.5 wt.%, 1 wt.%, 1.5 wt.% and 2 wt.%	20 nm	Nitrate salt (sodium nitrate and potassium nitrate).
33	(Song et al., 2018)	SiO_2	1 wt.%	20 nm	Quaternary nitrate salt ($Ca(NO_3)_2 \cdot 4H_2O$-KNO_3-$NaNO_3$-$LiNO_3$).

No	Name of authors	Type of nanoparticles	Concentration of nanoparticles	Size of nanoparticles	Type of molten salt used
34	(Chen et al., 2018)	SiO_2	1 wt.%	20 nm	$Ca(NO_3)_2$-KNO_3-$NaNO_3$-$LiNO_3$ (2:6:1:2 in mass ratio).

2.2.3 Experimental heat transfer study in the storage system

Any improvement in the heat transfer of storage system is needed to improve the efficiency of the solar thermal power plant and supply the energy under the requested time. PCMs have been implemented to be used as a storage medium in the storage system due to their higher energy density of both sensible and latent heat. However, the main problem of the solar energy heat storage system is the lower values of k and cp of the PCM which needs to be enhanced.

Therefore many techniques are used for this purpose in order to improve the solar energy storage system. For instance, dispersing of nanoparticles into the PCM can enhance the thermophysical properties of the storage material, as explained earlier. Another technique improves the storage system design by inserting fins with different designs in the storage tank to increase the performance of the storage system as discussed in details in the following sections.

2.2.3.1 Experimental use of PCM in the storage system

There are some researchers who studied the heat transfer of the PCM in the storage system in different applications using a different design of the storage system. There is some researcher who designed the storage system as a vertical or horizontal cylindrical shape reporting it had a simplicity in design. For example, heat transfer of melting and solidification processes in a vertical cylinder has been studied by (Farid et al., 1989). They used two different types of PCM (n-eicosane and n-hexadecane). Additionally, the 99-percent pure n-eicosane paraffin as a PCM in a vertical cylinder is studied by (Sparrow and Broadbent, 1982). The PCM does not completely fill the experimental setup and this is to consider the expansion during the solid phase change to a liquid phase. According to (Sparrow and Broadbent, 1982), during the melting process, the heat transfer from the hot side to the PCM is in a radial direction. However, this is not the only method of heat transfer through the PCM. Furthermore, density decreases would cause an expansion of the PCM in the storage tank specifically in the air gap in the cylinder. This is why the heat dissipation occurs from the top as well as the walls along the hot pipe. An experimental work to study the melting of n-octadecane in an enclosure of dimensions 100 mm x 60 mm x 50 mm was examined by (Zhang et al., 1993). They reported that natural convection has a stronger effects during the charging process.

Sari and Kaygusuz (2001) studied heat transfer of stearic acid with melting temperature around 61 ^{0}C and a purity of 90%. Their experimental setup consisted of an annular cylinder where the HTF (heat transfer fluid, which is water here) flows in the inner pipe and the PCM is located in the gap between these two pipes with a total weight of 950 g. They used pipes made from copper. Furthermore, they measured temperatures in different axial and radial directions and recorded every 5 minutes. Sari and Kaygusuz (2001) concluded that the PCM does not have the ideal melting/solidification behaviours. They attributed this behaviour to the impurity of the PCM stating that after 10-15 cycles, the crystal structure of the stearic acid is not ideal anymore. They studied the effect of the inlet temperature of HTF on the results of charging/discharging processes. In case the inlet temperature increased from 74 ^{0}C to 81 ^{0}C, they obtained faster charging by 30%, while decreasing the HTF temperature from 45.5 ^{0}C to 34 ^{0}C accelerated the discharging process by 36%. This is because of the high conduction heat transfer between the PCM and HTF due to the higher temperature differences between them.

Trp (2005) studied experimentally the heat transfer of the PCM in shell and tube heat exchanger. HTF was flowing in the pipes by forced convection and the PCM was filling the shell side, as shown in Figure (2-2).

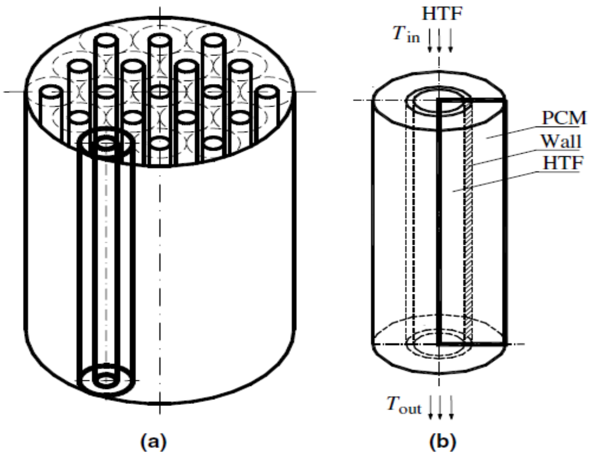

Figure 2-2 shows (a) Latent thermal energy storage system; (b) thermal energy storage unit (Trp, 2005).

The HTF pipe was made from copper with an outer diameter equals to 35 mm and thickness of 2 mm with the length of 1000 mm. Brass was the material of the large tube which was 133 mm outer diameter and 5 mm of thickness and same length (1000 mm). The PCM was a technical grade paraffin Rubitherm RT 30 which has a melting temperature of 27.7 ^{0}C. Their results demonstrated that the phase change process took place over a range of temperature (27.7 ^{0}C - 35 ^{0}C) and not in a single point (Trp, 2005). They related this to the different components of the PCM where each component has its own range of melting temperature and the mass ratio of each component that resulted in range melting points for the tested PCM (27.7 ^{0}C - 35 ^{0}C). They mentioned that natural convection was dominant during the entire charging process while it dominated only the beginning of the discharging. In discharging, the main heat transfer mode was conduction and the discharging occurred at a constant temperature 27.5 ^{0}C - 28 ^{0}C which is in similar to the melting/solidification temperature specified by the supplier (Trp, 2005).

In addition, Liu et al. (2005) examined an experimental study for the solidification process. The experimental setup geometry was horizontal three pipes which form two concentric cylindrical shapes. The heater was located in the small pipe of 19.9 mm diameter and 550 mm length. The PCM filled the annulus between the small and medium pipe with a diameter equal to 46 mm and 550 mm length. The HTF filled the outer pipe of 91 mm in diameter and 600 mm length. They used stearic acid as the PCM which had a melting temperature of 67.7 ^{0}C and water as the HTF. The material of the pipes was stainless steel. The temperature at different radial locations was studied. They explained that at the beginning of discharging process, there was a rapid drop in the PCM temperature. This was due to the heat transfer by convection at the start of cooling and the large temperature difference between the cold HTF and PCM which led to a high heat transfer rate between them. The heat transfer was mainly by the sensible heat released from the PCM toward the HTF. However, when the PCM started to change phase from the liquid phase to solid phase then the cooling process started to slow down; this was due to the increment in thermal resistance and the absence of natural convection. Additionally, the PCM had a lower value of thermal conductivity.

Moreover, Vaivudh et al. (2008) carried out a study of the charging/discharging processes in a co-axial cylindrical storage system. Thermal oil was used as an HTF and it was heated by an electrical heater to simulate the HTF in the solar thermal plant. Furthermore, thermal oil was used as PCM. They declared that the thermal oil was heated by the heater element to a maximum temperature of 340 ^{0}C. Any further increase in the temperature would lead to power off the heater. This was to prevent the decomposition of the material. Additionally, they used two different types of the heat exchanger, the first one was a coaxial cylindrical pipe and the second one was a helical coiled pipe. Both of these geometries were located vertically and their results were validated by a mathematical model. Their results showed that the highest storage efficiency was for a helical pipe by 0.4361% in charging and 0.631% during the discharging. This demonstrates the large effect of the storage system design on the charging/discharging processes. It might be that the higher contact surface area, which provided by the helical type with the PCM, was the reason for the higher efficiency concluded compared to the case of the vertical pipe.

Furthermore, Li et al. (2012) studied the heat transfer of PCM and foam-PCM composite material, the melting temperature of the used PCM was 46.48 ^{0}C. Their experimental setup is shown in Figure (2-3).

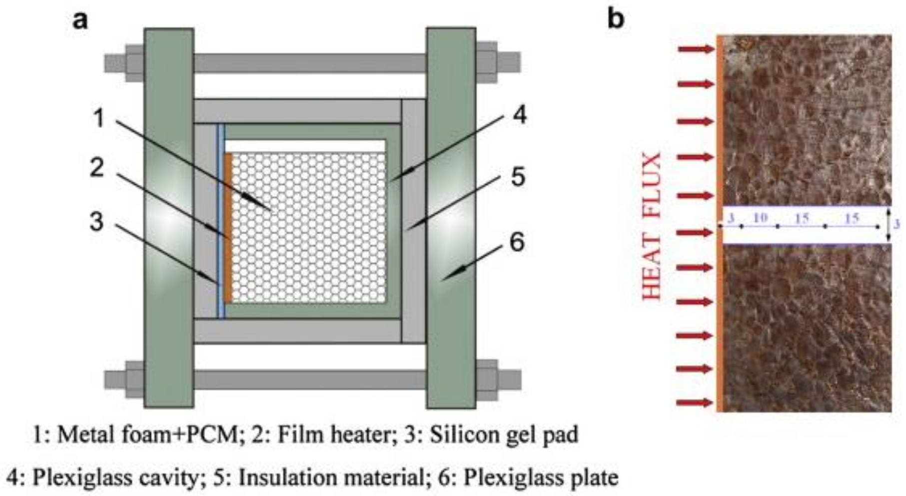

Figure 2-3 shows a- the experimental device and b- test section Li et al. (2012).

The heater is located on the left hand side with a constant heat flux (4000 W m^{-2}) and all other walls were insulated. According to their results, the natural convection clearly affects the heat transfer of the foam-PCM and it is the reason behind the hot liquid phase movement upward.

Longeon et al. (2013) used paraffin RT35 as a PCM with a melting temperature of 35 ^{0}C in a shell and tube heat exchanger. The concentric cylinder is the geometry of the experimental setup with an outer pipe diameter of 44 mm and length of 400 mm and made of Plexiglas, to allow the visibility of the phase change process. The inner pipe which contained the HTF (water) was made from stainless steel with a diameter of 15 mm and length equals to 400 mm. The PCM was located in the gap between the pipes with a mass of 480 g. The temperature distributions had been measured at different radial, theta, and axial locations. Longeon et al. (2013) showed that temperature distributions at different theta directions did not show differences between them and this meant that the problem could be treated as 2-D. They studied the effect of HTF injection from the top and the bottom on the melting process. Both injections showed a melting from the top to the bottom of the storage system. Longeon et al. (2013) explained that melting from the top in the bottom HTF injection was not what they expected, however, this was due to the natural convection effect which showed this trend. However, their results demonstrated the opposite in case of discharging for the bottom injection. This is due to less effect of the natural convection during the discharging.

Furthermore, Zhang et al. (2015) studied the charging and discharging of nitrate salt (50 wt. % $NaNO_3$: 50 wt. % KNO_3). The cylindrical tube was filled by 80% of salt and immersed inside a hot tank of HTF. Their results showed that the charging was affected highly by the convection, however, they improved their system with the use of metal foam which increased thermal conductivity and therefore improved the discharging process. This work used a higher melting temperature of PCM in comparison to others work.

Mao (2016) did a review study about the effect of the design of the geometry of the storage system. According to Mao (2016), the main geometry in the designing of the storage tank is the cylindrical and rectangular shapes. Additionally, Hosseini et al. (2014) studied the melting and solidification process in a horizontal cylindrical shape using paraffin RT50 as the PCM with a melting point around 50 ^{0}C. The HTF, which was water, flowed in the inner pipe while the PCM was located at the gap between the pipes. The effect of the HTF input temperature had been considered during the experiments and showed that any increment in this temperature would improve the charging process by 37%. They explained that at the beginning of the charging process the heat mode was primarily by conduction then it was dominated by convection. Hosseini et al. (2014) mentioned that Vyshak and Jilani (2007) did a comparative numerical study among three different geometries of the storage system such as rectangular, cylindrical, and shell and tube, as shown in Figure (2-4). They concluded that cylindrical geometry required the minimum time to store the same energy amount compared to other geometries.

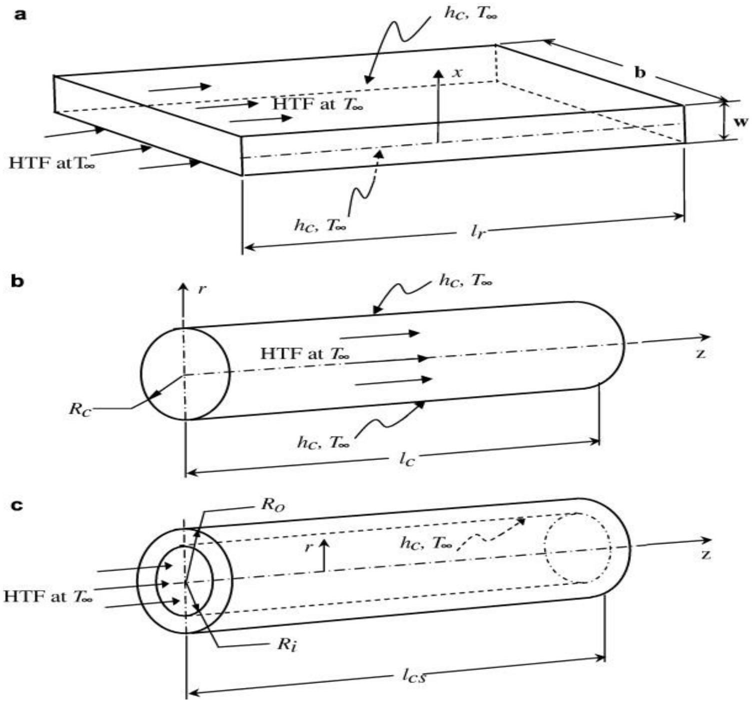

Figure 2-4 shows the storage geometries (a) Rectangular container, (b) cylindrical container and (c) cylindrical shell container (Vyshak and Jilani, 2007).

Fang et al. (2017) studied the heat transfer of PCM inside an annular cylinder geometry. The melting temperature of their PCM was around 65 ^{0}C. The inner heating element power was 20.528 W (heat flux was 2179.19 W m^{-2}) with 20 ^{0}C as a starting temperature for all experiments. They indicated that temperature distributions along the radial directions are uniform because of the gradual absorption of the energy in the r-direction. The heat dissipation in radial directions eventually makes the temperatures measurement homogeneous and the same in all the radial direction which means a steady state. They concluded that additives such as carbon fibre improve the charging process of the PCM.

2.2.3.2 Experimental use of nano-PCM in the storage system

The effect of dispersing nanoparticles into the PCM should improve the storage energy of nano-PCM and hence increase the heat transfer rate between the HTF and PCM. Therefore, some researchers have started to study the new nano-PCM, comparing their heat transfer experimentally with the base PCM (Jesumathy et al. (2012), Dhaidan et al. (2013c), Liu et al. (2009), Elgafy and Lafdi (2005)). These experimental publications studied the effect of adding different types of nanoparticles into different types of PCM in different applications. For instance, Liu et al. (2009) studied the effect of dispersing 1.13 vol. % of TiO_2 nanoparticles into the $BaCl_2$ aqueous solution for cooling storage application. Their results showed a faster melting rate as it reduced the charging time from 269 min to 160 min. On the other hand, Wu et al. (2010) dispersed Cu, Al, and C/Cu nanoparticle into the paraffin to improve the charging and discharging processes. Different types of surfactant were used to ensure the stability of the nano-PCM material. They concluded that Cu nanoparticles gave better enhancement than Al and C/Cu types. 1 wt.% of Cu nanoparticle decreased the charging time by 30.3% and discharging time by 28.2% and this showed that adding nanoparticles has a significant effect on the melting and solidification processes.

Jesumathy et al. (2012) dispersed different weight concentrations of CuO nanoparticle (2 wt. %, 5 wt. % and 10 wt. %, with a size of 40 nm) into PCM which was paraffin wax with melting temperature around 59 ^{0}C. The storage system was concentric tubes with PCM in the annular cylinder with a mass of 700 g and water as the HTF following in the HTF pipe. The temperatures distributions had been measured. According to the experimental data by Jesumathy et al. (2012), the Nusselt number in the case of nanoparticle dispersed into PCM can be calculated from Equation (2-6).

$$\mathrm{Nu} = 0.4328\ (1.0 + 11.285\ \varphi_n{}^{0.754}\ \mathrm{Pe}^{0.218})\ \mathrm{Re}^{0.333}\ \mathrm{Pr}^{0.4} \qquad \textbf{Equation 2-6}$$

Where φ_n represents the weight fraction of nanoparticles, Pe is a Peclet number which is the ratio of heat transported by convection to that transports by conduction, Re is Reynolds number and Pr is Prandtl number. According to Jesumathy et al. (2012), the higher concentrations of nanoparticles (10 wt. %) would cause the higher improvement in heat transfer coefficient by 78% during solidification, in the same time, 10 wt. % nano-PCM reduced the melting and solidification times by 35% and 34%, respectively. This enhancement could be due to the increase of k values of nano-PCM material due to higher k of CuO nanoparticles. However, large concentrations of the order of 10 wt. % do not give good stability of nanoparticles and it will be easier to sediment after a few melting/solidification cycles. A similar conclusion had been conducted by Elgafy and Lafdi (2005) who reported that dispersing carbon nanofibers in paraffin wax with different concentration (1%, 2%, 3%, and 4% by weight) enhances k of the nano-PCM and reduces discharging time in the discharge process with the increase of mass fraction of nanoparticles.

Additionally, Dhaidan et al. (2013c) demonstrated the effect of CuO nanoparticles on PCM (*n*-octadecane with melting temperature of 28 ^{0}C). They studied a lower range of nanoparticles concentrations (1 wt. %, 3 wt. % and 5 wt. %) than the range conducted by Jesumathy et al. (2012). Dhaidan et al. (2013c) built up an experimental setup to study the charging/discharging processes. Their experiment consisted of horizontal concentric cylinders where the heater element was located in the inner pipe and PCM filled the gap between the pipes. They reported that the charging process was improved in the case of nano-PCM compared to PCM alone. However, the concentrations of nanoparticles should be selected carefully, because higher concentrations of nanoparticles in the nano-PCM will lead to higher viscosity, agglomerations, and settlement of nanoparticles. Furthermore, larger amounts of nanoparticles mean reducing the mass of the PCM which resulted in a reduction in energy storage capacity. Therefore the concentrations should be optimum and be ensuring there is a good improvement in the storage system.

Another study had conducted the effect of CuO nanoparticles on n-octadecane by Dhaidan et al. (2013a). Similar to Dhaidan et al. (2013c), Dhaidan et al. (2013a) used the same weight concentrations of nanoparticles into the PCM. However, the storage system had another design which was a square container. The system is located inside a Styrofoam insulation box and the square container was heated by an electrical heater from the wall at the left side. The nano-PCM is stirred for half hour at a temperature higher than melting temperature before putting samples in the test cell in order to delay any effect of sedimentation and agglomeration. Dhaidan et al. (2013a) concluded that an increase in hot wall temperature led to a reduction in charging time and improvement in heat transfer rate. Moreover, the melting process was improved with the increasing of nanoparticles concentrations. However, concentration values should be chosen carefully to avoid any effect of viscosity augmentation and precipitation. Additionally, they reported that at an early stage of melting, conduction is dominant and melting font took the shape of a planar vertical interface parallel to the heating wall. Later, when convection started to dominate the melting process then the solid-liquid interface had a curved shape, as shown in Figure (2-5). Dhaidan et al. (2013b) also did a similar study but in a cylindrical capsule.

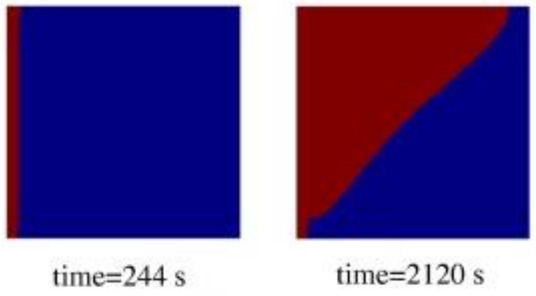

a- 0 wt%

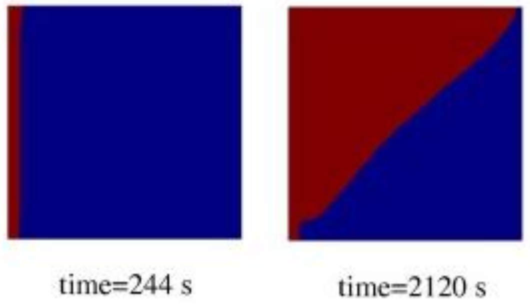

b- 5 wt%

Figure 2-5 shows the melting interfaces (red for liquid and blue for solid) for (0 and 5 wt. %) CuO-PCM with Ra = 1.22 × 10^8 (Dhaidan et al., 2013a)

In contrast, the charging process was not improved by the MWCNT-PCM in comparison to PCM by a study conducted by Zeng et al. (2013). Their experimental setup was a cylinder filled with 1-dodecanol ($C_{12}H_{26}O$) as a PCM, with a melting point of 22 ^{0}C. The cylinder walls were insulated except the bottom wall where the heat was supplied to the PCM by an HTF pipe attached to the experimental rig at the bottom and water was used as HTF. They studied the effect of two different concentrations of MWCNT such as 1 wt. % and 2 wt. %. They measured temperature distributions at different locations of each case, only PCM vs 1 wt. % or 2 wt. % nano-PCM. However, in most of thermocouples measurement in the PCM, none of these concentrations showed improvements in the charging process and they believed this was because of the increase in the viscosity which led to the limitation of the effect of natural convection and thus weakened the melting process. A similar study had been conducted by (Fan et al., 2014) with graphene as the additive material. They concluded a similar behaviour was the increase in the viscosity led to decrease the effect of natural convection in the presence of nanoparticles in the nano-PCM.

In addition, Ho and Gao (2013) reported the effect of 5 wt. % and 10 wt. % Al_2O_3 nanoparticles on the charging process of PCM. They selected paraffin wax n-octadecane as the PCM. Their experimental setup consisted of a square enclosure with a hot left side wall using an electric heater while the right side wall was a cold copper wall and the front and back wall were transparently made from glass plates to allow the visualization. In case of pure PCM, their results demonstrated that increasing the hot wall temperature is more effective as it accelerated the melting process due to increments in natural convection. This was more effective than increasing cold wall temperature and reducing the hot wall temperature at the same time. Their results showed that the decrement in the Nusselt number was higher in the case of both nano-PCM compared to a cause of PCM alone. This was due to the increment in viscosity which was higher than the increments in thermal conductivity of nano-PCM therefore a degradation was observed in nano-PCM during the melting. Furthermore, this effect on natural convection increased by increasing the weight fraction of nanoparticles in the nano-PCM. Furthermore, Ho et al. (2010) did a study using the same square enclosure set up but the base material was water. Their aim was to study the effect of nanofluid on the natural convection heat transfer because they focused only on one phase of water which was a liquid phase (Ho et al., 2010). Al_2O_3 was used for this work with a different range of volume fraction between 0.1 vol. % to 4 vol. %. They concluded an improvement in heat transfer of 0.1 vol. % nanofluid by 18% while the increments in volume fraction (> 2 vol. %) would give a decrement in heat transfer.

Most of these papers were concerned with the heat transfer of nanoPCM and showed the effect of nanoparticles on the natural convection or conduction during the melting and cooling processes. However, they did not consider the high temperatures PCM and the literature was mostly about the effect of nanoparticles on low temperature PCM applications.

2.2.3.3 Experimental study of PCM-fins structure in the storage system

Finned structures can be defined as thermally conducting structures which assist to increase the surface area that helps to transfer more heat. Fins are plates which extend from the surface of the container that contains either PCM or the tubes containing the HTF in the case of shell and tube heat exchanger of the storage tank system. It is used to enhance the heat transfer mechanism between the HTF and PCM. Many studies report the benefits of adding fins in the energy storage system to improve the charging and discharging processes. For instance, the effect of the number of fins and the effect of the pipe size has been studied experimentally by Velraj et al. (1997). It indicated that the inclusion of four or six internal fins in vertical tubes, which contain paraffin RT60 as a PCM with melting temperature range from 58 ^{0}C to 60 ^{0}C, could improve the storage tank for the application of domestic hot water system. The material of the PCM tube was aluminium and the fins materials were made from aluminium. The results showed that fins improved the discharging process.

Ismail et al. (2001) reported an experimental and numerical study on the solidification process of PCM with the existence of internal and axial fins. There are many factors affecting the discharging process and the mass fraction of the solid phase such as the number of fins, fins dimensions (length and thickness) and the gap space between the concentric cylinders. Their results showed that the thickness of the fins has a small effect on the solidification time while the number and length of fins has a strong effect on the discharging process.

Liu et al. (2005) reported an experimental study of the discharging process using stearic acid as the PCM and cold water as the HTF. A finned structure was used to improve the heat transfer rate between the PCM and HTF. The finned structure was attached to the inner pipe, which was the HTF pipe, and was made from copper. The structure of these fins was spiral twisted tape and they were extended over the full annular gap which was filled with PCM. They concluded a faster cooling with the existence of fins in comparison to the case without a fin. Furthermore, they studied the different width of the fin (2.5 mm and 5 mm). Their results showed that the fine fins are more effective in improving the solidification process due to the fact that the surface area of these fine fins was a little larger than the larger fins structures. Moreover, in building application, the use of fins with an encapsulated PCM show a good improvement in the total time required by the discharging process by 65-72 % and the charging process was enhanced by 72% (Siva et al., 2010).

Experimental work was performed by Castell et al. (2008) and they concluded that bigger fins will reduce the solidification time. According to Murali and Mayilsamy (2015), an experimental test for circular fins around the PCM tube showed an improvement in the melting process by 5 % in a hot water tank application. Furthermore, CFD software was used in this paper and similar results were obtained comparing with the experimental ones.

On the other hand, Agyenim et al. (2009) studied the effect of different shapes of the fin on the enhancement of heat transfer in a horizontal concentric cylinder storage system. Erythritol was used as PCM with a melting temperature of 117.7 ^{0}C in the shell side and the oil represented the HTF following in the inner tube. Moreover, they studied the effect of the finned structure shape by considering either longitudinal or circular fins. They used eight as a number of longitudinal/circular fins and both of them were made from copper. Their results showed that longitudinal fins provide a complete melting with faster rate compared to circular fins and the case without fins.

Al-Abidi et al. (2013b) conducted an experimental study on the charging process of rubitherm gmbh-germany (RT82) as PCM in horizontal triplex tube heat exchanger. The HTF flowed into the inner and outer tubes while the PCM was located in the middle tube. Three different heating methods were used such as heating from the inner tube, heating from the outer tube and heating from both sides, and a comparison among these three methods was studied in term of melting time and temperature distributions in axial and radial directions. Their results indicated that both side heating is better than other two methods as the PCM needs a shorter time to melt. In addition, the increase the flow rate of HTF leads to increase in the average temperature of PCM and reduce the melting time of the PCM. However, this increase in mass flow rate should be with an optimum value where beyond this value any extra increase in flow rate values causes an increase in the charging time. In addition, Al-Abidi et al. (2014) reported an experimental study on the triplex tube heat exchanger by modifying the storage system to a finned triplex heat exchanger. Four internal fins were extended from the inner HTF pipe and four external fins extended from the inner surface of the middle pipe, PCM pipe, to enhance the heat transfer process in the storage system.

Tay et al. (2013) experimentally tested a solidification process in a storage system. The effect of fin structure shapes was studied such as circular finned tubes and pinned tubes. The pins number was 16 while circular fins number was 5. Their results indicated that circular finned tubes are the best design with faster phase change time by 25% compared to pin type due to the higher surface area provided by this shape structure. Furthermore, increasing the tube volume leads to a decrease in solidification time. However, this increase is limited by the volume of the HTF tube to the total volume of a storage tank, approximately 3%, there is no change in solidification duration.

Mat et al. (2013) studied the addition of internal and external fins in a horizontal triplex tube heat exchanger numerically and verified the results experimentally. RT82 was used as a PCM inside the middle tube of the triplex tube heat exchanger while the HTF flowed into the inner and outer tubes of the triplex tube heat exchanger. The fins were extended either from the inner tube (internal fins) or from the middle tube (external fins). Also, internal-external fins were studied in this paper. Moreover, copper was used as the fins material. However, this work is at a low temperature as the range of melting temperature of RT82 lies between 70 ^{0}C - 82 ^{0}C and hot water with approximately 90 ^{0}C was used as HTF. The results showed that inserting internal-external fins with 42 mm in length inside the triplex tube heat exchanger decreased the melting time by 43.3% in comparison with the case of no fins.

Rahimi et al. (2014) used paraffin RT35 with melting temperature between 29 ^{0}C - 35 ^{0}C as a PCM in a finned tube in order to study the charging and discharging processes in a compact heat exchanger. They studied the effect of fins on the storage system with others factors such as inlet temperature and mass flow rate of the HTF. The tubes material was made from copper and fins material was aluminium. Their results demonstrated that fins decrease the melting time by 56% and fins lead to an increase in the average temperature. Moreover, the effect of the inlet temperature of the HTF (water) on the decreasing of melting time of PCM was variable. For example, in the case of 50 ^{0}C - 60 ^{0}C reducing charging time by 42% while in the temperature range 60 ^{0}C - 70 ^{0}C the decreasing in charging time was 26%. This indicates that the optimum working temperature of HTF needs to be chosen carefully. Furthermore, the mass flow rate effect was more noticeable in case of a bare tube (without fins) and in the solidification process.

Al-Abidi et al. (2014) focused on studying melting and solidification processes in term of different temperature variations in radial and axial directions, the mass flow rate of HTF, and charging/discharging times. The results of the Al-Abidi et al. (2014) study showed there is an effect of the HTF condition on the melting time as inlet temperature of HTF has a larger effect on the melting time compared with mass flow rate. Fins made from copper were used to enhance the melting process by reducing the charging time.

Kamkari and Shokouhmand (2014) studied the effect of fins on an enclosure heated from one side and the other side kept isothermal. The addition of one and three fins at one side of the enclosure PCM was studied where the fins’ side wall was heated and the other was insulated. The results demonstrated that fins gave a good enhancement in the melting time especially at the fins’ surface because of the existence of a vortex and the disordered motion of the liquid state of the PCM. Moreover, the benefit of increasing fins number seems to be more efficient at lower working temperatures of the walls.

The effect of fins’ height on the charging process was reported by (Hosseini et al., 2015). The shell was made of iron while the inner tube and fins material was copper. The internally finned tube contained 8 rectangular fins and the HTF flowed inside the inner pipe. The fins with length 26 mm were found to be more efficient because they provide a smoother distribution of temperature profile than fins of 13 mm in length. In order to avoid the asymmetric distributions of melting rate longer fins are preferable because they keep the symmetric distribution as much as possible compared with the smaller fins' length. Furthermore, during melting, longer fins lead to form large vortices because it prevents the merge between PCM layers in contrast to the smaller fins as smallest vortices formed.

Later Al-Abidi et al. (2016) studied the effect of fins in the triplex tube heat exchanger in term of angular temperature distribution. The temperature variations in the angular directions were measured and the results indicated that in case of no fins, a higher temperature distribution occurred in the angular direction observed at 0^0 because of natural convection effects at this position. Moreover, the average temperature in the angular direction did not show significant changes due to the two effects of the storage system. One was the vortex in the bottom and natural convection effect at the top. Temperature distributions have a higher average temperature of 157.5 ^{0}C due to higher thermal distributions there. The results of Al-Abidi et al. (2016) indicated that inlet conditions of the HTF such as temperature and mass flow rate have a significant effect on the charging process as charging time decreased by 86% if the inlet temperature increased from 85 ^{0}C to 100 ^{0}C. Furthermore, adding fins had a significant effect on reducing the melting time compared with the case of no fins. Moreover, the effect of mass flow rate of HTF on the melting process showed significant effect (Abdulateef et al., 2017). The same experimental setup by Al-Abidi et al. (2013b) had been used by (Abdulateef et al., 2017) to show the effect of HTF input on the melting process of finned PCM. Different values of mass flow rate were studied such as 16.2 kg/min., 29.4 kg/min., and 37.4 kg/min. The results found that 29.4 kg/min consumed less time during the melting process. Any increase or decrease in this value showed an increment in the charging process period. They carried out simulation work concerning the effect of fin shape on the melting process. This is discussed in section 2.3.3.

Most of the previously reviewed fin-PCM study was about the low temperature applications using PCM with a lower melting point. In contrast, other work has been conducted concerning the improvement of the storage system using inorganic salt as the PCM. For instance, Laing et al. (2009) who used $NaNO_3$ as a PCM used to store energy in lab scale tests with a high melting temperature of around 306 ^{0}C. They mentioned that using steam as HTF required specific conditions to meet the phase change requirement such as high temperature and pressure during charging and discharging processes. Using steam as the HTF would require many safety concerns such as 107 bar and 316 ^{0}C in charging and 81 bar and 296 ˚C during discharging. Therefore, they used therminol oil as HTF in their lab scale test. In order to enhance the k value of $NaNO_3$, fins made of aluminium were used for higher levels of temperature and graphite fins were suitable for temperature up to 250 ^{0}C. Their results showed that the presence of fins structure in the storage system would improve the charging process.

2.3 Simulation state of art

Numerical programs have been used widely by many researchers such as Shmueli et al. (2010); Gowreesunker et al. (2012); Bhaumik (2012); Wu et al. (2012); Gharebaghi and Sezai (2007). Most of the numerical study was either validated by experimental work by the same authors or other work done in the literature.

Compared to experimental work, it is faster and easier to build up computer models and to study the heat transfer of storage systems considering many parameters. This section aims to provide a state of art review for simulation of the PCM using the enthalpy porosity method, the effect of nano-PCM on the heat transfer inside the storage system, and finally focusing on simulating different shapes, lengths, arrangements of fin structures on heat transfer of PCM inside the PCM tank, as explained intensively in the following sections.

2.3.1 Simulation study of PCM in the storage system

There is an increasing demand for storing energy using PCMs, for instance, the solar energy storage system integrated with PCM. Therefore, many researchers tried to simulate the PCM using different methods to eliminate the effort and cost needed during the experiments. For instance, there are different methods implemented to solve the PCM numerically such as Gauss-Seidel iteration, TRNSYS, Matlab and enthalpy porosity technique by finite volume method in Ansys (Esen and Ayhan (1996), TOPLOTE and STRUKTURAH (2012) and ANSYS (2009)).

Using simulation, the heat transfer during the melting and solidification process of different types of PCM/types of a container can be intensively studied more easily than in the experiments. One of the most softwares used to simulate the PCM is Ansys-Fluent. Fluent can solve the physical problem of melting and solidification. The melting/solidification model in Fluent is basically an enthalpy- porosity technique. The enthalpy porosity model depends on the summation of both sensible and latent enthalpies, as shown in Equations (2-7 and 2-8) (ANSYS, 2009)

$$\text{Enthalpy (H)} = \text{Sensible enthalpy} + \text{Latent enthalpy}$$ **Equation 2-7**

$$\text{Sensible enthalpy} = \mathrm{H_{ref}} + \int_{\mathrm{T_{ref}}}^{\mathrm{T}} \mathrm{cp\ dT}$$ **Equation 2-8**

Where $\mathrm{h_{ref}}$ is reference enthalpy, $\mathrm{T_{ref}}$ is reference temperature and cp represents specific heat capacity at constant pressure.

The effect of the liquid fraction (β) is included in the model as shown in Equation (2-9). Enthalpy porosity method is sensitive to the phase change through the value of the fraction values (β), as indicates in Equation (2-10) (ANSYS, 2009).

$$\beta = \left\{ \begin{matrix} 0 & \mathrm{T} < \mathrm{T_{solidus}} \\ \frac{T - \mathrm{T_{solidus}}}{\mathrm{T_{liquidus}} - \mathrm{T_{solidus}}} & (\mathrm{T_{solidus}} < T < \mathrm{T_{liquidus}}) \\ 1 & \mathrm{T} > \mathrm{T_{liquidus}} \end{matrix} \right\}$$ **Equation 2-9**

$$\text{Latent enthalpy} = \beta\ \mathrm{L}$$ **Equation 2-10**

Where L represents the latent heat (J/g). Equation (2-11) shows the energy equation used in the enthalpy porosity method (ANSYS, 2009).

$$\frac{\partial}{\partial \mathrm{t}}(\rho\ \mathrm{H}) + \nabla.\left(\rho\ \vec{\vartheta}\ \mathrm{H}\right) = \nabla.(\mathrm{k}\ \nabla \mathrm{T}) + \mathrm{S}$$ **Equation 2-11**

Where ρ density (kg/m^3), $\vec{\vartheta}$ is the fluid velocity represented during the phase change and in the liquid phase, and S is the source term. Momentum equation in enthalpy porosity method consists of a source term which treats the PCM as a porous medium and the liquid fraction represents the porosity factors in a mushy zone. Equation (2-12) shows the source term in the momentum equation (ANSYS, 2009).

$$\mathrm{S} = \frac{(1-\beta)^2}{(\beta^3 + \mathrm{e})}\ (\mathrm{A})\ \vec{\vartheta}$$ **Equation 2-12**

Where e represents a constant with a small value (0.001) to avoid dividing by zero when the material is in a solid phase. A is mushy zone constant and the default value in the range 10^4-10^5 kg/ m^3.sec. Furthermore, the effect of natural convection can be represented by the Boussinesq effect.

In the enthalpy porosity method, the mushy zone is treated as a porous medium, where the porosity is represented by the liquid fraction. The porosity value is zero at the solid state of PCM, equal to one at the liquid phase and in between zero and one in the mushy zone of combined solid-liquid.

ANSYS Fluent was used to simulate the PCM inside a container by many researchers as Shmueli et al. (2010), Gowreesunker et al. (2012), Bhaumik (2012), Muhammad et al. (2015a) and Hossain et al. (2015)). The physical phenomena of the melting process in a vertical cylinder had been studied by Shmueli et al. (2010). The PCM was RT27 (Rubitherm GmbH). They concluded that the shape of solid PCM becomes conical and shrinks from the top of the cylinder toward the bottom due to the effect of natural convection during the melting. Conduction heat transfer is only dominant during the solidification process while natural convection is the dominant heat transfer mode during the melting process Shmueli et al. (2010).

For cold storage application, PCMs can be used to store energy and to keep the low temperature of the cold store temperature specifically during the loss of electrical power (Gin et al., 2011). During losses in electrical power, the temperature of the cold store can be increased which is not preferred and bad effects on the quantity and quality of the storage substance. Therefore, PCM can be used to absorb this heat. ANSYS CFX 11.0 software was used to simulate the PCM in the cold storage application (Gin et al., 2011). The model solved the air flow and temperature changes during the melting process. The results confirmed that PCM can absorb the increase in temperature of the cold store. The CFX data were validated against experimental work in domestic freezer and showed an acceptable match.

PCMs may be used to store the energy in a domestic hot water storage tanks. This was simulated using ANSYS ICEM software to build the geometry and ANSYS-Fluent to solve the charging process (Bhaumik, 2012). The effect of insulation around the storage tank had been studied to show the normal performance of PCM tank without insulation. Therefore, two cases had been conducted one insulated PCM tank and the other non-insulated PCM tank (Bhaumik, 2012). It indicated that an optimum thickness of the insulation needs to be considered

A validation for ANSYS Fluent results with experimental was conducted by Longeon et al. (2013). Their experimental study has already been discussed in the previous section (2.2.3.1). The results showed there was a large effect of natural convection during the charging process while the opposite during the discharging, Figure (2-6) showed the results of the visualized charging in the experiment compared to simulated - Fluent results by Longeon et al. (2013).

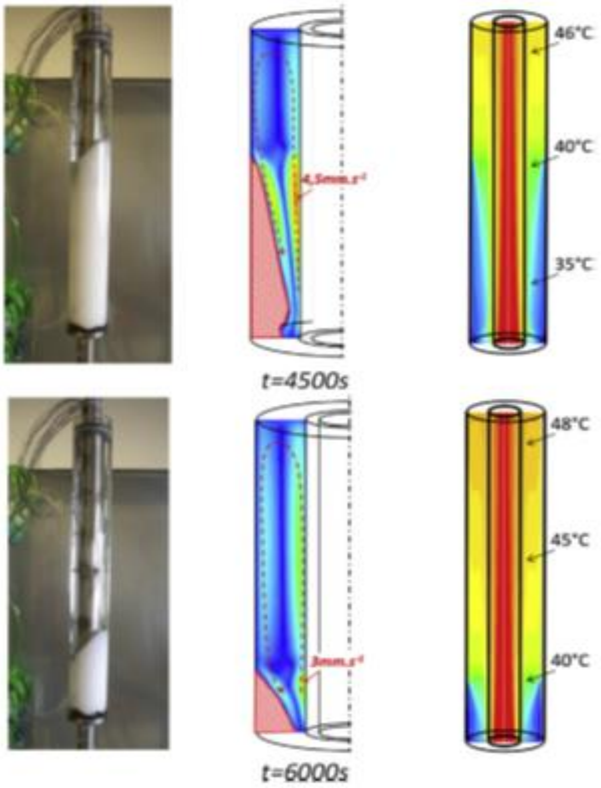

Figure 2-6 shows the melting front shots (left), numerical velocities magnitude in the PCM (middle) and temperature (right) profiles during charge with bottom HTF injection Longeon et al. (2013).

Cylindrical shapes of storage systems are preferred over rectangular enclosures due to high efficiency, lowest volume with fewer heat losses compared with other geometries (Muhammad et al., 2015b). A vertical cylinder representing the storage system geometry filled by PCM, which was n-eicosane, was studied by (Muhammad et al., 2015b). They used the effective cp in their model in order to increase the accuracy of their results, as shown in Equation (2-13). It showed that the accuracy of the results increased by the cp effective model in the solid phase while there was no effect on the liquid phase. Because the $\mathrm{cp}_{\mathrm{eff}}$ was used only for the solid phase due to the lower value of cp in a solid phase (Muhammad et al., 2015b).

$$cp_{eff} = cp_{solid} \frac{\rho_{solid}}{\rho_{liquid}}$$ **Equation 2-13**

The melt fraction is the volume melted of PCM to the total container’s volume (Hossain et al. (2015). In the melting/solidification model, it is preferable to include the measured values of thermophysical properties of PCM Gowreesunker et al. (2012). Significant changes in thermal conductivity values showed an important effect on the results concluded by this model Gowreesunker et al. (2012).

For high temperature application, the melting/solidification processes were studied by (Muhammad et al., 2015a). PCM was $NaNO_3$ with melting temperature of around 306 ^{0}C. The geometry consisted of a shell and tube heat exchanger. The aspect ratio can be defined as the ratio of the length of the shell to the radius of the HTF pipe, and it was 153. The mushy zone represents a range of temperature where the change of phases takes place in the cells (Muhammad et al., 2015a). Furthermore, the mushy zone is modelled as a porous zone at which the liquid fraction starts to increase from 0 to 1 in the case of melting and decreases from 1 to 0 at the solidification process. Usually the value of the mushy zone constant in a range between (10^4 kg/m^3. sec) and (10^7 kg/m^3. sec). A mushy zone constant with the value of (10^5 kg/m^3. sec) was used by (Muhammad et al., 2015a). At the beginning of melting, it was reported that the absence of convection was due to the smallest distance between the HTF pipe wall and the PCM solid-liquid interface. This interface moves away from the wall of the HTF pipe causing an increase in melting thickness and at the same time reducing the temperature difference between PCM and HTF.

The solidification process was studied by (Muhammad et al., 2015a). Their results showed a longer time needed to finish the solidification of PCM ($NaNO_3$) compared to the melting process. Because the discharging depended mainly on the conduction heat transfer whereas during the conversion of PCM from the liquid phase to solid phase the thickness of solid increased which affected on the convection and minimized its effect. However, the model carried on with a consideration of constant of density using the liquid density value at melting temperature for both phases, which was not correct in the experiments work, and this was why they got slightly differences between simulation and experimental work when they compared with experiments performed by Jones et al. (2006), cited in Muhammad et al. (2015, p.8). Furthermore, the density of the solid phase is larger than that of the liquid phase (Hossain et al. (2015)). Moreover, Suárez et al. (2015) used CFD software to simulate the cooling process of nitrate salt as a PCM. Furthermore, Zhang et al. (2015) used Fluent software to simulate the charging/discharging process of nitrate salt (50 wt. % $NaNO_3$: 50 wt. % KNO_3) as a PCM, as discussed earlier in section (2.2.3.1).

The melting processes of an inorganic salt as a PCM have been reported by (Chen et al., 2016). The PCM was nitrate Hitec salt ($NaNO_3$–$NaNO_2$–KNO_3, with 7 wt. %: 40 wt. %: 53 wt. %, respectively) with melting point 142 ^{0}C located inside a square geometry. The geometry had a width of 19 mm and length 1000 mm. It reported that due to the buoyancy effect and the decrease in density of molten salt with increasing temperature, the vortex formed during melting had the shape of an ellipse rather than a circle.

2.3.2 Simulation study of nano-PCM in the storage system

The addition of small nanoparticles with a dimension of 10^{-9} m has a significant effect on thermophysical properties of the PCM in the storage applications. Therefore, simulation studies of nano-PCM have been conducted to show the improvement of the charging/discharging processes. The effect of types, shapes, size, and concentrations of nanoparticles on the PCM have been studied using simulation tools and the literature is reviewed here in this section.

The melting process of nano-PCM has been studied using CFD software by many researchers such as (Arasu and Mujumdar, 2012). Arasu and Mujumdar (2012) carried out the simulation of nano-PCM inside a square enclosure using paraffin wax as PCM with 2 vol. % or 5 vol. % Al_2O_3 nanoparticles. Additionally, they considered the study of different heating sides such as heating form the left wall or heating from the bottom wall of the enclosure. It concluded that during the melting process, buoyancy force could not overcome the effect of the viscous force, therefore the conduction mode dominated heat transfer at the beginning of the melting process. The results found that higher concentrations of nanoparticles did show a longer time of melting due to a higher effect of viscosity which caused lower natural convection effects. Furthermore, higher amounts of nanoparticles would reduce the amount of the base material in turn and result with the reduction in mass of the storage density which is not preferred in solar energy storage applications. In conclusion, lower concentrations of nanoparticles improved the melting process of nano-PCM in a square enclosure. Additionally, a faster melting process occurred in the case of heating from the vertical left side compared to heating from the bottom wall. Moreover, according to Wu et al. (2012), the charging process of paraffin wax (PCM) with the addition of Cu nanoparticles was simulated by the ANSYS Fluent software with the volume of fluid (VOF) model. A large amount of the melted PCM was found in the top of the cavity. This was due to the buoyancy effect (natural convection). In addition, at the beginning of the melting process, the buoyancy-induced velocity started small and continued to increase. The result demonstrated that 1 wt. % of Cu reduced the melting time by 13.1%. The possible reason for the enhancement in the melting rate was due to the higher value of k which enabled the PCM to absorb more heat compared with a case without nanoparticles.

Moreover, ANSYS Fluent software was used to simulate the effect of dispersing 2 vol.% and 4 vol.% of Cu nanoparticles into RT27 (Hosseinizadeh et al., 2012). The VOF model was used to simulate the internal interface between two working fluids but no interpenetration occurred. The higher concentration of nanoparticles meant higher values of k and lower latent heat with results of reduction in melting time. Additionally, Cu nanoparticles were dispersed in RT50 (act as a PCM) with different concentration such as 3 vol. % and 5 vol. % (Hosseini et al., 2013). They concluded that 5 vol. % of concentration leads to enhance the charging process by 14.6%.

The effect of heating source location showed remarkable changes in the melting process (Arıcı et al., 2017). PCM (paraffin wax) and nano-PCM (1 vol. %, 2 vol. % and 3 vol. % Al_2O_3-paraffin wax) were located inside a square enclosure. There were two cases for a heat source, either partial heating from the right vertical wall, or partial heating from the horizontal bottom wall (Arıcı et al., 2017). They concluded that higher improvement in melting process was observed for 1 vol. % nano-PCM with heating from the bottom.

The input temperature of the HTF could show a significant effect on the melting process of PCM/nano-PCM. Therefore, Sciacovelli et al. (2013) studied the melting process inside a single vertical shell and tube heat exchanger. PCM had a melting temperature in the range 37.8 ^{0}C - 44.23 ^{0}C, and the nanoparticle material was Cu with 0.5 vol. %, 1 vol. %, 2 vol. %, and 4 vol. %. It was observed that increasing input temperature of HTF caused faster charging time by 38% due to the higher temperature difference between the storage medium and HTF, therefore natural convection increased. Additionally, 4 vol. % nano-PCM showed faster melting than PCM by 15%.

ANSYS Fluent (version 6.2.16) was used to solve the solidification process in a square cavity with both top and bottom walls insulated (Khodadadi and Hosseinizadeh, 2007). The PCM was water and CuO nanoparticles (0.1 vol. % and 0.2 vol. %) were added to improve thermal conductivity during the cooling process of nano-PCM. It was observed that faster solidification occurred due to increases in thermal conductivity. It was found that Grashof number decreased due to liquid-solid layer movement and conduction dominated over natural convection during the cooling process.

Additionally, the transient solidification process of nano-PCM was studied numerically using ANSYS Fluent software by (Mahdi and Nsofor, 2016). The geometry mode was different from (Khodadadi and Hosseinizadeh, 2007). 2-D of the triplex tube heat exchanger with HTF in the outer and inner pipe while PCM/nano-PCM in the middle pipe had been designed and studied numerically by (Mahdi and Nsofor, 2016). PCM was RT82 and nanoparticles material was Al_2O_3 with following concentrations 3 vol. %, 5 vol. %, and 8 vol. %. At the beginning of solidification, the results demonstrated that solidification time was reduced by 20% at 8 vol. % nano-PCM. However, the advantages of nanoparticles became noticeable when the conduction was the dominant heat transfer mode and the 20% saving occurred specifically during the final period of the cooling process.

On the other hand, Sebti et al. (2011) investigated the discharging process also with the use of Cu nanoparticles but the base material was water inside a concentric cylinder in a horizontal position. Volume fractions of Cu nanoparticles were 0.025 and 0.05 and temperature differences were 5 ^{0}C, 10 ^{0}C, and 20 ^{0}C. Additionally, the effect of natural convection was also studied. During the progress of the solidification process, the discharging started from the inner cylinder towards the outer one and after a while, the temperature difference in the annulus vanished with the convergence of the velocity to zero leading to disappearing of the convection. According to Wang et al. (2012) in the solid phase, there is no motion of the fluid which means there is no slip in the melt region. The buoyancy forces depend on the density of the liquid phase. The value of cp at the solid phase was calculated depending on the effective value which is to make sure that energy equation contains the thermal capacity of a solid phase and thus temperature distribution is physically corrected, as shown in Equation (2-13).

Moreover, the effect of geometry on the progress of solidification for PCM/nano-PCM was considered by a comparison between a square cavity and trapezoidal cavity with different inclination angles ($\theta = 2.72^0$, 5.42^0 and 7.69^0) by (Sharma et al., 2014). Water represented the PCM and nano-PCM was Cu-water with different volume concentrations such as 10 vol. % and 20 vol. % (Sharma et al., 2014). It was found that faster cooling occurred with increasing inclination angle. Using the same internal area, the trapezoidal cavity found to have less time of solidification than the square shape. This demonstrates the large effect of geometry on the discharging process.

Both charging and discharging processes of PCM and nano-PCM have been studied by the use of ANSYS Fluent software. For instance, Valan et al. (2013) used the enthalpy porosity technique to study melting/solidification of PCM (paraffin wax) and nano-PCM

(2 vol. %, 5 vol. % and 10 vol. % Al_2O_3-Paraffin wax) inside a concentric double pipe heat exchanger. The model setup was a concentric cylinder with inner wall as isothermal constant temperature and the outer wall was adiabatic, PCM/nano-PCM was located in the annular gap between the pipes. The results found that nano-PCM showed better improvements in both of charging and discharging. They suggested that using lower concentration (2 vol. %) was more preferable due to higher energy storage density and lower cost of nanoparticles in comparison to 10 vol. %.

Many researchers have performed simulation studies for nano-PCM compared to PCM inside different geometries for energy storage application. They focused for low temperature application using PCM with low melting temperature. It would be beneficial to use the design tool for the medium/high temperature PCM for solar thermal power plant applications. For instance, simulation design tools can be used to study different parameters for nitrate salt/nanosalt (melting point around 220 ^{0}C) as the PCM and improve this kind of storage medium and thus improve the overall efficiency of both the solar energy storage system and solar thermal power plant as a result.

2.3.3 Simulation study of PCM-fins structure in the storage system

In addition to the experimental work carried out regarding the PCM-finned storage system, there are many simulation studies on this area. Many factors have been studied numerically and compared regarding the fin structures such as fins materials, fins shapes, fins thickness, fins length, number of fins and so on, as discussed in detail in this section.

The arrangement of fins inside the storage system can have a remarkable effect on the melting/solidfication processes. Mat et al. (2013) simulated a triplex tube where the inner and outer tubes were filled with water (HTF) and the middle tube was filled with RT82 (PCM) using ANSYS Fluent. Different dimensions and arrangement of fins were located between the inner and middle tubes as internal fins, external fins, and internal-external fins. The fins material was made of copper. Three methods of heating were studied to simulate the charging process as inner heating which is wall of inner tube act as a heating source, outside heating method where the outer wall of the middle tube as a heating source and the last method where the heating was from both sides of the wall of both the inner tube and middle tube. Their results indicated that the case of two side heating methods and internal-external arrangement of fins gave a reduction in the time required of melting of PCM by 43.3% compared to the case of without fins. A similar study was carried out on the solidification process by (Al-Abidi et al., 2013a). It was found that longer fins improved the solidification process by 35%. Furthermore, the effect of fin length on solidification time was higher than fin thickness.

Moreover, the input parameter of HTF had an impact on the overall heat transfer during the charging/discharging of the fin-PCM system. The effect of the input mass flow rate and input temperature were studied by Lv et al. (2008). ANSYS Fluent simulations were conducted by Lv et al. (2008) with consideration of Naphthalene as PCM and water as HTF. Fins material was made from aluminium. Both of inlet velocity and temperature of HTF were studied to explore their effect on the charging and discharging processes. The values of inlet velocity and temperature of the HTF were varied between 0.1 m/sec, 0.05 m/sec, 0.025 m/sec, 356 K, 359 K, 363 K, 366 K, and 369 K, respectively. The optimum values for the melting process were between 356 K and 363 K and 0.1 m/sec. On the other hand, for solidification process, the velocity was the same as that for the melting process, while the inlet temperatures of the HTF were 293 K, 303 K, 308 K, 313 K and 323 K. The results showed that raising the inlet velocity leads to minimizing solidification time. Overall, fins improved the heat transfer of the PCM system by decreasing the melting/cooling times.

Furthermore, the finned-PCM system was simulated using ANSYS Fluent software by (Yang et al., 2015). The PCM was Naphthalene and fins were made from aluminium. Tetrahedral meshing was employed using Gambit software. The geometry was divided into two layers. The above layers contained PCM while the below layers contained the HTF water. The results showed that improving the melting/solidification processes required an increase in the temperature difference. In addition, maximizing the velocity of the HTF caused a decrease in the storage time. The results also showed that smaller fins pitches caused a reduction in the charging/discharging period because of the smaller volume of the PCM compared to the volume of the HTF in the storage system.

In addition, the effect of thermophysical properties can have a large impact on the improvements of the charging process. Thermophysical properties were defined as a function of temperature using user-defined functions (UDFs) in ANSYS Fluent, Ye et al. (2011). Paraffin was used as the PCM. The plate-fin unit was made of aluminium material. The VOF model was used to describe a problem with a moving internal interface but without inter-penetration of the two phase fluids. The heat was transferred through fins by conduction.

The geometrical parameters of finned structures were studied and reported Gharebaghi and Sezai (2007). Fins geometrical parameters were height, thickness, and spacing. The thickness of fin was in a range from 0.15 mm to 1.2 mm. Paraffin wax was used as PCM to solve the melting problem with fins made of aluminium. Boussinesq approximation had been used because of the assumption that all the properties were assumed to be constants except the effect of the buoyancy term. They concluded that convection is more noticeable than conduction where in the liquid phase the convection depends on the geometrical parameters of the model and the value of the melt fraction. Fin spacing parameters have the biggest effect where the closest fins are preferred to reduce the melting time required.

The effect of fins dimension plays an important role in their performance. Eight external vertical fin structures, with two different dimensions, were located inside a cylindrical storage system (Castell et al., 2006). The sizes of the fins structure were either 20 mm x 310 mm or 40 mm x 310 mm. The PCM was sodium acetate trihydrate with graphite (90:10 vol. %) with melting temperate equal to 58 ^{0}C (Castell et al., 2006). The results demonstrated that solidification time decreased with the existence of finned structures and this decreasing is higher with the longer fins (40 mm) due to improvements in conduction heat transfer mode. The heat transfer was increased by 28.45 % and 44.28 % for 20 mm and 40 mm in length of the fin, respectively.

Furthermore, ANSYS Fluent software was used to solve the melting process in a rectangular PCM container without and with 5 fins from the right side (Varol and Okcu, 2013). PCM was paraffin. The time required for the phase change depended on the properties of the PCM, the number of fins and thermal differences between PCM and the heat source. The results showed that the addition of fins enhanced heat transfer during the charging process due to the higher increase in the surface area.

The effect of the shape of the finned structure has a significant effect on the PCM mass and the heat transfer enhancements by increasing the heat rate between PCM and HTF. Three shapes of a fined structure were studied numerically by (Sciacovelli et al., 2015), using paraffin wax as a PCM. The numerical solution was conducted through the use of a combination of Fluent software and the response surface method, where the response surface method was used for the case of variations in the input parameters. The results indicated an increase in the discharge efficiency by 24% in the case of two bifurcations shapes (Sciacovelli et al., 2015).

In addition, Tay et al. (2013) performed a numerical simulation using a CFD program for cooling application of shell and tube geometry with embedded pins or fins on the HTF tube compared to the case of no fins or pins. Water was used as a PCM. According to Tay et al. (2013), the effect of buoyancy was more valuable in the large tank while it could be neglected in the small tank, which showed how much the dimensions of the storage tank can effect on the results. The number of pins used was 16 pins with different length and diameter. On the other hand, fins were 5 in number with a variation in thickness and diameter of fins. The neglecting buoyancy was done because heat transfer in the frozen application does not depend on the buoyancy, as concluded in the experimental work of Tay et al. (2012), cited in Tay et al. (2013, p.3), which demonstrated this assumption. It was concluded that fins provide better enhancement comparing to pins type because fins have a higher surface area which results 25% faster for the phase change time. The time required for phase change decreases with the increasing of tube volume to 0.03 (which is a ratio of the volume of the tube over total volume). After this number, the phase change duration remains constant.

In contrast, Agyenim et al. (2009) carried out a study of finned-PCM system and showed rectangular fins are better than circular ones. The circular shape of fins provided a reduction in the weight of the fin-body which resulted in increasing the heat transfer and efficiency. On the other hand, the comparison between the circular shapes of the fins and the longitudinal shapes were studied to find the best one which enhances the heat transfer between the PCM and HTF Agyenim et al. (2009). The PCM was Erythritol, with a melting point of 117.7 ^{0}C. The results showed that longitudinal fins were found to be better than circular fins, as longitudinal fins reduce the discharge time.

Moreover, the effect of fins shapes on the melting process could show different results (Abdulateef et al., 2017). The same geometry setup by Al-Abidi et al. (2013b) was used by (Abdulateef et al., 2017) to show the effect of longitudinal and triangular fin structures on the charging process. The external triangular fins showed the highest improvement in melting time by 15% in comparison to longitudinal fins.

As stated above, most of these simulation papers used paraffin or another material such as (water, Naphthalene, and RT82) that have a low melting temperature. Further work needs to be carried out on the high melting point temperature such as molten salt i.e. eutectic nitrate salt ($NaNO_3$: KNO_3 with 60:40 molar ratio).

2.4 Summary of the state of art

This state of the art literature review has shown that

i) The synthesis method to prepare nanosalt is mainly a 2-step method using water dispersion. The 1-step method to prepare nanoparticle directly inside salt has reported by our group papers (Awad et al., 2018a; Luo et al., 2017; Lasfargues et al., 2017). The 1-step method of preparation is a novel method which will be used in this research to prepare nanosalt in the next chapter (Chapter 3). The nanoparticles will be prepared inside the salt at a higher level of temperature without any needs for purchasing nanoparticles or adding water to disperse nanoparticles as the sonication and evaporation processes are excluded more explanation about this new method is provided in Chapter 3. Additionally, in the 2-step method, we prepared nanosalt using a new type of nanoparticles (Fe_2O_3) with different concentrations into different types of salt (single or binary nitrate salt) as shown in the next Chapter 3, (Awad et al., 2018b).

ii) Though much work has been done to measure different thermophysical properties such as cp and k of the salt with and without nanoparticles, there is a limited study for nanosalts at high temperature, especially for thermal conductivity measurements. Therefore, one goal of this research project is to focus on the preparation of selective types of nanoparticles dispersed into the salt and to measure their thermophysical properties such as cp, latent heat of fusion, melting point, and k of the nitrate salt and nanosalt in a wide range of temperatures up to 500 ^{0}C.

iii) Most of the work studied nano-PCM experimentally in the low range of temperature with limited heat transfer study of nanosalt. Therefore, we did an experimental study of nitrate salt (single and binary eutectic salt) and nanosalts for high temperature application up to 350 ^{0}C. The effect of nanoparticles types and concentrations are considered on both types of nitrate salt. In addition, we studied the effect of isothermal wall temperature or constant heat flux condition for the hot inner pipe on the heat transfer of melting and cooling on the salts or nanosalts, as explained in detail in Chapter 4.

iv) PCM has been simulated with a main focus on the charging and discharging processes with and without nanoparticles or fin. However, the simulation and validation of salt, nanosalt, finned-salt storage system and combined effect of nanoparticle and fins inside the storage tank for high temperature applications has not been reported. Therefore, one objective of this research is to build melting code to simulate the charging process of salt, nanosalt, finned-salt system, and a combination of nanosalt-finned system. This code is validated against our experimental data of salt and nanosalt using the same dimensions of the geometry setup as the experimental rig and thermophysical properties of salt/nanosalt were measured which are explained in both Chapters 5 and 6. Moreover, the effect of different parameters on the code was studied to show the sensitivity study by varying k, cp, density (ρ), latent heat (L), and mushy zone constant.

In summary, this work will formulate novel nanosalts, design and build an experimental system to study the heat transfer behaviour of different types of salts and nanosalts. ANSYS CFX code will be developed with validation against experimental data and used to predict heat transfer performance of a storage tank containing the combined effect of both nanoparticles and fins in order to improve the solar storage system by both enhancing material thermophysical properties and the design of the storage system for high temperature applications.

Chapter 3 Nanosalt material preparation and properties measurements

3.1 Introduction

This chapter includes the full details of the materials preparations by two different methods. Moreover, the other aspect of this chapter is the measurements of thermophysical properties of the salt/nanosalt samples. The main focus is on specific heat capacity (cp), latent heat, melting temperature (T_{melt}), thermal diffusivity and thermal conductivity (k). Additionally, the material characterizations are studied using different devices such as thermogravimetric analyser (TGA), scanning electron microscopy (SEM), transmission electron microscopy (TEM), and dynamic light scattering (DLS). Finally, conclusions are drawn on the comparison between these methods at the end of this chapter.

3.2 Preparation method

Nanoparticles have been recently proposed to solve the problem of low cp/k values of the nitrate salt, as explained earlier in Chapter 2 in the literature review.

Additionally, nanosalt samples are prepared by two different methods, i.e. the 2-step method and the 1-step method. Although the procedure is different between these methods, both of these methods result with a nanosalt sample. Shin and Banerjee (2010) are among the first researchers who prepared nanosalt samples using a 2-step method for nanosalt preparation. On the other hand, a 1-step method for nanosalts was first conducted by (Lasfargues et al., 2016; Luo et al., 2017; Awad et al., 2018a; Lasfargues et al., 2017). In depth details of these methods are explained in the next sections.

3.2.1 Two-step (2-step) method

The 2-step method is a well-known method for the preparation for nanosalt. It was explained extensively in the previous chapter (Chapter 2). In this method, nanoparticle materials are purchased or prepared in advance before the start of the nanosalt preparation. One of the advantages of this method is that the sizes of nanoparticles are approximately controlled because they are prepared in advance and many stabilizers could be used for this purpose. Additionally, different types of nanoparticles can be tested. For instance, preparation of nanoparticle-type A was under the temperature of 1000 ^{0}C. Then the produced nanoparticle-type A can be used with a salt material that decomposes around 550 ^{0}C. However, this method has drawbacks such as the need for other devices to disperse the mixture (the mixture of water, salt and nanoparticles). These devices are the probe sonication or water bath sonication. In addition, it is a time consuming method (e.g. evaporation time). Moreover, the expense of nanoparticles, which is variable depending on many parameters such as the price and purity of nanoparticles, and they are different from one company to another. For instance, the purity of nanoparticles can be not high quality, where some nanoparticles are provided with some components in order to stabilize them. Moreover, these components could have a negative effect on the base material (molten salt).

The preparation procedure of the 2-step method is shown in Figure (3-1), NP represents the nanoparticles and DW is distilled water. First of all, the 2-step method mixes the correct mass percentage of salt and nanoparticles (by considering NP weight concentrations such as 0.5 wt. %, 1 wt. %, 1.5 wt.%) then adds distilled water (30 ml) to the mixture. As it is known, molten salt is an ionic liquid containing anions and cations. Due to this ionic nature, it is a good solvent for oxides especially the metal oxides which are not soluble in water (Einarsrud and Grande, 2014). Furthermore, salt is dissolved in water, therefore, the nanosalt material will be well mixed. Secondly, the nanosalt material is sonicated by the probe sonicate to ensure a good dispersion of nanoparticles within the sample. Thirdly, water is evaporated from nanosalt sample using a hot plate which is set at a temperature of 150 ^{0}C. The evaporation process is located inside a fume-cupboard. The evaporation process takes place until the water is fully evaporated from the samples.

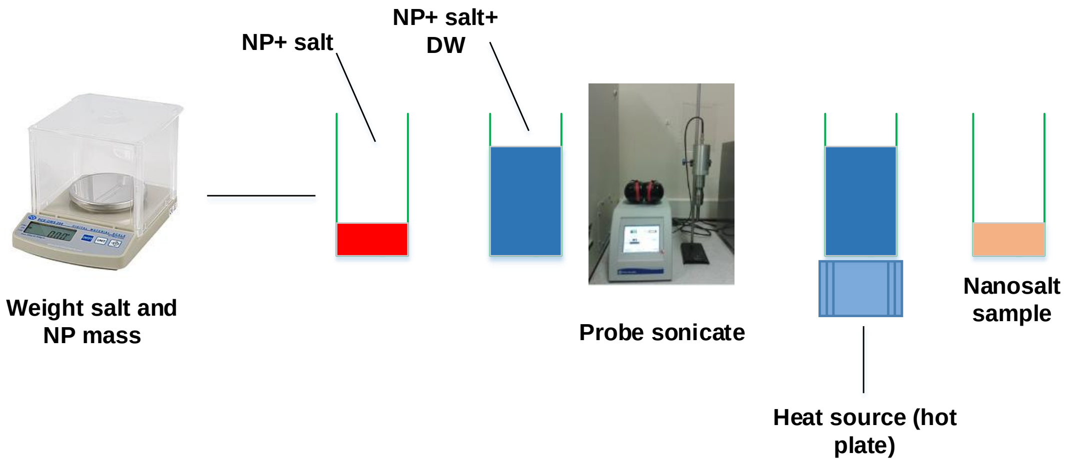

Figure 3-1 shows the schematic of the 2-step method, NP represents the nanoparticles and DW is distilled water.

The nitrate salt type is used as a base material with different types or concentrations of additive materials. Two different types of nitrate salt are studied which are the single salt of potassium nitrate (KNO_3 purchased from Sigma-Aldrich, Suffolk, UK, with 98% purity) and mixture nitrate solar salt ($NaNO_3$: KNO_3 with 60:40 molar ratio) is named as solar salt (s.s). Sodium nitrate ($NaNO_3$) is purchased from Fisher, Loughborough, UK, with 98% purity.

Furthermore, the additive materials used are nanoparticles which are explained below with their specification from their supplier manufacturer

Copper oxide (CuO nanoparticles) purchased from Sigma-Aldrich Company

- Purity: 99.99%
- PS: <50 nm particle size (TEM).
- Appearance: Form (powder) and the colour is black.
- Density: 6.320 g/cm^3.

Iron oxide (Fe_2O_3 nanoparticles) purchased from US research Nanomaterials, Inc. Company

- Purity: 98+%
- APS: 20-40 nm (TEM).
- Appearance: Iron Oxide Nano-powder (Fe_2O_3, Alpha) and the colour is red-brown.
- Density: 5.24 g/cm^3.
- Morphology: spherical.

Titanium dioxide (TiO_2 nanoparticles) purchased from nanostructured & amorphous materials Inc.

- Purity: 99.8%
- APS: 60 nm.
- Appearance: Nano-powder and colour is white.
- Density: 4.23 g/cm^3

3.2.2 One-step (1-step) method

This method is a direct preparation of nanoparticles inside a molten salt. The in-situ method for nanosalts has been conducted by a few researches in this area (Luo et al., 2017; Lasfargues et al., 2016; Lasfargues et al., 2017; Awad et al., 2018a). This method depends on a direct preparation of nanoparticles by a chemical decomposition of the precursor. This reaction takes place inside a muffle furnace with the existence of salt in the sample, as shown in the schematic in Figure (3-2).

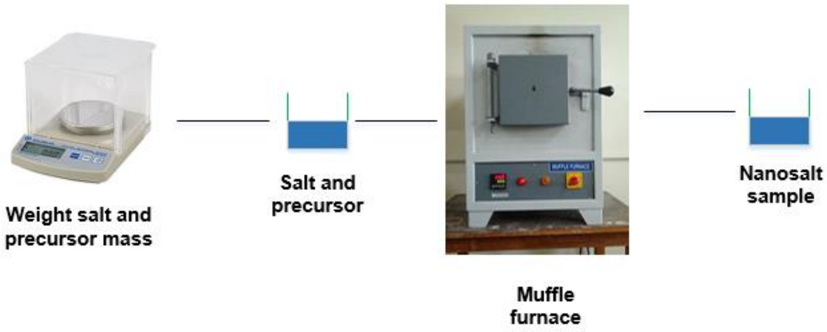

Figure 3-2 shows a schematic of the 1-step method.

This method of preparation has advantages and disadvantages. The 1-step method is efficient where the in-site method produces nanoparticles quickly with no need for the default method (2-step method). Unlike the 2-step method, there is no need to purchase nanoparticles or to add distilled water (especially in a large scale, i.e. scale of kg) in the sample, or use the sonication device or the evaporation procedure, etc.

From an economic point of view, the 1-step method is economically efficient because it is a direct producer of nanoparticles (NP), especially for this expensive nanoparticle.

On the other hand, the materials produced by the 1-step method suffer from some issues such as the size of NP which cannot be controlled. The NP size will be as it's produced which depends on the reaction of the precursor. Additionally, during the preparation, the sample might contain a stabilizer (surfactant) that can control the size of the prepared nanoparticles. At the same time, this surfactant should have a higher average life in which it should have a higher decomposition temperature, and it should be stable under the condition of the 1-step method. If the sample of the 1-step method does not have any type of stabilizer then the size of the prepared nanoparticles cannot be controlled by this method. This is one of the limitations of this method. Detrimental effects of clusters of nanoparticles are produced. Moreover, most precursor chemicals can produce nanoparticles at higher levels of temperature. However, the decomposing temperature of molten salt could be lower than this. Therefore, there are no many nanoparticles can be produced by the 1-step method when the molten salt presences. For instance, decomposition of nitrate salt starts around 550 ^{0}C and some of the precursor decompose to nanoparticles component at a temperature more than 550 ^{0}C. Therefore, there are limitations of nanoparticles production. In addition, from a safety aspect, it is very important to consider all the fumes that could result from the chemical reaction and the amounts of these chemicals which can be handled safely, especially for the application to large values encountered in the real storage system.

In addition, the in-situ production of copper oxide (CuO) nanoparticles inside binary molten salt has been produced by a chemical decomposition of copper sulphate $CuSO_4.5H_2O$ (Wiberg et al., 2001). The production of CuO nanoparticles is by a decomposition process of copper sulphate inside a muffle furnace under different time and temperature conditions, as shown in Figure (3-2).

The procedure of in-situ production is mixing the correct mass concentrations of powder of nitrate solar salt ($NaNO_3$: KNO_3 with 60:40 molar ratio) and copper sulphate ($CuSO_4.5H_2O$). This mixture is put inside a muffle furnace to help a chemical reaction to happen. The copper sulphate is heated up to 100 ^{0}C. Four water molecules will be evaporated leaving copper sulphate with one molecule of water. Further heating up to 200 ^{0}C will produce the $CuSO_4$ and increase the heating, resulting in CuO (Wiberg et al., 2001). Therefore, the mixture of copper sulphate pentahydrate and solar salt is heated up to a higher temperature up to 450 ^{0}C for half an hour or longer (Lasfargues et al., 2017; Awad et al., 2018a), as shown in Equation (3-1).

$$CuSO_4.5H_2O \xrightarrow{\text{Temp, time}} CuO + 5\,H_2O + SO_3 \qquad \textbf{Equation 3-1}$$

With the assumption of 100 % conversion, 1 mole of $CuSO_4.5H_2O$ produces 1 mole of CuO. Where the molar mass of $CuSO_4.5H_2O$ is 250 g/mole and 80 g/mole for CuO. From Equation (3-1), the atom efficiency of CuO = (80/250) * 100% = 32 %. Before starting the heating in the muffle furnace, 5 g was the total mass of solar salt and copper sulphate (by considering the concentration of $CuSO_4.5H_2O$ as 3 wt. %), that means the weight of the produced CuO in the nanosalt is (0.32 * 0.15=0.048 g). This makes the actual concentration of CuO nanoparticles equal to 0.96 wt. % (where this concentration represents the weight of CuO nanoparticles over the total weight of nanosalt).

In addition, there are 9 samples prepared using the same mass mentioned above for the precursor ($CuSO_4.5H_2O$) and the base material (solar salt) under different conditions inside the muffle furnace. These conditions were temperature and time of the reactions. These different controls for the preparation method enable one to find the optimum conditions in term of time and temperature of the preparation method. The temperature of the muffle furnaces is set to be 450 ^{0}C, 400 ^{0}C and 300 ^{0}C. Additionally, the time of reactions is set to be 30 minutes, 1 hour, 2 hours and 4 hours. Full details for the results are discussed in the results section (section 3.4).

Furthermore, the copper oxalate (CuC_2O_4) precursor can be used to produce the CuO nanoparticles directly inside the molten salt. The decomposition temperature is 350 ^{0}C by heating for 2 hours (Luo et al., 2017), as shown in Equation (3-2).

$$CuC2O_4.0.5H_2O \xrightarrow{\qquad} CuO + 0.5\ H_2O + CO + CO_2 \qquad \textbf{Equation 3-2}$$

3.3 Measurements

3.3.1 Differential Scanning Calorimetry (DSC) Device

Differential Scanning Calorimetry (Differential scanning calorimetry, DSC1/700, Mettler Toledo, Leicester, UK) is used for the sensible heat and latent heat measurements.

An endothermic process represents the melting of the PCM (salt/nanosalt) where the sample absorbs heat and changes phase from a solid phase to liquid phase. In contrast, the exothermic process is the process where the heat is released from the PCM (salt/nanosalt), e.g. during the solidification process when the PCM changes phase from liquid phase toward solid phase.

There are some specifications that need to be considered in order to obtain accurate measurements in the DSC. First of all, the method used for the run has to include at least (isothermal- dynamic ramp- isothermal). This type of thermal cycle must be considered to get the cp/ latent heat measurements. Additionally, the thermal cycle depends on some parameters such as the range of working temperature, heat rate (5 ^{0}C/min, 10 ^{0}C/min, 20 ^{0}C/min, etc.), and the atmosphere used (nitrogen gas (N_2) or air (O_2)). The thermal method used by the DSC device should start with a temperature calculated as shown in Equation (3-3).

$$\text{Starting T in DSC} = 3\ (\text{min})\ \text{x heat rate}\ (\text{K/min}) \qquad \textbf{Equation 3-3}$$

This allows stability for the baseline before any effects start, where starting temperature in the DSC is less than the starting effect appears on the sample. Furthermore, the final temperature is preferred to be less than the decomposition temperature of the PCM (salt/nanosalt) to prevent any contamination which could effect on the device or damage the sensor.

In addition, the sample loading inside a crucible is important and should be carefully considered during the measurements. The material weight should be optimum inside the crucible where a low amount of mass would result in maldistribution of the sample at the bottom of the crucible. This is because it needs to cover the base to ensure a full distribution of temperature from the sensor to the PCM through the crucible material. In contrast, higher amounts of PCM inside the crucible would cause a negative effect to the device or could damage the sensor. For instance, due to the volume expansion of molten salt, the solid mass inside the crucible should be considered carefully to avoid any overflow and then damage the sensor. Furthermore, there are different types of the crucible used with the DSC device such as aluminium pan, alumina, platinum, glass, high pressure, Cu type, gold, etc. The size of the crucible could be small, medium or large. For instance, platinum crucibles could be small (30 µl), medium (70 µl), or large (150 µl). Those crucibles types depend on the temperature ranges where at the very high temperature it cannot use aluminium type crucibles. Additionally, there should be no chemical reactions between the type of PCM samples and the crucible. Figure (3-3) shows the optimum mass loading inside the crucible and the platinum crucible (70 µl) used in the experiments.

a- The optimum mass loading

b- The crucible used in the experiments

Figure 3-3 Shows a- the mass loading inside the crucible for the DSC measurement, b- the crucible used in the experiments.

The method used to measure the cp by the DSC device depends on the heat flow measurements of the sample versus the heat flow of the reference. Where there is an empty crucible in the furnace worked as a reference crucible. For cp measurements in DSC device, the crucibles should be the blank crucible, the second crucible containing sapphire as a standard material, and the third crucible containing the sample (salt/nanosalts). Then, cp is calculated using STARe software which connected to the DSC device as shown in Equation (3-4)

$$\mathrm{cp}_{sample} = \mathrm{cp}_{sapphire} \times \frac{\mathrm{weight}_{\,sapphire}}{\mathrm{heat\ flow}_{sapphire}} \times \frac{\mathrm{heat\ flow}_{sample}}{\mathrm{weight}_{sample}} \qquad \textbf{Equation 3-4}$$

The cp, latent heat and T_{melting} are measured using the DSC device for the materials mentioned earlier in the preparation method section. The base materials are KNO_3, and binary solar salt ($NaNO_3$: KNO_3 with 60:40 molar ratio). Different types of nanoparticles are considered such as Fe_2O_3, CuO and TiO_2 with different concentrations such as 0.5 wt. %, 1 wt. % and 1.5 wt. %. In DSC measurements, the samples' weight is measured by the Ultra-microbalance Mettler Toledo balance (UMX2 Ultra-microbalance, Mettler Toledo, Leicester, UK) with an uncertainty of 0.1 µg. Furthermore, the thermal cycle was modelled at a rate of 150 ^{0}C for 10 min, ramped from 150 ^{0}C to 450 ^{0}C at a rate of 10 ^{0}C/min, then held isothermally for 10 min at 450 ^{0}C and finally cooled down from 450 ^{0}C to 150 ^{0}C at -40 ^{0}C/min, as shown in Figure (3-4). It should be noted that the maximum temperature in case of KNO_3 base material is less than 400 ^{0}C.

Each sample was run 3 times at least to ensure the repeatability of the measurements. The standard error for the DSC device measurements was less than 2.29%.

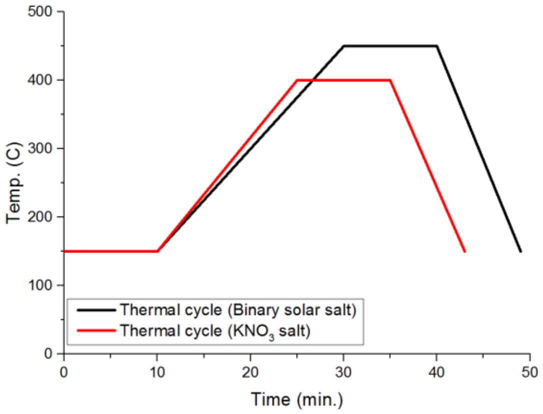

Figure 3-4 Shows the thermal cycle used in DSC.

3.3.2 Laser Flash Analysis (LFA) Device

The second important thermophysical property of salt/nanosalt is thermal conductivity. We used LFA (laser flash analysis LFA, model LFA 427, Netzsch Company, Selb, Germany) to measure thermal diffusivity. From the measurements of thermal diffusivity and cp then thermal conductivity can be calculated as explained in this section.

Thermal diffusivity was determined by heating the front face of the sample using the laser with an instantaneous recording of the temperature profile on the rear face. The model of three layers is used by the LFA device. These three layers represent the samples' holder and crucible lid with known properties and the third layer is the sample layer which the diffusivity is unknown, as shown in Figure (3-5).

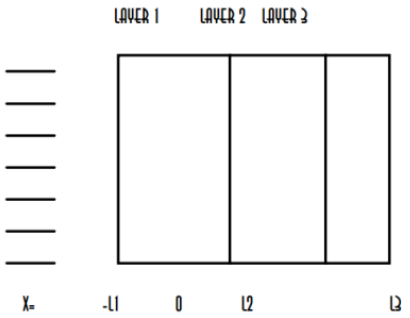

Figure 3-5 Shows the three layer model (NETZSCH, 2017)

The elegance of the method lies in the fact that the troublesome measurement of the absolute quantity of laser energy absorbed by the sample and of the resulting absolute temperature increase is replaced with a more accurate and direct measurement of time and relative temperature increase.

The thermal conductivity of the samples can be calculated depending on the measurements of cp and thermal diffusivity and the calculated density as shown in Equation (3-5).

$$\mathrm{k} = \mathrm{cp} \times \rho \times \mathrm{a}$$ **Equation 3-5**

where k is thermal conductivity W/(m. K), cp is specific heat capacity J/(g. K) (measured in the DSC device), ρ is density in g/m^3 and a is the measured thermal diffusivity m^2/s. According to Janz et al. (1972), the density of binary nitrate solar salt can be calculated as a function of temperature depending on the Equation (3-6).

$$\rho = 2064.31 - (4.76248 \times 10^{-4} \times \mathrm{T}^2) - (3.36495 \times 10^{-7} \times \mathrm{T}^2)$$ **Equation 3-6**

The range of temperatures in Equation (3-5) is from ambient temperature (298 K) up to 773 K. For the case where PCM is nanosalt, Equation (3-7) has been used to calculate the density of nanosalt (Vajjha et al., 2009). Equation (3-7) is a function of the concentrations of nanoparticles, the density of base salt (calculated by Equation (3-6) earlier) and the density of nanoparticles (which assumed to be constant from the msds of the material). For instance, the density of CuO nanoparticles is equal to 6320 kg/m^3 and the density of Fe_2O_3 nanoparticles is 5240 kg/m^3 (from the msds of the materials). Therefore the density of nanosalt in Equation (3-7) is dependent on the same range of temperatures in Equation (3-6).

$$\rho_{nanosalt} = (\varphi_{np} \times \rho_{np}) + ((1-\varphi_{np}) \times \rho_{salt})$$ **Equation 3-7**

where φ_{np} is a volume concentration of nanoparticles, $\rho_{nanosalt}$, ρ_{np} and ρ_{salt} are the density of nanosalt, nanoparticles and solar salt, respectively.

Furthermore, the uncertainty of LFA diffusivity measurements and calculated thermal conductivities of different samples are considered. Each sample is tested three times.

Repeatable results were found with a standard error of less than 2.6% of thermal diffusivity measurements using the LFA instrument. It is obvious that the error for thermal conductivity is higher than the error of cp or thermal diffusivity because k is calculated depending on cp, density and diffusivity. Therefore, the error of k is an accumulated error. However, the errors are within acceptable values with maximum error 0.0496.

3.3.3 Thermogravimetric Analyser (TGA)

A Thermogravimetric Analyser (Thermogravimetric Analyser, TGA/DSC, Mettler Toledo, Leicester, UK) is used to measure the mass of the sample against time and temperature. It can work on a higher temperature range up to 1600 ^{0}C. The weight changes (due to evaporation, absorption, oxidation and so on) can be measured under different atmospheres (N_2 or O_2). Therefore, this device helps to detect the starting of the decomposition of the salt (or nanosalt).

On the other hand, the cp can be measured by the TGA/DSC device. However, the measurement would not be accurate in comparison to the DSC measurements. This is because there are fewer thermocouples in the TGA sensor than in the DSC sensor. Therefore, it is preferred to measure cp, latent heat and $T_{melting}$ using the DSC device while the decomposition temperature (or the stability of the sample) is measured by the TGA/DSC device. In case only the stability of the sample is needed to be measured, therefore the required thermal cycle is the only dynamic ramp, e.g. 30 ^{0}C- 850 ^{0}C with 10 ^{0}C/min. Additionally, the sample will be tested once without repeatability because there will be a weight loss after the first run and sample could be already decomposed, therefore it cannot be repeated.

3.3.4 Scanning Electron Microscopy

A Scanning Electron Microscopy device (Scanning Electron Microscopy, SEM, model Hitachi SU8230, Hitachi company, Berkshire, UK) was used to create an image for a sample surface by scanning the sample’s surface using a focused electron beam (nanoscience, 2018). By this electron beam, the data analysed by the SEM has a resolution on a nanometre scale. SEM was used to show the surface morphology of nitrate salt without and with nanoparticles. The samples were in powder form and their morphology before and after repeatable thermal cycles was studied. The distribution of nanoparticles on the surface of the salt was observed using the high resolution SEM where an agglomeration of nanoparticles in the nanosalt has been observed.

Moreover, from the Energy Dispersive X-ray Spectroscopy (EDX), the samples prepared by the 1-step method were checked to see whether there is an existence of CuO nanoparticles or another element. This EDX helps to detect and analyse the elements in the sample.

3.3.5 Transmission Electron Microscopy

Transmission electron microscopy (Transmission Electron Microscopy, TEM, FEI Tecnai TF20, Oxford instrument, UK) was used to check the size and the shape of the nanoparticles. A very small amount of the sample is requested to perform the test on the TEM. This device produces a high resolutions image with a very small scale in the nanometre. Therefore it is preferred to detect the size of the nanoparticles which is used through our experiment.

TEM helps to measure the average size and shape of the purchased nanoparticles to indicate their size or the size of their agglomerates. Furthermore, the nanoparticles prepared by the novel 1-step method under different conditions of the preparations were tested in the TEM device to check whether they are of the nanoscale size or they are not.

3.3.6 Dynamic Light Scattering

Dynamic light scattering (dynamic light scattering DLS, Malvern Zetasizer ZS, Malvern Zetasizer, Malvern, UK) was used to measure the size of nanoparticles. The principle of this device depends on light scattering techniques. Under Brownian motion, diffusion of particles is measured then converted to size in the DLS technique. Small amounts of samples are placed inside the cell up to 15 mm and this cell placed inside the instrument in order to perform the test, as shown in Figure (3-6). DLS device is connected to the software. Intensity vs particles size was measured and other data was calculated, such as the number (or volume) vs the size of nanoparticles.

Furthermore, the sample has to be in nanofluid form with the existence of water. Therefore, the nanoparticles were dispersed in distilled water by the use of the probe sonicate to ensure a good dispersion of nanoparticles in the nanofluid sample. After that, the sample was measured by DLS where the intensity vs particles size was obtained. Four different samples, three of them are for three different nanoparticles purchased (Fe_2O_3, CuO, and TiO_2) and one sample prepared by the 1-step method, were prepared to be tested in the DLS. We did not use any type of surfactant to stabilise the nanofluid, and as nanoparticles might have suffered from agglomerations, which result with a large particle size. The maximum error analysis obtained was 3.4%.

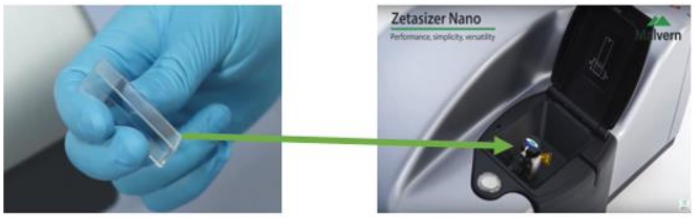

Sample cell cuvette

Sample cell cuvette holder place

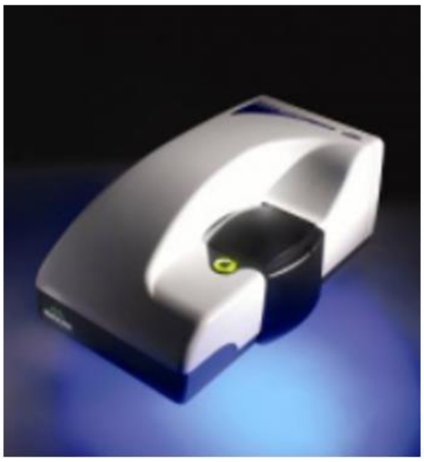

DLS device

Figure 3-6 Shows the DLS instrument and the sample cell.

3.4 Results and discussions

The measured thermophysical properties of PCM (salt/nanosalt) are discussed in detail in the following sections for the cp, latent heat, melting temperature, and thermal conductivity. Furthermore, the material characterizations are considered during the analysis and discussion section to help further understanding of the results. The base materials studied are two different types of nitrate salt which are single salt (KNO_3) and binary solar salt ($NaNO_3$: KNO_3 with 60:40 molar ratio) without and with nanoparticles. Different types and concentrations of nanoparticles materials were employed throughout this study as explained in details below. Additionally, the effects of nanosalt preparation methods are considered.

3.4.1 Specific heat capacity (cp)

Seeding nanoparticles into nitrate salt showed a noticeable effect which could be negative or positive depending on many parameters such as concentration, size or type of the nanoparticles used.

Figures (3-7, 3-8, 3-9, and 3-10) demonstrate the cp vs temperature relationship for different types of PCM, e.g. binary solar salt (or single nitrate salt KNO_3), without and with nanoparticles.

For the solid phase case, Figures (3-7 and 3-8), higher concentrations of nanoparticles (1.5 wt. %) have a maximum increment in cp of nano-binary solar salt, while lower concentrations (0.5 wt. %) showed the highest increases in the cp of nano-single salt. Using the same 2-step method of the nanosalt preparation, Chieruzzi et al. (2013a) indicated that 1 wt. % silica-nanosalt had greater cp than 0.5 wt. % or 1.5 wt.%. The slight difference could be due to the fact that they tested different types of nanoparticles. Also, there were differences in the preparation procedure between ours and the work of Chieruzzi et al. (2013a). In our experiments, probe sonicate was used to sonicate the nanosalt samples with 150 ^{0}C to evaporate the water. On the other hand, Chieruzzi et al. (2013a) used another technique to sonicate the nanosalts samples by an ultrasonic bath for 100 minutes and then evaporated the water at 200 ^{0}C. On the single salt side, KNO_3 was highly dependent on the type of nanoparticles, which is similar to what was concluded by Chieruzzi et al. (2015a). Tables (3-1 and 3-2) show the cp values in a solid phase for different materials.

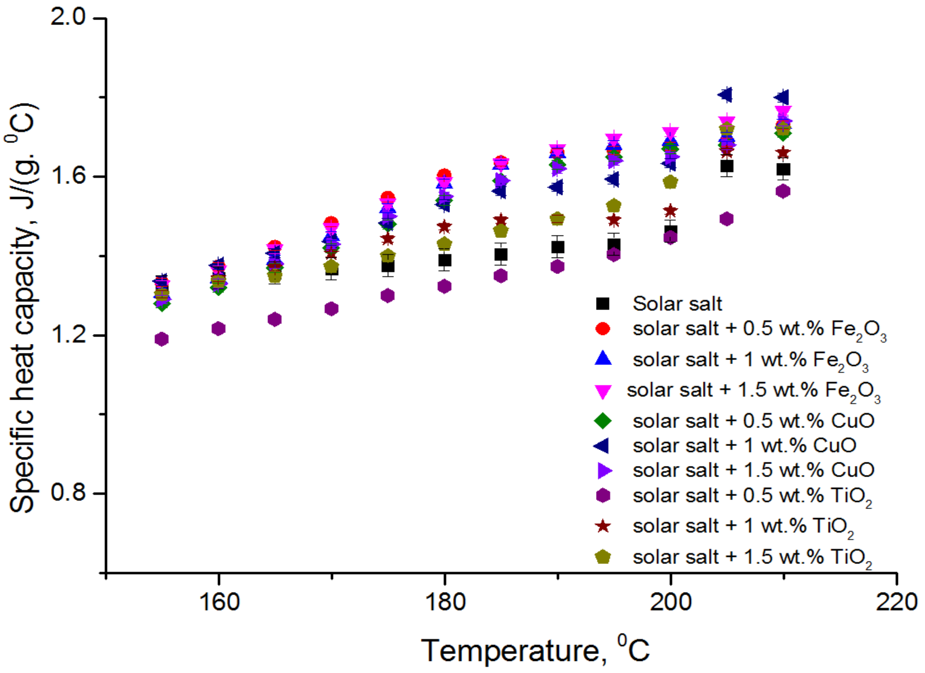

Figure 3-7 Solid phase of cp of different types and concentrations of nanoparticles dispersed into binary nitrate salt (solar salt).

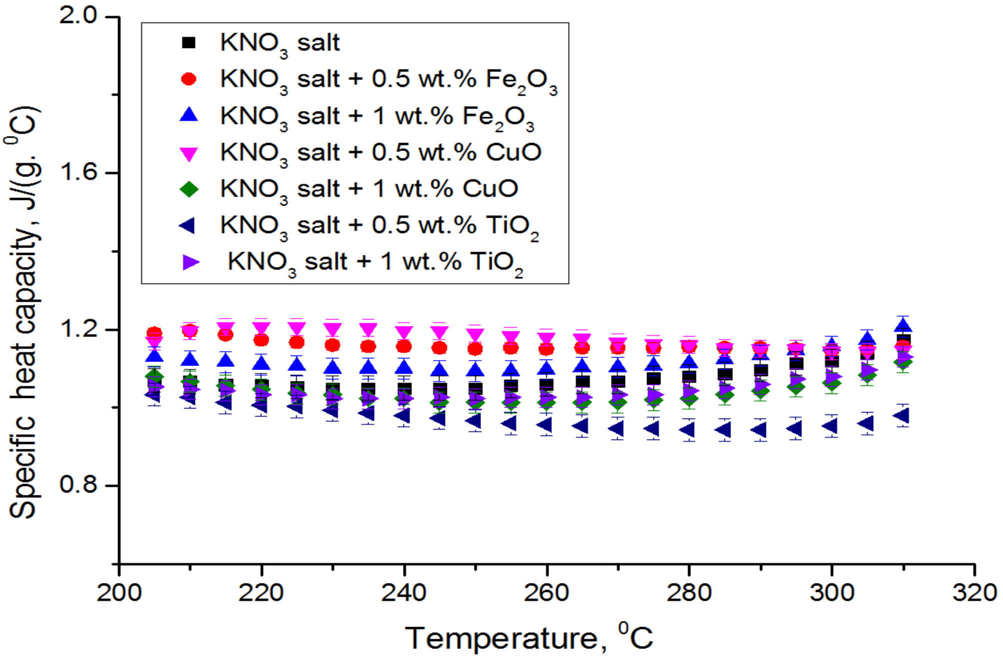

Figure 3-8 Solid phase of cp of different types and concentrations of nanoparticles dispersed into single nitrate salt (KNO_3 salt).

Figures (3-9 and 3-10) show the dependence of cp of liquid phase on temperature. It can be seen that nanosalts have higher cp than the nitrate salt (KNO_3 or binary salt). However, this increment in cp depends on the type of base material (KNO_3 or binary salt), and the type and concentrations of nanoparticles. For instance, TiO_2-nanosalt showed a negative effect on the cp of nano-binary salt, as shown in Table (3-4). In contrast, Lasfargues et al. (2015) indicated a positive effect of TiO_2-nanosalt and CuO-nanosalt. They prepared their nanosalt using a different methodology from ours. For the single salt case, Table (3-4) indicates that cp increases with increasing concentrations of nanoparticles in most cases. According to Chieruzzi et al. (2015a), 1 wt.% of silica-KNO_3 salt has higher cp than KNO_3 while 1 wt.% of alumina-KNO_3 salt has lower cp than KNO_3. This demonstrates the sensitivity of KNO_3 salt to the additives materials types. This is similar to the results we got for 1 wt. % nano-KNO_3. However, Chieruzzi et al. (2015a) studied only a fixed concentration of nanoparticles (1 wt.%) and they did not consider the effect of other concentrations (0.5 wt.%). Furthermore, the improvements in the cp of nanosalt in solid phase are slightly higher than that of liquid phase especially for the case of solar salt as the base material, which is in agreement to Chieruzzi et al. (2017). Because at higher temperatures, nanoparticles could suffer from agglomeration or sedimentation, they tend to become bigger in size which could effect on the performance of the nanosalt materials.

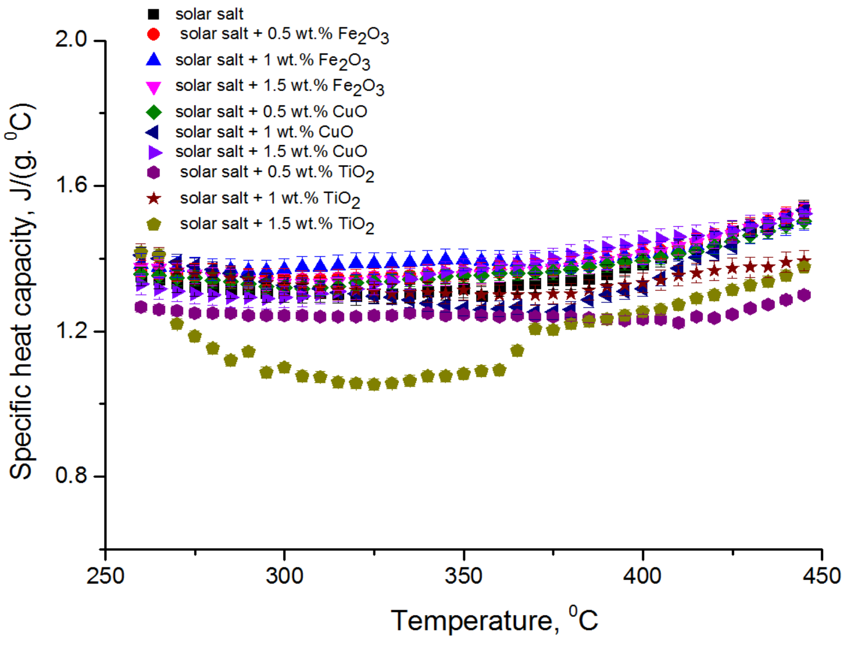

Figure 3-9 liquid phase of cp of different types and concentrations of nanoparticles dispersed into binary nitrate salt (solar salt).

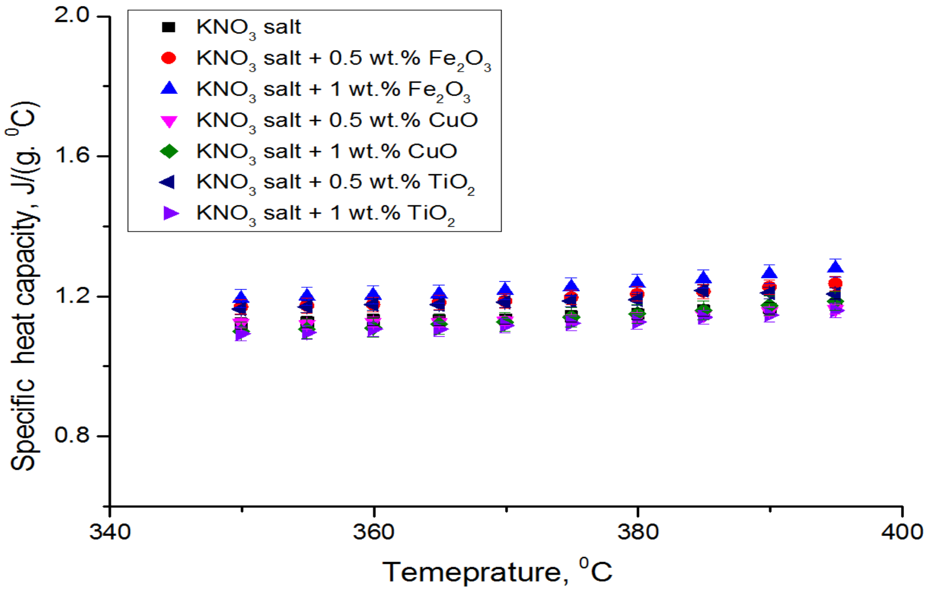

Figure 3-10 liquid phase of cp of different types and concentrations of nanoparticles dispersed into single nitrate salt (KNO_3 salt).

From Tables (3-1 to 3-4), Fe_2O_3 nanoparticles seem to be the best option in term of cp increments for both of solid and liquid phases. TiO_2 nanoparticles achieve small improvements in the cp of nanosalt and in most cases, it gives a negative effect for the cp value.

Table 3-1 Solid phase of cp (J/ (g. °C), in range 150 °C-215 °C) of different types and concentrations of nanoparticles dispersed inside solar salt ($NaNO_3$: KNO_3 by 60:40 molar ratios).

Run	Solar salt	+ Fe_2O_3			+ CuO			+ TiO_2		
	-	0.5 wt.%	1 wt.%	1.5 wt.%	0.5 wt.%	1 wt.%	1.5 wt.%	0.5 wt.%	1 wt.%	1.5 wt.%
1	1.43	1.67	1.63	1.67	1.59	1.37	1.64	1.27	1.31	1.3
2	1.44	1.49	1.54	1.53	1.48	1.63	1.49	1.41	1.52	1.53
3	1.43	1.54	1.51	1.53	1.51	1.56	1.48	1.36	1.53	1.52
Avg.	1.43	1.57	1.56	1.58	1.53	1.52	1.54	1.35	1.453	1.45
%	-	9.8%	9.1%	10.5%	7%	6.3%	7.7%	-5.6%	1.6%	1.4%

Table 3-2 Solid phase of cp (J/ (g. ^{0}C), in range 200 ^{0}C-315 ^{0}C) of different types and concentrations of nanoparticles dispersed into KNO_3 salt.

Run	KNO_3 salt	+ Fe_2O_3		+ CuO		+ TiO_2	
	-	0.5 wt.%	1 wt.%	0.5 wt.%	1 wt.%	0.5 wt.%	1 wt.%
1	1.09	1.17	1.12	1.16	1.06	0.78	1.06
2	1.072	1.15	1.11	1.151	1.03	1.085	1.04
3	1.073	1.13	1.13	1.150	1.04	1.065	1.039
Avg.	1.078	1.15	1.12	1.154	1.043	0.98	1.046
%	-	6.68%	3.9%	7.05%	-3.25%	-9.09%	-2.97%

Table 3-3 Liquid phase of cp (J/ (g. ^{0}C), in range 250 ^{0}C-450 ^{0}C) of different types and concentrations of nanoparticles dispersed inside solar salt ($NaNO_3$: KNO_3 by 60:40 molar ratios).

Run	Solar salt	+ Fe_2O_3			+ CuO			+ TiO_2		
	-	0.5 wt.%	1 wt.%	1.5 wt.%	0.5 wt.%	1 wt.%	1.5 wt.%	0.5 wt.%	1 wt.%	1.5 wt.%
1	1.38	1.36	1.33	1.37	1.36	1.37	1.35	1.14	1.27	0.9
2	1.37	1.363	1.46	1.39	1.37	1.34	1.34	1.3	1.35	1.32
3	1.35	1.46	1.42	1.39	1.4	1.32	1.45	1.31	1.39	1.30
Avg.	1.37	1.394	1.4	1.383	1.377	1.343	1.38	1.25	1.34	1.17
%	-	1.75%	2.19%	0.95%	0.51%	-1.97%	0.73%	-8.76%	-2.19%	-14.6%

Table 3-4 Liquid phase of cp (J/ (g. ^{0}C), in range 350 ^{0}C-395 ^{0}C) of different types and concentrations of nanoparticles dispersed into KNO_3 salt

Run	KNO_3 salt	+ Fe_2O_3		+ CuO		+ TiO_2	
	-	0.5 wt.%	1 wt.%	0.5 wt.%	1 wt.%	0.5 wt.%	1 wt.%
1	1.18	1.22	1.28	1.21	1.18	1.14	1.171
2	1.2	1.28	1.27	1.18	1.22	1.28	1.17
3	1.2	1.27	1.28	1.17	1.216	1.245	1.16
Avg.	1.19	1.26	1.28	1.187	1.205	1.222	1.167
%	-	5.9%	7.56%	-0.25%	1.261%	2.69%	-1.93%

On the other hand, the effect of preparation method has been studied. The direct preparation for CuO nanoparticles into nitrate binary salt has been conducted and compared with the well-known 2-step method. Approximately similar concentrations of 1 wt. % CuO were considered in both methods. 9 samples of 0.96 wt. % CuO-nanosalt were prepared by the use of the 1-step method under different preparation conditions. The time and temperatures of reactions were controlled by 300 ^{0}C, 400 ^{0}C, and 450 ^{0}C for 30 minutes, 1 hour, 2 hours and 4 hours. Figures (3-11 and 3-12) demonstrate the cp of solid and liquid phases of nitrate binary salt and nanosalts which are prepared by the 2-step method and the 1-step method. Furthermore, the 1-step method prepared under 300 ^{0}C or 400 ^{0}C indicated that improvements in cp values enhanced with an increase in time of reaction during the preparation. In contrast, in the case where the temperature of the muffle furnace was 450 ^{0}C, the optimum time for preparation was 1 hour. In the case where preparation temperature was 450 ^{0}C, any increase or decrease of the preparation time would show a lower improvement (or decrease in the liquid phase) in cp of nanosalt in comparison to the 1 hour. It can be seen that 1-step showed higher improvement in the cp than the conventional 2-step method. Table (3-5) shows the improvement in the cp values of the nanosalt (1 wt. % CuO + binary solar salt) prepared by both methods. Figures (3-13 and 3-14) show the improvement in cp of solid and liquid phases for the 2-step method and the 1-step method. The maximum increase in the sensible heat of CuO-nanosalt prepared by 1-step method was at 450 ^{0}C for 1 hour. The largest effect of the preparation method of nanosalt is on the cp of solid phase rather than the liquid phase. In both methods, it is clearly shown that the increment in cp of the liquid phase is lower than in the solid phase. This could be due to the stability issue of nanoparticles at high temperature. The less stable nanoparticles yield smaller improvements on the cp of nanosalt (Awad et al., 2018a; Luo et al., 2017; Lasfargues et al., 2015). In conclusion, for most cases of both preparation methods, cp of nanosalt is higher than cp of molten salt.

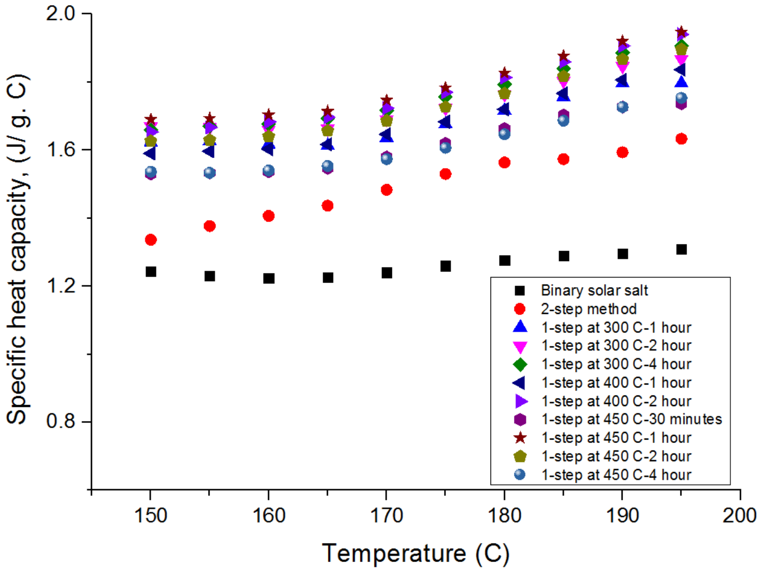

Figure 3-11 Solid phase of binary solar salt and nanosalt at (1 wt. % CuO+ binary solar salt) prepared by different methods.

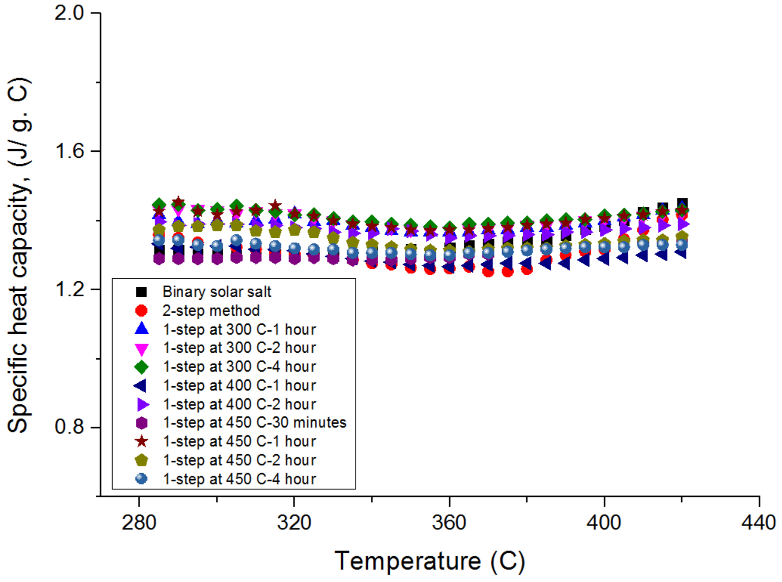

Figure 3-12 liquid phase of binary solar salt and nanosalt at (1 wt. % CuO+ binary solar salt) prepared by different methods

Table 3-5 cp improvement in nanosalt (1 wt. % CuO + binary solar salt) of the 2-step method and 1-step method under different preparation conditions in both of solid and liquid phases

Material	cp improvement in solid phase	cp improvement in liquid phase
Nanosalt prepared by 2-step method	6.3 %	-1.97 %
Nanosalt prepared by 1-step method at 300 ^{0}C and 1 hour	14.6 %	2.212 %
Nanosalt prepared by 1-step method at 300 ^{0}C and 2 hour	18.27 %	3.31 %
Nanosalt prepared by 1-step method at 300 ^{0}C and 4 hour	19.41 %	3.723 %
Nanosalt prepared by 1-step method at 400 ^{0}C and 1 hour	14.8 %	-4.321 %
Nanosalt prepared by 1-step method at 400 ^{0}C and 2 hour	20.24 %	0.892 %
Nanosalt prepared by 1-step method at 450 ^{0}C and 30 minutes	10.43 %	-4.601 %
Nanosalt prepared by 1-step method at 450 ^{0}C and 1 hour	21.24 %	3.119 %
Nanosalt prepared by 1-step method at 450 ^{0}C and 2 hour	18.21 %	-0.796 %
Nanosalt prepared by 1-step method at 450 ^{0}C and 4 hour	10.77 %	-3 %

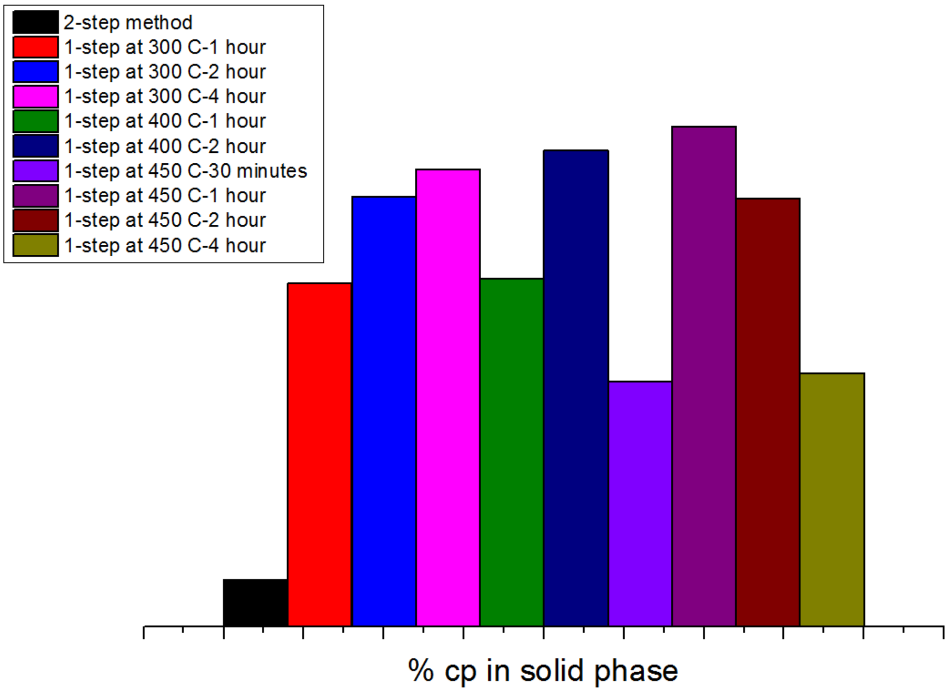

Figure 3-13 shows the improvement in cp in the solid phase in different nanosalt prepared by 2-step and 1- step methods.

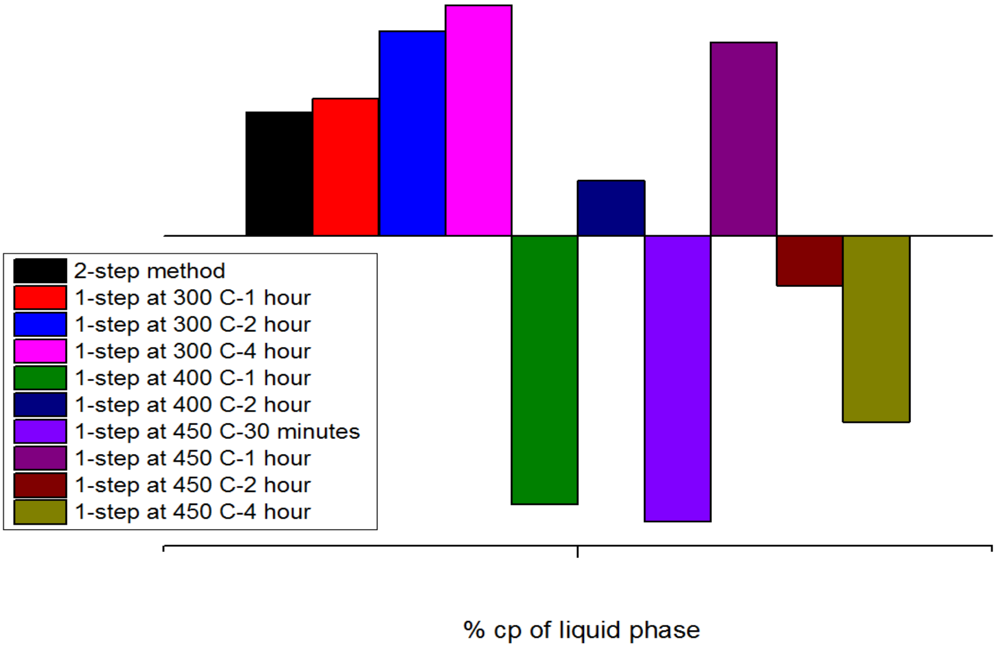

Figure 3-14 shows the improvement in cp in the liquid phase in different nanosalt prepared by 2-step and 1- step methods.

In order to explain the reasons behind the effects of nanoparticles on the cp of nanosalts, there are some models used to predict the improvement in the cp when nanoparticles are added. These models are discussed by many researchers, for example, Seo and Shin (2014). The classical model of the effective specific heat capacity can be given by Equation (3-8).

$$\mathrm{cp_{nf}} = \frac{\rho_{np}\,\emptyset_{np}\,\mathrm{cp_{np}} + \rho_{salt}\,\emptyset_{salt}\,\mathrm{cp}_{\,salt}}{\rho_{np}\,\emptyset_{np} + \rho_{salt}\,\emptyset_{salt}}$$ **Equation 3-8**

Where $\mathrm{cp_{nf}}$, cp_{np} and $\mathrm{cp_{salt}}$ represent cp of nanosalt, nanoparticle, and salt with a unit of (J/g. ^{0}C). $\emptyset_{np}$ and $\emptyset_{salt}$ are the volume fraction of nanoparticles and salt, respectively. ρ_{np} and ρ_{salt} are the density of nanoparticle and salt, respectively, with a unit of kg/m^3.

The range of temperatures in Equation (3-8) depend on the tested material (nitrate salt), as shown below

- In case of binary solar salt (and nano-solar salt):
  Solid phase (150 ^{0}C < Temperature < T_{onset})
  Liquid phase (250 ^{0}C < Temperature < 450 ^{0}C)
- In case of KNO_3 salt (nano-KNO_3):
  Solid phase (200 ^{0}C < Temperature < T_{onset})
  Liquid phase (350 ^{0}C < Temperature < 395 ^{0}C)

Unlike the experimental data, there are no enhancements in the cp of nanosalt predicated by the classical model Equation (3-8). This disagreement between the model prediction and the experimental data is due to some reasons such as the lowest cp values of nanoparticles in comparison to the base material (nitrate salt). For instance, the Fe_2O_3 nanoparticle has cp smaller than that of nitrate salt. Additionally, cp of Fe_2O_3 nanoparticles around (0.9 J/g. ^{0}C) which is slightly higher than its bulk material (0.84 J/g. ^{0}C) in the range of (150 ^{0}C - 450 ^{0}C) (Snow et al., 2010).

For more emphasis, we measured the cp of all nanoparticles used for the experiments. It was found that the cp of Fe_2O_3 equals to (0.9 J/g. ^{0}C), cp of CuO equals to (0.59 J/g. ^{0}C) and cp of TiO_2 is (1.06 J/g. ^{0}C). Likewise, Luo et al. (2017) demonstrated the cp value for the bulk CuO was (0.54 J/g. ^{0}C). This bulk value of cp is slightly lower than the cp of CuO nanoparticles (0.59 J/g. ^{0}C). However, cp values of nanoparticles (Fe_2O_3, CuO, TiO_2 nanoparticles) are still lower than that of nitrate salt. This indicates that the improvements in the cp of the nanosalt are not due to the cp values of the nanoparticle. Therefore, the classical model cannot predict the enhancement in cp of nanosalt where the cp of nitrate salt is larger than that of the nanoparticles used in the respective work. Therefore, the classical model needs to be expanded to include the effects of other factors such as the interfacial area formed at the surface of the nanoparticle and the nitrate salt or other forces between nanoparticles and so on.

In addition, nanoparticles have a higher surface area which causes an increase in the thermal resistance between nanoparticles and the molecules of the molten salt, resulting in a rise in the interfacial interaction between them, which could increase the cp of nanosalt. Moreover, during the preparation protocol for nanosalt samples (i.e. sonication and evaporation stages in 2-step method or during the chemical reaction in 1-step method), molten salt molecules could form a compressed layer on the surface of nanoparticles. Different properties could be possessed by the interfacial layers such as higher cp, which may lead to increase the value of cp of nanosalt according to the Equation (3-9).

$$\mathrm{cp_{nf}} = \frac{\rho_{np}\, \emptyset_{np}\ \mathrm{cp_{np}} + \rho_c\, \emptyset_c\ \mathrm{cp_c} + \rho_{salt}\, \emptyset_{salt}\, \mathrm{cp}_{\ salt}}{\rho_{np}\, \emptyset_{np} + \rho_c\, \emptyset_c + \rho_{salt}\, \emptyset_{salt}}$$ **Equation 3-9**

where $\mathrm{cp}_{,c}$, $\emptyset_c$ and ρ_c represent cp, volume fraction, and density of the compressed layer (interfacial layer), respectively. Equation (3-9) has the same temperature range as Equation (3-8). In addition, the mass fractions of these layers depend on size and concentrations of nanoparticles. It is assumed that the cp of an interfacial layer has a significant effect on the overall cp of nanosalt when there is no agglomeration of nanoparticles. For instance, an assumed value of cp= 6.2 J/g. ^{0}C (of the interfacial layer) would predict the experiment well. Furthermore, it is possible that the forces (such as sedimentation of nanoparticles, the Van der Waals force, and surface charge between the nanoparticles, as well the attractive force among the nanoparticles) between the nanoparticles might have an effect on the cp of nanosalt. These forces could lead to agglomerations of these nanoparticles, which impact negatively on nanoparticles' dispersion in the nanosalt samples. Therefore, there is a need to find a proper surfactant that could work efficiently at this high temperature condition, which could help to solve the dispersion and stability issue of nanoparticles in the nanosalt samples. We tried some types of surfactant, however, they burned during the measurements of the cp (at a higher temperature up to 450 ^{0}C) due to their short life temperature. Additionally, in the results, they caused a decrease in the cp of the nanosalt samples. Therefore, the type of surfactant should have a higher decomposition temperature and should be stable enough for the repeatable cycles.

3.4.2 Latent heat

Latent heat is the heat released or absorbed from the samples due to phase change. In case of salt/nanosalt, the phase is changed from a solid state to liquid state. Latent heat is extensively affected by dispersing nanoparticles into nitrate salt. Particularly, 1 wt. % of Fe_2O_3 and CuO in binary salt, 0.5 wt. % of Fe_2O_3 and CuO-single salt increases the latent heat. The highest increases in latent heat found within CuO-binary salt were up to 15% and Fe_2O_3-single salt up to 3%. This increment will give more energy stored per unit volume.

As explained earlier, the interface layer is formed in nanosalt samples during the preparation procedure. These layers are formed because of nanoparticles rearrangements inside the nanosalt sample. Therefore, nanosalt requires more heat to melt these interfacial layers, which may be one of the reasons for increasing latent heat. Additionally, clusters of nanoparticles could lead to an increase in the latent heat as suggested by Chieruzzi et al. (2015a) and Lasfargues et al. (2015). According to their suggestions, more heat is required to melt these clustering of nanoparticles. However, increasing or decreasing the latent heat of nanosalt samples depends on the presence of nanoparticles in the sample. For instance, nanosalt (1 wt. % CuO-binary solar salt) has a higher value of latent heat than other materials (nitrate salt or other nanosalt materials) as shown in Table (3-6). From the SEM result in Figure (3-15), clusters of 1 wt. % CuO-nanosalt are clearly shown and this sample possesses a higher value of latent heat. This could be due to the clustering requiring more heat to melt which leads to an increase in latent heat.

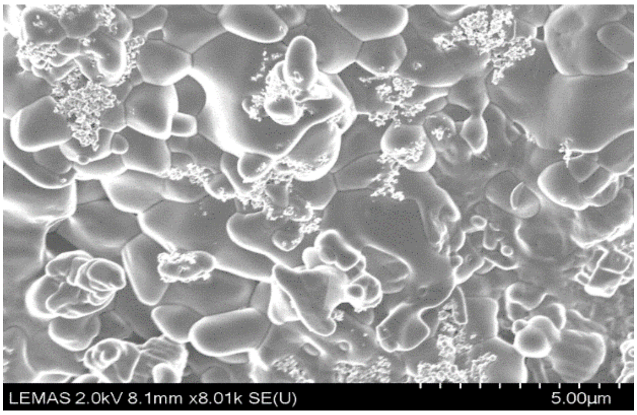

Figure 3-15 shows the SEM test of 1 wt. % CuO dispersed in binary solar salt by the 2-step method.

Additionally, as shown in Figure (3-16) of the samples tested by SEM results, there is a presence of agglomerations and clustering of the nanoparticles in the nanosalt samples. In Figure (3-16) the SEM data is for nano-binary solar salt samples after the melting/solidification cycles in the DSC device. These results are consistent with the observation from Chieruzzi et al. (2015a) and Lasfargues et al. (2015) for latent heat improvements in nanosalt samples.

Table 3-6 latent heat, onset temperature and total thermal energy storage capacity of different types and concentrations of nanoparticles dispersed in solar salt ($NaNO_3$: KNO_3 by 60:40 molar ratios).

Material	Latent heat (kJ/kg)	Onset temperat-ure (^0C)	T_{onset} differences (^0C)	Total TES capacity (kJ/kg)	% TES
Pure salt	107.03	219.11	-	466.83	-
Salt + 0.5 wt. % Fe_2O_3	109.27	216.22	2.89	482.27	3.31%
Salt + 1 wt. % Fe_2O_3	119.09	219	0.11	492.69	5.54%
Salt + 1.5 wt % Fe_2O_3	115.25	216.66	2.45	486.65	4.25%
Salt + 0.5 wt % CuO	118.08	216.01	3.1	485.28	3.95%
Salt + 1 wt % CuO	122.5	218.21	0.9	482.3	3.31%
Salt + 1.5 wt % CuO	110.32	217.05	2.06	478.72	2.55%
Salt + 0.5 wt % TiO_2	95.41	216.33	2.78	426.41	-8.66%
Salt + 1 wt % TiO_2	100.37	215.88	3.23	455.55	-2.42%
Salt + 1.5 wt % TiO_2	89.65	213.31	5.8	410.65	-12.03%

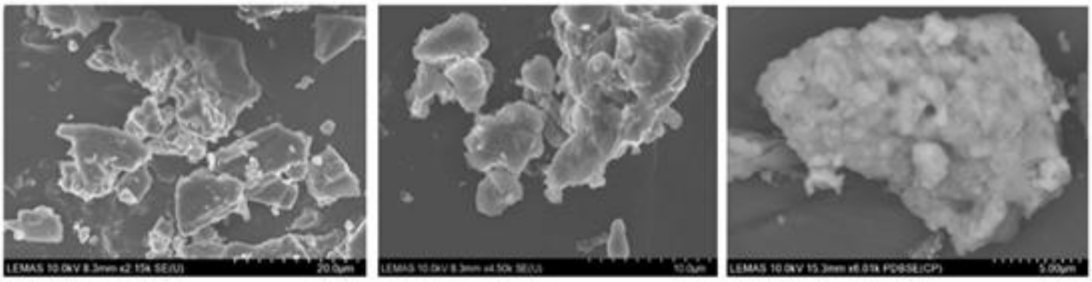

1 wt. % Fe_2O_3 dispersed in solar salt.

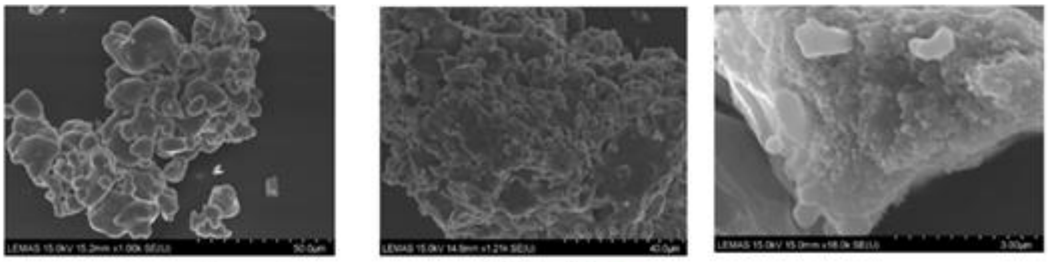

1 wt. % Fe_2O_3 dispersed in KNO_3 salt.

0.5 wt. % CuO dispersed in solar salt

0.5 wt. % CuO dispersed in KNO_3 salt.

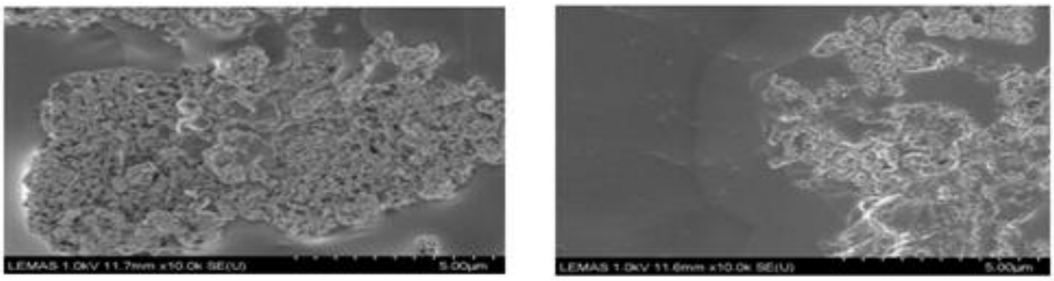

0.5 wt. % Fe_2O_3 dispersed in KNO_3 after melting/solidification cycles

0.5 wt. % TiO_2 dispersed in KNO_3 after melting/solidification cycles

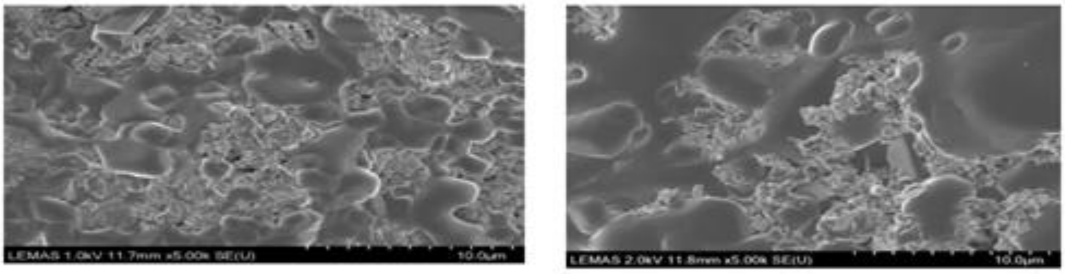

0.5 wt. % CuO dispersed in solar salt after melting/solidification

0.5 wt. % Fe_2O_3 dispersed in solar salt after melting/solidification

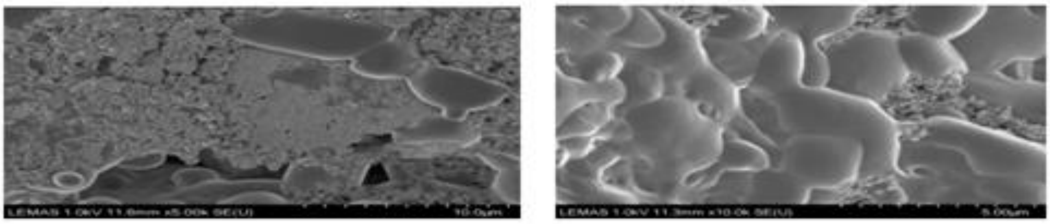

1 wt. % Fe_2O_3 dispersed in solar salt after melting/solidification

1 wt. % TiO_2 dispersed in solar salt after melting/solidification

Figure 3-16 shows SEM test for nanoparticle agglomerations after the preparation.

On the other hand, nanosalt (CuO- binary solar salt), prepared by the 1-step method, has a higher increment in latent heat than nanosalt prepared by the 2-step method. The value of the latent heat of binary solar salt was 107.03 kJ/kg, and for nanosalt prepared by the 2-step method, it was 122.5 kJ/kg and 178.87 kJ/kg of the nanosalt prepared by the 1-step method. In comparison between the preparation methods, it seems that the 1-step method increases the latent heat more than the 2-step method. This could be due to higher agglomerations of nanoparticles in nanosalt samples prepared by the 1-step method. As explained earlier, nanoparticles clusters help the nanosalt sample to absorb more heat in order to change phase and this causes an increment in latent heat of nanosalt. Figure (3-17) shows the large agglomerations of nanoparticles in nanosalt prepared by the 1-step method. These large chunks of nanoparticles could explain the higher increases in latent heat of nanosalt prepared by the 1-step method.

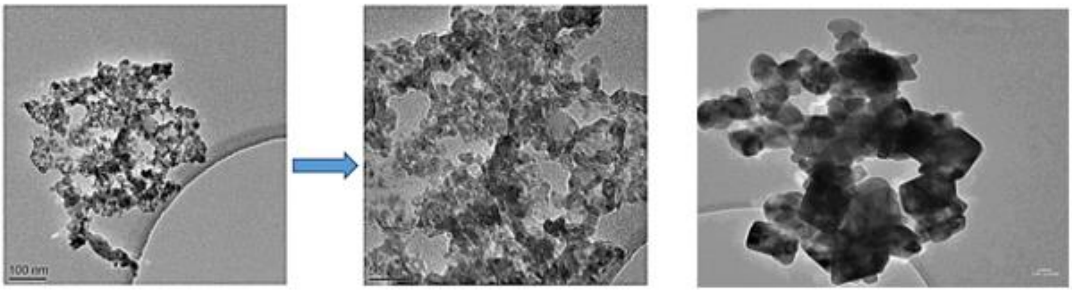

Sample (a) 300 ^{0}C for 1 hour

Sample (b) 400 ^{0}C for 2 hour

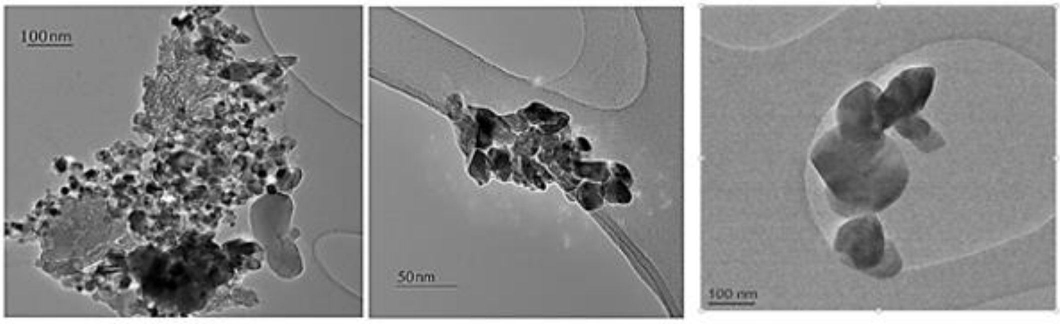

Sample (c) 450 ^{0}C for 30 min

Sample (d) 450 ^{0}C for 4 hour

Figure 3-17 TEM image of 1 wt. % of CuO nanoparticle and solar salt ($NaNO_3$: KNO_3 with 60:40 molar ratio) prepared by novel 1-step method.

On the other hand, Figure (3-18) shows the TEM of CuO nanoparticles purchased from the company and used in the 2-step method. Additionally, DLS measurements for different types of nanoparticles are shown in Figure (3-19). The sizes of nanoparticles (purchased (Fe_2O_3, TiO_2, CuO) or prepared CuO) are bigger than the size mentioned by the companies or the TEM image. This could be due to the fact that we did not use any type of surfactant during the DLS measurements.

Furthermore, it can be noticed that the clustering of the purchased nanoparticles is less than those in the prepared CuO nanoparticles, as explained earlier in Figures (3-17 and 3-18). This could be one of the reasons behind the differences in latent heat values in both preparation methods (1- step and 2- step methods). For instance, the methodology used to prepare the purchased nanoparticles is different from the one prepared directly inside the molten salt. Furthermore, the company could use any type of stabilizer that helps to control the size of nanoparticles while in our case no size controller is used.

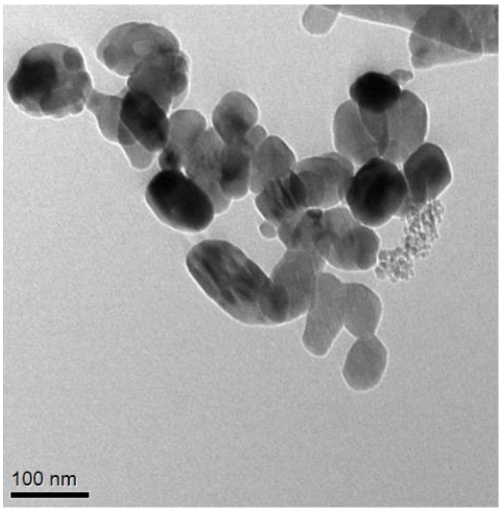

Figure 3-18 shows the TEM image of CuO nanoparticles purchased.

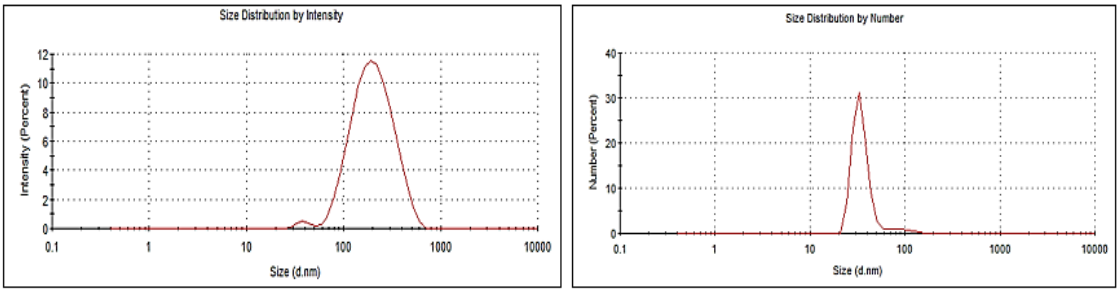

(a) Fe_2O_3-nanofluid with an average size of (175.5 nm)

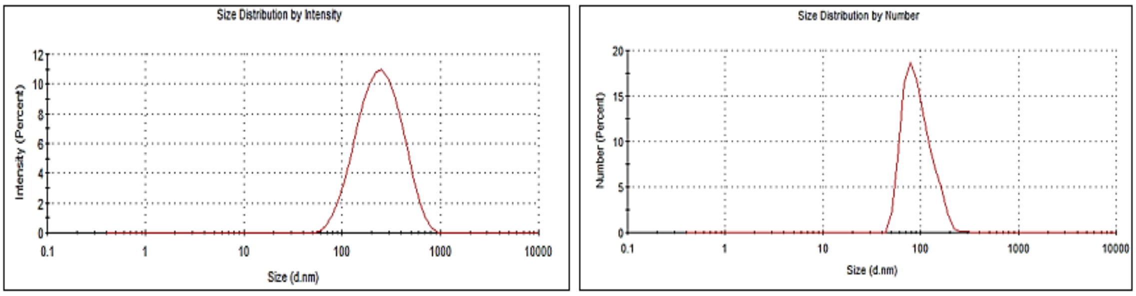

(b) TiO_2-nanofluid with an average size of (214 nm)

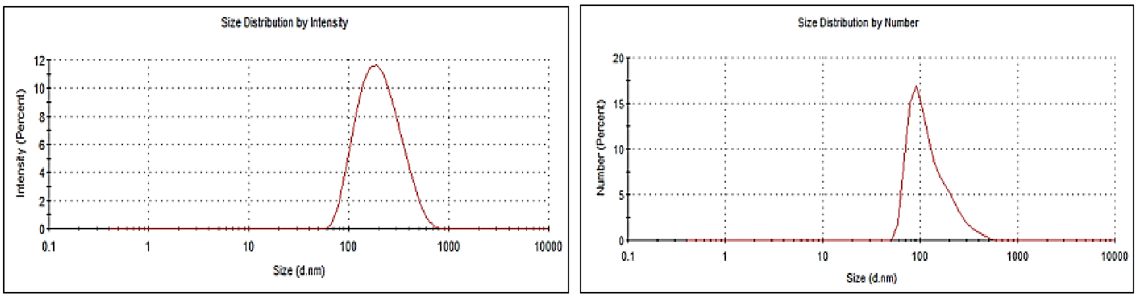

(c) CuO-nanofluid with an average size of (182.5 nm)

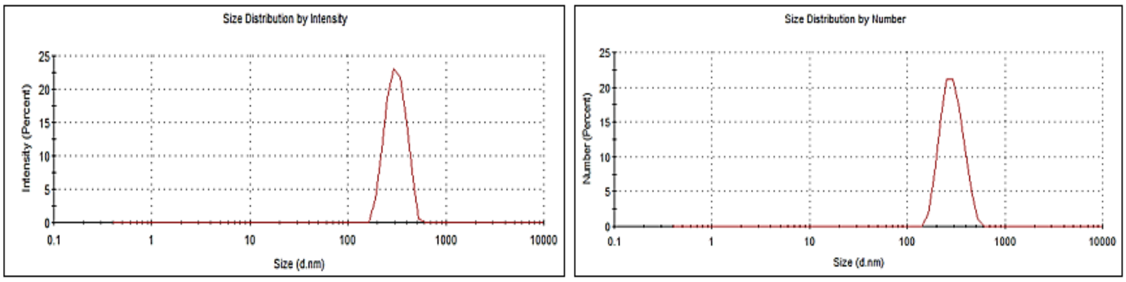

(d) CuO (prepared by 1-step method)-nanofluid with an average size of (438.1 nm)

Figure 3-19 Shows the size measurement in the DLS device for different nanofluid samples (a, b, and c) of purchased nanoparticles and sample (d) of CuO nanoparticles prepared by 1-step method.

Additionally, the EDX device is used to check the elements of the samples prepared by the 1-step method to ensure the existence of CuO nanoparticles in the nanosalt samples. Figure (3-20) shows the EDX from the TEM test for nanosalt prepared by the 1-step method. The existence of CuO nanoparticles can be seen in the sample. Additionally, the element of Au is due to the type of grid used (gold), C is due to the carbon coating for the sample and CuO represents the samples. Figure (3-21) indicates the EDX from the SEM device, therefore the salt ($NaNO_3$: KNO_3) material are present in the EDX data.

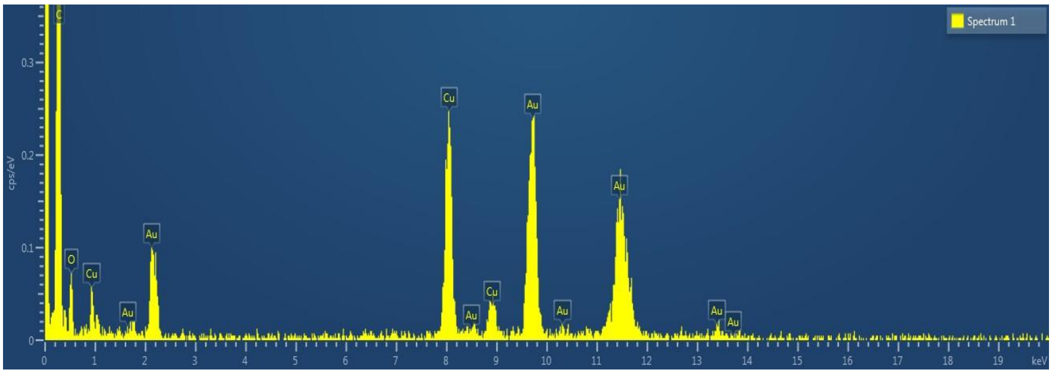

Figure 3-20 Elemental spectra from EDX analysis from TEM device of CuO nanoparticle prepared by the 1-step method.

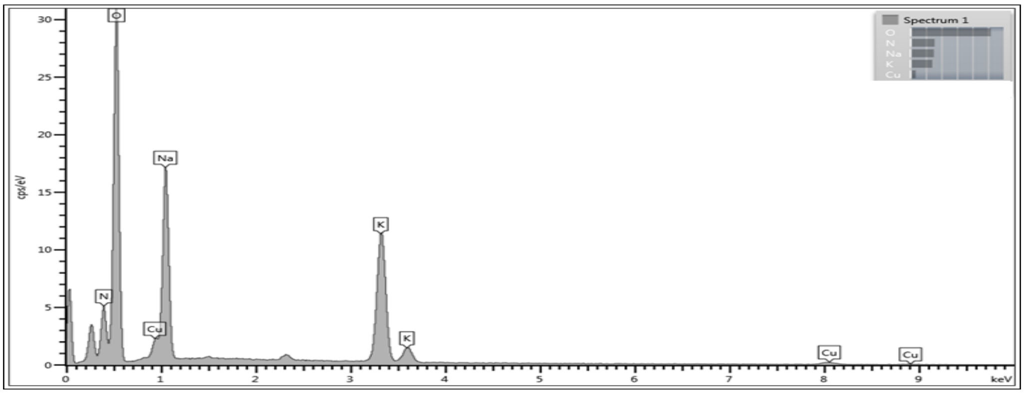

Figure 3-21 Elemental spectra from EDX analysis from SEM device of CuO nanoparticle and solar salt ($NaNO_3$: KNO_3 with 60:40 molar ratio) prepared by the 1-step method.

Moreover, the onset temperature represents the starting of the phase change for the storage material (salt/nanosalt). In most cases of nanosalt, the melting temperature ($T_{melting}$) is affected by the addition of nanoparticles. In particular, $T_{melting}$ of binary solar salt decreases by 5 ^{0}C with the addition of nanoparticles to the samples. $T_{melting}$ of binary solar salt is 230 ^{0}C while $T_{melting}$ of all the nano-binary solar salt is between 225 ^{0}C and 226 ^{0}C. On the other hand, in the case that KNO_3 is the base material, similar behaviour was observed where $T_{melting}$ of nano-KNO_3 samples decreased by 1 ^{0}C. This is similar to the results from Gimenez-Gavarrell et al. (2015), Chieruzzi et al. (2013a), Lasfargues et al. (2015) and Chieruzzi et al. (2015a).

According to Lasfargues et al. (2015), the $T_{melting}$ decrease in nanosalt relies on the method of heat transfer over nanosalt sample and the size of the clustering of these nanoparticles. Moreover, nanoparticles in the sample could work as nucleation agents, which brings the phase change earlier in comparison with the base salt, (Gimenez-Gavarrell et al., 2015). Although this decrement in melting temperature is low, it is still considered an advantage because it means the phase change starts earlier. As a result, melting time will reduce which improves the heat transfer in the storage system with the support of enhanced conduction by nanoparticles.

Additionally, the phase change of the binary solar salt is in a range of temperatures rather than at a single temperature point. Because of this, the mixture binary salt behaves as a non-pure mixture showing that it needs more heat to be melted or frozen completely. According to Kramer and Wilson (1980), the addition of 60% molar ratio of $NaNO_3$ would result in a melting temperature of the binary salt in a temperature range 221 ^{0}C > $T_{melting}$ > 241 ^{0}C. On the other hand, KNO_3 with a composition of 100% has one value for the $T_{melting}$ 335 ^{0}C as it is a pure single material (Kramer and Wilson, 1980), as shown in Figure (3-22). However, the KNO_3 material used in this experiment was 98% pure. From the DSC measurements, $T_{melting}$ of KNO_3 was in a range caused by its non-purity. The purity of the material has an impact that influences the behaviour of the salt and nanosalt properties. In addition, the decomposition temperature of different samples has been measured by the TGA/DSC device, as shown in Figure (3-23). The starting of decomposition appears to be from 550 ^{0}C as indicated in Figure (3-23). TGA/DSC measurement demonstrates that there is no big difference in the starting of the decomposition process among the different materials tested such as binary salt, 0.5 wt.% Fe_2O_3+binary salt, 1 wt.% CuO+ binary salt prepared by 2-step method, two samples of CuO + binary salt prepared by 1-step method under different conditions (300 ^{0}C and 450 ^{0}C).

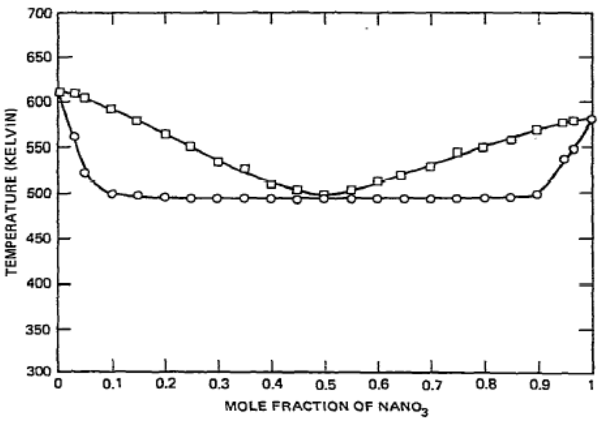

Figure 3-22 phase diagram of solar salt with different composition of $NaNO_3$ (Kramer and Wilson, 1980).

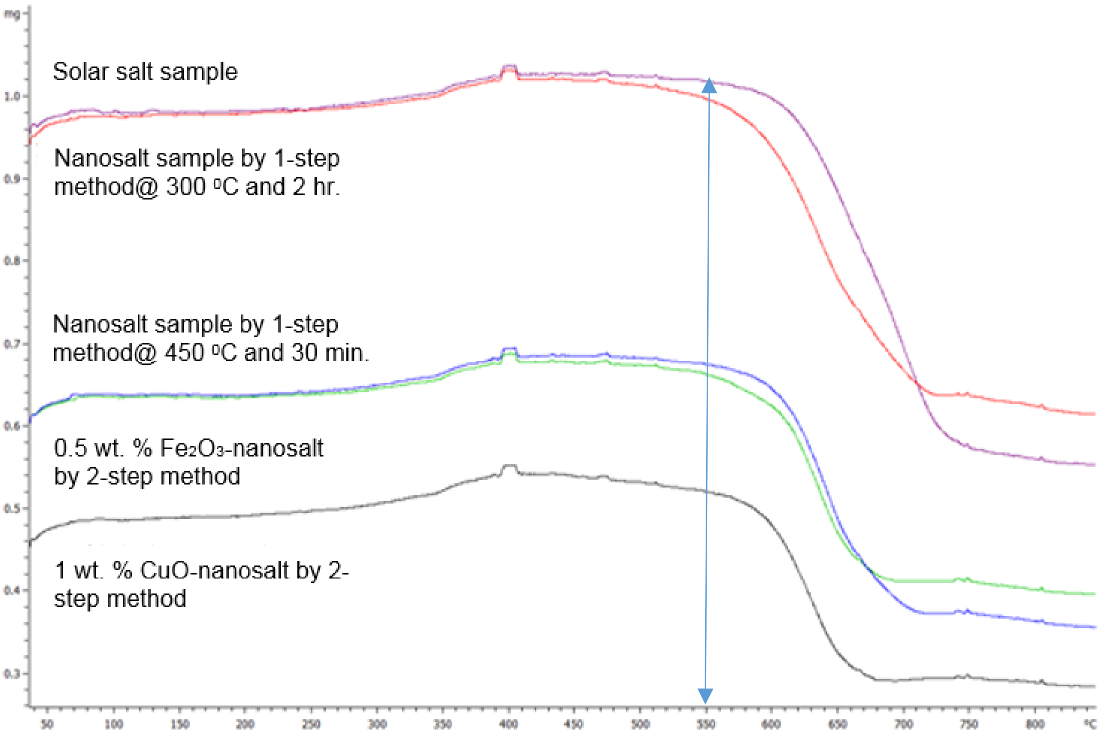

Figure 3-23 Shows the decomposition temperature of binary solar salt and nanosalts.

3.4.3 Total thermal energy storage (TES)

TES represent the summations of the sensible and latent energies. In most cases, nanosalt samples have higher TES than nitrate salt alone, as shown in Tables (3-6 and 3-7). From Table (3-6), 1 wt. % of Fe_2O_3-binary salt and 0.5 wt. % of CuO-binary salt represent the maximum increment in TES. This is due to the accumulated increment of an energy of both sensible and latent energies. For instance, 1 wt. % of Fe_2O_3-binary salt possesses a higher increase in latent heat than other concentrations alongside with the advantages of sensible increment in both solid and liquid phases. Although, 1 wt. % of CuO-binary salt gave the maximum increase in latent heat, it shows less increment in the sensible heat in comparison to the 0.5 wt. %. Therefore, 0.5 wt. % of CuO-binary salt gave a higher TES than that of 1 wt. % of CuO-binary salt. In the case of the 1-step method, the TES is 485.08 kJ/kg which is slightly higher than the TES of the 2-step method (482.3 kJ/kg).

In the case of nano-single salt, higher increments in TES were observed with the minimum concentrations of nanoparticles (0.5 wt. %). For instance, 0.5 wt. % Fe_2O_3-KNO_3 showed the maximum increment in TES by 5.26%, as shown in Table (3-7).

Table 3-7 Latent heat, onset temperature and TES capacity of different types and concentrations of nanoparticles dispersed inside KNO_3 salt.

Material	Latent heat (kJ/kg)	T_{onset} (^0C)	T_{onset} differences (^0C)	Total TES capacity (kJ/kg)	% TES
KNO_3 salt	93.89	332.47	0	331.47	-
KNO_3 salt + 0.5 wt. % Fe_2O_3	96.41	332.12	0.35	348.91	5.26%
KNO_3 salt + 1 wt. % Fe_2O_3	94.08	325.53	6.94	345.28	4.17%
KNO_3 salt + 0.5 wt. % CuO	95.14	332.3	0.17	340.78	2.81%
KNO_3 salt + 1 wt. % CuO	94.42	330.78	1.69	329.65	-0.55%
KNO_3 salt+ 0.5 wt. % TiO_2	91.02	327.56	4.91	321.02	-3.15%
KNO_3 salt+ 1 wt. % TiO_2	92.9	325.55	6.92	324.66	-2.05%

As mentioned earlier, TES is represented by the summation of sensible heat (in the range of working temperatures of solid and liquid phases) and of latent heat as shown in Equations (3-10, 3-11, and 3-12).

$$\mathrm{TES} = \mathrm{q_{sensible}} + \mathrm{q_{latent}}$$ **Equation 3-10**

$$\mathrm{q_{sensible}} = \mathrm{q_{sensible\ in\ solid\ phase}} + \mathrm{q_{sensible\ in\ liquid\ phase}}$$ **Equation 3-11**

$$\mathrm{q_{storage}} = [\int_{\mathrm{T_{ambient}}}^{\mathrm{T_{melt}}} \mathrm{cp} * \mathrm{dT} + \int_{\mathrm{T_{liquid}}}^{\mathrm{T_{max.}}} \mathrm{cp} * \mathrm{dT}] + \mathrm{q_{latent}}$$ **Equation 3-12**

The range of temperatures in Equation (3-12) depends on the nitrate salt type (single nitrate salt or binary nitrate salt), as shown below

- In case of binary solar salt (and nano-solar salt):
  $T_{ambient}$ = 150 ^{0}C, $T_{max.}$ = 450 ^{0}C,
- In case of KNO_3 salt (nano-KNO_3):
  $T_{ambient}$ = 200 ^{0}C, $T_{max.}$ = 395 ^{0}C.

The storage capacity increased if the thermophysical properties of the PCM (salt) increased. Therefore, seeding nanoparticles would give an improvement in the sensible and latent heat of the nano-PCM (nanosalt). In most cases, nanosalt has higher cp and latent heat than the nitrate salt alone and this leads to a higher efficiency of the storage system, which indicates a higher level of the solar thermal power plant efficiency. According to Feldhoff et al. (2012), 9 hours is the recommended storage time inside a two tank (hot and cold sensible tanks) in the solar thermal plant. The working temperatures in the cold and hot tanks are 292 ^{0}C and 386 ^{0}C respectively. Dispersing nanoparticles into the base material will improve the cp of the base material. 14% is the efficiency of TES using molten salt alone, (Feldhoff et al., 2012), while with nanosalt as a storage medium this efficiency increases. For instance, at T= 386 ^{0}C, the sensible heat of solar salt is 220.744 J/kg. However, this sensible heat (220.744 J/kg) can be increased when dispersing 1.5 wt. % of CuO in solar salt to 233.044 J/kg. As a result, the sensible heat of the nano-binary salt increases by 5.6% in comparison to solar salt only, which means increasing the efficiency of the TES system. Furthermore, at T=386 ^{0}C, the value of cp of nanosalt (KNO_3+ 1 wt. % Fe_2O_3) equals 1.253 J/kg. ^{0}C, while the cp of molten salt (KNO_3) = 1.1615 J/kg. ^{0}C. Therefore the sensible heat is increased by 7.88% by the presence of nanoparticles. This indicates the large impact of nanoparticles on the efficiency of the storage system.

3.4.4 Thermal conductivity

Thermal conductivity (k) of binary solar salt, Fe_2O_3-nanosalt, and CuO-nanosalt has also been investigated. The k value is measured for the nanosalt samples which are prepared by the 2-step method. Nanoparticles significantly affect k values of nanosalt at both low and high temperatures. Increasing concentration of Fe_2O_3, from 0.5 wt. % to 1.5 wt. % has a positive effect on k of nanosalt while 1 wt. % showed a decrease. In contrast, increasing concentrations of CuO nanoparticles showed a decrease in k of nanosalt. It can be concluded that lower concentrations of nanoparticles are preferred for improvement of k of nanosalt samples. With temperature increments, the Brownian motion of particles is increased and this could cause an improvement in the values of k. In addition, nanoparticles have a higher value of k than binary nitrate salt, therefore, mixing these nanoparticles with the binary nitrate salt could lead to higher values of k. However, the increase in k value of nanosalt is selective and depends on some parameters such as the type or concentration of nanoparticles. For instance, the sample prepared by the mixing of base salt and the additive material (Fe_2O_3) seems to be a more conductive material than the CuO-nanosalt ones as shown in Figure (3-24).

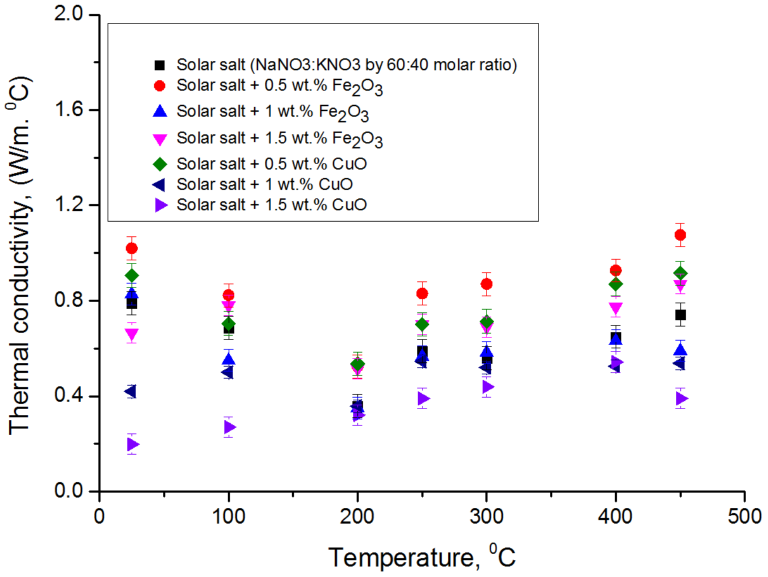

Figure 3-24 Shows thermal conductivity vs. temperature of different samples.

As explained earlier, k is calculated depending on the measurement of cp and thermal diffusivity. Figure (3-25) shows thermal diffusivity measurements of binary salt and different nanosalt samples.

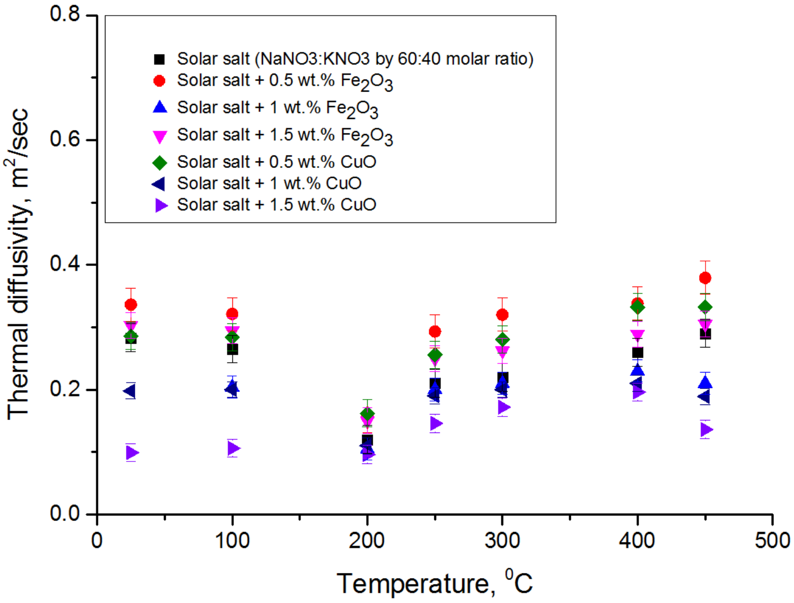

Figure 3-25 Shows thermal diffusivity vs temperature of binary nitrate solar salt and nanosalt.

It is clearly shown that the thermal diffusivities of some nanosalts are higher than the binary salt without any additives. This indicates the effect of nanoparticles types on the nanosalt samples. Furthermore, k (or thermal diffusivity) of nanosalt could be improved because of the higher surface area possessed by nanoparticles**.** In addition, Fe_2O_3 nanoparticles have a smaller particle size, which implies a higher surface area than CuO nanoparticles. This could be one of the reasons behind the high improvements in Fe_2O_3-nanosalt compared to CuO-nanosalt samples (Yoo et al., 2007). According to Hwang et al. (2006), k of the base material and the additives materials are highly affected by the overall value of k of nanofluid. This is consistent with the current data because k of both types of nanoparticles used is higher than the value of k of nitrate solar salt which leads to a higher k of the nanosalt sample.

There are some parameters that affect the overall improvement in thermal conductivity of nanosalt samples such as particles loading, the temperature range of the test, nanoparticles size and stability of the sample. Table (3-8) shows the results of thermal conductivity of binary nitrate salt and nanosalt samples.

Table 3-8 Thermal conductivity (k, W/m. ^{0}C) of different types and concentrations of nanosalt

T, ^{0}C	Molten salt	Molten salt+ 0.5 wt.% Fe_2O_3	Molten salt+ 1 wt.% Fe_2O_3	Molten salt+ 1.5 wt.% Fe_2O_3	Molten salt+ 0.5 wt.% CuO	Molten salt+ 1 wt.% CuO	Molten salt+ 1.5 wt.% CuO
25	0.79	1.02	0.828	0.665	0.906	0.42	0.198
100	0.687	0.823	0.55	0.78	0.705	0.5	0.27
200	0.359	0.524	0.35	0.515	0.536	0.358	0.32
250	0.589	0.83	0.566	0.7	0.701	0.545	0.39
300	0.558	0.87	0.583	0.69	0.713	0.52	0.439
400	0.649	0.927	0.632	0.774	0.87	0.525	0.543
450	0.742	1.076	0.59	0.87	0.915	0.538	0.39

Moreover, different types of nanoparticles (CuO or Fe_2O_3) almost show that the lowest concentration (0.5 wt. %) gives higher increment in thermal conductivity values than higher concentrations (1 wt. % or 1.5 wt. %). On the other hand, 1.5 wt. % Fe_2O_3-nanosalt showed a higher improvement than 1 wt. % Fe_2O_3-nanosalt case. Table (3-9) demonstrates the enhancement of the thermal conductivity of different types of nanosalt samples at different temperatures including the solid phase and liquid phase. It can be seen that the maximum increment in thermal conductivity was observed for lower concentrations of nanosalt (0.5 wt. %) over the range of concentrations tested. Figure (3-26) shows the effect of the weight fraction of nanoparticles on thermal conductivity.

Table 3-9 Enhancement in thermal conductivity of different types and concentrations of nanosalt

T, ^{0}C	Molten salt+ 0.5 wt.% Fe_2O_3	Molten salt+ 1 wt.% Fe_2O_3	Molten salt+ 1.5 wt.% Fe_2O_3	Molten salt+ 0.5 wt.% CuO	Molten salt+ 1 wt.% CuO	Molten salt+ 1.5 wt.% CuO
25	29.1	4.81	-15.8	14.68	-46.84	-74.94
100	19.8	-19.94	13.54	2.62	-27.22	-60.7
200	45.96	-2.51	43.45	49.3	-0.28	-10.86
250	40.92	-3.9	18.85	19.02	-7.47	-33.79
300	55.91	4.48	23.66	27.78	-6.81	-21.33

400	42.84	-2.62	19.26	34.05	-19.11	-16.33
450	45.01	-20.49	17.25	23.32	-27.49	-47.44

In general, k of nanofluid increases with increasing concentration of nanoparticle (Mintsa et al., 2009). However, Figure (3-26) does show a certain discrepancy as the results for 0.5 wt. % nanosalt is slightly above others concentrations.

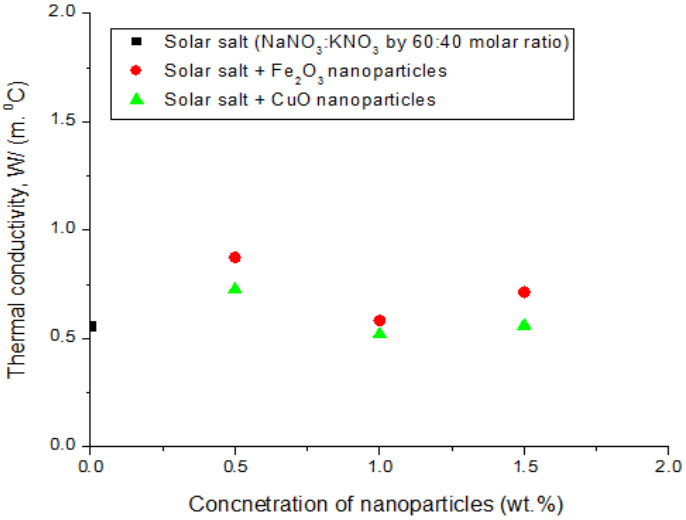

Figure 3-26 Thermal conductivity of nanosalt vs concentration of nanoparticles.

According to (Saidur et al., 2011), k increases with nanoparticles concentrations. This has some differences with the current work due to the effect of the base material. Molten salt behaves differently than water, in addition, the effect of the surface charge of molten salt could play an important role in the result of k-Temp (T dependence of k). Furthermore, Assael et al. (2005) mentioned that increasing concentrations from 0.1 to 6 % weight loading gave a decreasing in k by 0.3% to 5% in respective. This is consistent with the results that we obtained, as an increment in particle concentrations would cause a decreasing k. Although we tested Fe_2O_3-nanosalt and CuO-nanosalt, which are different from the material tested by Assael et al. (2005), their material was carbon nanotube-water based material. It indicates the large effect of the concentration on the improvement of k of nanosalt. More work needs to be considered in order to measure k of nanosalt over a wide range of concentrations to compare the effect of k with nanoparticles' loading in the nanosalt samples.

Thermal conductivity was calculated theoretically by considering the Hamilton-Crosser model as shown in Equation (3-13) Shin (2011). Table (3-10) illustrates the calculated values of k for solid phase of different types of samples (salt/nanosalts).

$$k_{nanosalt} = k_{salt}\left[\frac{k_{NP}+(n-1)k_{salt}-(n-1)\emptyset_{NP}\,(k_{salt}-k_{NP})}{k_{NP}+(n-1)k_{salt}+\emptyset_{NP}\,(k_{salt}-k_{NP})}\right]$$ **Equation 3-13**

where $k_{nanosalt}$, k_{salt}, k_{NP} are thermal conductivity of nanosalt, salt and nanoparticles (W/m^2. K), respectively. The shape factor of nanoparticle is represented by n and it assumed equal to 3 for spherical nanoparticles while the concentration of nanoparticles represented by $\emptyset_{NP}$.

Table 3-10 theoretical calculations of thermal conductivity for different types and concentrations of nanosalt

T, ^{0}C	Molten salt+ 0.5 wt.% Fe_2O_3	Molten salt+ 1 wt.% Fe_2O_3	Molten salt+ 1.5 wt.% Fe_2O_3	Molten salt+ 0.5 wt.% CuO	Molten salt+ 1 wt.% CuO	Molten salt+ 1.5 wt.% CuO
25	0.8	0.81	0.821	0.802	0.814	0.826
100	0.696	0.705	0.714	0.697	0.708	0.718
200	0.364	0.369	0.374	0.364	0.37	0.375

According to this model, the calculated values of k do not match the experimental data of k, as shown in Figure (3-27).

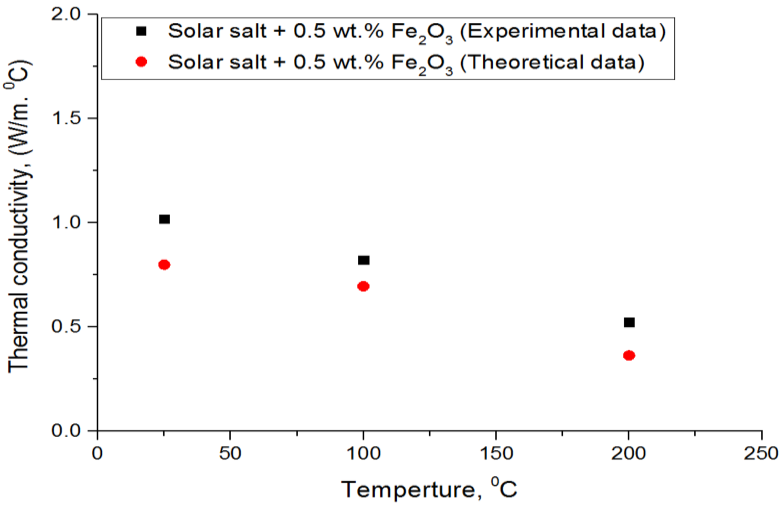

Figure 3-27 thermal conductivity vs temperature for 0.5 wt. % Fe_2O_3-nanosalt both experimental and calculated values.

The differences between them could be due to some assumptions considered during the calculation by the Hamilton-Crosser model. One of these assumptions is that the same size of nanoparticles is homogeneously dispersed in all of the nanosalt samples which is not the case in the experiment. In the experiment, it is very difficult to achieve the same size of nanoparticles because of the sedimentations and agglomerations of these nanoparticles in the nanosalt sample. The issue of sedimentations and agglomerations is due to the effect of different forces such as gravity or Van der Waals. Therefore, a careful consideration for all these parameters needs to be taken into account in order to achieve better theoretical predictions for thermal conductivity values for nanosalt.

Furthermore, any increase in cp and k would improve the heat transfer of nanosalt materials. For instance, natural convection affects the phase change, therefore any increase in both of cp or k would lead to an increase in the heat transfer rate according to Equation (3-14).

$$\mathrm{Ra} = \frac{\mathrm{g}\,\rho^2\,\alpha_T\,\Delta\mathrm{T}\,\mathrm{L_c}}{\mu} * \mathrm{cp} * \mathrm{k}$$ **Equation 3-14**

$$\mathrm{Nu} = \mathrm{C}\,\mathrm{Ra}^n$$ **Equation 3-15**

Where Ra is Rayleigh number, g is gravity (m/sec^2), ρ is a density of the material (kg/m^3), $\boldsymbol{\alpha_T}$ represents thermal expansion coefficient (K^{-1}), L_c is the characteristic length (m), μ is the dynamic viscosity (mPa. s). From Equation (3-15), Nusselt number (Nu) is related to Rayleigh number (Ra) with some correlations constants, e.g. C and n are constant depending on the case. In addition, any increase in Nu will cause an increment in the heat transfer coefficient according to (h=Nu*k/Lc) where h is heat transfer coefficient, L_c is the characteristic length and k is thermal conductivity. Therefore, any increase in Nu will give a higher heat transfer.

3.4.5 Economical study

The cost of copper sulphate ($CuSO_4{\cdot}5H_2O$) is £41 for each 500 g (purchased from Sigma Aldrich company). Through our calculations, we estimate that from 100% of $CuSO_4{\cdot}5H_2O$ only 30% will be the CuO nanoparticles. That would mean £6.83 is the price for 25 g CuO nanoparticles prepared by the 1-step method. On the other hand, the cost of CuO nanoparticles (purchased from Sigma Aldrich Company) is £60.5 for only 25 g. There is a big difference in the cost between the two products around (£53.67). Furthermore, there is a lot of costs that can be avoided in case of nanosalt applications especially for the large scale where it is not practical to purchase a large number of nanoparticles at a high price.

3.4.6 Validation of the measured properties

The measured thermophysical properties in this work are compared with the literature data to check the accuracy of the measured data.

Both cp and latent heat of nitrate salt sample have been compared with other experiments literature data. The average value of cp of the KNO_3 salt in Chieruzzi et al. (2015c) was reported to be (1.118 J/g. ^{0}C) and in the current work is (1.19 J/g. ^{0}C) in the liquid phase. The average value of cp of the binary solar salt ($NaNO_3$: KNO_3 with 60:40 molar ratio) for the liquid phase equals to 1.315 J/g. ^{0}C in the range 250 ^{0}C - 495 ^{0}C (Jung and Banerjee, 2011) and cp has a value equals to 1.38 J/g. ^{0}C in the range 250 ^{0}C - 450 ^{0}C by the work of (Xie et al., 2016). In the current work, cp of the binary solar salt for the liquid phase equals to (1.37 J/ g. ^{0}C) in the range 250 ^{0}C -450 ^{0}C.

On the latent heat data side, KNO_3 salt has 91.61 J/g and T_{onset} is 335.7 ^{0}C according to Chieruzzi et al. (2015c). Similarly, the current study KNO_3 salt has a value equal to 93.89 J/g with T_{onset} equal to 332.47 ^{0}C. Additionally, the latent heat of binary solar salt is equal to 107.03 J/g with T_{onset} equal to 219.11 ^{0}C similar to 110.01 J/g and T_{onset} is 219.88 ^{0}C measured by (Chieruzzi et al., 2013a). The standard error of the DSC device used for these experiments is less than 2.29% and each sample was tested for three times and they showed repeatable and coincidental results. Tables (3-11 and 3-12) show the error from the DSC device for each sample measured. The errors were calculated using MS Excel.

Table 3-11 Shows error from DSC device for the cp measurements of solar salt and nano-solar salt

	Solar salt	+ Fe_2O_3			+ CuO			+ TiO_2		
		0.5 wt.%	1 wt.%	1.5 wt.%	0.5 wt.%	1 wt.%	1.5 wt.%	0.5 wt.%	1 wt.%	1.5 wt.%
Solid phase	0.015	0.02	0.023	0.023	0.023	0.023	0.022	0.017	0.017	0.021
Liquid phase	0.011	0.009	0.006	0.009	0.008	0.012	0.012	0.002	0.005	0.018

Table 3-12 Shows the error from DSC device for the cp measurements of KNO_3 and nano-KNO_3 salt

	KNO_3 salt	+ Fe_2O_3		+ CuO		+ TiO_2	
	-	0.5 wt.%	1 wt.%	0.5 wt.%	1 wt.%	0.5 wt.%	1 wt.%
Solid phase	0.0007	0.0029	0.0062	0.0049	0.006	0.0061	0.0059
Liquid phase	0.0056	0.0073	0.0092	0.0046	0.0094	0.0057	0.007

Overall, there is a small difference between the measured data and the data in the literature. This discrepancy between the data is more related to the precision of the device used and the thermal cycle of the test along with the samples used (each salt purchased from different sources in literature papers and the current work) and the types of the crucible used in DSC device may cause these small differences. Moreover, the k of binary nitrate salt has been reported by (Serrano-López et al., 2013). At a range of temperature 250 ^{0}C- 400 ^{0}C, the difference between current experiment values and the literature seems to be acceptable in term of different methods used to perform the measurements as shown in Figure (3-28).

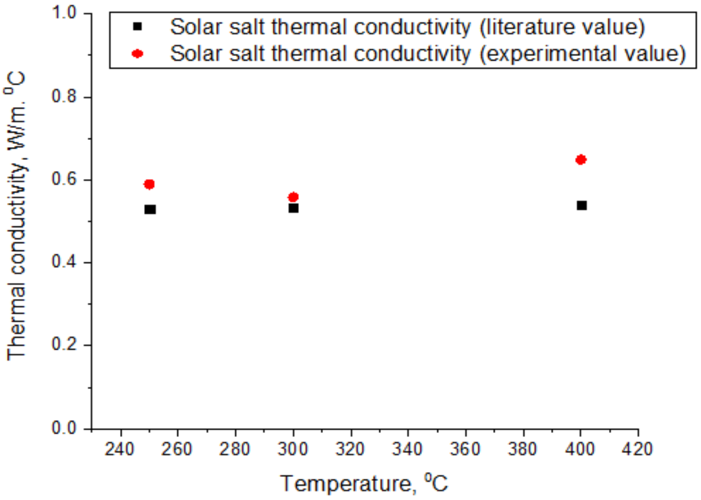

Figure 3-28 thermal conductivity of current experiment and in the literature (Serrano-López et al., 2013).

According to Serrano-López et al. (2013), none of the cited literature has employed laser flash analysis as a measurement device for thermal conductivity of molten salts. The methods used for the measurements are transient hot wire, coaxial cylinder, etc. In our experiment, laser flash analysis has been used to measure the thermal diffusivity of the samples. Also, with the input of known values of density (based on the literature) and cp (based on our experiments), the thermal conductivity has been calculated, which approximately matches the reported values. Table (3-13) shows the error of thermal diffusivity measurements from the LFA device for each sample measured. Furthermore, Table (3-14) shows the error of the calculated thermal conductivity for each sample. The errors were calculated using MS Excel.

Table 3-13 Shows the error from LFA device for the diffusivity measurements of solar salt and nanosalts samples.

Solar salt	+0.5 wt.% Fe_2O_3	+1 wt.% Fe_2O_3	+1.5 wt.% Fe_2O_3	+0.5 wt.% CuO	+1 wt.% CuO	+1.5 wt.% CuO
0.0223	0.0266	0.0181	0.0206	0.0217	0.0128	0.0145

Table 3-14 Shows the error for the calculated thermal conductivity of solar salt and nanosalts samples.

Solar salt	+0.5 wt.% Fe_2O_3	+1 wt.% Fe_2O_3	+1.5 wt.% Fe_2O_3	+0.5 wt.% CuO	+1 wt.% CuO	+1.5 wt.% CuO
0.0485	0.0486	0.0453	0.0423	0.0496	0.0266	0.0429

3.5 Conclusion

The cp, $T_{melting}$, latent heat and thermal conductivity of nitrate salt were studied using differential scanning calorimetry and laser flash analysis, respectively. Different concentrations of nanoparticles (0.5 wt. %, 1 wt. % and 1.5 wt. %) were dispersed in single salt (KNO_3) and binary salt ($NaNO_3$: KNO_3 with 60:40 molar ratio) to achieve good properties. These nanosalts were prepared by the conventional 2-step method. Using Fe_2O_3 nanoparticles, we obtained a higher improvement of cp up to 11% and thermal conductivity by up to 60%. In particular, the latent heat was increased up to 15% with 1 wt. % CuO-binary salt. The storage energy was improved up to 6% with Fe_2O_3 nanoparticles in comparison to solar salt only, which mean an increase in the efficiency of the TES system. Moreover, an increase in the sensible energy of nano-KNO_3 by 7.88% was observed.

In addition, different methods to prepare nanosalt were studied. The first method was the conventional 2-step method using water dispersion with purchased nanoparticles. The second method was the 1- step method which directly prepared CuO nanoparticles inside the molten salt. Different factors for the proportions such as time and temperature were studied in the 1- step method to study the effect of them on the prepared nanoparticles and then on the thermophysical properties of the nanosalt samples. The comparison between these two methods was studied and illustrated the energy storage properties in term of sensible heat (cp), latent heat and the melting temperature. The 1-step method showed a higher increment in case of sensible heat and latent heat than the 2-step method, especially with the preparation of CuO-nanosalt at 450 ^{0}C for 1 hour. It is concluded that each method of preparation results with nanosalt samples behaving differently in term of sensible heat, latent heat or melting temperature. Furthermore, in most cases, nanoparticles show a good effect on the nanosalt samples and this will lead to improvements in the energy storage medium. As a result, an improvement in the thermal solar power plant is expected.

In summary, the use of nanosalt to store thermal energy in term of charging/discharging processes will be very helpful, due to their positive effects on both thermal conductivity and heat capacity.

Chapter 4 Heat transfer study

4.1 Introduction

This chapter aims to explain the design of the experimental rig setup up to 3 kg. The full details of the design, the devices, the materials used in the tests, the difficulties faced in this project, and the results and discussions of the experiments are explained in this chapter. The main aim of this experimental setup is to study the heat transfer of nitrate salt / nanosalt at high temperature up to 350 ^{0}C.

The heat transfer study was conducted in different radial, theta and axial directions. The aim of the experimental rig is to simulate the work of the shell and tube heat exchanger, where the PCM (phase change material; salt or nanosalt) is located in the shell side and the heater element which simulates the work of the HTF (heat transfer fluid) is in the inner pipe. In addition, the descriptions and analysis of the experimental results for PCMs tested in the experimental setup are included in this chapter. The PCMs are nitrate salt (either binary solar salt ($NaNO_3$: KNO_3 with 60:40 molar ratio) or single salt, $NaNO_3$) or nanosalts. At the end of this chapter, a conclusion section is presented to summarize the results.

4.2 Rig design

The experimental rig is designed to study the heat transfer of PCM (nitrate salts or nanosalts) up to 350 ^{0}C. The scale of the rig is up to 3 kg. The rig is basically a concentric double pipe configuration made from stainless steel. The dimensions of the rig are 25 mm diameter for the inner pipe with a 1.5 mm thickness and 101.4 mm diameter for the outer pipe with 2 mm thickness. The length of both pipes is z= 300 mm. Moreover, similar dimensions to our rig are studied for the case of PCM material (Sarı, 2003). Additionally, Muhammad et al. (2015a) designed a shell and tube cylinder with aspect ratio 153 (aspect ratio is defined as the height divided by the radius of inner pipe z/ri), using sodium nitrate ($NaNO_3$) as a PCM. According to Muhammad et al. (2015a), a large aspect ratio

(>20) is used for solar plant applications. Therefore, the aspect ratio in our experimental setup is equal to 27.273, as shown in Figure (4-1).

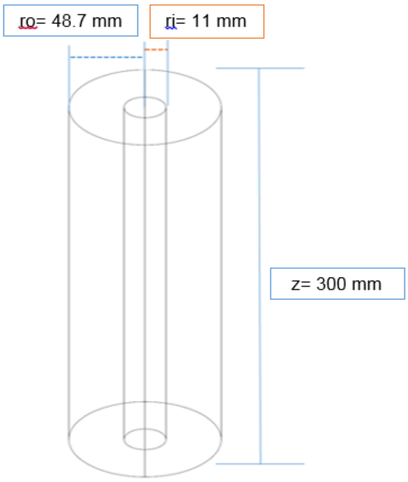

Figure 4-1 Schematic for the annular cylinder of the rig cylinders, the rig was vertically oriented at z-direction (z is height in z-direction).

The rig (concentric double pipe configuration) is positioned vertically during the experimental tests. The heating element (cartridge heater) is located at the centre of the annular cylinder, and PCM (nitrate salts or nanosalts) fills the gap between the two pipes. In order to study the heat transfer of PCM and nano-PCM, this rig is designed for the purpose of studying high levels of temperature up to 350 ^{0}C. The PCM materials are single nitrate salt, binary nitrate salt, nano-single nitrate salt or nano-binary nitrate salt. Therefore, these experiments were conducted under the same experimental setup to show and estimate the differences in the heat transfer between salt and nanosalts in term of charging time, cooling time and power consumption.

4.3 Rig components

The main rig components are shown briefly below.

4.3.1 Cylinders

There are two cylindrical pipes made from stainless steel with dimensions mentioned in section (4.2). The rig cylinders are shown in Figure (4-2).

Figure 4-2 Shows the experimental cylinder of the rig cylinders.

4.3.2 Cartridge heater

The maximum power of the heater is 2400 Watt at 230 volts equipped with a type K thermocouple with a lead made from ceramic and suitable for a temperature up to 600 ^{0}C. The cartridge heater is the part that supplies the thermal power in the experimental rig. Moreover, our experiments were divided into two main parts with a cartridge heater of constant average wall temperature or cartridge heater with constant heat flux.

In the first part condition, the cartridge heater is subjected to an average constant temperature. This means that the temperature distribution along the heating element was controlled to give average temperatures of 350 ^{0}C, 300 ^{0}C and 270 ^{0}C for the different materials being tested. The maximum power used in this condition is 30% of the maximum heater power which is 720 Watts. However, the values of this power were changeable (< 720 Watts) to maintain the constant average wall temperature of the heater.

The second condition studied is constant heat flux along the heater element, where the constant power is supplied to the heating element through a Variac device. The optimum power is 380 Watts. Figure (4-3) shows the heater element.

Figure 4-3 Shows the heater element.

4.3.3 Variac

This device is used to control the power supplied to the cartridge heater through the control box. Figure (4-4) shows the Variac.

Figure 4-4 Shows the Variac.

4.3.4 Control box

The control box is used to connect the experimental rig with a PC computer through LabVIEW code using a national instrument device (NI). There are a few input connections in the control box such as the input from the heater, the Variac and the LabVIEW software through NI instrument cable. Figure (4-5) shows the control box.

Figure 4-5 shows the control box and the National Instrument device (NI) connected to the LabVIEW software.

4.3.5 National Instrument device

This is (NI 9213, C Series Temperature Input Module, National Instruments UK & Ireland, Berkshire, UK) the device that is used to connect all the thermocouples located in the material side inside the cylinders to the PC through LabVIEW software code. Figure (4-5) shows the National Instrument device.

4.3.6 LabVIEW software

The purpose of this software code is to collect the data of our experiments. The measurements from the thermocouples are recorded and saved in the computer. Furthermore, multiple inputs can be entered at the same time before starting the experiments, such as the maximum temperature of the heater, maximum safety temperature, and the power value.

4.3.7 Thermocouples

Thermocouples (type K with a 3 mm diameter, TC direct company, London, UK), as shown in Figure (4-6), are inserted at different locations inside the PCM to measure the temperatures in radial, theta, and axial locations. We studied the heat transfer in four different radial directions, from the nearest to the farthest location to the heating element. The thermocouples labelled with (TD1*, TD2*, TD3* and TD4*) at the axial location, z1 = 150 mm, also three thermocouples of (T2*, T3* and T4*) at the axial location, z2 = 200 mm, as shown in Figures (4-7 and 4-8). Furthermore, at the deepest point and far from the heat source there is a thermocouple that measures the lowest temperature, T5*. In addition, we located four thermocouples at z2 (T3*, T3'*, T3''* and T3'''*) in different theta directions (0^0, 90^0, 180^0, and 270^0) to measure the homogeneity distributions of heat transfer of the PCM during the experimental tests. The temperature measurements were recorded and saved in the computer via the LabVIEW code. The uncertainty of these thermocouples are checked and it was ±0.1 ^{0}C. Moreover, temperature loses from the top and bottom flanges are measured through two additional thermocouples connected with two thermometers, as shown in Figure (4-9). Furthermore, all thermocouples were fitted in their locations by the compression fitting.

Figure 4-6 The Thermocouple type K.

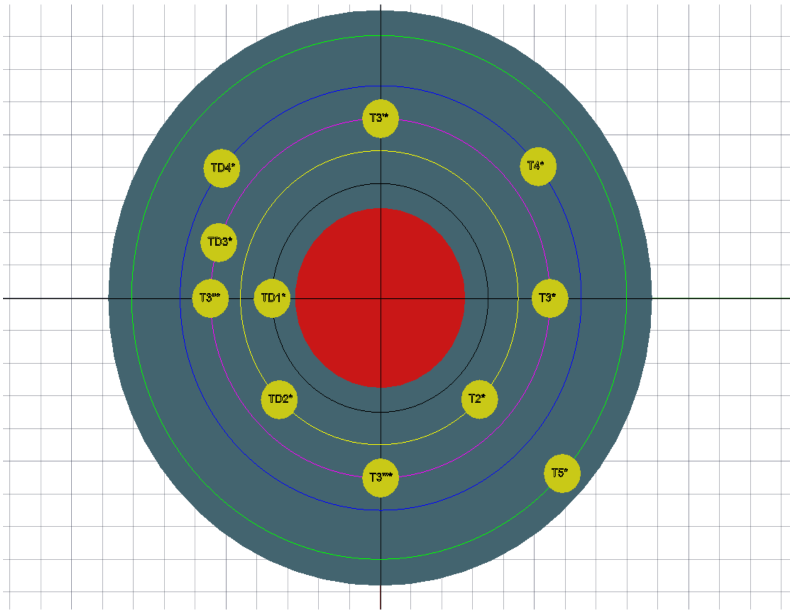

Figure 4-7 Shows a top view of thermocouples locations.

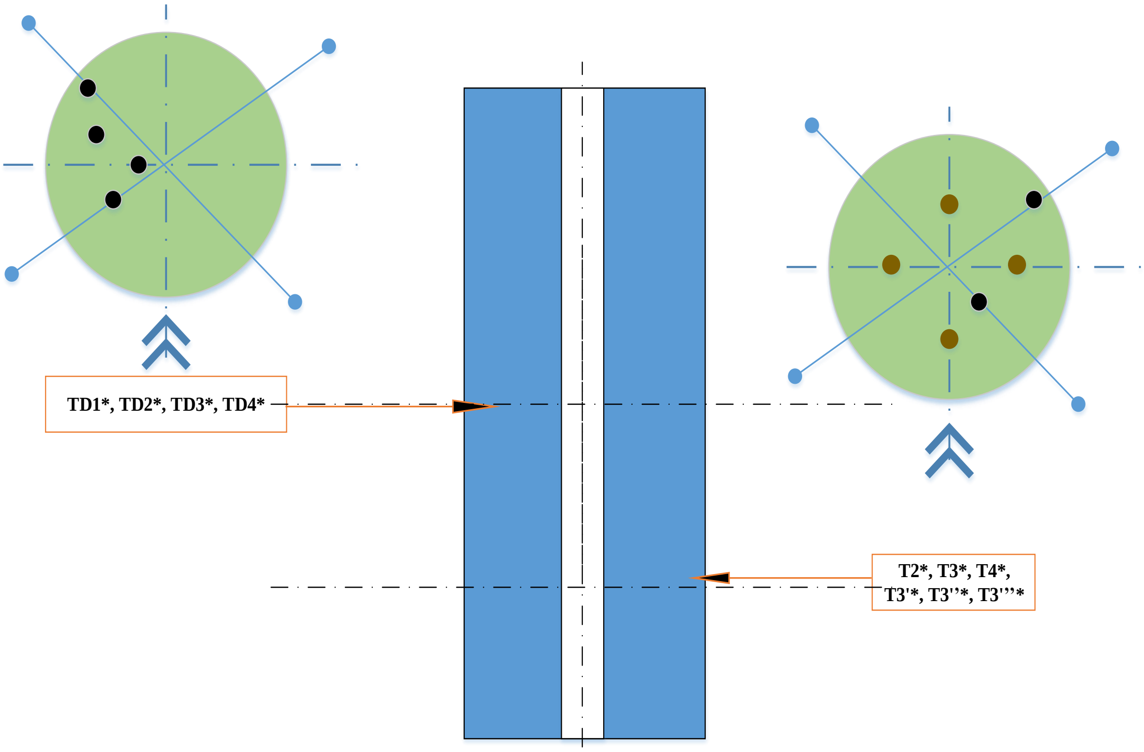

Figure 4-8 Thermocouples locations in radial, theta, and axial directions. TD1, TD2*, TD3* TD4* located at z1 (150 mm), T2*, T3*, T4*, T4’, T4’’, T4’’’ located at z2 (200 mm) and T5* at the bottom of the rig.

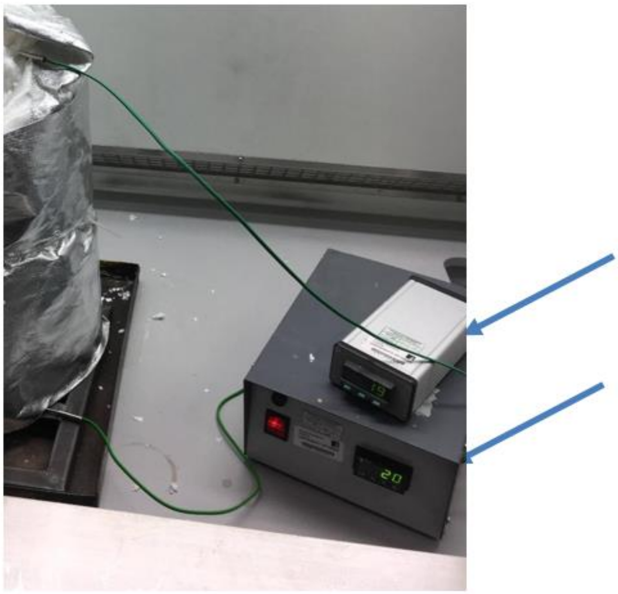

Figure 4-9 shows the thermometers.

4.3.8 Power measurement device

We measured the power consumed by the heating element using a KWh meter in each experiment to compare the power consumption among the different experiments. Figure (4-10) shows the KWh meter. The current range is 0.005–13 A (±0.02) and the power range 0.1 to 3120 Watt (±0.02).

Figure 4-10 The KWh measurement device.

4.3.9 Pressure relief valve

For safety considerations, we added a safety pressure relief valve to ensure there would be no excessive pressure built up inside the rig. Figure (4-11) shows the pressure relief valve.

Figure 4-11 The pressure relief valve.

4.3.10 Clamp meter

This device is used to measure the voltage and the current supplied to the heater. Figure (4-12) shows the Clamp meter. The accuracy for voltage measurements was ±0.01 and ±0.02 for the current measurements.

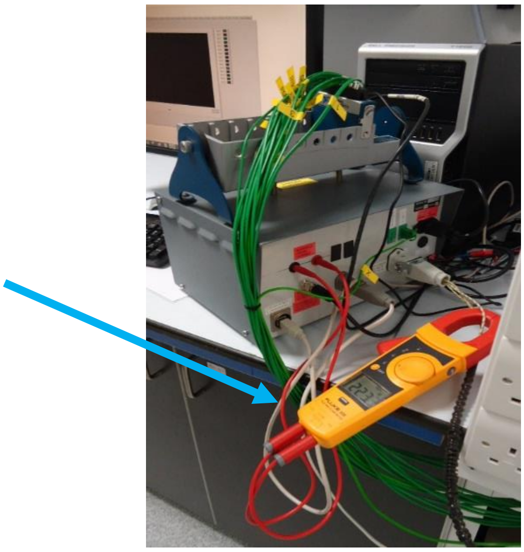

Figure 4-12 The Clamp meter.

4.3.11 Aluminium fibre thermal insulation

The experimental rig is well isolated by aluminium fibre thermal insulation by 10 cm thickness. It is used for a maximum temperature up to 1600 ^{0}C. Figure (4-13) shows the Aluminium fibre thermal insulation.

Figure 4-13 The Aluminium fibre thermal insulation.

4.3.12 Casket material

This is used to ensure there will be no leakage between the two flanges of the cylindrical pipes. It is shown in Figure (4-14).

Figure 4-14 The Casket material.

4.3.13 Scale weight measurement

This is used to measure the amount of the salt or nanosalt. It measures up to 2100 g with the uncertainty of 0.1 g, as shown in Figure (4-15).

Figure 4-15 shows the scale weight measurement.

4.4 Difficulties

Some difficulties were faced in this project. The first issue that arose concerned the thermocouples' diameter. Thermocouples with a diameter of 1.5 mm were bending easily and therefore gave incorrect measurements for the temperatures, as shown in Figure (4.16). We changed the diameter of the thermocouples to 3 mm and this took consequently a time from ordering until receiving and re-doing the experiments. Another issue that arose concerned the heater element. The cartridge heater broke down and this caused a delay as we needed to order a new one.

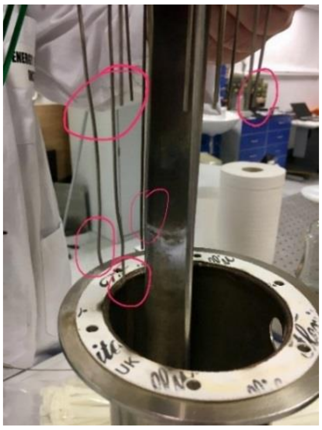

Figure 4-16 Thermocouples with a diameter of 1.5 mm were bending easily.

4.5 Materials

The materials used for our work in this research were nitrate salt and nano-nitrate salt. Sodium nitrate ($NaNO_3$) was purchased from (VWR International, Lutterworth, UK). Potassium nitrate (KNO_3) was purchased from (VWR International, Lutterworth, UK) used in a mixture salt of (60 $NaNO_3$: 40 KNO_3) by molar ratio. The additive materials were iron oxide nanoparticles or copper oxide nanoparticles. Iron oxide nanoparticles (Fe_2O_3) were purchased from US research Nanomaterials, Inc. with an average diameter of 20-40 nm. Copper oxide nanoparticles (CuO) were purchased from Sigma-Aldrich with an average diameter less than 50 nm.

The nitrate salt materials are prepared for the test by uniformly mixing the correct ratio in case of binary salt 60 $NaNO_3$:40 KNO_3 molar ratio. The salt is heated up to a high temperature until it melts then pulverized for the next experiments, similar to the work carried by (Tian et al., 2017).

The nanosalt material was prepared by the use of the mechanical dispersion method similar to (Lasfargues et al., 2015; Tian et al., 2017). In this method, the same procedure was implemented as that used previously to prepare the base material (nitrate salt). The prepared salt is uniformly mixed with the correct mass ratio of nanoparticles. Then the nanosalt samples are poured into the rig followed by a heating up until the material is melted (Tian et al., 2017). After melting, the experimental setup is turned off to leave the sample to cool down. After the material is solidified and all the temperature measurements are reading the room temperature the rig is ready for the experiments.

Weight measurements for the materials were made by using the device mentioned in section (4.3.13). Up to 3 kg weight of nitrate salt, this is in case salt is the PCM. On the other hand, in the case of nanosalt, weight percentages of the nanoparticles were considered. We studied different nanoparticles weight percentages such as 0.1 wt. %, 0.5 wt. % and 1 wt. %.

4.6 Experimental procedure

The procedures for the experiments are as shown in the following steps:

1. Fill the rig with the materials (salt or nanosalts) prepared as in section 4.5.
2. Cover the rig with an aluminium fibre insulation to well insulate the rig.
3. Connect the heater to the controller.
4. Connect the controller to a power source.
5. Switch on the PC computer and turn on the LABVIEW program.
6. In case of constant temperature condition from the LABVIEW program, insert the input of the cartridge heater (the average temperature of the heater and the maximum safety temperature).
7. In case of constant heat flux condition, instead of step 9, control the power amount by Variac.
8. Start recording and saving the data through the LABVIEW program.

Figure (4-17) shows the schematic of the experimental rig and the full experimental rig after setup.

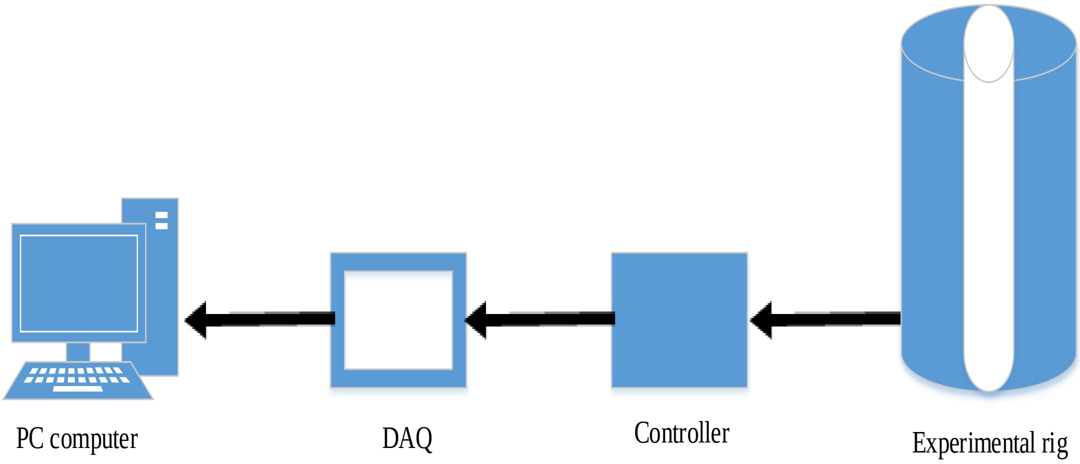

a) The schematic of the experimental rig.

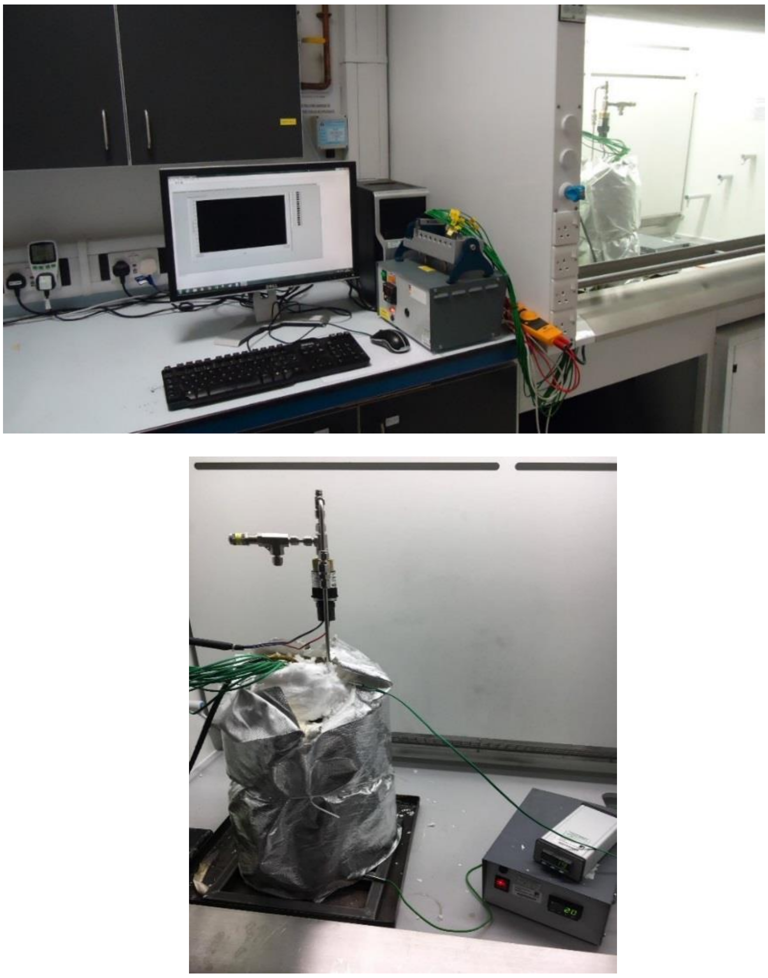

b) The experimental rig after setup.

Figure 4-17 Shows the schematic of the experimental rig and the full experimental rig after setup.

4.7 Experimental validation

In order to validate the experimental data for the pure conduction stage, a numerical study was conducted which compared temperature measurements in the experiment with numerical predictions for the case of a single phase solid without phase change. The good agreement should be expected to occur in the early part of the experiment before the solid PCM starts to melt.

The geometry was built by AutoCAD (version 2018) using the same dimensions as the experimental, and the mesh was by Ansys-Workbench (version 17.0). ANSYS-CFX (version 17.0) was used for the numerical simulation. The physical setup was pure conduction transient heat transfer for the solid phase of salt only. As the solution to this problem is cylindrically symmetric, it was sufficient to perform the simulation over a thin annular wedge, as shown in Figure (4-18 a). The mesh type was hexahedral with a number of elements equal to 1620. The boundary conditions were fixed temperature on the boundary of the inner cylinder, and zero heat flux (adiabatic) on the outer cylinder. All other boundaries were treated as symmetry planes. A time step equal to 1 second was used. As shown in Figure (4-18 b, c, and d), the numerical data is well predicted by the experimental measurements at early times. Small differences occur at larger times, probably due to the onset of the physical effects of melting which are not accounted for in this simulation.

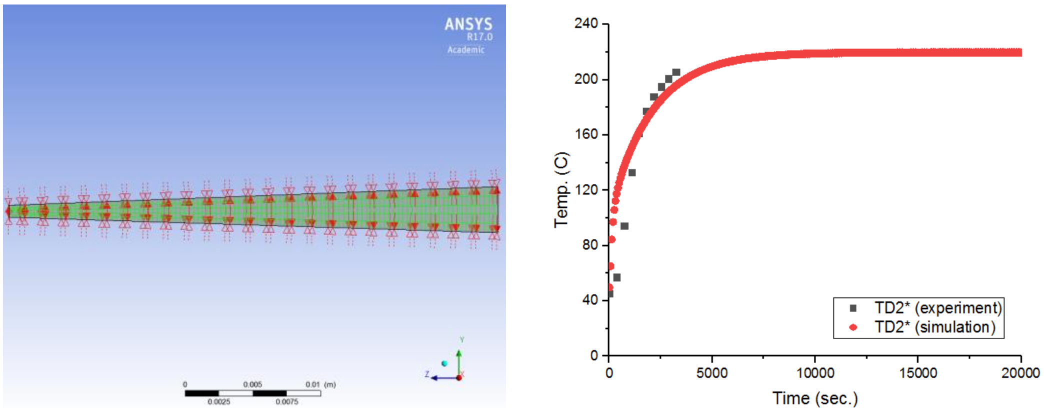

(a) The mesh of the wedge.

(b) Temperature data from the experiment vs data from the CFX, at TD2*

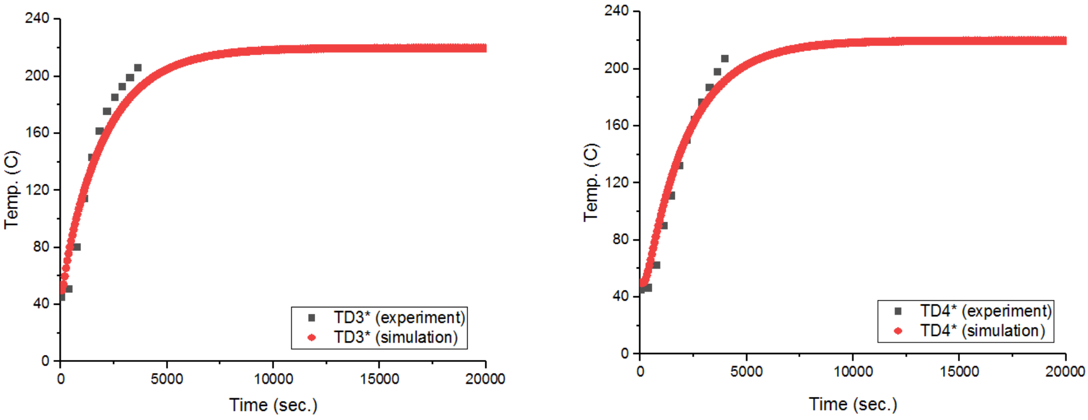

(c) Temperature data from the experiment vs data from the CFX, at TD3*

(d) Temperature data from the experiment vs data from the CFX, at TD4*

Figure 4-18 shows (a) the mesh of the wedge (b, c, and d) the temperature measurement experimentally vs numerical using CFX software at different radial directions.

4.8 Results and discussions

The results obtained from the experimental rig are discussed in detail in this section. The experimental rig is an annular cylinder designed for heat transfer study of phase change material (PCM) up to 350 ^{0}C. The boundary conditions of the annular cylinder were i) inner hot pipe (contains cartridge heater) during the charging or inner cold pipe during the cooling (cartridge heater is off), ii) the PCM, which are salts or nanosalts, filling the annular gap between the pipes, iii) the adiabatic outer wall which is insulated by thick insulation layer.

In addition, there are two different experimental conditions studied which are constant average wall temperature of the cartridge heater or constant heat flux of cartridge heater. Furthermore, the PCM used during the experimental tests can be divided into two different types such as binary nitrate salt ($NaNO_3$: KNO_3 with 60:40 molar ratio) or single nitrate salt ($NaNO_3$). Nanoparticles are added to the base materials to improve the charging and cooling processes. Two different types of nanoparticles materials were studied, namely Fe_2O_3 or CuO. In addition, the weight concentrations of nanoparticles were 0.1 wt. %, 0.5 wt. % and 1 wt. %.

4.8.1 Results and discussions of binary salt vs nano-binary salt

This section discusses the results for the binary nitrate solar salt, which is called a binary solar salt (which can be written as s.s), or nanosalt. Nanosalt is a nano-binary solar salt with a different weight concentration or different types of nanoparticles materials. Transient temperature profiles were presented for different materials showing solid phase, phase change transition and liquid phase. Temperature profiles were measured over different radial locations, axial locations and theta locations. For the presented results below, the boundary condition of the cartridge heater was constant heat flux. In addition, the maximum temperatures studied were 270 ^{0}C and 300 ^{0}C. The binary solar salt started melting around 220 ^{0}C while nanosalts materials started melting at a temperature less than 220 ^{0}C as shown in the temperatures measurements at most measurements.

Figure (4-19) shows the distributions of temperature in the radial locations for a binary solar salt without any additives, at different times during the experiment. The axial location is 150 mm. The temperature measurements are at four radial locations with equal spaces between them. They are located from the nearest to the heater element to the farthest wall (the adiabatic wall).

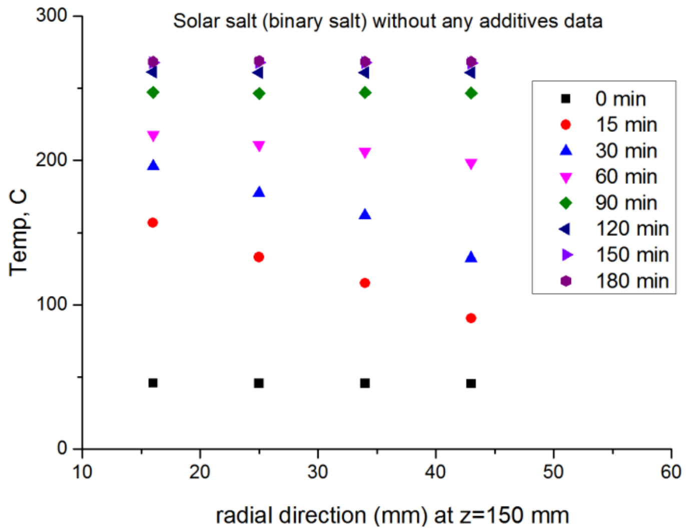

Figure 4-19 shows the temperatures distributions vs radial directions in an axial direction of z=150 mm, for binary solar salt material at a different time during the experiment. The maximum temperature is 270 ^{0}C.

As expected, the temperature is distributed gradually from the hot wall near to the heater wall to the coldest reading in the last thermocouple away from the heating source. For instance, after 15 minutes there is a large increase in temperature measurements at TD1*, TD2*, TD3* and TD4*. This is due to the large difference between the heater temperature and the temperatures of the surrounded PCM. However, the large increments in temperatures at radial directions become less and less when the radial direction is far from the hot medium (e.g. TD4*). This is because of smaller temperature differences between TD3* and TD4*. Additionally, conduction heat transfer is the dominant mode at the early stage of the charging process. Therefore, the small thermal diffusivity of material results in a longer time needed to melt.

Basically, under the heat flux condition in the inner pipe, the temperature of PCM goes up during the solid phase till it reaches the phase change point where nitrate salt starts changing from solid phase to liquid phase over a range of temperatures until it fully melts and becomes pure liquid. The temperatures continue to increase up to the maximum input temperature. Figure (4-20) presents a similar behaviour to Figure (4-19) but in axial location of z2= 200 mm.

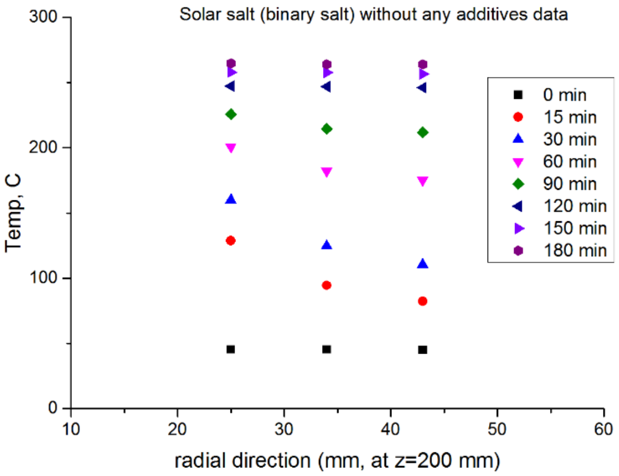

Figure 4-20 shows the temperatures distributions vs radial directions in axial directions of z=200 mm, for binary solar salt material.

Additionally, the radial temperature profile distributions in a cylindrical geometry are shown in Figure (4-21) which is similar to the radial temperature profile distributions of the current results in Figures (4-19 and 4-20) (Faghri, 2010).

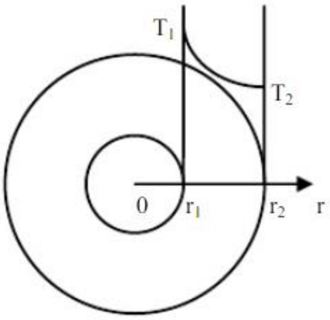

Figure 4-21 temperature distributions vs radial direction in a hollow cylinder (this is in similar to our experimental setup where the heat source in the centre and it show a similar distribution of Temperature vs radial directions) (Faghri, 2010)

It is clear from Figure (4-20) the effect of the axial location, where at 150 minutes temperature measurements in thermocouples at z2 did not reach the maximum input condition (270 ^{0}C) yet. However, in the case of z1=150 mm, temperature measurements reached 270 ^{0}C at 150 minutes. This could be due to the effect of gravity, as the experimental rig is oriented vertically with the axial location of z. Moreover, the effect of gravity can be seen in Figure (4-22) which shows transient temperature measurements at different axial locations (z1 and z2) and same radial location (TD3*/T3*). This demonstrates the effect of natural convection where the melting is from the top downward where the axial location of z1 melted before z2 due to the density differences during the phase change.

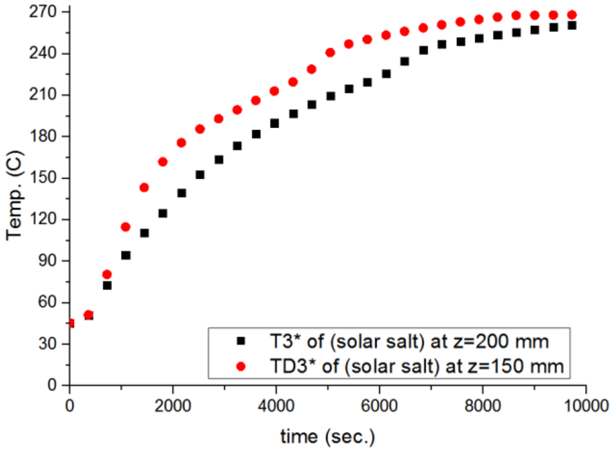

Figure 4-22 shows the temperatures distributions vs time in different longitudinal directions (z=150 mm and z=200 mm) with the same radial direction, for binary solar salt material.

The measurements in the axial locations are affected by the convection effect in addition to the conduction heat transfer from the hot surface side through the material side (the material side is the salt). As soon as salt starts melting, a volume expansion occurs due to the density differences between the solid and liquid phases. The lighter liquid phase will flow up and therefore a moving boundary condition helps to melt the PCM from the top and downward. As a result, temperature indicates a higher value at z1 (150 mm) than z2 (200 mm). Wen and Ding (2006) showed a similar behaviour to our result of the transient temperature distributions in different axial locations, as shown in Figure (4-23a). However, their work concerned a different application for a gas flow through a packed bed. Furthermore, Farid et al. (1989) studied the charging and cooling process of PCM and their result show a similar behaviour to ours as shown in Figure (4-23b). However, the PCM was for a low temperature application.

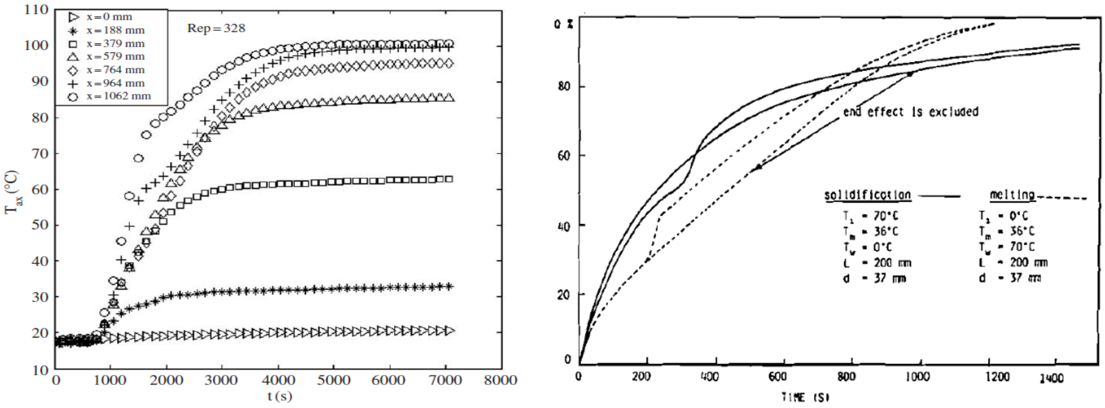

a) Transient temperature distributions in axial directions by (Wen and Ding, 2006)

b) Transient temperature distributions in PCM by (Farid et al., 1989)

Figure 4-23 shows the (a) Transient temperature distributions in axial directions by (Wen and Ding, 2006) and (b) Transient temperature distributions in PCM by (Farid et al., 1989)

Also, we measured the homogeneity of the material by measuring temperatures in four different theta locations (0^0, 90^0, 180^0 and 270^0), which were located in a same axial location of 200 mm and same radial location of 34 mm. Figure (4-24) shows the homogeneity of the solar binary salt material at different times during the experiments. Although there are little differences between these four thermocouples, it can still be assumed to be a homogenous material. The differences could be due to the fact that salt properties are not exactly the same in all the locations where small differences in measurements occur. Furthermore, the impurities percentage of salt might effect on the homogeneity measurements.

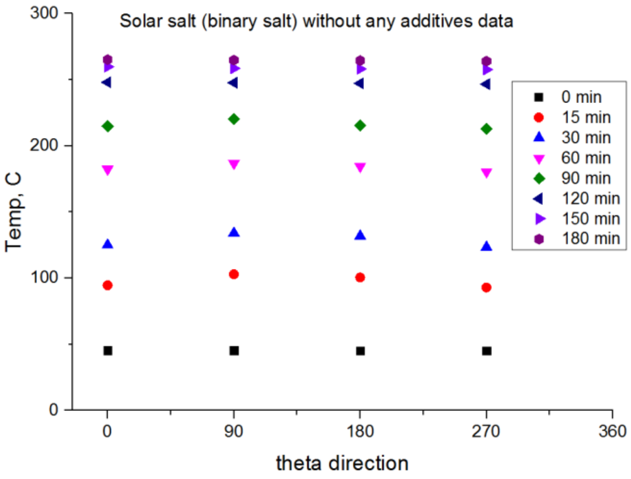

Figure 4-24 shows the temperatures distributions vs theta directions in an axial direction of z=200 mm, for binary solar salt material. The maximum temperature is 270 ^{0}C.

The effect of different types of nanoparticles with a same weight concentration (0.5 wt. %) is studied. Figure (4-25) demonstrates the temperature distributions in different radial locations for different materials (binary solar salt vs. nanosalts). At two times selected through the experiments, Figure (4-25) shows the differences of the temperature distributions in radial locations among three materials (binary solar salt, 0.5 wt. % Fe_2O_3 + solar salt and 0.5 wt. % CuO + solar salt). It indicates 0.5 wt. % Fe_2O_3 + solar salt is the best material while CuO-nanosalt is better in liquid phase than in solid phase in comparison to the binary salt without any additives. In addition, CuO-nanosalt was better in liquid phase than solid phase which could be due to the overall improvements of latent heat then the liquid phase due to clusters of these nanoparticles in the nanosalt as explained earlier in Chapter 3. It can be observed that nanoparticle types play an important role in the heat transfer enhancement of nanosalt material. The conduction heat transfer can be improved by the presence of nanoparticles due to a higher thermal conductivity of nanosalt than salt alone while the improvements in natural convection are decreased with the increase of the viscosity of nanosalts. The concentration of nanoparticles was small (0.5 wt. %), therefore, the effect on natural convection (increasing the viscosity) could be small or negligible.

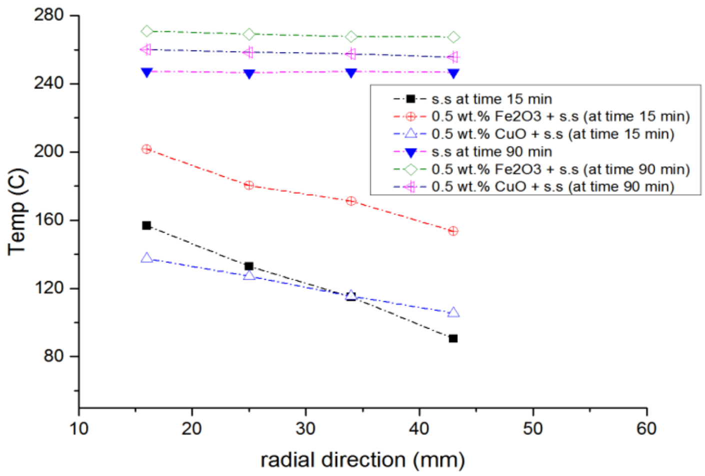

Figure 4-25 shows the temperatures distributions vs radial directions at z=150 mm for binary solar salt material vs. 0.5 wt. % Fe_2O_3 + salt vs. 0.5 wt. % CuO + salt. The maximum temperature is 270 ^{0}C.

The previous results showed that Fe_2O_3-nanosalt is better than CuO-nanosalt in term of improving the charging process of PCM in the storage system. Therefore, the range of concentrations of Fe_2O_3 nanoparticles is enlarged to 0.1 wt. % and 1 wt. %. At two times selected through the experiments, Figure (4-26) shows the results for the binary solar salt in comparison to 0.1 wt.%, 0.5 wt.% and 1 wt.% of Fe_2O_3 + binary solar salt. It indicates 0.5 wt. % of nanosalt is optimal as the temperatures increase faster than the others. Furthermore, 1 wt. % Fe_2O_3 + binary salt in a liquid phase is better than in the solid phase which may be due to vortices forming in the liquid phase due to natural convection. It seems that the decrement in the concentration of the nanoparticles minimizes the improvements in the nanosalt sample, where lower concentrations do not benefit from the surface area of nanoparticles in the nanosalt sample. However, increasing the concentrations could lead to agglomeration effects and sedimentation of the nanoparticles which could negatively affect the results. Additionally, the higher concentration of nanoparticles in the nanosalt sample would increase the viscosity as well as increment the agglomeration and precipitation effect and that would weakening natural convection heat transfer (Fang et al., 2017). Therefore the lower improvements in temperature measurements at higher weight loading of nanoparticles (e.g. 1 wt. %) could be due to the suppression of natural convection. In our results, the weight concentration of 0.5% improves the overall heat transfer by increasing the thermal inertia (thermal conductivity time’s specific heat capacity time’s density) and natural convection are greater than other concentrations.

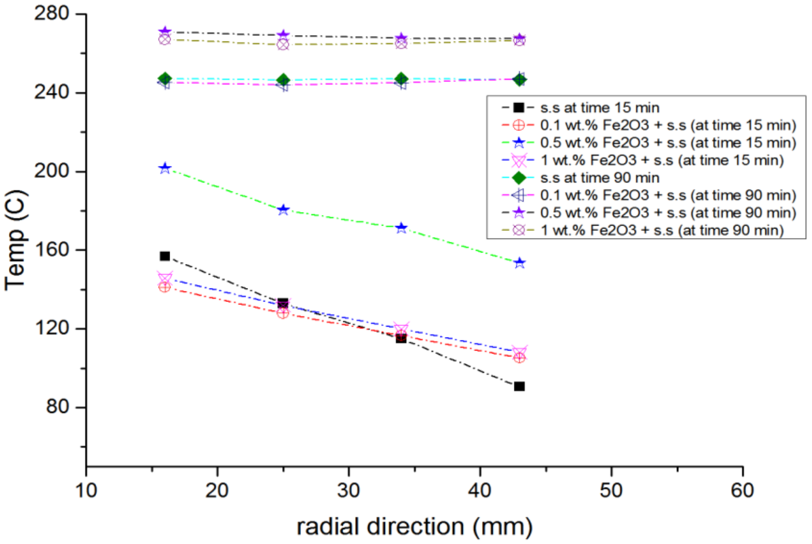

Figure 4-26 shows the temperatures distributions vs radial directions at z=150 mm for binary solar salt material vs. 0.1 wt. %, 0.5 wt. % and 1 wt. % of Fe_2O_3 + salt.

In Figures (4-19, 4-20, 4-25, 4-26), once PCM is melted, the temperature distribution (in the same axial location, z-location) turns into a more uniform distribution. Similar behaviour has been concluded by (Cao et al., 2018) as shown in Figure (4-27). This uniformity of temperature could be due to the decreasing of the temperature differences between the inner hot pipe and the surrounded PCM until reaching the maximum input temperature. Another possible reason might rely on the natural convection role which improves the heat transfer during the liquid phase.

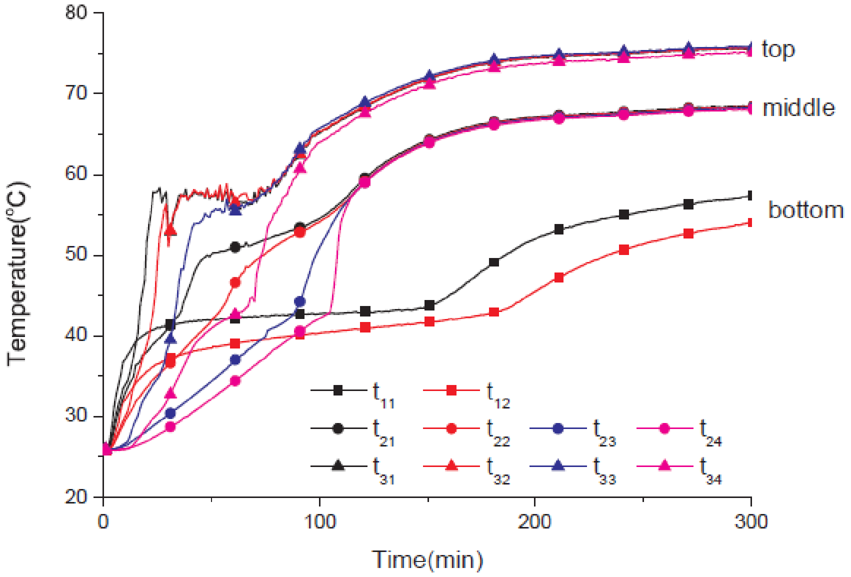

Figure 4-27 shows Variation in the temperature of the measurement points in the same position (Tw=80 °C) (Cao et al., 2018).

The temperature distributions in different axial locations of solar salt (s.s) and nanosalt (0.5 wt. % Fe_2O_3+ s.s) are measured, as shown in Figure (4-28).

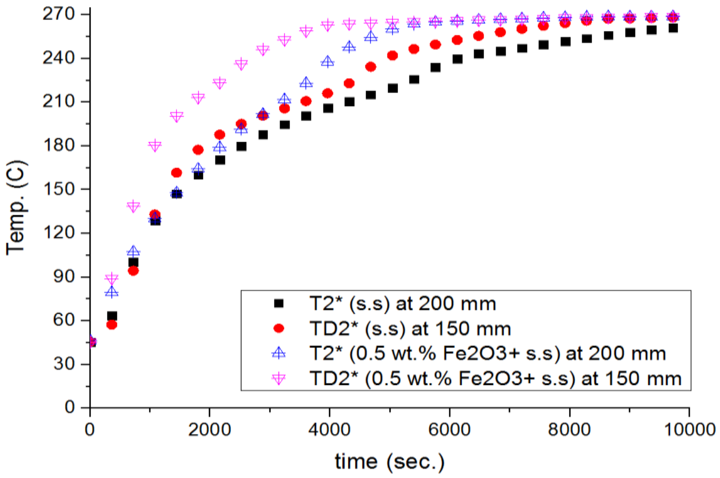

Figure 4-28 shows the temperatures distributions vs time at different z-direction for binary solar salt material and 0.5 wt. % Fe_2O_3 + solar salt.

Temperature increases more rapidly in the axial location of z1 (z1=150 mm) than z2 (z2=200 mm). This is because at the beginning of the test when the PCM is in a solid phase, the heat transferred is from the heater element to solid PCM by conduction, and after that, it starts to heat up due to the interface between the liquid phase layers (in the melted area near to the hot wall) and the surrounded solid phase of PCM. The moving boundary starts to move toward the solid region resulting in an increase in the melting fraction of the PCM. Additionally, circulation is formed due to the natural convection effect, which results in a hot liquid fluid at the top of the rig and the solid phase at the bottom. Therefore the material at z1 has a higher temperature than that at z2. Actually, fast melting of solid PCM leads to form molten layers over the nearest solid salt and due to the density variation (volume expansion) the molten salt is transported upwards, which results in an improvement in the melting fraction (Farid et al., 1989). This is faster in the case of nanosalt rather than salt alone without any additives because nanoparticles are a more conductive material that improves salt conductivity.

We did all the experimental tests under two different conditions. The first condition is a constant heat flux through the heater where all the results are shown and discussed above. The second condition is constant average wall temperature of the heater. In Figure (4-29), there are no big differences between these two conditions. The small differences between the two conditions are due to the fact that in case of constant average wall temperature of the heater, the initial power from the heater was 720 W and the power of the heater is changeable to maintain the constant average wall temperature condition. However, in the case of constant heat flux condition the power supplied was constant value with 380 W. Therefore, it can be observed that the constant temperature condition was faster than constant heat flux especially at the beginning. This is due to the higher power used. However, after the value of power became similar, there were no significant differences between the two conditions. Due to the similarity of the results with similar behaviours concluded from the constant average wall temperature condition and the constant heat flux condition, the results presented in this chapter are at constant heat flux condition to avoid repetition of the data.

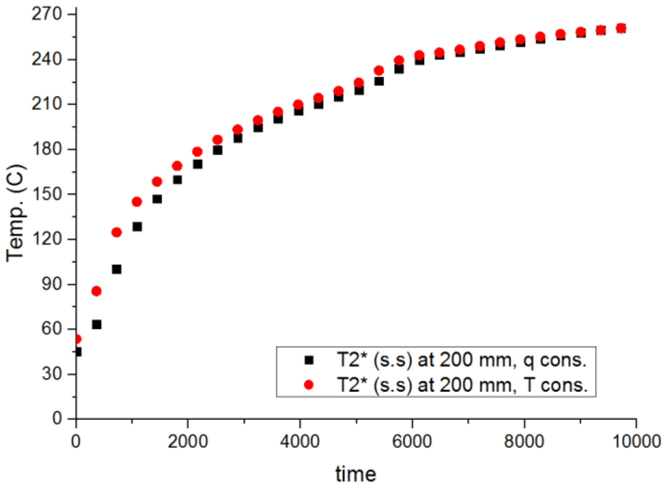

Figure 4-29 shows the temperatures distributions vs time at different power input condition for binary solar salt material and 0.5 wt. % Fe_2O_3 + salt.

Furthermore, for the case of constant heat flux, the optimum value of power (380 W) has been chosen over different tested power. Any increment in the power causes a fluctuation over the temperature readings. Furthermore, decreasing the power value would result in an increase in the experiment performance.

In addition, the cooling processes of different PCMs are studied. Figure (4-30) shows cooling behaviour at the same radial and axial locations for the nanosalt (0.5 wt. % Fe_2O_3 + s.s) and binary solar salt (s.s). It indicates that nanosalt cooled faster than binary solar salt. Therefore, for the application of solar energy storage, nanosalt would be a powerful PCM especially in case of transferring the heat from its side to the cold heat transfer fluid (HTF) side. As a result, efficient heating of the HTF leads to an improvement in the solar thermal power plant over the night or when no solar source is available. Conduction is the dominant heat transfer mode during the cooling process. The PCM starts to cool down due to the temperature differences between the liquid PCM and the inner cold pipe. The cooling process depends on the thermal conductivity of the PCM therefore, nanosalt discharged faster because they have higher thermal conductivity values than salt alone, as shown in Figure (4-30).

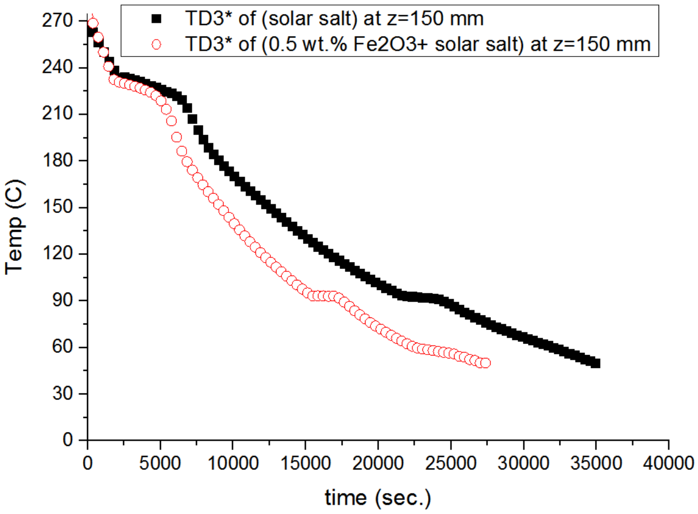

Figure 4-30 shows the cooling process of different materials (binary solar salt material vs 0.5 wt. % Fe_2O_3 + salt) at different z-direction.

Figure (4-31) shows the full process from the start of the experiments until the end of the cooling. The temperature is time dependent in the charging process, followed by a steady state, then a transient cooling until it reaches 50 ^{0}C. It shows that nanosalt (0.5 wt. % Fe_2O_3 + binary solar salt) is charging faster and discharging the energy faster than the case of solar salt without any additives. In the case of 0.5 wt. % Fe_2O_3 + binary solar salt, the charging process improves by 21.21 % and the cooling process by 23 %. Additionally, charging time was shorter in other cases of nanosalt by 6.06%, 5.724%, 1.515% for (0.5 wt. % CuO + binary solar salt, 1 wt. % Fe_2O_3 + binary solar salt, and 0.1 wt. % Fe_2O_3 + binary solar salt), respectively. On the other hand, cooling time was faster for all other types of nanoparticles where 0.5 wt.% CuO + binary solar salt was faster by 15.79%. Moreover, cooling time reduced by 7.37% and 1.0526% for (1 wt. % Fe_2O_3 + binary solar salt and 0.1 wt. % Fe_2O_3 + binary solar salt), respectively.

Nanosalts are superior to binary solar salts because they have better thermophysical properties such as specific heat capacity, thermal conductivity and latent heat. Another reason is the higher surface area of these nanoparticles which helps to transfer heat in nanosalt sample better than salt without any additives where the heat could be diffusive over a wider range than salt alone.

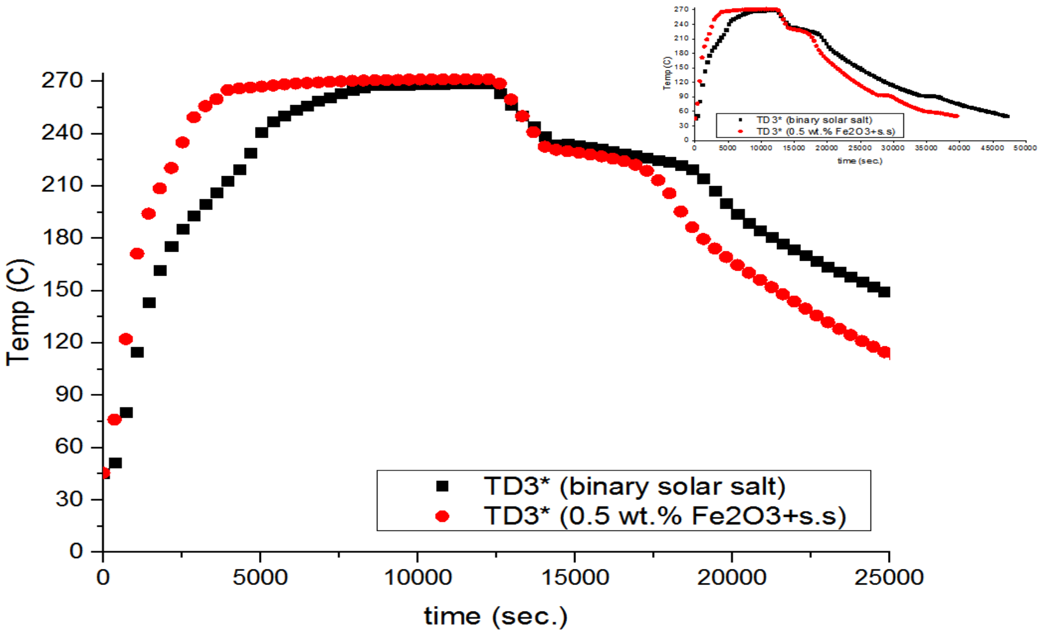

Figure 4-31 shows the full charging and cooling process of different materials (binary solar salt material vs 0.5 wt. % Fe_2O_3 + salt).

Energy storage can be calculated from Equation (4-1)

$$\mathrm{q_{storage}} = \mathrm{q_{\,sensible}} + \mathrm{q_{\,latent}}$$ **Equation 4-1**

The sensible energy storage is calculated as shown in Equations (4-2, 4-3, and 4-4)

$$\mathrm{q_{\,sensible}} = \mathrm{q_{\,sensible\ in\ solid\ phase}} + \mathrm{q_{\,sensible\ in\ liquid\ phase}}$$ **Equation 4-2**

$$\mathrm{q_{\,sensible\ in\ solid\ phase}} = \left(\int_{\mathrm{T_{ambient}}}^{\mathrm{T_{melt}}} \mathrm{cp} * \mathrm{dT}\right)_{\mathrm{solid\ phase}}$$ **Equation 4-3**

$$\mathrm{q_{\,sensible\ in\ liquid\ phase}} = \left(\int_{\mathrm{T_{liquid}}}^{\mathrm{T_{max.}}} \mathrm{cp} * \mathrm{dT}\right)_{\mathrm{liquid\ phase}}$$ **Equation 4-4**

It is assumed that:

$$q_{sensible\ in\ solid\ phase\ of\ salt} = q_{sensible\ in\ solid\ phase\ of\ nanosalt}$$ **Equation 4-5**

$$q_{\text{sensible in liquid phase of salt}} = q_{\text{sensible in liquid phase of nanosalt}}$$ **Equation 4-6**

where $q_{sensible}$ represents the heat (J/g. ^{0}C). Therefore, from Equations (4-3, 4-4, 4-5, and 4-6) nanosalt gives the same value of sensible energy of the salt but in shorter or longer time depending on the types or the concentrations of the nanoparticles materials. For instance, the same sensible energy could be delivered by 0.5 wt.% Fe_2O_3 + salt faster than binary salt and 0.5 wt.% CuO + salt, as shown in Figure (4-32).

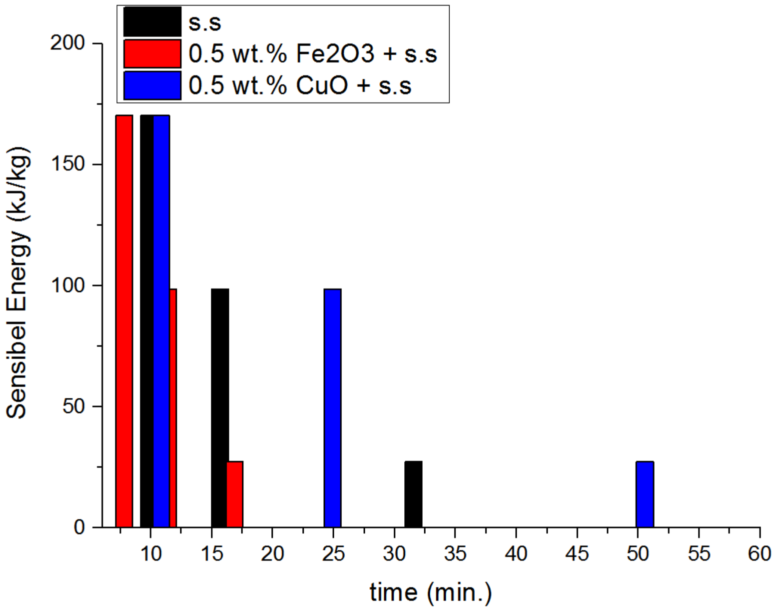

Figure 4-32 shows the sensible energy storage vs time for different materials (solar salt vs. 0.5 wt. % Fe_2O_3-nanosalt vs 0.5 wt. % CuO-nanosalt) for the solid phase. It indicates that the same value of energy can be stored but in shorter time within 0.5 wt. % Fe_2O_3-nanosalt in comparison to other types of materials.

On the other hand, sensible energy in a liquid phase shows that 0.5 wt.% Fe_2O_3 + salt and 0.5 wt.% CuO+ salt gives same energy but in a shorter time than solar salt alone, as shown in Figure (4-33). Although 0.5 wt. % CuO + salt shows an improvement, 0.5 wt. % Fe_2O_3+ salt still the best type in storing energy within a shorter time. This demonstrates the effect of nanoparticles types on the improvement of nanosalt sample in term of sensible energy storage. Additionally, the size of Fe_2O_3 was less than CuO type which could be one of the reasons behind this improvement of 0.5 wt. % Fe_2O_3+ salt.

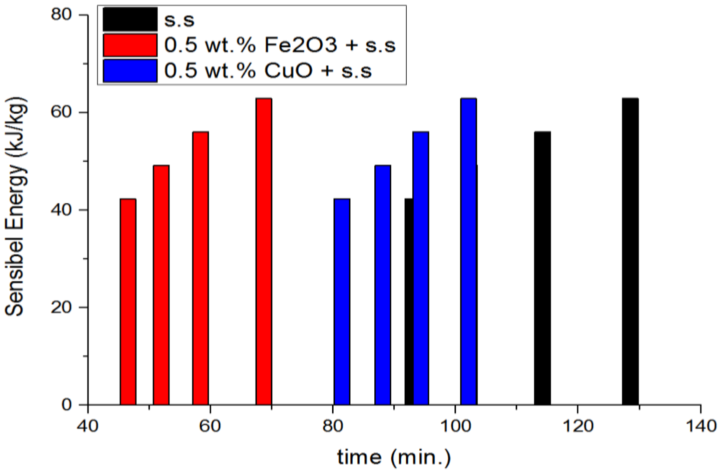

Figure 4-33 shows the sensible energy storage vs time for different materials (solar salt vs. 0.5 wt. % Fe_2O_3-nanosalt vs 0.5 wt. % CuO-nanosalt) for the liquid phase. It indicates that the same value of energy can be stored but in shorter time within 0.5 wt. % Fe_2O_3-nanosalt in comparison to other types of materials.

We studied the effect of increasing the input temperature (270 ^{0}C or 300 ^{0}C) on the material behaviour. The results in Figures (4-19 to 4-33) were at maximum input temperature condition of 270 ^{0}C.

The effect of increasing the maximum input temperature to 300 ^{0}C on the materials (salts or nanosalts) in the rig has been conducted. This maximum input temperature (300 ^{0}C) has been studied under two different conditions of constant average wall temperature of the cartridge heater or constant heat flux. The results shown below are for constant heat flux condition with a maximum input temperature of 300 ^{0}C.

Figure (4-34) shows a similar behaviour to Figure (4-19) for the temperatures distributions in different radial locations and fixed axial location (z1=150 mm) at constant heat flux conditions. However, increasing the maximum input temperature to 300 ^{0}C leads to a faster charging process as shown in Figure (4-34). Thermocouples measured the maximum input value (300 ^{0}C) in a shorter time by 30 minutes, as shown in Figure (4-34). This could be due to the higher input condition helping to transfer more heat to the PCM side because of the higher temperature differences between the inner pipe and the surrounded PCM.

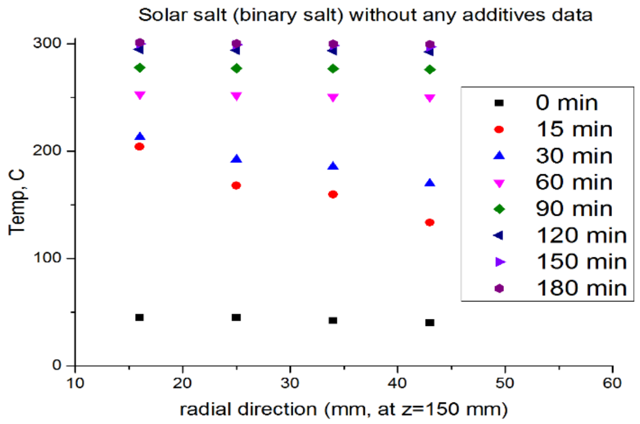

Figure 4-34 shows the temperatures distributions vs radial directions in the axial direction of z=150 mm, for binary solar salt material. The maximum temperature is 300 ^{0}C.

Figures (4-35, 4-36, 4-37) show a similar behaviour to Figures (4-20, 4-22, 4-24), respectively. All of these graphs show the temperature distributions at different radial locations (and the axial location is z2= 200 mm) and different theta locations (and the axial location is z2=200 mm), apart from Figure (4-36) which shows the transient temperature distributions. The only difference among Figures (4-20, 4-22, 4-24, 4-35, 4-36, 4-37) is that the maximum input temperature is 300 ^{0}C instead of 270 ^{0}C. Similar behaviour is obtained for the two different input temperatures (270 ^{0}C or 300 ^{0}C). However, the required time to finish the charging process is shorter at the higher input temperature (300 ^{0}C) where thermocouples measured higher temperature in the short period from the start of the experiments. This is due to the higher temperature differences between the inner hot pipe and surrounded PCM which caused increases in heat conduction mode according to Fourier equation (q_r= k A dT/dr).

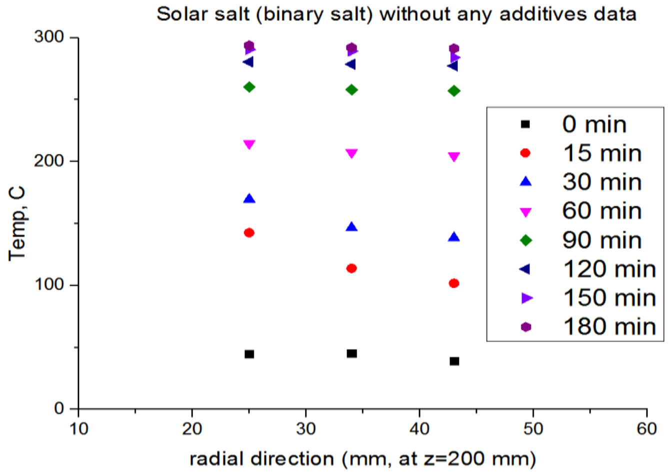

Figure 4-35 shows the temperatures distributions vs radial directions in axial directions of z=200 mm, for binary solar salt material. The maximum temperature is 300 ^{0}C.

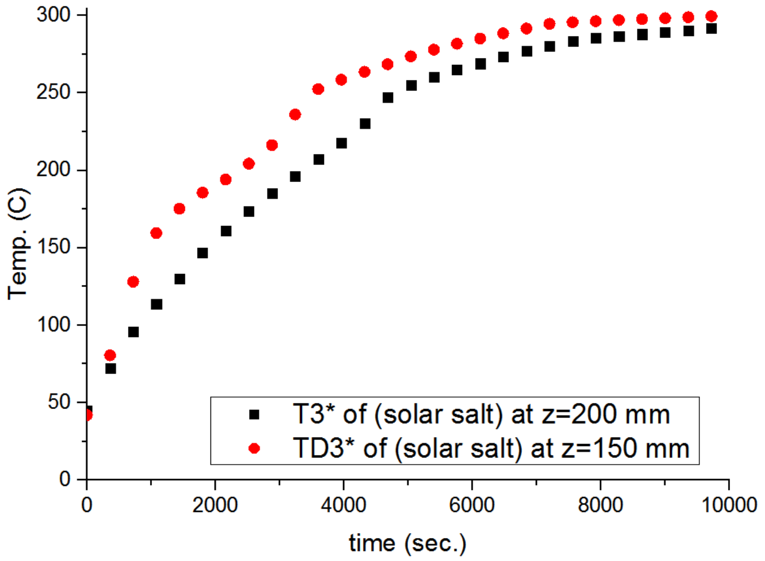

Figure 4-36 shows the temperatures distributions vs time in different axial directions (z=150 mm and z=200 mm) with the same radial direction, for binary solar salt material. The maximum temperature is 300 ^{0}C.

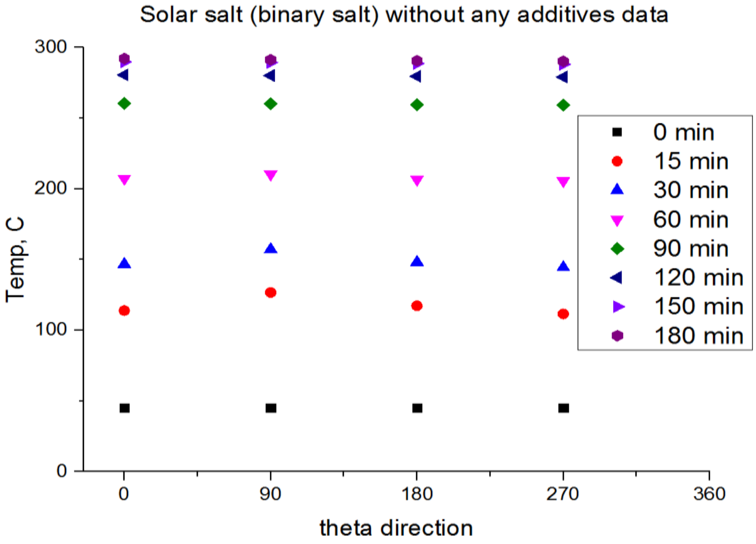

Figure 4-37 shows the temperatures distributions vs theta directions in the axial direction of z=200 mm, for binary solar salt material. The maximum temperature is 300 ^{0}C.

Figures (4-38, 4-39) show a similar behaviour to Figures (4-25, 4-26). The same condition of constant heat flux has been used with a maximum input temperature of 300 ^{0}C in Figures (4-38, 4-39) while maximum input temperatures was 270 ^{0}C in Figures (4-25, 4-26). However, the increase of the input temperature has a negative effect especially on the solid phase of those materials (0.5 wt. % CuO + salt, 0.1 wt. % Fe_2O_3 + salt and 1 wt. % Fe_2O_3 + salt). There is an increment in the solid phase for the case of

(0.5 wt. % Fe_2O_3 + salt) in Figures (4-38, 4-39), but they are lower than the improvement in the Figures (4-25, 4-26). The increase in the input temperature for this kind of base material (binary solar salt) may cause more aggregation or sedimentation of nanoparticles which could be the reason behind this behaviour. The agglomeration or sedimentation of nanoparticles could be behind the lowest improvement in charging time. Therefore, at a higher input of 300 ^{0}C, the charging time was less improved for nanosalt case than in the case of maximum input at 270 ^{0}C. For instance in the case of 0.5 wt. % CuO + solar salt, charging time improved by only 6.061% at a maximum input of 300 ^{0}C while it was 15.78% in case of 270 ^{0}C is the maximum input. The same behaviour is observed for case 1 wt. % Fe_2O_3 + solar salt and 0.1 wt. % Fe_2O_3 + solar salt with 3.87% and 0.76% only. The higher input temperature causes less stable nanoparticles with more probability of sedimentation or agglomeration of nanoparticles in the nanosalt materials. Therefore nanoparticles would be increased in size, largely due to the agglomerated nanoparticles and this would lower the benefit of the surface area of these nanoscales. All of these reasons could be behind this behaviour of nanosalts materials at the two different input conditions tested.

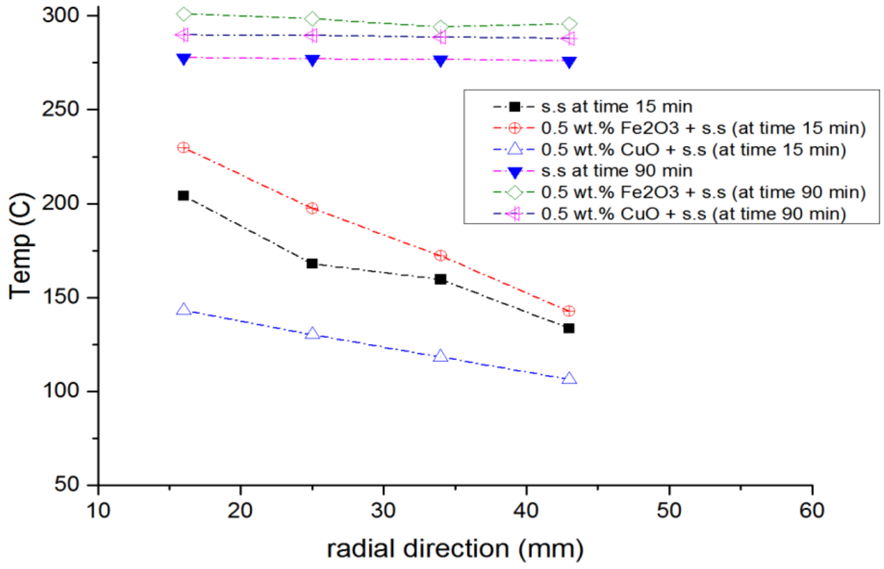

Figure 4-38 shows the temperatures distributions vs radial directions at z=150 mm for binary solar salt material vs. 0.5 wt. % Fe_2O_3 + salt vs. 0.5 wt. % CuO + salt.

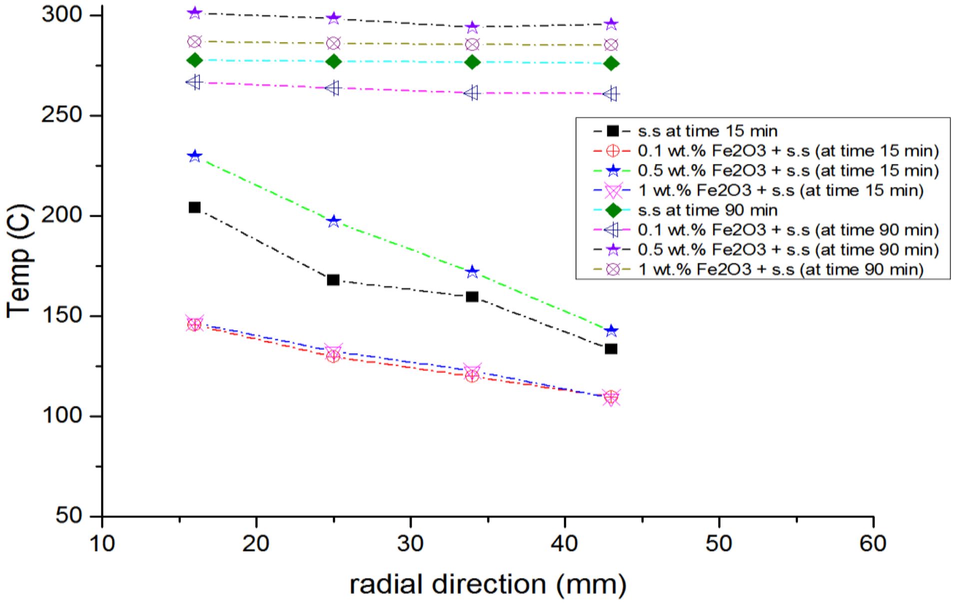

Figure 4-39 shows the temperatures distributions vs radial directions at z=150 mm for binary solar salt material vs. 0.1 wt. %, 0.5 wt. % and 1 wt. % of Fe_2O_3 + salt. The maximum temperature is 300 ^{0}C.

Figure (4-40), with 300 ^{0}C as the maximum input temperature, show similar behaviour to Figure (4-28), with 270 ^{0}C as the maximum input temperature. Figures (4-28 and 4-40) show the transient temperatures at different axial locations (z1 and z2) for nitrate binary solar salt and nanosalt (0.5 wt. % Fe_2O_3 + binary nitrate salt). The higher input temperature (300 ^{0}C) shows bigger differences between the measured temperatures at z1 and z2, for both of salt and nanosalt materials than the case of maximum temperature equals to 270 ^{0}C, especially at the beginning of charging process. This could be due to the high temperatures differences between the hot inner pipe and the surrounded PCM which causes an improvement in the conduction heat transfer at the early stage of the charging process. This could lead to starting the melting (including the effect of natural convection) earlier in case of 300 ^{0}C (time < 3000 seconds) than the case of 270 ^{0}C (time around 4000 seconds). It's clearly shown that nanosalt charged faster than salt alone which could be due to the higher thermal conductivity that improves the heat conduction mode of the nanosalt at the beginning of the charging process. Furthermore, the sensible and latent heat of nanosalt is improved for the nanosalt than salt alone. All of these parameters could be the reasons behind the behaviour shown in Figure (4-40) for nanosalt and salt materials.

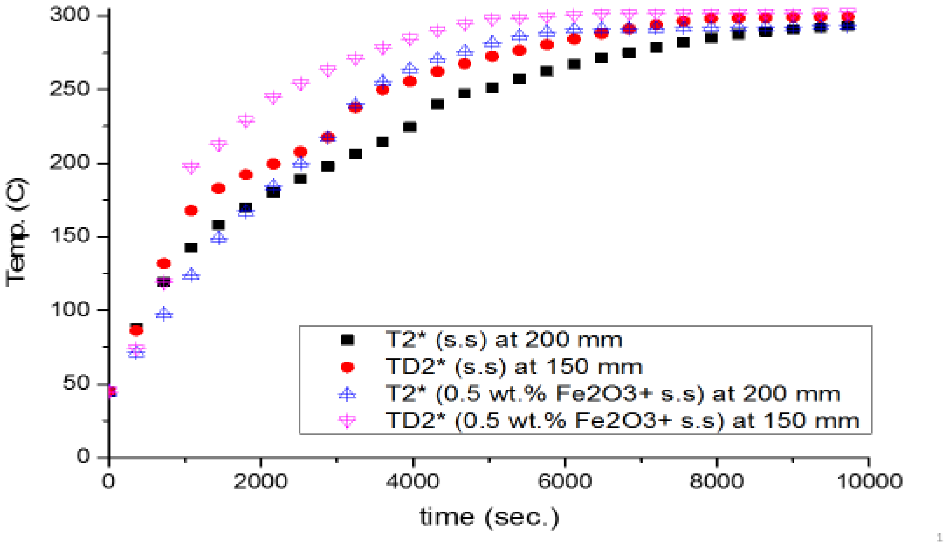

Figure 4-40 shows the temperatures distributions vs time at different z-direction for binary solar salt material and 0.5 wt. % Fe_2O_3 + salt. The maximum temperature is 300 ^{0}C.

On the other hand, Figure (4-41) shows the behaviours of temperature measurements from the two different conditions that were tested through the experiments (constant average temperature and constant heat flux of the inner heater) at the maximum input temperature of 300 ^{0}C. Similar behaviour was obtained for the case of constant average temperature and constant heat flux condition. There are minimal differences which could be due to the method used to run each condition. For instance, the Variac was used to run the constant heat flux condition with 380 W while the constant average wall temperature case did not use the Variac. For the constant average temperature, the maximum power was 720 W and this power was changeable to maintain the constant temperature. Due to similar behaviour obtained by both conditions, the results presented in this chapter for the maximum input temperature of 300 ^{0}C were for the constant heat flux condition to avoid repetition of the results.

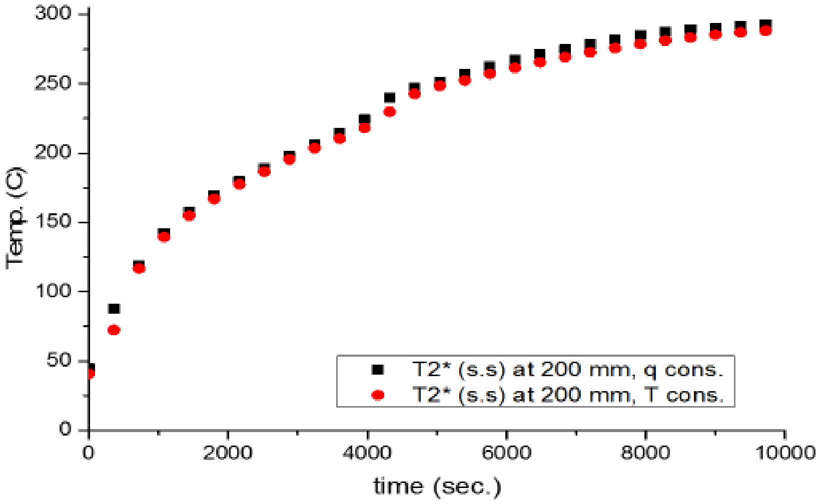

Figure 4-41 shows the temperatures distributions vs time at different power input condition for binary solar salt material and 0.5 wt. % Fe_2O_3 + salt. The maximum temperature is 300 ^{0}C.

Figures (4-42, 4-43) show a similar behaviour to Figures (4-30, 4-31) because the inner cartridge heater is off during the cooling process. Therefore, the only effect of the maximum input temperature is on the amount of the time required to finish the cooling process. For instance, Figure (4-42) requires a longer time to be cooled from 300 ^{0}C to 50 ^{0}C, while a shorter time is needed for the case of maximum input temperature of 270 ^{0}C in Figure (4-30). In all cases, nanosalt cooled faster than salt alone as discussed earlier. The improvement percentages were 28%, 18%, 14% and 0.28% for (0.5 wt. % Fe_2O_3 + solar salt, 0.5 wt. % CuO + solar salt, 1 wt. % Fe_2O_3 + solar salt and 0.1 wt. % Fe_2O_3 + solar salt) respectively. The conduction heat transfer dominates the cooling process and due to the lower thermal conductivity of salt, it required a longer time to finish the cooling process. The nanosalt material cooled faster than salt alone due to a higher thermal conductivity of nanosalt than salt because of the higher thermal conductivity values of these small nanoparticles resulted with an improvement in the conduction heat transfer mode of the nanosalt materials. The effect of nanoparticles types or concentrations played an important role on the improvements of the cooling process where increasing (1 wt. %) or decreasing (0.1 wt. %) the weight loading of Fe_2O_3 nanoparticles would not show higher improvement in the cooling process of nanosalts in comparison to 0.5 wt. % Fe_2O_3. This could be due to the agglomerations or sedimentations effect of nanoparticles at higher concentrations. In case of lower concentration, the nanoparticles might not improve the thermophysical properties of the nanosalt material sufficiently to show higher improvements.

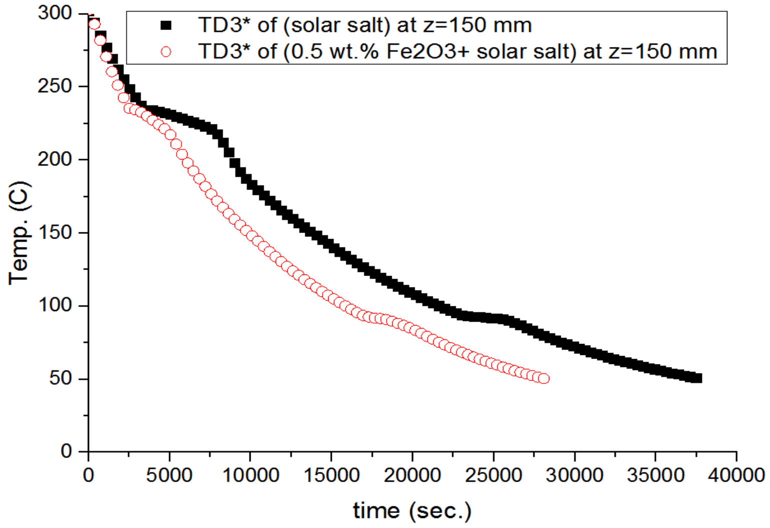

Figure 4-42 shows the cooling process of different materials (binary solar salt material vs 0.5 wt. % Fe_2O_3 + salt) at different z-direction. The maximum temperature is 300 ^{0}C.

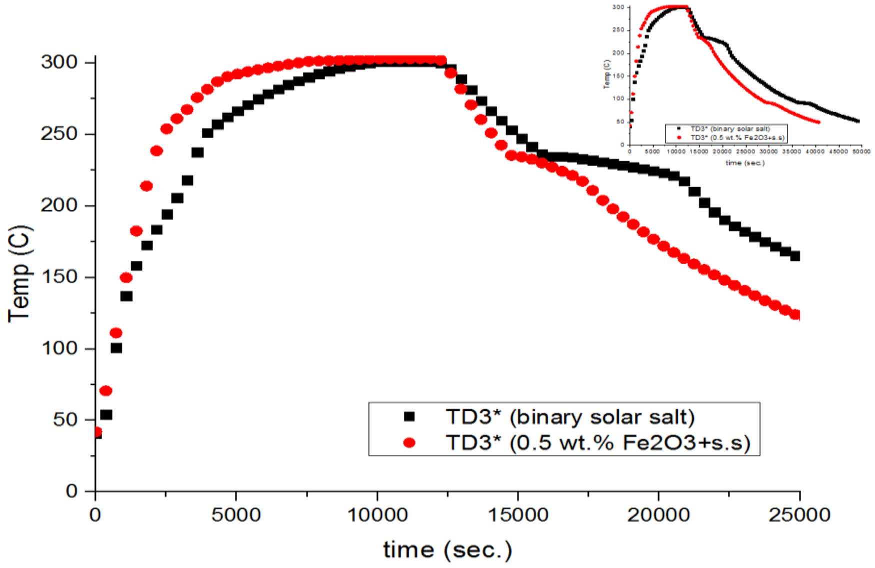

Figure 4-43 shows the full charging and cooling process of different materials (binary solar salt material vs 0.5 wt. % Fe_2O_3 + salt). The maximum temperature is 300 ^{0}C.

Figure (4-44) shows the temperature ratios vs the radial ratios of different materials (binary solar salt material vs 0.5 wt. % Fe_2O_3 + solar salt vs 0.5 wt. % CuO + solar salt) after 60 minutes from the starting of the experiments. It is clear that 0.5 wt. % Fe_2O_3 +

solar salt is better than other types. This ensures that Fe_2O_3-nanosalt is better than CuO-nanosalt as discussed earlier. The nanosalt has a higher thermal conductivity which increases the heat conduction mode especially at the beginning of the charging process of the nanosalt. Furthermore, the weight concentration of nanoparticle was not large (0.5 wt. %) therefore, no large effect on the natural convection might be observed. Additionally, other thermophysical properties of nanosalt were higher than salt alone such as cp, k, and latent heat with a lower melting point than salt (as demonstrated in Chapter 3). All of these reasons could play an important role in improving the melting process of nanosalt in comparison to salt alone. Furthermore, the improvements depend on the type of nanoparticles used as shown in Figure (4-44) where Fe_2O_3 appears to be better than the CuO type.

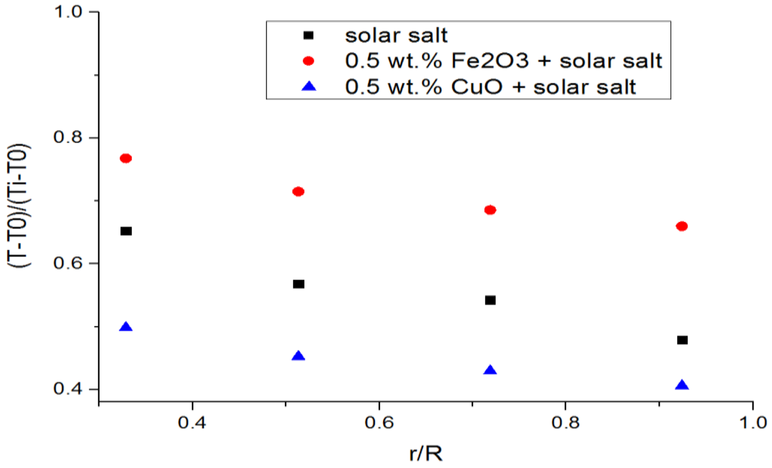

Figure 4-44 shows the comparison among different materials (binary solar salt material vs 0.5 wt. % Fe_2O_3 + solar salt vs 0.5 wt. % CuO + solar salt) after 60 minutes from the starting of the experiments at z1. The maximum temperature is 300 ^{0}C.

Figure (4-45) indicates the power consumed by each material for a full experiment. The materials that consume a minimum amount of power through the experiment in comparison to salt without any additives are as follows: 0.5 wt.% Fe_2O_3 + salt, 0.5 wt.% CuO + salt, 1 wt.% Fe_2O_3 + salt, 0.1 wt.% Fe_2O_3 + salt by 32.459 %, 26.411 %, 10.081 % and 0.9 % respectively. This shows the positive impact of nanoparticles on the binary solar salt. As stated above, the amount of power needed to finish an experiment can be reduced by the use of nanosalt and this saving is variable depending on the type and concentrations of nanoparticles material. The consumption of power is related to the length of the charging process, where 0.5 wt. % Fe_2O_3 + binary salt required less power because it finishes the melting earlier than other types of nanosalts or salt. This could be due to higher thermophysical properties of nanosalt (0.5 wt. % Fe_2O_3+ binary salt) such as k, cp, and latent heat. 0.5 weight loading seems to be the optimum weight concentration that improves charging of nanosalt.

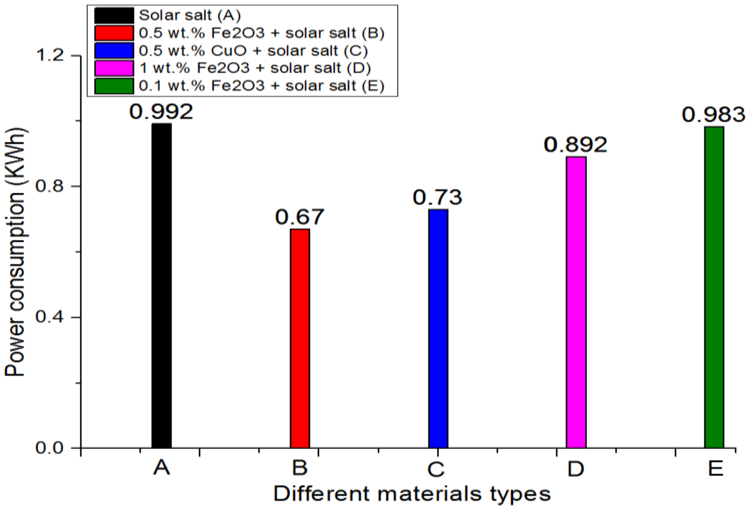

Figure 4-45 shows the power consumption measured by KWh device of different materials (binary solar salt, vs 0.5 wt. % Fe_2O_3 + salt, 0.5 wt.% CuO + salt, 1 wt.% Fe_2O_3 + salt and 0.1 wt. % Fe_2O_3 + salt). The maximum temperature is 270 ^{0}C.

4.8.2 Single salt vs nano-single salt results and discussions

Figure (4-46) shows the temperatures distributions at different radial locations at the axial location of 150 mm. It clearly shows similar behaviour to the binary salt in Figures (4-19 and 4-34). However, the single salt ($NaNO_3$) took a longer time to reach the steady state condition than binary salt because the melting temperature is higher (around 306 ^{0}C). Therefore, the improvements due to natural convection come late, at around 120 min during the experiment. Around 120 min., the activated phase change starts and then natural convection is included. However, in binary solar salt, (with a maximum input temperature of 300 ^{0}C), phase change starts at less than one hour from the start of the experiment. This is because of the lower melting temperature in the case of binary salt (around 220 ^{0}C).

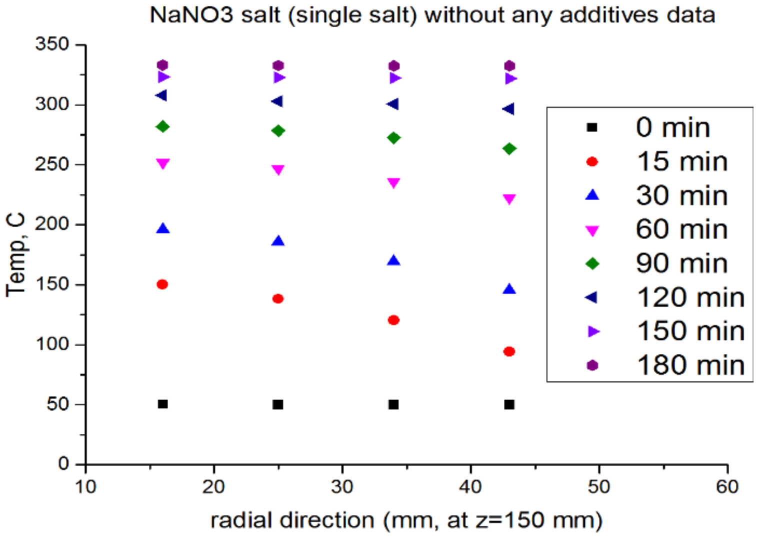

Figure 4-46 shows the temperatures distributions vs radial directions in the axial direction of z=150 mm, for single salt material. The maximum temperature is 350 ^{0}C.

It is obvious that $NaNO_3$ salt at the axial location of z2=200 mm takes longer to reach the maximum input value (up to 350 ^{0}C), as shown in Figure (4-47), than the results in Figure (4-46). This is a similar behaviour to the case of binary salt for similar reasons as discussed earlier. Heating up from ambient temperature to the point of phase change mainly depends on heat conduction. During the phase change region, the effect of natural convection starts. Heating up to the maximum input temperature depends on both natural convection and conduction. Figures (4-46) and (4-47) show the effect of natural convection on the results where PCM at the axial location of z1 melt faster than PCM at axial locations of z2.

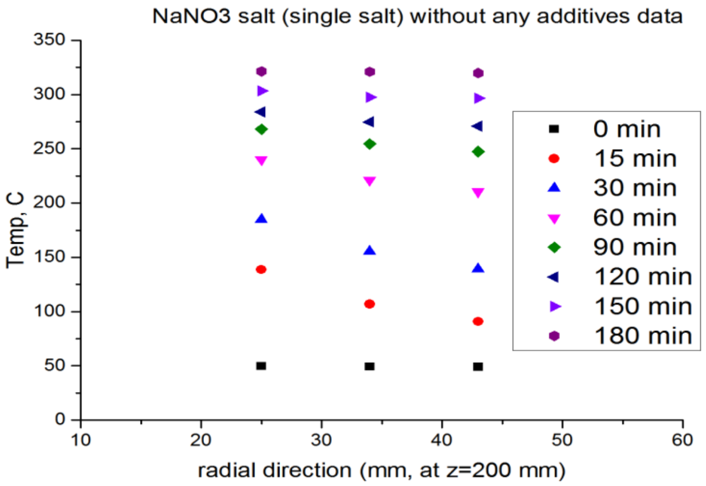

Figure 4-47 shows the temperatures distributions vs radial directions in axial directions of z=200 mm, for single salt material. The maximum temperature is 350 ^{0}C.

Figure (4-48) indicates the transient temperature distributions at different axial locations of z1 and z2. Similar behaviour is obtained in Figure (4-48) of the single salt to that of the binary salt in Figures (4-22, 4-36). Due to the large scale of time in the case of single salt ($NaNO_3$), the axial differences in the temperature distributions are not clear enough in comparison to the case of binary salt under different maximum input temperatures (270 ^{0}C in Figure (4-22) and 300 ^{0}C in Figure (4-36)). The single salt ($NaNO_3$) melts around 306 ^{0}C, therefore the heating up form ambient to the phase change region mainly depends on the thermal conductivity of the single salt. On the other hand, binary salt has the combined effect of natural convection and conduction from 220 ^{0}C. Overall, the effects of natural convection are noticeable in Figure (4-48) where PCM at z1 melted before PCM at z2.

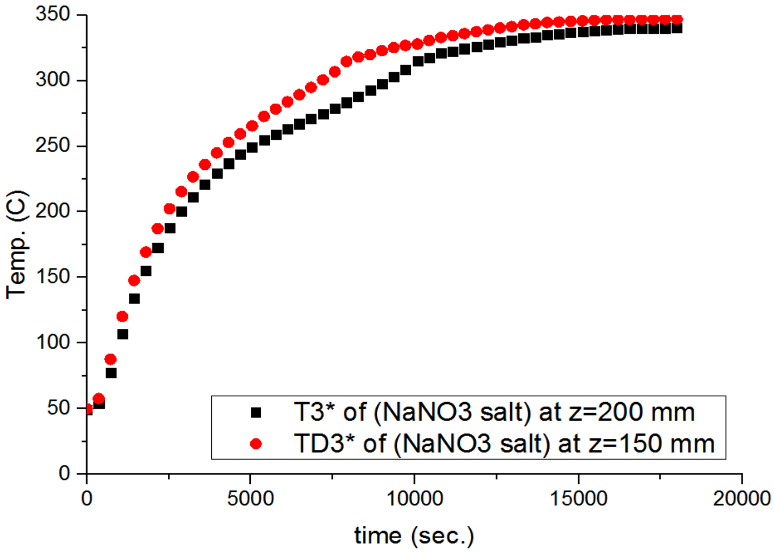

Figure 4-48 shows the temperatures distributions vs time in different axial directions (z=150 mm and z=200 mm) with the same radial direction, for single salt material.

There are four thermocouples located at same radial and axial locations but at four different theta locations. These four thermocouples used to measure the homogeneity of the material. The homogeneity of the material is clear in Figure (4-49) with small differences similar to those obtained for the binary salt in Figures (4-24 and 4-37). This is means that the material (single nitrate salt) was homogeneous in theta directions with minimal differences due to the purity of the material ($NaNO_3$ salt) or the uncertainty during the experiments.

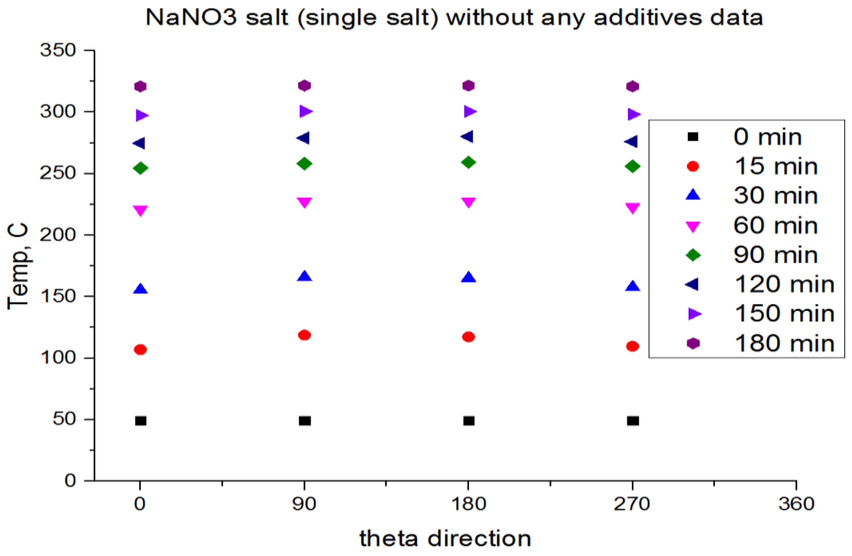

Figure 4-49 shows the temperatures distributions vs theta directions in the axial direction of z=200 mm, for single salt material. The maximum temperature is 350 ^{0}C.

In Figure (4-50), both types of nanoparticles show a positive effect on the single salt. However, in the solid phase of the binary salt, CuO nanoparticles show a negative effect. As shown in Figure (4-50), nanosalt heats up faster than salt alone. This could be due to the effect of the base material effect on the nanosalt material. For example at time= 3600 sec, $NaNO_3$ salt measures temperatures of T3*=220.9 ^{0}C while nanosalt (0.5 wt. % Fe_2O_3 + $NaNO_3$) measures a value of 244.6 ^{0}C. This indicates that nanosalt (0.5 wt. % Fe_2O_3 + $NaNO_3$) is a more conductive material than salt ($NaNO_3$) only. This could be due to the higher thermal conductivity of these nanoscale particles that cause this improvement in the conductivity of the nanosalt in compassion to the salt material. Improvements of thermal conductivity of the nanosalt material would improve the heat conduction mode that enhances the charging process of nanosalt. The enhancement of the properties of the nanosalt (i.e., because of the added nanoparticles) is one of the key points that shows this improvement in temperature distributions over time.

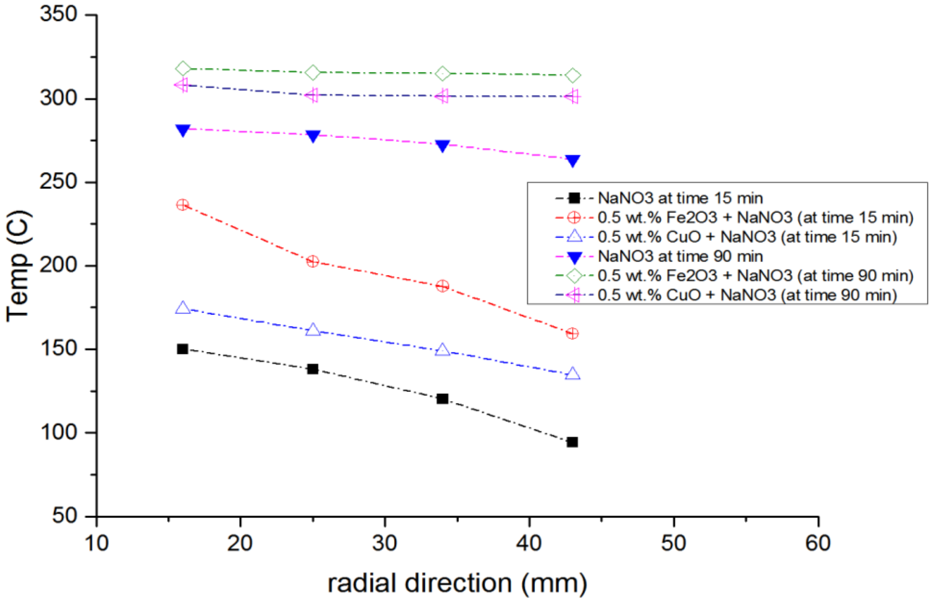

Figure 4-50 shows the temperatures distributions vs radial directions at z=150 mm for single salt material vs. 0.5 wt. % Fe_2O_3 + $NaNO_3$ salt vs. 0.5 wt. % CuO + $NaNO_3$ salt. The maximum temperature is 350 ^{0}C.

Furthermore, Figure (4-51) shows that even the lowest concentration of nanoparticles (0.1 wt. % Fe_2O_3 + $NaNO_3$) gives an overall improvement in the nanosalt storage medium. This behaviour is different in the case where the base material is a binary salt. This indicates the effect of the base material on the total improvements by the nanosalt material. This could be due to the overall enhancements on the storage energy by improving the cp and latent heat, and the improvements in the heat conduction mode where thermal conductivity of nanosalt (nano-single salt) increases because of these nanoparticles in comparison to single salt alone. The increase of thermal diffusivity with an overall increase in thermal conductivity values leads to an improvement in the charging process. Natural convection of nanosalts seems to be better than single salt alone. All of these reasons show an overall effect on the results of the temperature measurements by nanosalts vs. single salt.

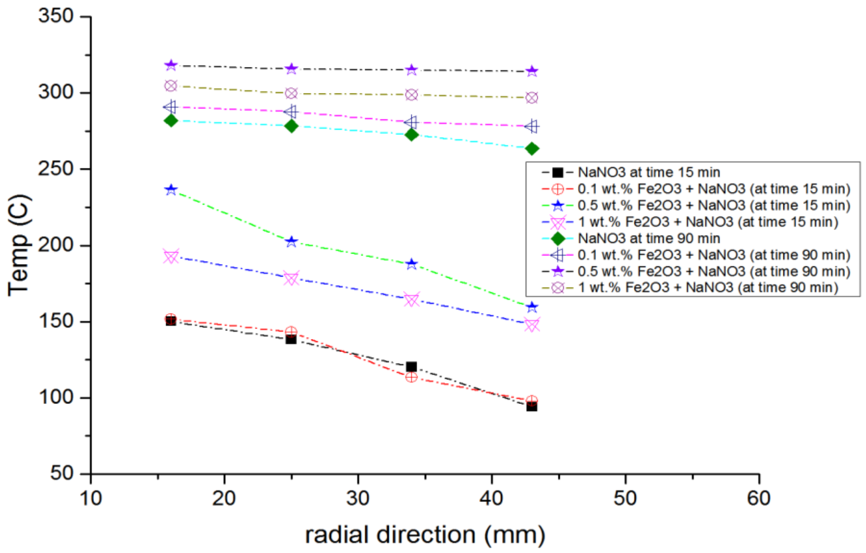

Figure 4-51 shows the temperatures distributions vs radial directions at z=150 mm for single salt material vs. 0.1 wt. %, 0.5 wt. % and 1 wt. % of Fe_2O_3 + $NaNO_3$ salt. The maximum temperature is 350 ^{0}C.

Figure (4-52) shows a similar behaviour to the case of binary salt and nano-binary salt in Figures (4-28, 4-40). Similar behaviour is observed for the transient temperatures measurement of salt in comparison to nanosalt material. Due to the effect of natural convection, TD2* started melting before T2* in both cases of salt ($NaNO_3$) or nanosalt (0.5 wt. % Fe_2O_3 + $NaNO_3$). Furthermore, T2* (or TD2*) measurements of nanosalt (0.5 wt. % Fe_2O_3 + $NaNO_3$) are higher than T2* (or TD2*) measurements of single salt ($NaNO_3$). This could be due to the surface area of nanoparticles which helps to conduct more heat in the nanosalt material resulting in a faster charging than salt alone. Furthermore, a higher thermal conductivity of these nanoparticles is responsible for the higher heat conduction from the hot medium toward the PCM medium.

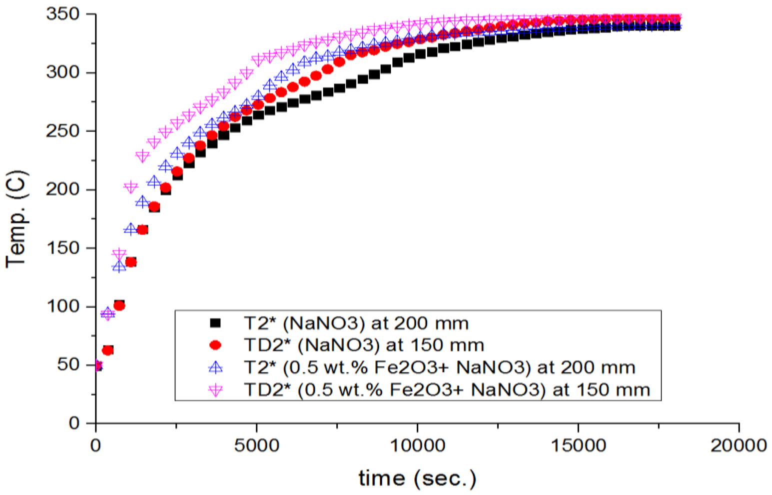

Figure 4-52 shows the temperatures distributions vs time at different z-direction for single salt material and 0.5 wt. % Fe_2O_3 + $NaNO_3$ salt. The maximum temperature is 350 ^{0}C.

Additionally, we did two different condition tests of the heat supplied. One is by a constant average wall temperature condition and the second is a constant heat flux condition. There are no significant differences between these two conditions, as shown in Figure (4-53). The small difference, in the beginning, is due to the fact that the heater power (720 W) is used at the beginning of the test and reduced rapidly to maintain the temperature in the case of the constant wall temperature. On the other hand, the constant heat flux supplied the same value of the power which is 380 W. Furthermore, the constant average wall temperature was controlled directly through the control system while an extra device (Variac) was used for the case of constant heat flux condition. All of these differences in these conditions could cause this small difference.

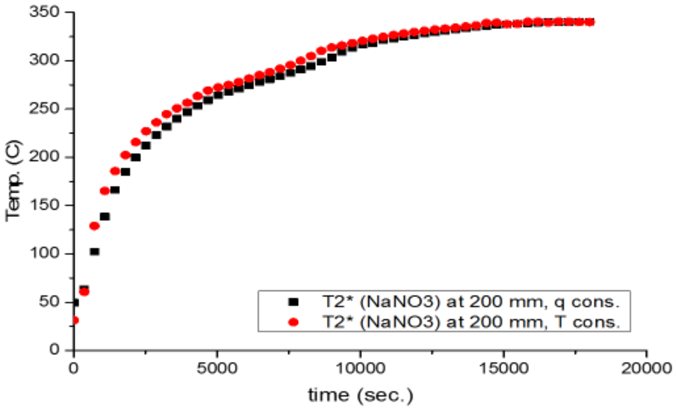

Figure 4-53 shows the temperatures distributions vs time at different input power condition for single salt material and 0.5 wt. % Fe_2O_3 + $NaNO_3$ salt. The maximum temperature is 350 ^{0}C.

The completion of the melting time of the storage material is indicated by reaching the melting temperature in the coldest location of the rig, i.e., thermocouple (T5*). In addition, the energy of the PCM can be calculated from Equation (4-7).

$$\mathrm{Energy} * \mathrm{time\ of\ charging} = \mathrm{mass} * [\int_{\mathrm{T_{ambient}}}^{\mathrm{T_{melt}}} \mathrm{cp}_{solid\ phase} * \mathrm{dT} + \int_{\mathrm{T_{liquid}}}^{\mathrm{T_{max.}}} \mathrm{cp}_{liquid\ phase} * \mathrm{dT} + \mathrm{q_{latent}}]$$

Equation 4-7

$$\mathrm{Energy}\ \alpha\ (\mathrm{time\ of\ charging})^{-1}$$ **Equation 4-8**

In the ideal case without any losses, the energy input equals to the energy absorbed. The charging time calculated according to Equation (4-7) was around 17000 sec while the experimentally measured value was 18200 sec. indicating a difference of about 6.5%. This difference between the estimated value and the experimental value could be due to heat losses or the accuracy during the measurements.

In addition, from Equation (4-8), the decrease of the charging time helps the PCM to save more energy with shorter time. For instance, the $NaNO_3$ material took around 18200 sec to finish the charging process while the nanosalt (0.5 wt. % Fe_2O_3 + $NaNO_3$) needed only 14740 sec. Therefore, nanosalt (0.5 wt. % Fe_2O_3 + $NaNO_3$) improved the charging process by (19%). This indicates that nanosalt will save energy in a shorter time than $NaNO_3$ salt. Furthermore, the thermophysical properties (specific heat capacity (cp) and latent heat) of nanosalt are better than salt alone. We have investigated separately in a DSC device the cp and latent heat of the nanosalt (0.5 wt. % Fe_2O_3 + $NaNO_3$), and salient increase in those properties was obtained for nanosalt.

The cooling process is studied and compared among the different materials we used. In Figure (4-54), $NaNO_3$ salt takes around 33600 sec to reach 50 ^{0}C while nanosalt (0.5 wt. % Fe_2O_3 + $NaNO_3$) takes 30448 sec. It is clear that the nanosalt material cooled faster than the salt material by 9.38%. The cooling process is controlled by heat conduction mode which is controlled by thermal conductivity and the temperature differences between the inner hot medium and the PCM medium. Nanosalt cools down in a shorter period than salt alone due to the higher thermal diffusivity of nanosalt material than salt alone.

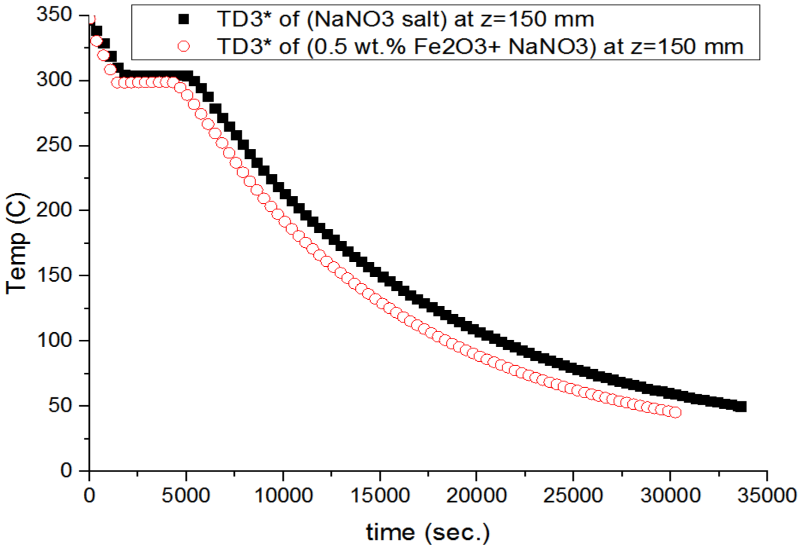

Figure 4-54 shows the cooling process of different materials (single salt material vs 0.5 wt. % Fe_2O_3 + $NaNO_3$) at different z-direction. The maximum temperature is 350 ^{0}C.

Figure (4-55) shows the full process including the charging and the cooling down to the lowest temperature of 50 ^{0}C. The nanosalt is better than the single salt without any additives. This could be due to the higher surface of these nanoscales and their higher thermal conductivity which could help to conduct the heat faster results with a faster cooling.

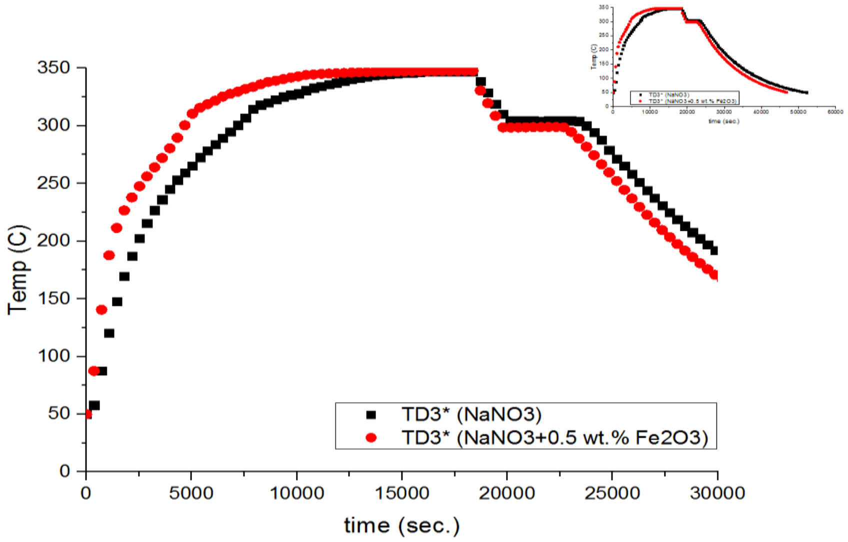

Figure 4-55 shows the full charging and cooling process of different materials (single salt material vs 0.5 wt. % Fe_2O_3 + $NaNO_3$). The maximum temperature is 350 ^{0}C.

In Figures (4-56 and 4-57), the Equations (4-2 to 4-6) are used for the calculation of the data. They show that the same values of sensible energy are produced by the nanosalt materials at a shorter time than in the case of the single salt alone without any additives. In all the cases, the single salt was the worst one and any types of nanoparticles produce an improvement in the sensible energy stored. This could be due to higher specific heat capacity and latent heat with a lower melting point of nanosalt material than salt alone without any additives. Nanosalt material could form layers between salt and nanoparticles that could have higher properties than salt and this could be one of the reasons for the improvement in stored energy by nanosalts materials.

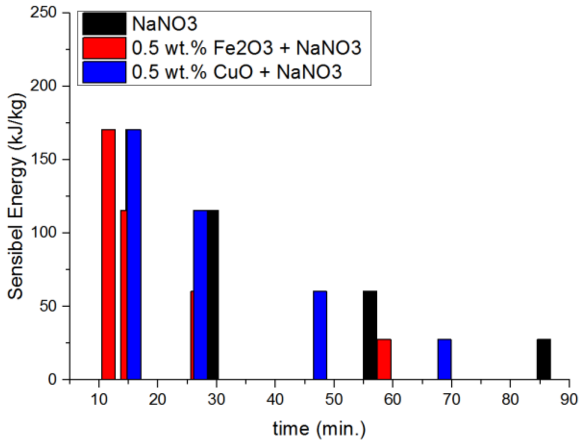

Figure 4-56 shows the sensible energy storage vs time for different materials ($NaNO_3$ salt vs. 0.5 wt. % Fe_2O_3-nanosalt vs 0.5 wt. % CuO-nanosalt) for the solid phase. It indicates that the same value of energy can be stored but in shorter time within 0.5 wt. % Fe_2O_3-nanosalt in comparison to other types of materials.

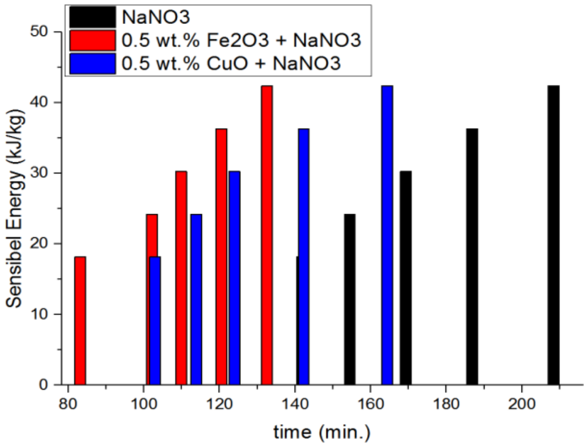

Figure 4-57 shows the sensible energy storage vs time for different materials ($NaNO_3$ salt vs. 0.5 wt. % Fe_2O_3-nanosalt vs 0.5 wt. % CuO-nanosalt) for the liquid phase. It indicates that the same value of energy can be stored but in shorter time within 0.5 wt. % Fe_2O_3-nanosalt in comparison to other types of materials.

The power consumption was measured in all the experiments as shown in Figure (4-58). In the case of $NaNO_3$ salt as the PCM, the energy consumed was 1.193 KWh while for nanosalt it was 1.084 KWh. Therefore, the use of nanosalt saved energy by 9.14%. It showed similar behaviour to the binary salt/nano-binary salt in Figure (4-45). However, in the cases of single salt ($NaNO_3$) or nano-$NaNO_3$ materials, the power consumption was bigger than the case of binary salt or nano-binary salt. This is because the working temperature range of the single salt (or nano-single salt) is higher up to 350 ^{0}C and the melting temperature is higher up to 306 ^{0}C. All of these help to consume more power until the experiment is finished.

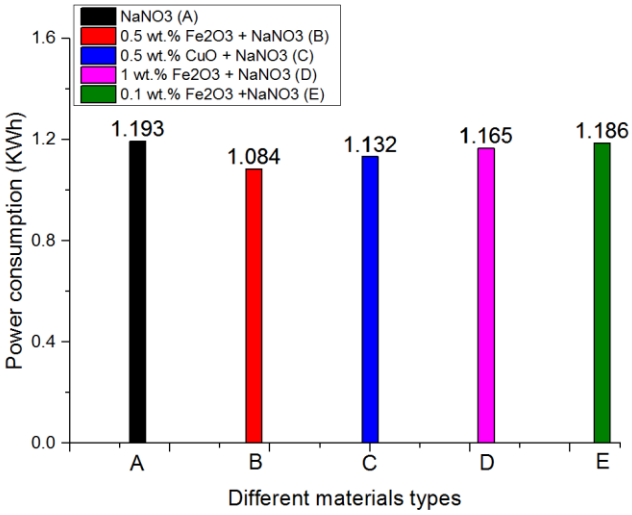

Figure 4-58 shows the power consumption measured by KWhr device of different materials (single salt ($NaNO_3$), vs 0.5 wt. % Fe_2O_3 + $NaNO_3$ salt, 0.5 wt.% CuO + NaNO3 salt, 1 wt.% Fe_2O_3+ $NaNO_3$ salt and 0.1 wt. % Fe_2O_3 + $NaNO_3$ salt).

Figure (4-59) shows the ratio of (T-T0)/(Ti-T0) at different r/R in the radial locations. The best material is 0.5 wt. % Fe_2O_3-nanosalt followed by 0.5 wt. % CuO-nanosalt in comparison to the salt ($NaNO_3$) alone without any additives. This indicates the positive effect of the nanosalt materials compared to salt without any additives, as discussed earlier the advantages of nanosalt, which could be due to the higher thermophysical properties of nanosalt (e.g. higher cp, latent heat and thermal conductivity) that improve the conduction and natural convection heat transfer modes.

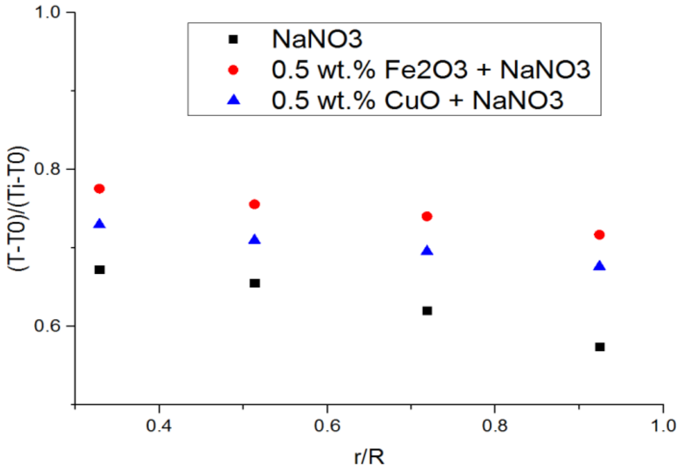

Figure 4-59 shows the Comparison between different materials (single salt material vs 0.5 wt. % Fe_2O_3 + single salt vs 0.5 wt. % CuO + single salt) after 60 minutes from the starting of the experiments. The maximum temperature is 350 ^{0}C.

4.9 Further discussion of heat transfer for salt vs nano-salt

Enthalpy is calculated according to Equation (4-9) (Gibout et al., 2018)

$$\text{Enthalpy} = \begin{cases} C_w^S\,(T - T_{melt}) & T < T_{melt} \\ L\,\beta & T = T_{melt} \\ L + C_w^L\,(T - T_{melt}) & T > T_{melt} \end{cases} \qquad \textbf{Equation 4-9}$$

Where the C^S_w, C^L_w are the specific heat capacity of the solid phase and liquid phase (J/g. ^{0}C) respectively, assumed constant here. T_{melt} is the melting temperature (^{0}C). Latent heat is represented by L, (J/g). β is the dimensionless liquid mass fraction which is calculated from Equation (4-10).

$$\beta = \min(\max((T - T_{solidus}) / (T_{liquidus} - T_{solidus}), 0), 1) \qquad \textbf{Equation 4-10}$$

The total enthalpy of nanosalt is improved by the addition of nanoparticles to the PCM, as shown in Figure (4-60). The calculation of the enthalpy is mainly dependent on the value of the specific heat capacity (cp) and latent heat (*L*) as shown in Equation (4-9). This calculation has an error less than 1.5 % in case of binary solar salt and less than 2.02 % in case of nanosalt (0.5 wt. % Fe_2O_3 + binary solar salt), as measured by the DSC device. In most cases, nanosalt has higher cp and *L* than the base salt without any additives. As explained earlier in Chapter 3, that nanosalt has interfacial layers formed between the base material (nitrate salt) and nanoparticles in the nanosalt material which could have higher cp values than the base material alone without any additives. Additionally, the agglomerations of nanoparticles might require higher heat to allow the nanosalt to melt resulting with an increment in latent heat. The improvements in both cp and *L* improve the enthalpy of the nanosalt material. Therefore the nanosalt material appears to have higher enthalpy than salt in Figure (4-60). This would improve the total power of PCM in the storage system.

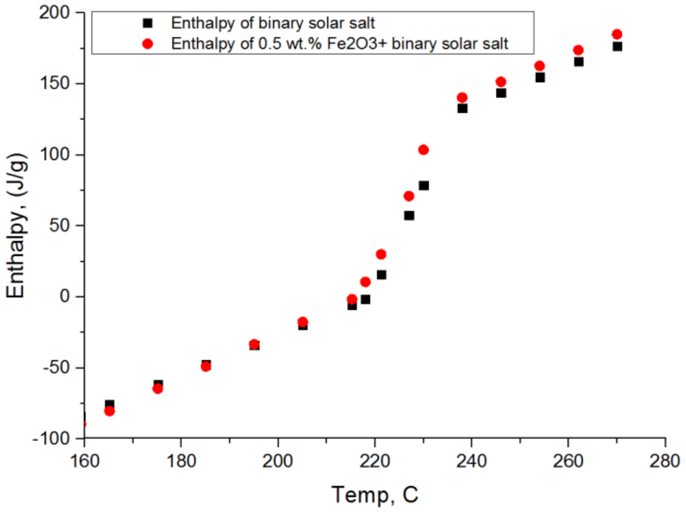

Figure 4-60 shows the total enthalpy vs temperatures comparison between different materials (binary solar salt material vs 0.5 wt. % Fe_2O_3 + binary solar salt). The maximum temperature is 270 ^{0}C.

Figures (4-61 and 4-62) show the melting progress in the radial locations of different materials we tested at a different axial location. It clearly indicates that the salts (single or binary salt) would require more time to complete the phase change process unlikely to the nanosalts materials were the phase change was faster under same experimental conditions (same heat flux from the cartridge heater). Similar trends have been concluded by (Fang et al., 2017). However, their materials are different from ours besides their presentations of data were in the dimensionless form of time vs radial locations. Furthermore, Figures (4-61 and 4-62) show the melting temperature at each thermocouple for different materials. Four thermocouples are located at different radial directions but at z1=150 mm which is at half of the rig shown in Figure (4-61). On the other hand, Figure (4-62) shows the melting time of different materials at three thermocouples in the radial direction and z2=200 mm. At the beginning of the melting process, the conduction mode is controlling the heat transfer of the salt/nanosalt materials. According to our measurements of thermal diffusivity (or our calculated thermal conductivity), an improvement of thermal diffusivity has been concluded when the nanoparticles are present in nanosalt samples (as discussed earlier in Chapter 3 under section 3.4.4). This could be the reason behind this improvement in the charging time at these locations.

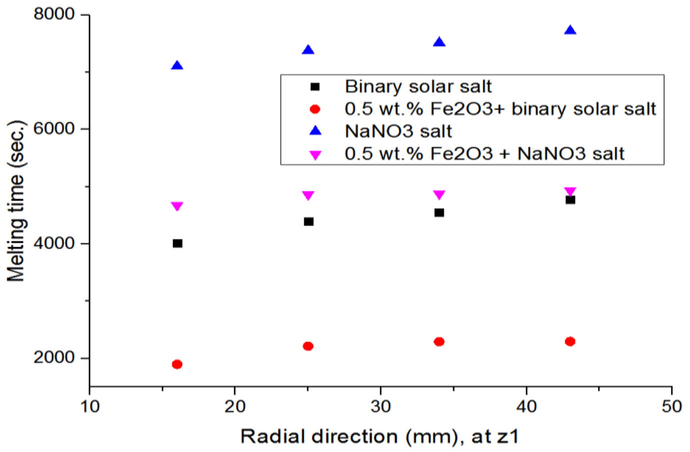

Figure 4-61 shows the melting time of different radial direction among different materials at axial direction is z1.

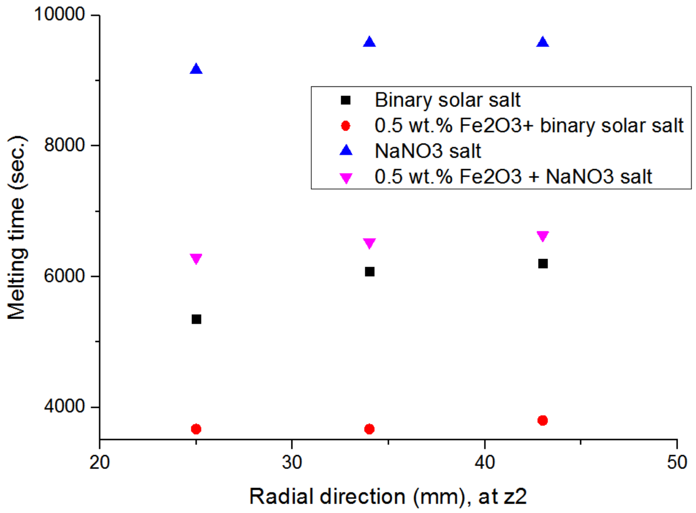

Figure 4-62 shows the melting time of different radial direction among different materials at axial direction is z2.

In the case of binary solar salt as the base material, we studied the effect of two different boundary conditions. Condition 1 is when the maximum temperature of the inner pipe is 270 ^{0}C while condition 2 is 300 ^{0}C. Figure (4-63) shows the melting time of binary solar salt (and nano-binary salt) at different radial locations with an axial location at z1. In all materials and conditions, it is clearly noticeable that the melting layer starts gradually from the innermost thermocouple to the heater toward the outmost one. It is observed that higher input temperature shortens the melting process. This could be due to higher temperature differences between the inner hot pipe and the surrounded PCM which gives a higher heat transferred from the hot medium to the near PCM (salt/nanosalt). Overall, nanosalt is better than binary solar salt in terms of shorter melting time. The nanosalt has better heat transfer than the binary solar salt as discussed above, where the nanosalt material could have higher thermophysical properties, particularly higher thermal conductivity because of the higher thermal conductivity of these small nanoparticles.

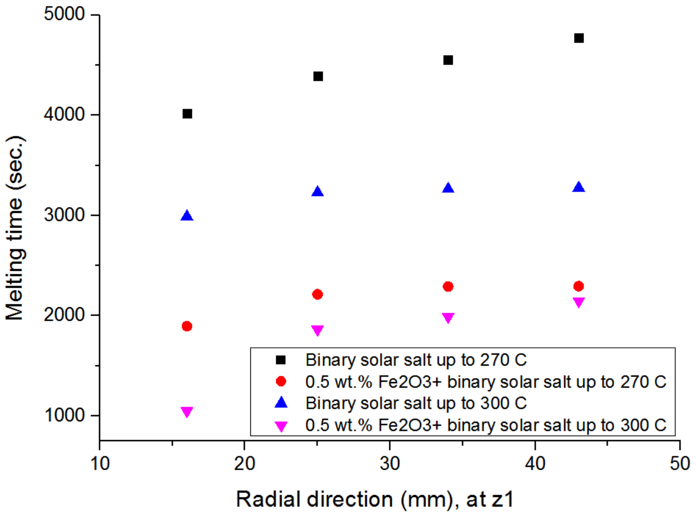

Figure 4-63 shows the melting time of different radial direction (axial direction is z1) for binary solar salt vs. nanosalt (0.5 wt. % Fe_2O_3 + binary solar salt) materials at two different condition. Condition 1 is when the maximum inner temperature is 270 ^{0}C and condition 2 is at the maximum temperature of 300 ^{0}C.

On the other hand, in the vertical annular cylinder experimental setup, heat transfer has to consider the effect of natural convection during the phase change, where melting is downward from the top to bottom of the cylinder due to the density differences between the two phases. A similar study of melting in a vertical cylinder has been considered by (Farid et al., 1989) but for low temperature application.

Additionally, the Nusselt number can be calculated from Equation (4-14) depending on Equations (4-11, 4-12, and 4-13) (Qi and Shiming, 1999). They studied the natural convection heat transfer in concentric vertical cylinders with a constant heat flux for heater locates in the inner pipe similar to our setup. Therefore, we depend on their equation to calculate the Nusselt number, Equation (4-14). According to Qi and Shiming (1999), Equation (4-14) can be used for a range of Rayleigh number of $7\text{x}10^7 < \text{Ra} < 1.1\text{x}10^9$. Additionally, the heat transfer coefficient can be calculated according to Equation (4-15)

$$\mathrm{Gr} = \frac{\mathrm{g}\,\rho^2\,\alpha_\mathrm{T}\,\Delta\mathrm{T}\,\mathrm{L_c}}{\mu^2}$$ **Equation 4-11**

$$Pr = \frac{\mu\, cp}{k_{avg}}$$ **Equation 4-12**

$$Ra = \mathrm{Gr.Pr}$$ **Equation 4-13**

$$\mathrm{Nu} = 0.304\,\mathrm{Ra}^{0.27}$$ **Equation 4-14**

$$\mathrm{h} = \mathrm{Nu\,k/L}$$ **Equation 4-15**

Where Ra is the Rayleigh number, ρ is density (kg/m^3), g is gravity (m/s^2), cp is specific heat capacity (J/kg. K), α_T is thermal expansion coefficient (K^{-1}), L represents the characteristic length (m), μ is viscosity ((N. s)/m^2), k is thermal conductivity (W/m. K), ΔT is temperature difference (K) between the maximum input temperature in the hot side and the average measured temperature in the PCM side, Nu is Nusselt number and h is the heat transfer coefficient (W/m^2. K).

The cp vs temperature equations of different materials are measured using the DSC device. Depending on our measurements, cp of binary solar salt or nanosalt (0.5 wt. % Fe_2O_3 + binary solar salt) can be calculated from the Equations (4-16 and 4-17).

For the case of binary solar salt, cp of the liquid phase is

$$\mathrm{cp} = \mathrm{T} + 784.4$$ **Equation 4-16**

For the case of nanosalt (0.5 wt. % Fe_2O_3 + binary solar salt), cp of the liquid phase is shown in Equation (4-17).

$$\mathrm{cp} = 0.8\,\mathrm{T} + 893.6$$ **Equation 4-17**

All units were SI units, T represents the temperature in K. From Figure (4-64), it shows the dimensionless relationships among the Rayleigh number (Ra), Grashof number (Gr) and Nusselt number (Nu) for the binary solar salt for an average temperature at the axial location of z1= 150 mm. The results in Figure (4-64) demonstrate that any increase in Ra number leads to an increment in both of Gr and Nu. This is due to a linear relationship between Ra and Gr, and the Ra and Nu.

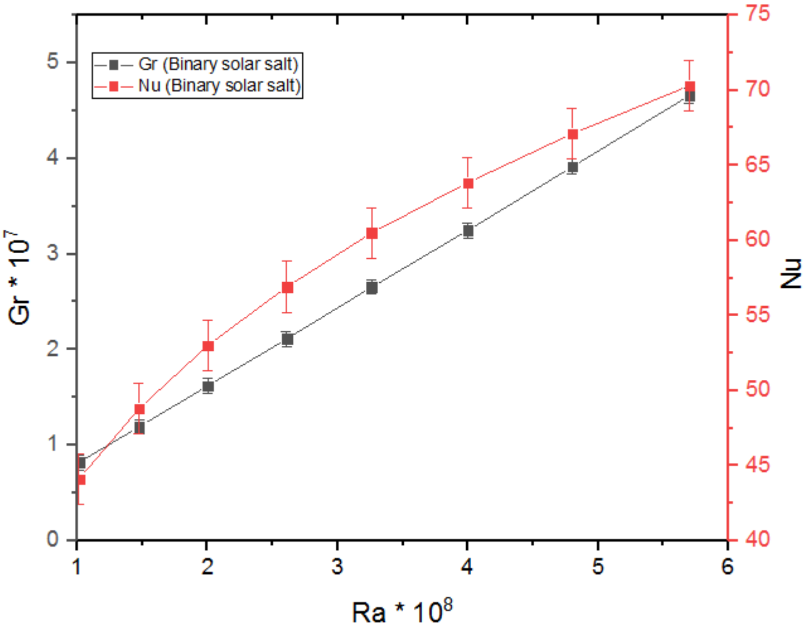

Figure 4-64 shows the Ra vs (Nu and Gr) numbers of binary solar salt with the average temperature at the axial direction of z1.

For salt vs nanosalt comparison side, it is clearly indicates that nanosalt (0.5 wt. % Fe_2O_3 + binary solar salt) is better than binary solar salt in term of heat transfer enhancement, as shown in Figure (4-65), because the ΔT in the Gr equation is between the maximum temperature in the hot medium (270 ^{0}C in this case) and the average temperature measured by the four thermocouples located at different radial directions with same axial location of z1=150 mm. The value of ΔT is decreased until the average temperature of PCM (salt or nanosalt) reached the maximum input value. Therefore, the calculated value of Ra, Nu and h are changed with time as shown in Figures (4-64 and 4-65) and Table (4-1).

Nanosalt (0.5 wt. % Fe_2O_3 + Binary solar salt) gives a similar value of Nu number for the binary salt at a short time. This gives an indication that nanosalt would save energy faster than binary salt. As a result, the total improvement of heat saved by nanosalt as a PCM in the storage system is more powerful than binary salt without nanoparticles.

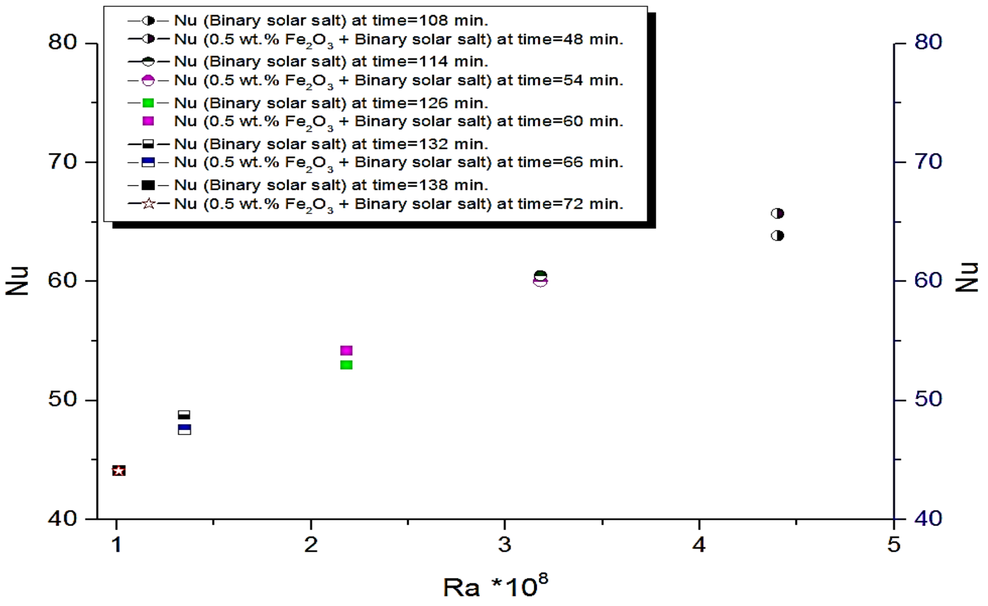

Figure 4-65 shows the Ra number vs Nu number of binary solar salt vs. (0.5 wt.% Fe_2O_3 + binary solar salt) at different times with average temperature at the axial direction of z1 during the liquid phase.

On the heat transfer coefficient side, nanosalt delivers a heat transfer coefficient with value of 1.062 kW / (m^2. ^{0}C) after 72 minutes from the start of the experiment, while binary solar salt showed an approximately similar value at 114 minutes after the start of the experiment, as shown in Table (4-1). It can be concluded that nanosalt reduces the time required to deliver a similar heat transfer coefficient to that of the binary solar salt by 36.84%. From Table (4-1), we conclude the advantages of nanosalt in comparison to solar salt without any additives. This indicates the large effect of nanoparticles in the nanosalt material compared to binary salt alone.

Table 4-1 the values of heat transfer coefficient of binary salt and nanosalt

Time (min.)	h, binary salt (kW/m^2. ^{0}C)	Time (min.)	h, 0.5 wt.% Fe_2O_3+ binary salt (kW/m^2. ^{0}C)
108	1.1	48	1.583
114	1.04	54	1.446
126	0.913	60	1.306
132	0.84	66	1.146
138	0.76	72	1.062

Figure (4-66) emphasizes that nanosalt (0.5 wt. % Fe_2O_3 + binary solar salt) has a higher heat transfer coefficient (h) than the case of binary solar salt alone. For instance, at z1=150 mm, the average temperature of nanosalt is 265.216 ^{0}C and the heat transfer coefficient of nanosalt (0.5 wt. % Fe_2O_3 + binary solar salt) is (1.062 kW / m^2. ^{0}C) at 4320 sec during the experiments. While at a similar average temperature of 265 ^{0}C, binary solar salt gives a value of heat transfer coefficient (0.84 kW/m^2. ^{0}C) at 7920 sec. In the case of 0.5 wt. % CuO + binary salt, the h value was (1.008 kW / m^2. ^{0}C) at time 6801 sec with an average temperature of 265.123 ^{0}C. Furthermore, the values of h were (0.6766 kW / m^2. ^{0}C) for the 0.1 wt. % Fe_2O_3 + binary solar salt (at time 7794 sec with an average temperature of 265.21 ^{0}C) and (0.8356 kW / m^2. ^{0}C) for 1 wt. % Fe_2O_3 + binary solar salt (at time 5218 sec with average temperature of 265.14 ^{0}C). The h value for the binary salt is less than of nanosalt due to the differences in the values of thermophysical properties (cp, k and others of nanosalt higher than those of binary solar salt). We conclude that nanosalt (0.5 wt. % Fe_2O_3 + binary solar salt) shows the highest improvement in the heat transfer coefficient in comparison to the nitrate binary solar salt by 26.27 %. On the other hand, at z1=150 mm, in the case of single salt ($NaNO_3$), the average temperature of nanosalt (0.5 wt. % Fe_2O_3 + $NaNO_3$) is 316 ^{0}C and the heat transfer coefficient of nanosalt is 0.497 (kW / m^2. K) at 5300 sec during the experiments. $NaNO_3$ gives a similar value of h (0.485 kW / m^2.K) at 8100 sec. We conclude that nanosalt shows an improvement in the heat transfer coefficient in comparison to the $NaNO_3$ alone.

This leads to an improvement in the overall heat transfer of the storage system. Overall, nanoparticles improve the heat transfer of PCMs due to their large specific surface area, increased thermophysical properties, or the formation of interfacial layers formed between the salt and nanoparticles. Further improvement in the heat transfer is concluded with the existence of nanoparticles due to the improvement in natural convection and the conduction. The higher thermal conductivity of nanosalts helps them to increase the heat transfer by conduction. Further improvement in other properties would result with an advantage in the natural convection heat transfer as these nanoscale particles have a higher surface area which helps to transfer more heat and therefore an intensification in heat transfer is observed.

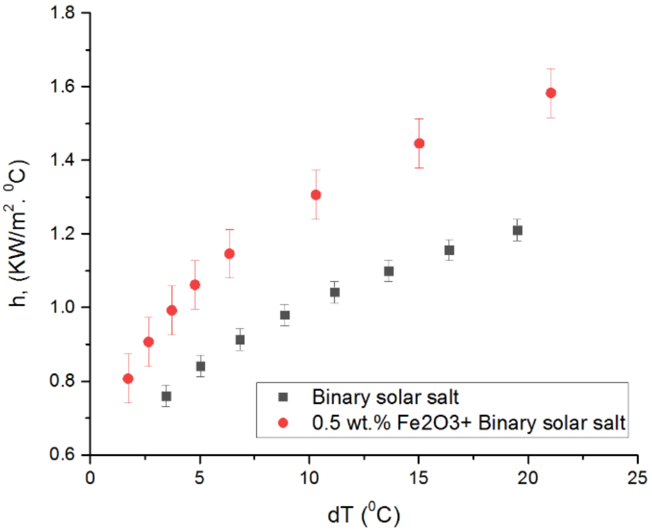

Figure 4-66 shows the heat transfer coefficient (h, kW/ m^2. ^{0}C) vs temperature differences of binary solar salt vs. (0.5 wt. % Fe_2O_3 + binary solar salt) with the average temperature at the axial direction of z1 during the liquid phase.

4.10 Conclusion

An experimental rig has been designed and manufactured for the purpose of the heat transfer study of nitrate salt or nano-nitrate salt up to 350 ^{0}C for the first time. The full details of the design, manufacturing and all the experimental rig components are discussed in this chapter. Furthermore, the preparation method of the experimental scale materials up to 3 kg is described for the different types of materials (salt or nanosalts). Different base materials have been selected for this study which are single nitrate salt (sodium nitrate, $NaNO_3$) and binary nitrate salt (solar salt of $NaNO_3$: KNO_3 with 60:40 molar ratio). There are different types and concentrations of nanoparticles have been studied such as Fe_2O_3 and CuO nanoparticles with weight loadings of 0.1%, 0.5% and 1%. In addition, both the charging and cooling processes of salts/nanosalts have been studied.

The cartridge heater located in the inner pipe was controlled by two different conditions of constant average wall temperature and constant heat flux. In case of single salt (nano-single salts) the maximum temperature was 350 ^{0}C. On the other hand, in the case of binary nitrate salt (nano-binary nitrate salts), two different input temperatures have been employed which are 270 ^{0}C and 300 ^{0}C.

Temperature profiles at different radial, theta and axial location were observed. Furthermore, at a fixed radius, a uniform temperature distribution was observed for both salts and nanosalts, as measured at four theta locations (0^0, 90^0, 180^0, and 270^0).

The charging time was found to be reduced by nanosalt. Heat transfer was improved in nanosalt than salts materials. This could be due to the higher thermophysical properties of nanosalts than salt. Moreover, the higher surface area of nanoparticles improved the heat transfer in the nanosalt materials.

During the charging process, the conduction mode dominated the heat transfer at the early stage and as soon as the phase change transition started then natural convection started to dominate the heat transfer phenomena alongside with conduction. In case of nanosalts materials, the conduction mode is highly improved due to the higher thermal conductivity of nanoparticles than those of salts. In the case of 0.5 wt. % Fe_2O_3 + binary solar salt, the charging process was improved by 21.21 %. Other types and concentrations of nanoparticles showed an improvement on the charging process. For instance, the melting time was shorter by 6.06% for (0.5 wt. % CuO + binary solar salt), 5.724% for (1 wt. % Fe_2O_3 + binary solar salt), and 1.515% for (0.1 wt. % Fe_2O_3 + binary solar salt).

The cooling process of salts and nanosalts has been studied. Nanosalts required a shorter time to discharge the energy. The cooling process was faster by 23 % for the case of 0.5 wt. % Fe_2O_3 + binary solar salt in comparison to binary solar salt alone without any additives.

Increasing the input temperature from 270 ^{0}C to 300 ^{0}C would result in a faster charging process. This could be due to the higher temperature differences between the inner hot pipe and the surrounded PCM (salts/nanosalts).

In the single nitrate salt, nanoparticles also showed positive improvements in both the charging and cooling processes. For instance, the charging process was shorter in the case of nanosalt (0.5 wt. % Fe_2O_3 + $NaNO_3$) by 19 % and the cooling process by 9.38 %

Most of the homogeneity measurements showed that most materials are homogenous with minimum temperature differences measurements at different theta locations.

All of these results demonstrate the advantages of nanosalt as a storage medium for future applications in solar thermal power plants.

Chapter 5 Computational Fluid Dynamics Simulations

5.1 Introduction

This chapter includes the full details of the simulation work using computational fluid dynamic software (CFD). The details of the geometry setup, mesh and the problem setup are investigated in this chapter. Furthermore, the enthalpy-porosity method is used to build a simulation code using ANSYS-CFX (version 17.0). The main reason for the CFD work is to compare with the experimental results and hence to assess the feasibility of using CFD as a design tool. Therefore a validation for the model is conducted.

5.2 Problem Setup (melting of phase change material)

The melting/solidification model is needed to simulate the phase change material (PCM). ANSYS-Fluent software has been used to solve the melting/solidification model by many researchers such as Shmueli et al. (2010), Gowreesunker et al. (2012), Bhaumik (2012), Muhammad et al. (2015a) and Hossain et al. (2015). On the other hand, we use ANSYS-CFX software (version 17.0) to solve this model for the PCM, because CFX has a flexible algebraic expression language that permits the user to define customised models, as discussed below. In our case, the PCM is represented by the binary solar salt ($NaNO_3$: KNO_3 with 60:40 molar ratio) or nanosalt (0.5 wt. % Fe_2O_3 + binary solar salt). CFX does not have a built in melting/solidification model. However, the expression language permits a customised model to be implemented that is straightforward to generalise to the case with nanoparticles in the nanosalt material.

The enthalpy porosity method is used to build the melting/solidification model in CFX. First of all, the heat transfer is governed by Equations (5-1 and 5-2) with two unknowns' variables (enthalpy, H and temperature, T) (Voller and Prakash, 1987).

Using Einstein's summation convention, the energy transport equation is given by (Voller and Prakash, 1987):

$$\frac{\partial}{\partial t}(\rho \mathrm{H}) + \frac{\partial}{\partial x_i}\left(\rho\, \mathrm{u}_i\, \mathrm{H} - \mathrm{k}\frac{\partial \mathrm{T}}{\partial x_i}\right) = \mathrm{S}$$ **Equation 5-1**

where ρ is density (kg/m^3), H is specific enthalpy (J/kg), u_i is the velocity (m/s), k is thermal conductivity (W/m. K), T is temperature (K), and S is the heat source and sink per unit volume (W/m^3).

The thermal equation of state is shown in Equation (5-2).

$$\mathrm{H} = \mathrm{f}\,(\mathrm{T}, \mathrm{P}, \beta)$$ **Equation 5-2**

where P is pressure (N/m^2), and β is the species mass fraction (dimensionless). The enthalpy method technique depends on the solution of Equation (5-1) and then obtaining the temperature values from the inversion of Equation (5-2).

There are three different cases which can be solved by this method. The first case is for pure substance (assuming single phase without phase change). Enthalpy is an increasing function of temperature only, as indicated in the schematic diagram in Figure (5-1). Therefore, temperature values can be found in the inversion of enthalpy values as shown in Equation (5-3).

$$\mathrm{T} = \mathrm{f}^{-1}(H)$$ **Equation 5-3**

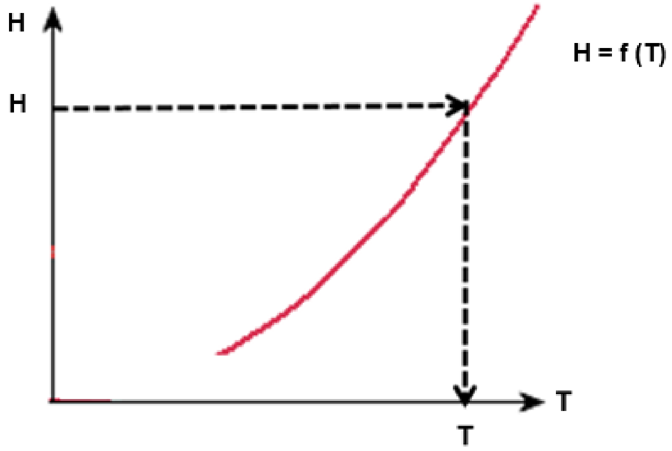

Figure 5-1 shows the schematic for enthalpy vs temperature of pure substance without phase change.

The second case is for a pure substance with a phase change process (melting/solidification process) occurring at a unique temperature point which is the melting point, as shown in Equation (5-4). The melting temperature is called the saturation temperature ($T_{sat.}$), at which point the enthalpy function $H = f(T)$ is discontinuous, as shown schematically in Figure (5-2).

$$H = \begin{Bmatrix} f_{sol}(T) & , & 0 \le T < T_{sat.} \\ f_{liq.}(T) & , & T_{sat} < T \\ H_{sat.,sol}\,\beta_{sol} + H_{sat.,liq}\,\beta_{liq}, & & T = T_{sat.} \end{Bmatrix}$$ **Equation 5-4**

where $H_{sat.,sol}$, $H_{sat.,liq}$ are the saturation enthalpies of the solid phase and liquid phase, respectively. $f_{sol}(T)$, $f_{liq.}(T)$ are the functions describing the solid and liquid phase enthalpies, respectively.

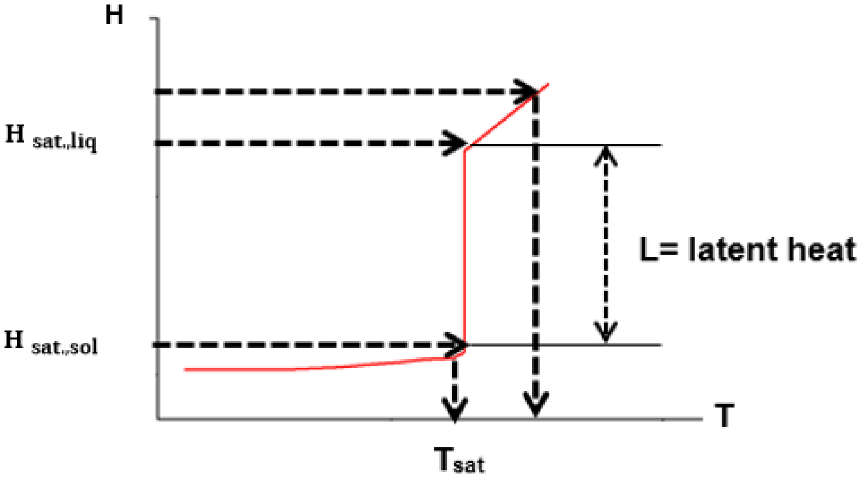

Figure 5-2 shows the schematic for enthalpy vs temperature of a pure substance with phase change at a single melting temperature (T_{sat}).

It can be noticed that when $T = T_{sat}$, the enthalpy varies linearly as a function of a solid phase mass fraction, from the saturated solid enthalpy ($H_{sat.,sol}$) to the saturated liquid enthalpy ($H_{sat.,liq}$). In this case, all three variables of temperature and solid and liquid mass fraction are obtained by the inversion of enthalpy (H), as shown in Equations (5-5, 5-6, and 5-7).

When (H < $H_{sat.,sol}$)

$$T = f_{sol}^{-1}(H), \qquad \beta_{sol} = 1,\ \beta_{liq} = 0$$ **Equation 5-5**

When ($\mathrm{H_{sat.,sol}} \leq H \leq \mathrm{H_{sat.,liq}}$)

$$T = \mathrm{T_{sat}},\ \beta_{\mathrm{liq}} = \frac{\mathrm{H - H_{sat.,sol}}}{\mathrm{L}},\ \beta_{\mathrm{sol}} = 1 - \beta_{\mathrm{liq}}$$ **Equation 5-6**

When (H > $\mathrm{H_{sat.,liq}}$)

$$T = f_{liq}^{-1}(H), \qquad \beta_{\mathrm{sol}} = 0,\ \beta_{\mathrm{liq}} = 1$$ **Equation 5-7**

$L = \mathrm{H_{sat.,liq}} - \mathrm{H_{sat.,sol}}$ represents the latent heat of melting (J/kg).

The third case occurs when the substance is a mixture with phase change taking place over a range of temperature $\mathrm{T_{sol}} \leq T \leq \mathrm{T_{liq}}$, $\mathrm{T_{sol}}$ is the solidus temperature and T_{liq} is the liquid temperature, as shown in the schematic in Figure (5-3). Additionally, Voller and Prakash (1987) described a simple linear enthalpy-temperature relationship in the mushy zone between the liquids and solidus temperatures as shown in Equation (5-3). On the other hand, (Prakash, 1990a; Prakash, 1990b) used a more advanced two-phase model in the mushy zone, and Prakash (1990a) provides more information about the thermodynamics in the mushy zone.

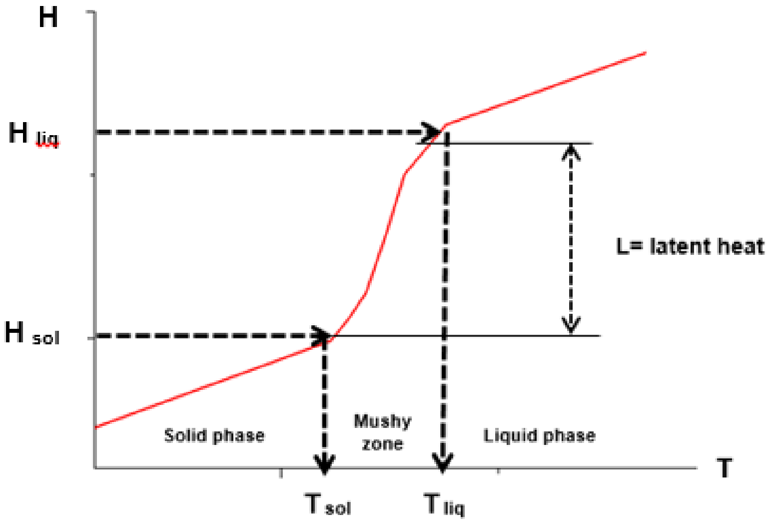

Figure 5-3 shows the schematic for enthalpy vs temperature of a binary mixture with a phase change at a range of melting temperatures (between $\mathrm{T_{sol}}$ and $\mathrm{T_{liq}}$).

In this case, Equation 5-6 is modified as follows:

When ($H_{\mathrm{sat.,sol}} \leq H \leq \mathrm{H}_{\mathrm{sat.,liq}}$)

$$\mathrm{T} = \beta_{\mathrm{sol}}\,\mathrm{T}_{\mathrm{sol}} + \beta_{\mathrm{liq}}\mathrm{T}_{\mathrm{liq}},\ \beta_{\mathrm{liq}} = \frac{\mathrm{H}-\mathrm{H}_{\mathrm{sat.,sol}}}{\mathrm{L}}, \beta_{\mathrm{sol}} = 1 - \beta_{\mathrm{liq}}$$ **Equation 5-8**

Hence, over the temperature range, $\mathrm{T}_{\mathrm{sol}} \leq T \leq \mathrm{T}_{\mathrm{liq}}$, both solid and liquid phases co-exist. This is called the mushy zone, and it is treated as a porous medium, with the porosity represented by the liquid fraction. The additional resistance to flow in the mushy zone is modelled using an additional source term in the momentum equation, as shown in Equation (5-9) (Mat et al., 2013). Equation (5-10) shows the continuity equation (Al-Abidi et al., 2013a), while Equation (5-11) shows the resistive source term (S) in the momentum equation.

$$\frac{\partial}{\partial \mathrm{t}}(\rho\,\vec{\mathrm{u}}) + \partial_i\,(\rho\,\mathrm{u}_i\,\vec{\mathrm{u}}) = \mu\,\partial_{ii}\vec{\mathrm{u}} - \nabla\,\mathrm{p} + \vec{\mathrm{S}}$$ **Equation 5-9**

$$\partial_{\mathrm{t}}\,\rho + \partial_{\mathrm{i}}(\rho\,\mathrm{u}_{\mathrm{i}}) = 0$$ **Equation 5-10**

$$\vec{\mathrm{S}} = -\mathrm{R}\vec{\mathrm{u}}$$ **Equation 5-11**

where R is the resistance coefficient (kg/ m^3.sec) as shown in Equation (5-12).

$$\mathrm{R} = \frac{(1-\beta)^2}{(\beta^3+\varepsilon)}\mathrm{K}^*$$ **Equation 5-12**

In Equation (5-9), ρ is density (kg/m^3), $\vec{u}$ is the fluid velocity, and $\vec{\mathrm{S}}$ is the source term which considers the resistive effects on the material in the mushy zone.

For the physics of the mushy zone, in solving the melting/solidification process with the fluid flow, it is necessary to ensure that flow becomes immobilised for the solid phase state. This is achieved by ensuring that the resistance term in the momentum Equation (5-9) becomes very large in the limit of a small liquid fraction, $R \gg 1$ as $\beta \to 0$. This is achieved using Equation (5-12), in which R value is a function of the porosity of the mushy zone. K* is the mushy zone constant. Additionally, in Equation (5-12), ε represents a constant with a small value (0.001) to avoid dividing by zero when the material is in the solid phase.

Additionally, the K* value is in range of (10^4-10^7 kg/ m^3.sec) (Muhammad et al., 2015a; Mat et al., 2013). Muhammad et al. (2015a) used K* value equal to 10^5 kg/ m^3.sec. However, we studied the effect of increasing or decreasing this value on the results. Different values of K* have been studied such as (10^4 kg/ m^3.sec, 10^5 kg/ m^3.sec, 10^6 kg/ m^3.sec). Full details will be mentioned in the results section. In addition, Kheirabadi and Groulx (2015) reported that the value of the mushy zone constant (K*) show a remarkable effect on the phase change solution. They concluded that higher value of K* leads to delaying the charging of PCM (Kheirabadi and Groulx, 2015).

Furthermore, the effect of Boussinesq buoyancy term is included in the PCM model. This is to study the effect of the natural convection during the phase change and in the liquid phase for the melting process. Additionally, the gravity force in equation (5-16) is calculated from Equations (5-13, 5-14 and 5-15)

$$\beta_{\mathrm{liq}=} = \min(\max\left(\frac{(\mathrm{T}-\mathrm{T}_{\mathrm{solidus}})}{(\mathrm{T}_{\mathrm{liquidus}}-\mathrm{T}_{\mathrm{solidus}})}, 0), 1\right)$$ **Equation 5-13**

$$\beta_{\mathrm{sol}} = 1 - \beta_{\mathrm{liq}}$$ **Equation 5-14**

$$\frac{1}{\rho_m} = \frac{\beta_{\mathrm{sol}}}{\rho_{sol}} + \frac{\beta_{\mathrm{liq}}}{\rho_{liq}}$$ **Equation 5-15**

$$\mathrm{Fz} = -(\rho_m - \rho_{ref})\ \mathrm{g}$$ **Equation 5-16**

where β_{liq} , β_{sol} are the liquid mass fraction and solid mass fraction, respectively. ρ_m, ρ_{sol}, ρ_{liq} represent the density of the mixture, solid phase and liquid phase, respectively.

The gravitational force in Equation (5-16) is added to the momentum Equation (5-9) to include the effect of the gravity on the results during the mushy zone.

After finishing the model setup in the CFX software, the customised melting/solidification model built in Ansys-CFX software is validated against the melting/solidification model in

Ansys-Fluent. We did this comparison study using the same geometry, the same mesh and the same problem setup in both of Ansys-CFX and Ansys-Fluent. Figures (5-8 and 5-9) indicate that there are negligible differences between the two softwares. This demonstrates that CFX code is correct to carry on with and it is ready to use for the heat transfer study of PCM.

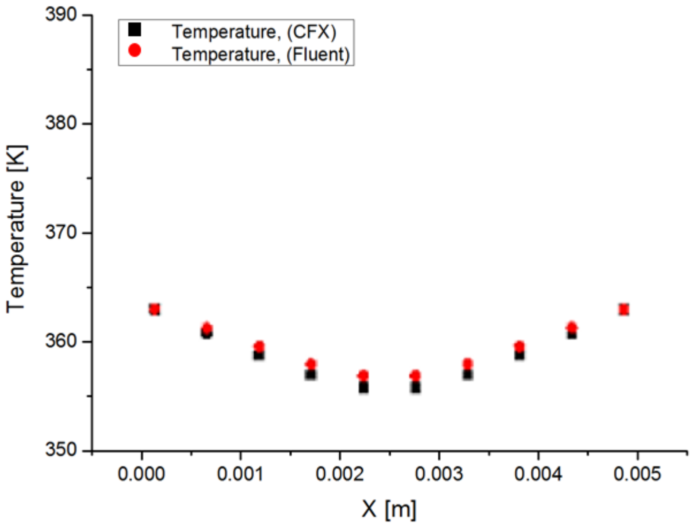

Figure 5-4 Shows temperature distributions data for both software Ansys-Fluent vs. Ansys-CFX data.

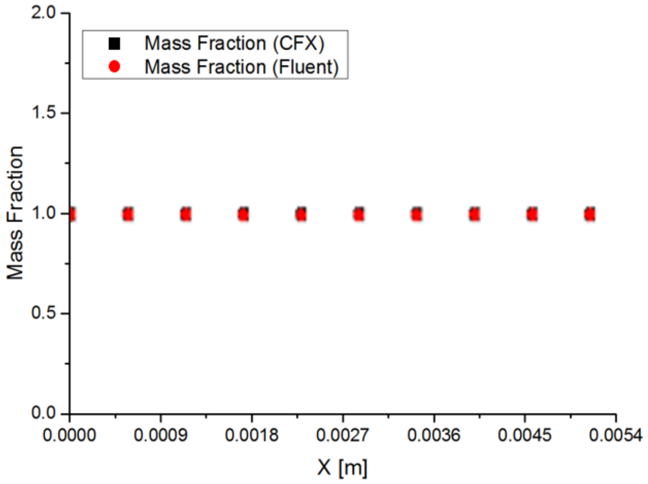

Figure 5-5 Shows liquid mass fraction data for both software Ansys-Fluent vs. Ansys-CFX data.

5.3 Geometry and mesh study

Firstly, Ansys workbench-design modeller (version 17.0) was used to build the 3-Dimensional model as shown in Figure (5-6). The geometry consists of two annular cylinders with a hollow pipe in the centre and a fluid located in the gap between the two pipes. The solid domain represents the outer wall with a finite thickness made from a stainless steel.

Furthermore, the dimensions are similar to our experimental rig. The dimensions of the large solid pipe are outer diameter 101.4 mm and thickness of 2 mm. The dimension of the fluid domain pipe is diameter 97.4 mm and at the centre, there is a hollow pipe with diameter of 25 mm. The lengths of both pipes are 300 mm with the z-direction as the axial direction. The material of the pipe is stainless steel for all walls such as the inner pipe wall, the outer pipe, thickness, top and bottom. The fluid domain contains the PCM which is salt or nanosalt. There is no inlet or outlet for this problem. Therefore, the top and bottom covers are assumed as wall boundary conditions with certain values of heat losses depending on the measurement of film temperature in the experiments and the full calculations for the values of heat transfer coefficient are discussed in detail later in section 5.5 of this chapter.

Secondly, the 3-D rig is meshed by ICEM (version 17.0), as shown in Figure (5-7). The mesh is of a hexahedral type as indicated by Figures (5-8 and 5-9). The quality of the mesh is measured by the aspect ratio which is the ratio between the length and height of the cell (Bakker, 2002). Figure (5-9) demonstrates that there are lowest values of the aspect ratio, these values are more related to the type of the mesh around the thickness of the solid domain pipe which was not hexahedral. More details about the mesh are given in section 5.6.

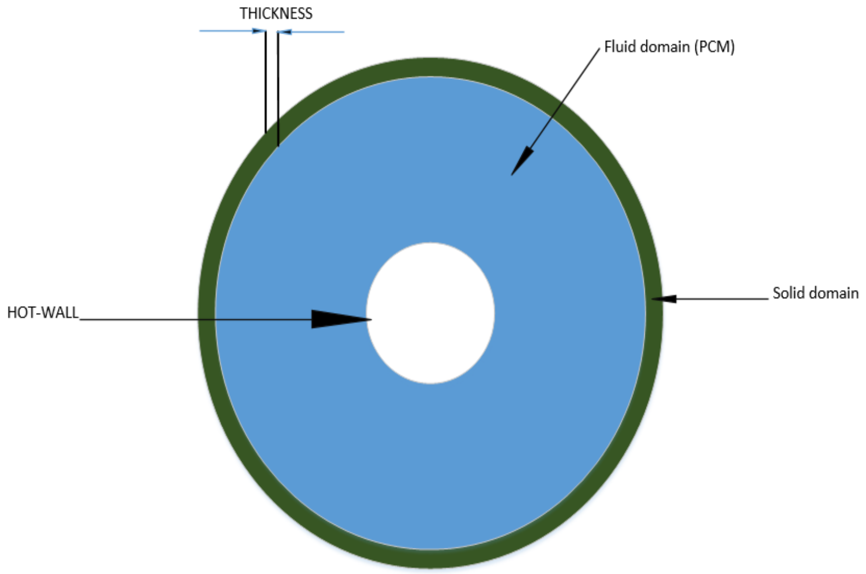

Top view

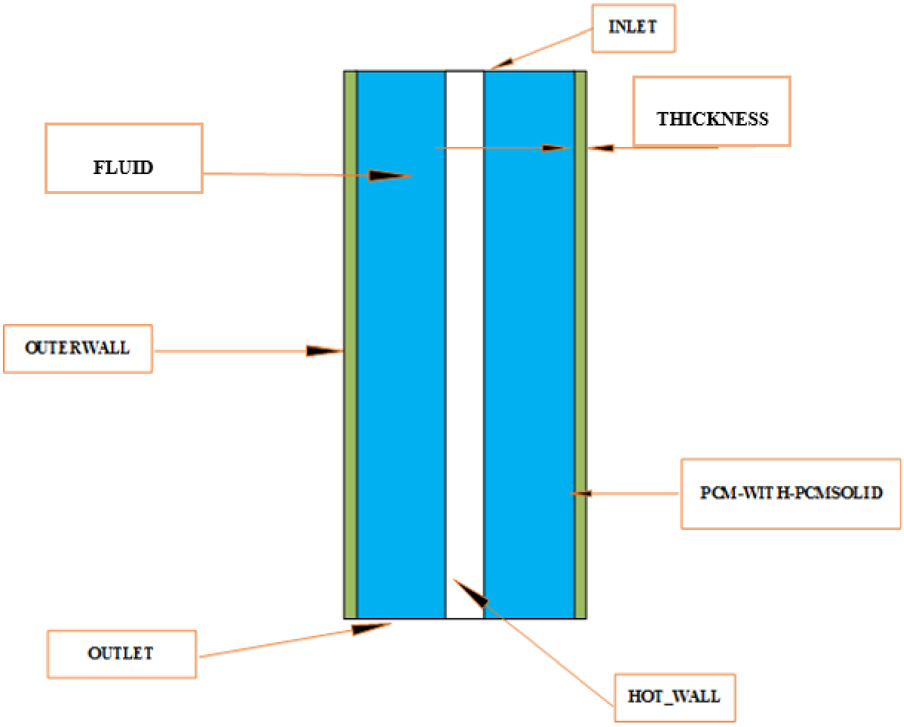

Side view

Figure 5-6 shows the side and top views for geometry boundary conditions.

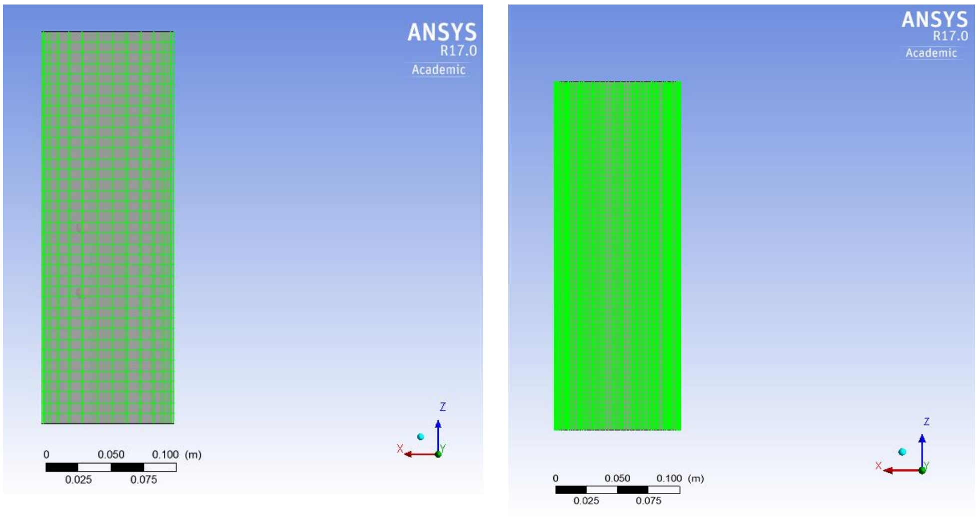

a- Side view

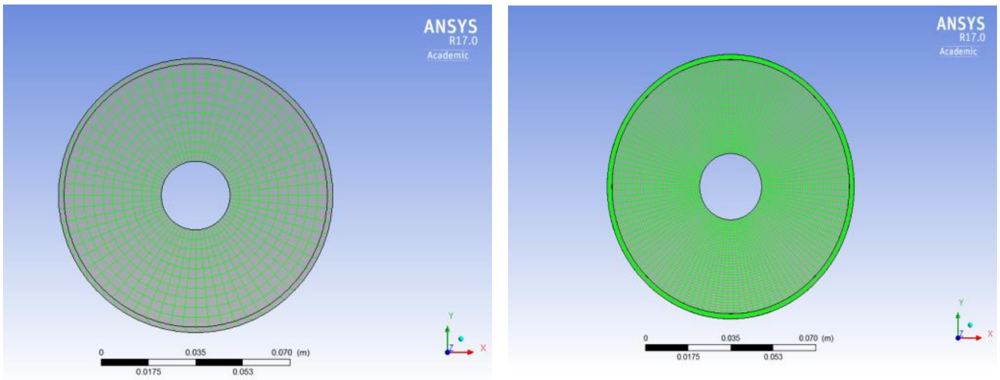

b- Top view

Figure 5-7 shows the Mesh dependent study with side view and top view. To the right is mesh number 1 and to the left mesh number 2.

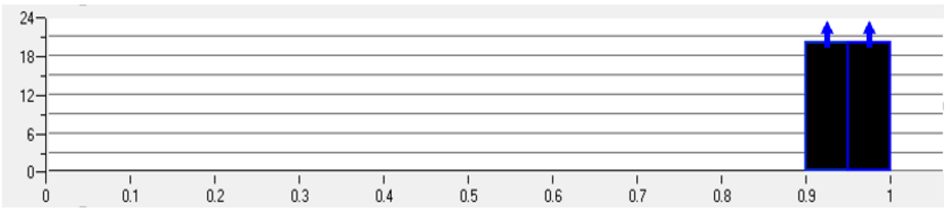

Figure 5-8 shows the quality of the mesh.

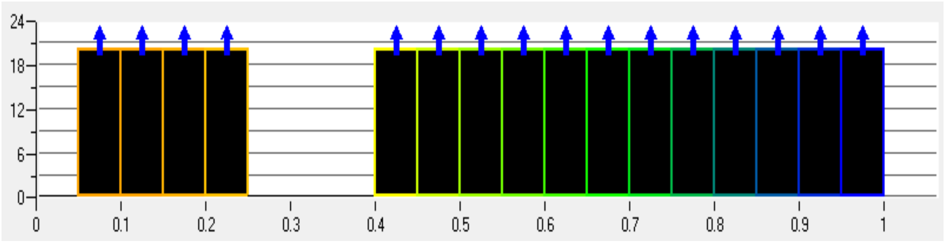

Figure 5-9 shows the aspect ratio of the mesh.

5.4 Thermophysical properties of PCM/nano-PCM

In order to obtain simulation data similar to the experimental data, we measured most of the thermophysical properties (Awad et al., 2018b). The measured thermophysical properties of PCM are specific heat capacity (cp), melting temperature, latent heat using dynamic scanning calorimeter device (DSC) and thermal conductivity (k) using laser flash analysis device (LFA).

According to Janz et al. (1972), the density of binary nitrate solar salt can be calculated as a function of temperature depending on Equation (5-17)

$$\rho_{\mathrm{salt}} = 2064.31 - (4.76248 \text{ x } 10^{-4} \text{ x } \mathrm{T}^2) - (3.36495 \text{ x } 10^{-7} \text{x } \mathrm{T}^2)$$ **Equation 5-17**

Equation (5-18) has been used to calculate the density of nanosalt (Vajjha et al., 2009)

$$\rho_{nanosalt} = (\varphi_{np} \text{ x } \rho_{np}) + ((1-\varphi_{np}) \text{ x } \rho_{salt})$$ **Equation 5-18**

All the units were in SI units with temperature (T) in Kelvin in Equation (5-17), and the unit of density (ρ) was kg/m^3. $\rho_{nanosalt}$, ρ_{np} and ρ_{salt} are the density of nanosalt, nanoparticles and solar salt in kg/m^3, respectively. φ_{np} is volume concentration of nanoparticles and it is dimensionless.

The specific heat capacity (cp) of the solid phase is different from the liquid phase of PCM (salt or nanosalt). The cp equations are conducted from material measurements in the DSC device as mentioned in Chapter (3).

For the case of binary solar salt, cp of the solid phase is shown in Equation (5-19) and for the liquid phase is in Equation (5-20)

$$\mathrm{cp} = 6.2 \text{ x } \mathrm{T} - 1410.5$$ **Equation 5-19**

$$\mathrm{cp} = \mathrm{T} + 784.4$$ **Equation 5-20**

For the case of nanosalt (0.5 wt. % Fe_2O_3 + binary solar salt), cp of solid and liquid phases are shown in Equations (5-21 and 5-22), respectively.

$$\mathrm{cp} = 7.2 \mathrm{~x~T} - 1695$$ **Equation 5-21**

$$\mathrm{cp} = 0.8 \mathrm{~x~T} + 893.6$$ **Equation 5-22**

In Equations (5-19, 5-20, 5-21 and 5-22), all the units were in SI units, T represents the temperature (in Kelvin unit) and cp is specific heat capacity (J/ g. K). Additionally, the latent heat, the melting temperature, liquids temperature and the solidus temperature are measured by the DSC device for the different materials (salt or nanosalt). Moreover, the liquids and solidus temperatures are measured using the DSC device and they were entered in the code to ensure a range of melting in the CFX code by using 220 ^{0}C for salt (for 0.5 wt. % Fe_2O_3 - nanosalt was 216.22 ^{0}C) as solidus temperature and 250 ^{0}C as liquids temperature of PCM. This is to simulate the third case of phase change with a range of melting temperatures.

For the thermal conductivity value, it has been measured using the LFA device (as mentioned earlier in detail in Chapter 3) and the average value of binary nitrate solar salt (or nanosalt) is considered in CFX code. Other properties (viscosity (0.0058 kg/m. sec) and expansion coefficient (0.047 K^{-1})) are assumed to be constant values and their values are obtained from (Janz et al., 1972; Pfleger et al., 2015b; Janz et al., 1979). Additionally, the model type was laminar.

5.5 Boundary Conditions

The full details of the physical model, geometry, and mesh have been mentioned earlier in this chapter. The boundary conditions were set carefully to consider as much as possible similar boundary conditions in the experimental rig. First of all, all the wall boundary are specified as no slip boundaries, i.e. velocity (u) =0. The boundary conditions for the setup are shown in Figure (5-10). In the solid domain, the thickness and the outer wall are assumed to be adiabatic walls because a thick insulation is already applied during the experimental setup (as explained in Chapters 4). The inner hot wall is to simulate the wall of the heat transfer fluid (HTF) where the constant heat flux boundary condition is applied similarly to the experimental work (constant heat flux from a cartridge heater). There is an interface between the two domains which is the interface between the solid domain wall and PCM fluid domain wall, as shown in Figure (5-10).

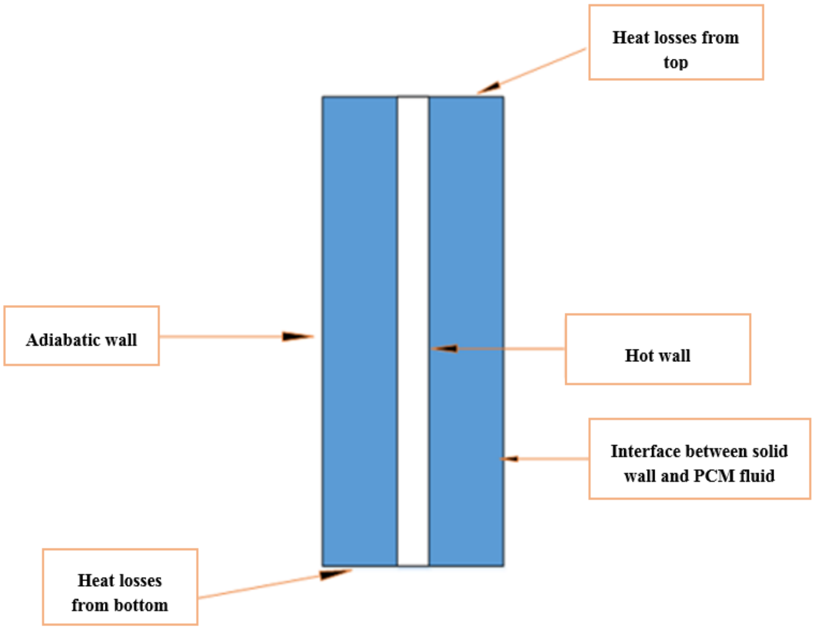

Figure 5-10 shows the boundary condition of the setup.

Additionally, the heat losses from the top and bottom covers are considered, using heat transfer coefficients based on correlations for natural convection from the outer surfaces as shown in Equation (5-23).

$$h = Nu.\frac{k}{L}$$ **Equation 5-23**

Nusselt number, Nu, is given by Equations (5-24 and 5-25) (Thirumaleshwar, 2009), and Rayleigh number, Ra, is given by Equation (5-26). These correlations are for convective heat transfer from surfaces. The range of Ra number in Equation (5-24) is 10^4 < Ra < 10^7 and for Equation (5-25) is 10^5 < Ra < 10^{11}.

Heat losses from top surface

$$Nu = 0.54\ Ra^{1/4}$$ **Equation 5-24**

Heat losses from bottom surface

$$Nu = 0.27\ Ra^{1/4}$$ **Equation 5-25**

$$\mathrm{Ra} = \frac{\rho^2 . g . \beta . (\ T_s - \ T_\infty)\ L_c{}^3}{\mu^2}\ \mathrm{Pr}$$ **Equation 5-26**

In Equation (5-26) material properties are evaluated at film temperature, which is the average values of the measured temperatures during the experiments with $T_f = \frac{T_s + \ T_\infty}{2}$. Where T_s is the surface temperature and T_∞ is the room temperature. L_c is the characteristic length which represents the surface (top or bottom) length. The heat transfer coefficient from the top cover was 8.53 W/ (m^2. K) while the heat transfer coefficient value from the bottom was 3.18 W/ (m^2. K).

Furthermore, the heating system has been controlled using a clipped heat flux. This control has been used to ensure the temperature does not get too large. This is considered by the built up the switch in the CFX code using probe measurement with the maximum input measurements.

In addition, the effect of time step on the results is studied by considering different values such as 0.5, 0.1, 0.05, 0.005 seconds. Decreasing the time step shows convergence in the results however it consumes more time for each case. A time step of 0.05 sec is selected for the results presented in this chapter where it shows a convergent behaviour.

5.6 Mesh independence study

A grid independence study is carried out in order to check the effect of a number of nodes on the results. Different meshes have been studied. The first mesh with the following information (Number of Nodes: 7942, Number of Elements: 5920). The number of nodes has been increased in the second mesh. This increase in the mesh nodes is to see the effects of the mesh refinement on the results. The finer mesh possessed 407680 nodes and 439632 elements, the specifications for each element parts are shown in Table (5-1).

Table 5-1 shows the number of elements for each boundary condition

Element boundary condition name	The number of elements	Element boundary condition name	The number of elements
FLUID (represents the PCM)	272136	PCM-WITH-PCMSOLID	25392
HOT-WALL (represents the inner pipe wall)	8236	SOLID (is the outer pipe thickness solid domain)	104328
INLET (is the top cover)	3944	THICKNESS (is the thickness)	4264
OUTLET (is the bottom cover)	3944	OUTERWALL (is the outer cover)	17388

The results from these two meshes did not show a big difference in term of temperature distributions vs time in Figure (5-11) and liquid fraction contours in Figure (5-12). As the differences are negligible, therefore, there was no need to use a finer mesh and consume more time for running. As a result, we depend on mesh number one (first mesh) for the results presented in this chapter. This is in similar to what was concluded by (Tay et al., 2015). According to them, if the PCM is static in the storage system then a small number of nodes should be enough to give an accurate data.

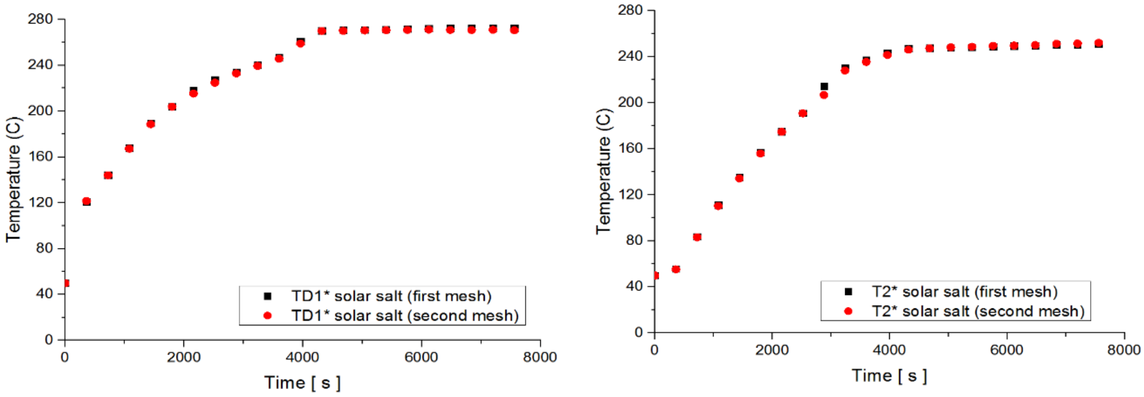

Figure 5-11 Temperatures distributions vs time for different mesh type, in the left is z=150 mm, and to the right z= 200 mm.

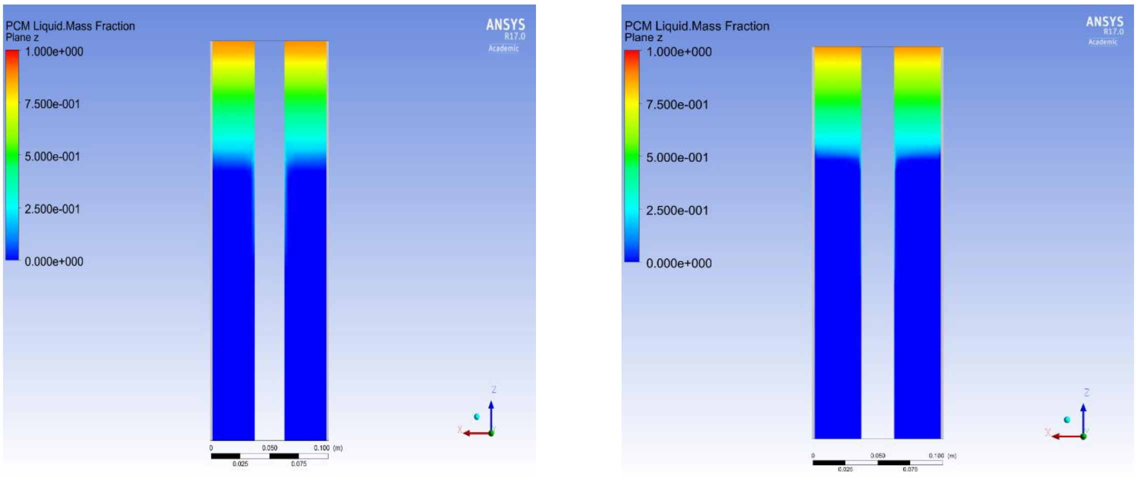

The liquid fraction at 30 min

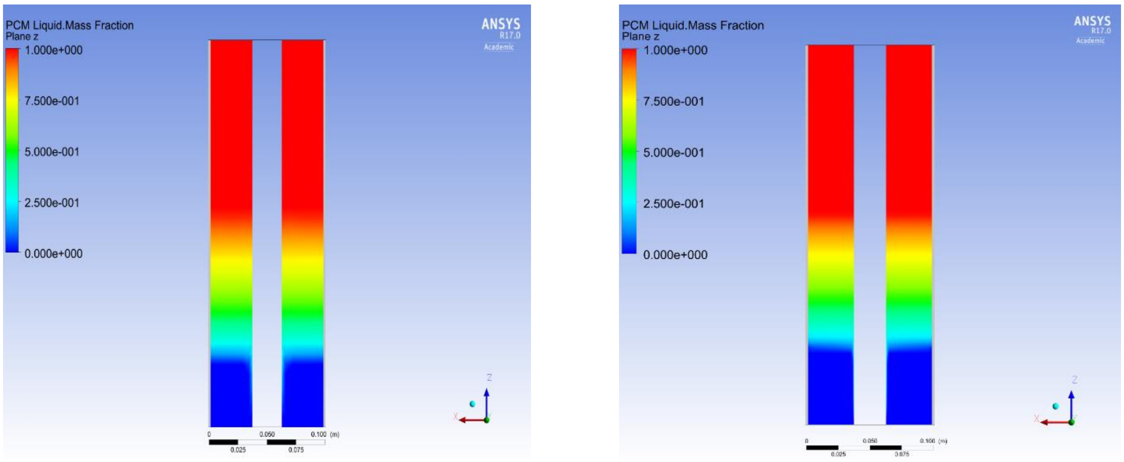

The liquid fraction at 60 min

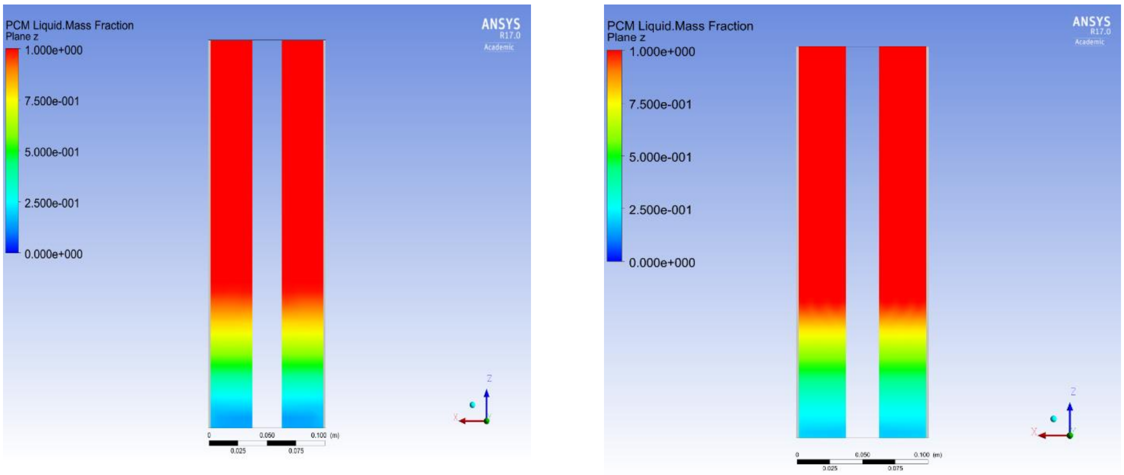

The liquid fraction at 90 min

Figure 5-12 liquid fraction for different mesh type at different times, in the right, is mesh number 1, and to the left mesh number 2.

5.7 Results and discussions

In order to understand the phase change process, CFD modelling is required. Because this charging process possesses a complex nature, numerical modelling helps to obtain the performance of the storage system.

First of all, we did a sensitivity study for the CFX code. This is to optimize the code by considering the effect of different parameters such as the modification of thermophysical properties or the mushy zone constant value. Additionally, this sensitivity study helps to improve the simulation results, reducing the difference between the simulation and the experimental data.

First and foremost, the sensitivity to the cp value is studied. The cp in CFX code is modified as shown in Equations (5-27 and 5-28) (for solid and liquid phases).

$$\text{Modified cp}_{\text{solid phase}} = \text{GS x cp}_{\text{solid phase}}$$ **Equation 5-27**

$$M\text{odified cp}_{\text{liquid phase}} = \text{GS x cp}_{\text{liquid phase}}$$ **Equation 5-28**

Where $\text{cp}_{\text{solid phase}}$ and $\text{cp}_{\text{liquid phase}}$ were calculated by Equations (5-19, 5-20, 5-21 and 5-22) for binary salt or nanosalt. GS is a constant factor, e.g. 0.5, 0.7, 1.2, 1.5, 1.6, 1.7 and 1.8.

It can be observed from Figure (5-13) that there was a large effect of the modified cp equation on the results. The optimum factor is 1.8, this factor decreases the differences between the simulation and experimental data.

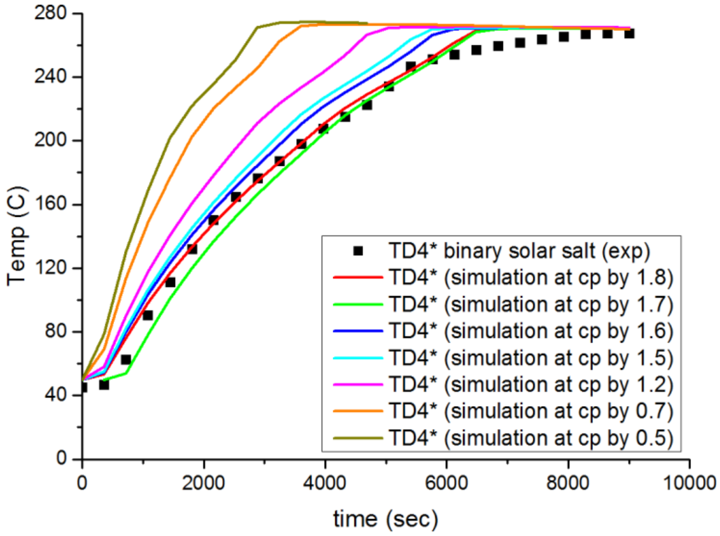

Figure 5-13 shows transient temperature (at radial direction TD4* and the axial direction of 150 mm) for the experimental vs simulation data of binary salt at different values of cp.

Similar behaviour was observed in the case of changing density as shown in Figure (5-14), where decreasing density values also showed the faster melting process and increased the difference between the simulation and the experimental data similar to decreasing cp behaviour. The factor of 1.8 showed approximately the same behaviour in case of changing the density (ρ) and keeping the cp constant without any changes or vice versa, as shown in Figure (5-15). This due to the higher sensitivity to the product of cp*ρ which depends on cp and ρ values as indicates by Equation (5-1), where in Equation (5-1) H=cp*T. It could be that the error of the experimental values of cp had an impact on this term due to the error measurements of cp which was around 2% and the equation used to calculated the ρ could be not accurate enough. The value of ρ is depended on the equation estimated by Janz et al. (1972), where their method used to estimate this equation may not be accurate enough in comparison with our experiments where density is highly affected by the condition such as temperature as shown in Equation (5-17). The condition or experimental setup they followed to calculate the density could show the effect on the accuracy of the calculated density values. These uncertainties caused these differences between the simulation and the experimental data before any modification carried out on either cp or ρ.

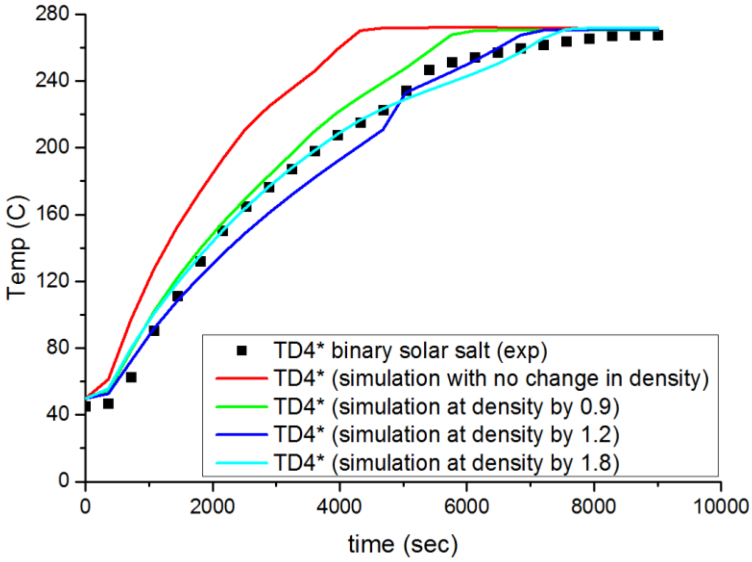

Figure 5-14 shows transient temperature (at radial direction TD4* and the axial direction of 150 mm) for the experimental vs simulation data of binary salt at different values of density.

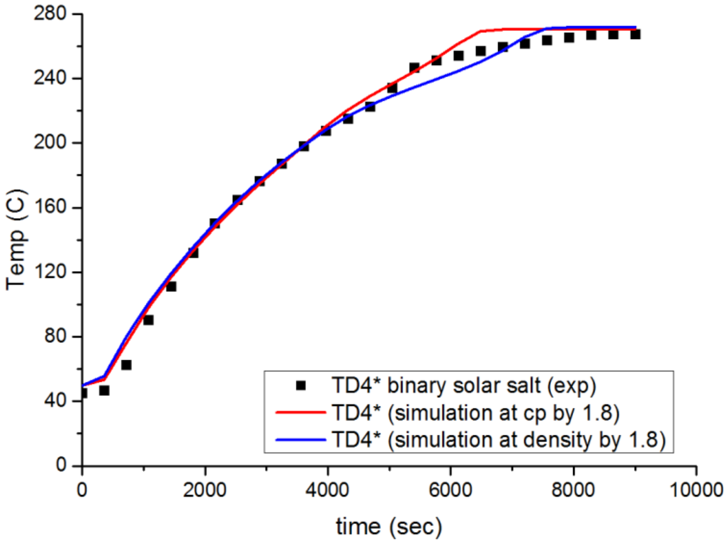

Figure 5-15 shows transient temperature (at radial direction TD4* and the axial direction of 150 mm) for the experimental vs simulation data of binary salt at both of cp and density multiplied by 1.8.

Moreover, the effect of modified latent heat is studied as well. The latent heat value measured by the DSC is modified as shown in Equation (5-29)

$$\text{Modified L} = \text{G x L}$$ **Equation 5-29**

Where L is latent heat and G is a constant value of 0.5, 0.7, 0.9 or 1.2. This is to study the effect of latent heat values on the code we built. Figure (5-16) indicates that modifying latent heat has little effect on the results where only small differences are concluded. Therefore, the same value of the measured latent heat is inserted in the code without any modification.

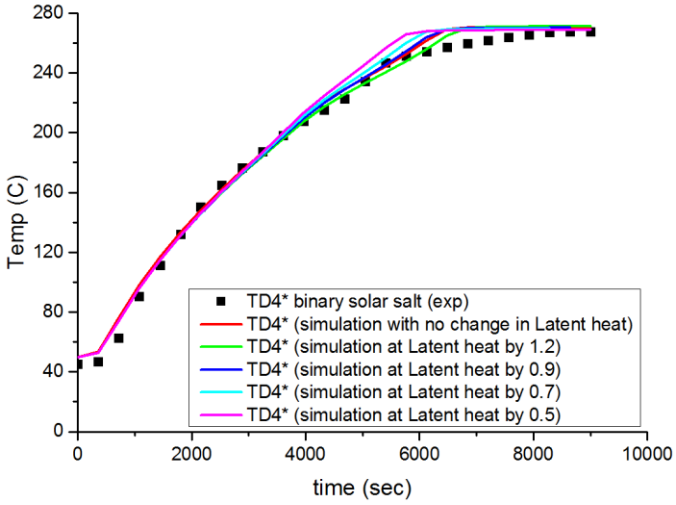

Figure 5-16 shows transient temperature (at radial direction (TD4*) and the axial direction of 150 mm) for the experimental vs simulation data of binary salt at different values of latent heat.

Furthermore, the effect of variations in thermal conductivity is studied using factors of 0.8, 1 and 1.2. Figure (5-17) demonstrates that increasing or decreasing k does not show differences between the experimental and simulation data. Therefore, the measured average value of k used in the code without any modification.

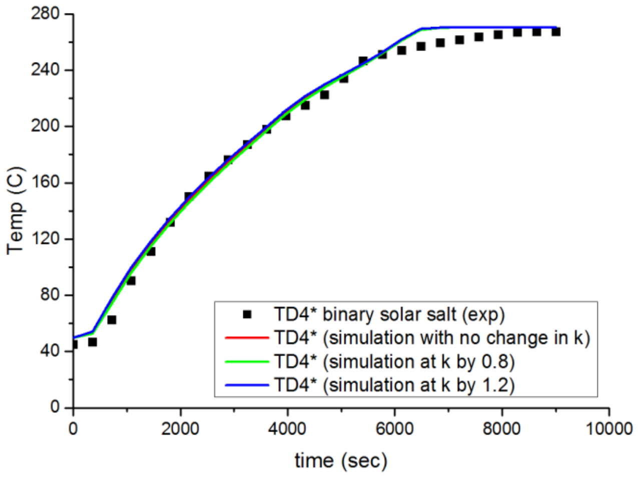

Figure 5-17 shows transient temperature (at radial direction (TD4*) and the axial direction of 150 mm) for the experimental vs simulation data of binary salt at different values of thermal conductivity.

K* represents the mushy zone constant in Equation (5-12). Three different values of K* were studied, i.e. (10^4 kg/ m^3.sec, 10^5 kg/ m^3.sec and 10^6 kg/ m^3.sec). The results of these three parameters are presented in Figures (5-18 and 5-19). Figure (5-18), K* values of (10^5 kg/ m^3.sec and 10^6 kg/ m^3.sec) show a big difference between the simulation and experimental data in comparison to K* value of (10^4 kg/ m^3.sec). Therefore, K* value of (10^4 kg/ m^3.sec) is selected for the data presented in this chapter. Additionally, there are other researchers who studied the sensitivity of K* on the melting behaviour such as (Kheirabadi and Groulx, 2015). They observed that a higher value of K* means slower melting. Because the higher value of K* leads to increase the resistance term that reduces the natural convection effect. Our result showed similar conclusion in cases 10^5 kg/ m^3.sec in comparison to 10^4 kg/ m^3.sec.

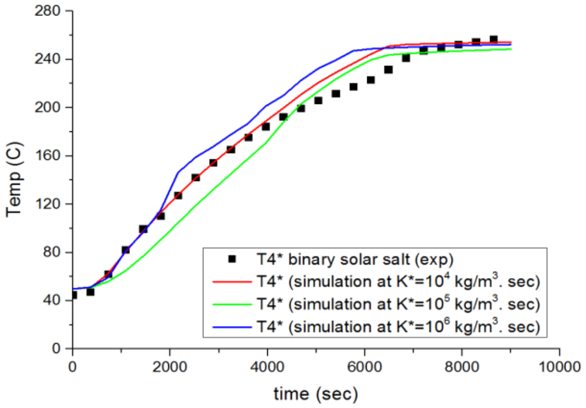

Figure 5-18 Shows transient temperature for the experimental vs simulation data of binary salt at different values of K* at Radial direction at T4* and axial direction z2=200 mm.

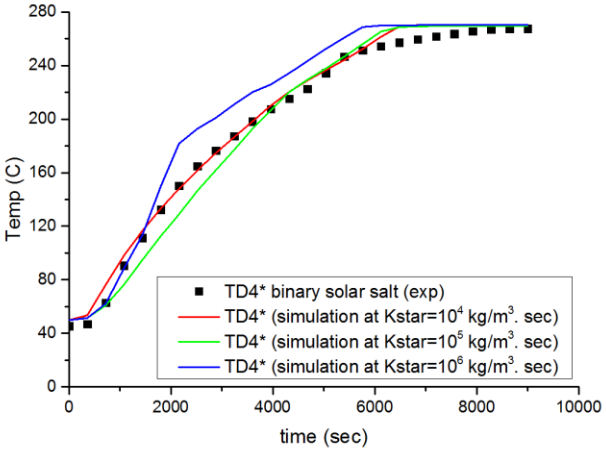

Figure 5-19 Shows transient temperature for the experimental vs simulation data of binary salt at different values of K* at Radial direction at TD4* and axial direction z1=150 mm.

In conclusion, the results presented in this chapter contains the following modification of cp by 1.8 for each phase separately. Other thermophysical properties kept same without any modifications such as k and latent heat. A mushy zone constant value of 10^4 kg/ m^3.sec is chosen as explained earlier.

In our code, we are trying to study the charging process of the PCM inside a storage system using the enthalpy porosity method. PCM is salt or nanosalt. In order to validate the CFX code, a comparison study between the experimental and simulation works are conducted. This comparison includes the temperatures measurements (at different radial/ axial directions) in both simulation and experimental. Additionally, Figure (5-20) shows the locations of thermocouples.

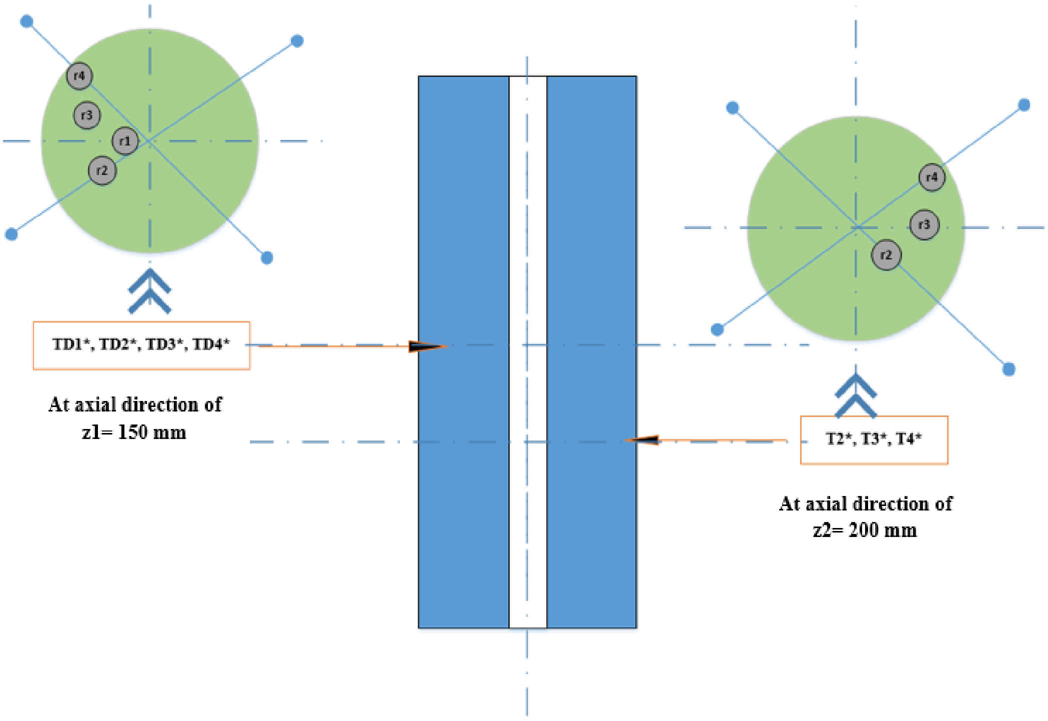

Figure 5-20 shows the locations of thermocouples at different radial/ axial directions. TD1*, TD2*, TD3* and TD4* are at the axial location of z1=150 mm and radial directions of r1, r2, r3 and r4 respectively. While, T2*, T3* and T4* are at the axial location of z2=200 mm and radial directions of r2, r3 and r4 respectively.

The experimental transient and the steady state temperatures in different locations (radial, theta, and axial directions) are studied and indicate the heat transfer effect by a different mechanism of conduction and convection during the charging process of PCM, as explained earlier in chapter 4. Furthermore, a comparison between the simulation and experimental data has been carried out for different PCMs (salt or nanosalt).

For the case of binary solar salt as PCM, the results are illustrated in Figures (5-21 to 5-27). Both the experimental and the simulation data are presented. Figures (5-21 to 5-27) show the transient temperature measurements at different radial directions (with a different axial direction of z1 and z2) for the binary solar salt.

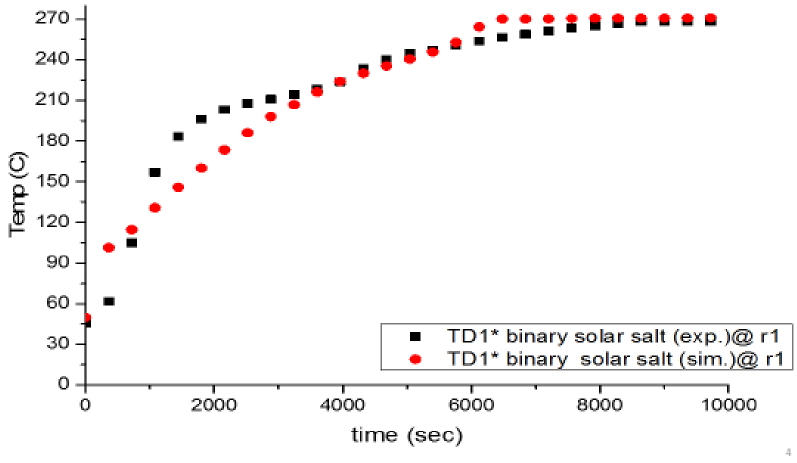

Figure 5-21 shows the transient temperature distribution (experiment vs simulation work) for the binary solar salt. At the axial direction of z1 (z1=150 mm) and radial direction of TD1* (locates at r1).

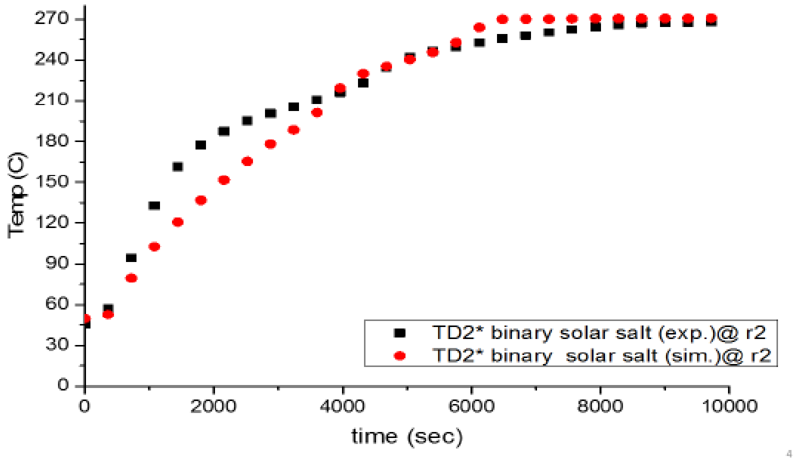

Figure 5-22 shows the transient temperature distribution (experiment vs simulation work) for the binary solar salt. At the axial direction of z1 (z1=150 mm) and radial direction of TD2* (locates at r2).

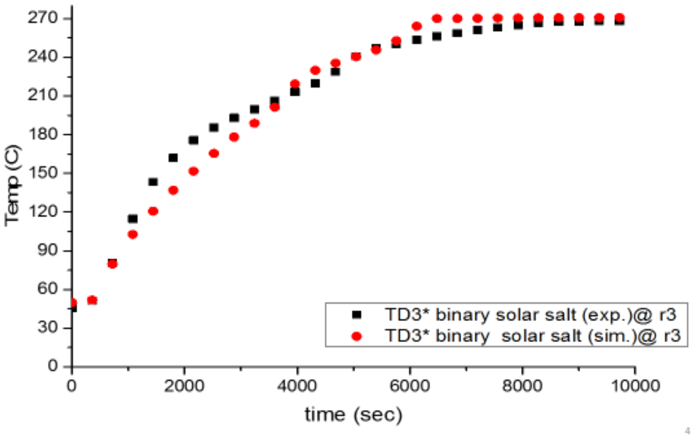

Figure 5-23 shows the transient temperature distribution (experiment vs simulation work) for the binary solar salt. At the axial direction of z1 (z1=150 mm) and radial direction of TD3* (locates at r3).

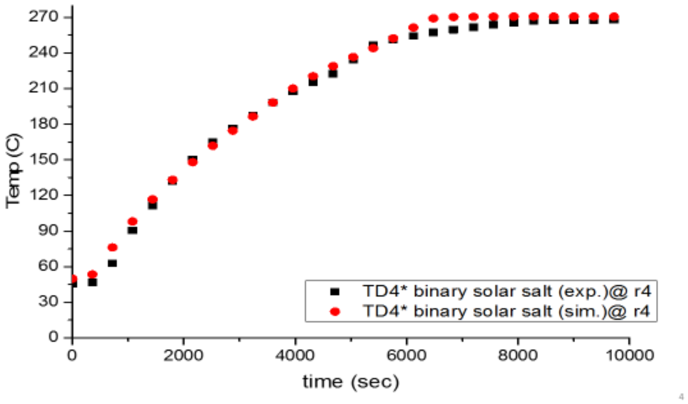

Figure 5-24 shows the transient temperature distribution (experiment vs simulation work) for the binary solar salt. At the axial direction of z1 (z1=150 mm) and radial direction of TD4* (locates at r4).

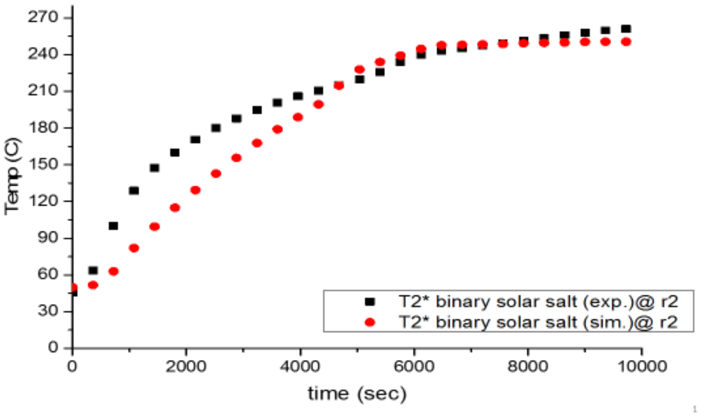

Figure 5-25 shows the transient temperature distribution (experiment vs simulation work) for the binary solar salt. At the axial direction of z2 (z2=200 mm) and radial direction of T2* (locates at r2).

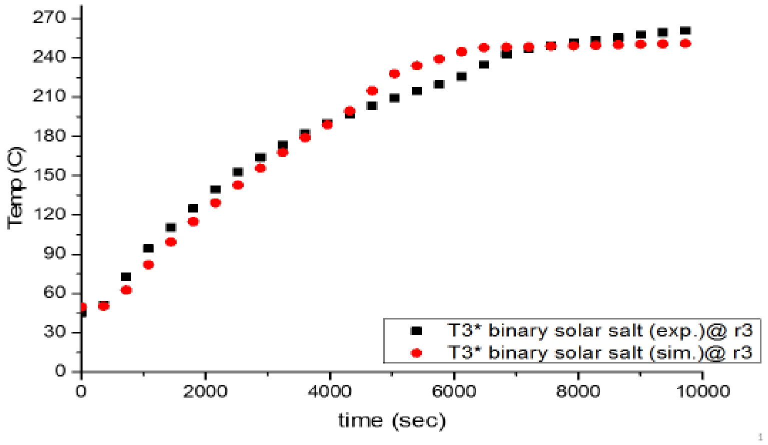

Figure 5-26 shows the transient temperature distribution (experiment vs simulation work) for the binary solar salt. At the axial direction of z2 (z2=200 mm) and radial direction of T3* (locates at r3).

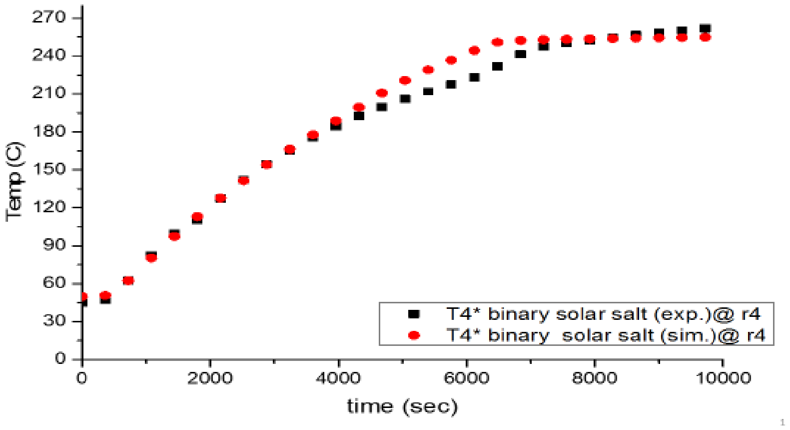

Figure 5-27 shows the transient temperature distribution (experiment vs simulation work) for the binary solar salt. At the axial direction of z2 (z2=200 mm) and radial direction of T4* (locates at r4).

In Figures (5-21 and 5-22), the differences between temperature measurements in the experiment and the simulation could be due to the fact that our model does not consider the effect of radiation which could have a higher effect during the experiments. Where higher heating observed by the salt experimentally due to diffusion of heat by radiation which is not considered in the simulation code. Therefore, it is noticeable that the experimental data shows higher temperature values than the simulated ones.

Additionally, far from heating source, there is a minimum difference between the simulation and the experiments as noticed by Figures (5-23 and 5-24). This indicates that, in the experiment, heat transferred through the salt would require larger time in order to melt and therefore minimum differences are present between the experiment and the simulation. This is because salt has a low value of thermal conductivity which lowered the heat transferred by the conduction mechanism. Furthermore, as soon as melt fraction is formed then the convection effect would affect the melting process and the mushy zone volume is enlarged which results in a liquid phase at the end when the temperature measurement exceeds the melting range.

Figures (5-25 and 5-26), the temperature measurements, in the solid domain, shows difference between the experiment and the simulation. In the experiment, the value of cp time's ρ could be higher than the one in the simulation. Furthermore, we assumed an average value for thermal conductivity in the simulation setup (as explained early, this average value depend on our measurement using LFA device) however, in the experimental, thermal conductivity is a function of temperature. As a result, thermal diffusivity could be higher in the case of the experiment. Figure (5-27) shows minimum differences between the simulation and the experiment during the phase change zone. This could be to some assumptions in the simulation that makes the phase change faster in comparison to the experiment. Overall, the differences between the experimental data and the simulation data are within an acceptable range. Similar to our results, Figure (5-28) indicates a comparison between the experiment and simulations work carried out by (Sciacovelli et al., 2013). They have differences between their experimental and simulation data which is similar to our case. However, the application of their PCM is for low temperature application.

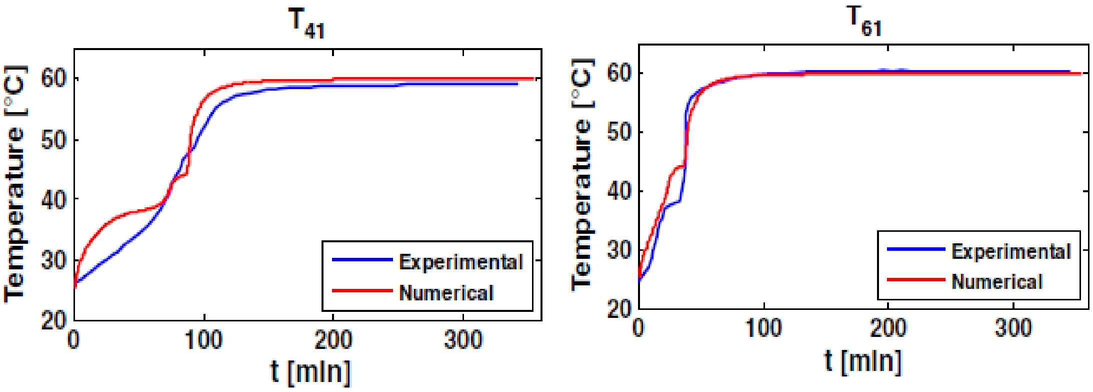

Figure 5-28 shows the transient temperature distribution by Sciacovelli et al. (2013).

In addition, Figures (5-21 to 5-27) demonstrate that at the beginning when the PCM is solid the dominant heat transfer is by conduction only and the simulation data in most thermocouples is less than the experimental data. As soon as the phase change starts, the simulation data of thermocouples readings are close enough or little higher than the experiments measurements. Muhammad et al. (2015b) demonstrated that at solid phase the simulation data are higher than the experiment data, as shown in Figure (5-29), which is opposite to our case. This is because they assumed the liquid density is the value of the density that is used throughout their model. However, in our case, we inserted the density as a function of temperature, therefore, it is not the same in solid or liquid phase. In addition, the melting temperature of their PCM is low and for a low temperature application Muhammad et al. (2015b). While our PCM is for high temperature application with melting temperature of around 220 ^{0}C.

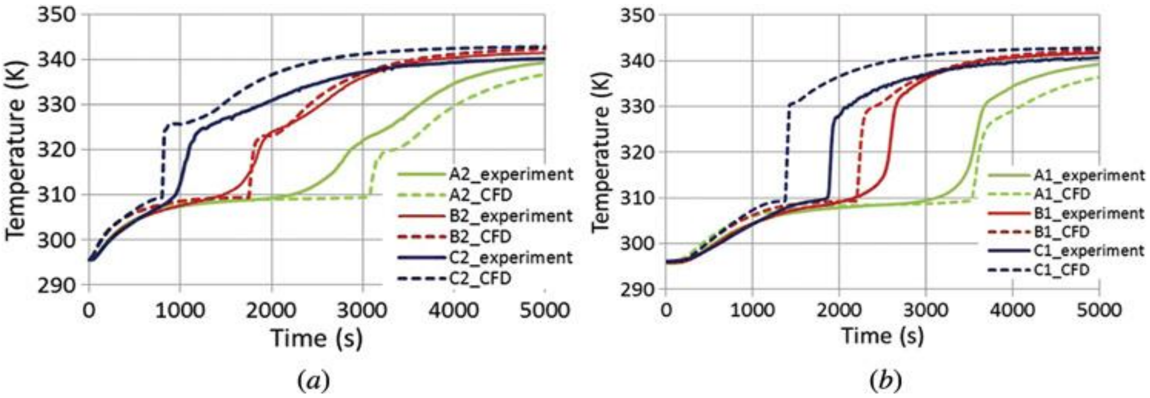

Figure 5-29 shows the transient temperature distribution (a) near to cylinder wall; (b) near the centreline by Muhammad et al. (2015b)

Figures (5-30 to 5-36) show the transient temperature distributions at different radial directions and different axial directions for nanosalt material. The differences could be due to the similar assumptions used for the case of binary solar salt. Furthermore, the material is not fully isotropic where the materials could be more conductive for the heat transfer from the inner hot pipe in some place than others. In addition, the nanosalt material has higher thermophysical properties due to the nanoscale nanoparticles that could enhance the overall properties of the nanosalt material such as k, cp, and latent heat. However, in the model we assumed an average value of thermal conductivity while in the real (the experimental work) any increases in conductivity would increase the diffusivity (as indicates by Equation 5-30 (Awad et al., 2018b)) and thus improve the amount of the heat transferred from the hot wall towards the material during the early stages of the charging process.

$$\text{Diffusivity} = \mathrm{k}/\,(\rho.\mathrm{cp})$$

Equation 5-30

In both materials (salt or nanosalt), the differences between the simulations data and experimental data are within an acceptable range.

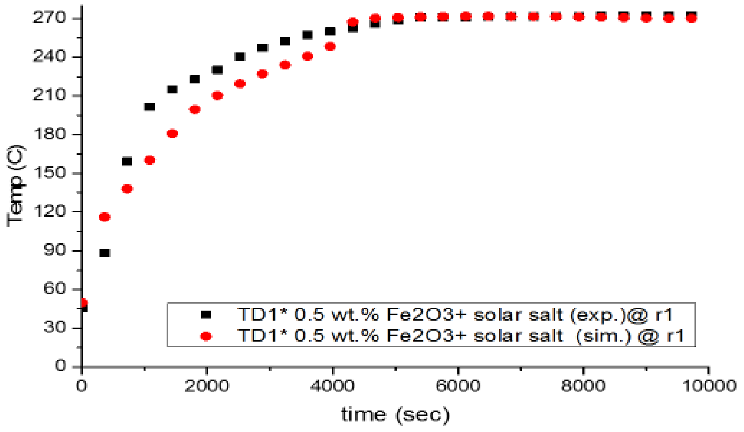

Figure 5-30 shows the transient temperature distribution (experiment vs simulation work) of nanosalt (0.5 wt. % Fe_2O_3+ binary solar salt). At the axial direction of z1 (z1=150 mm) and radial direction of TD1* (locates at r1).

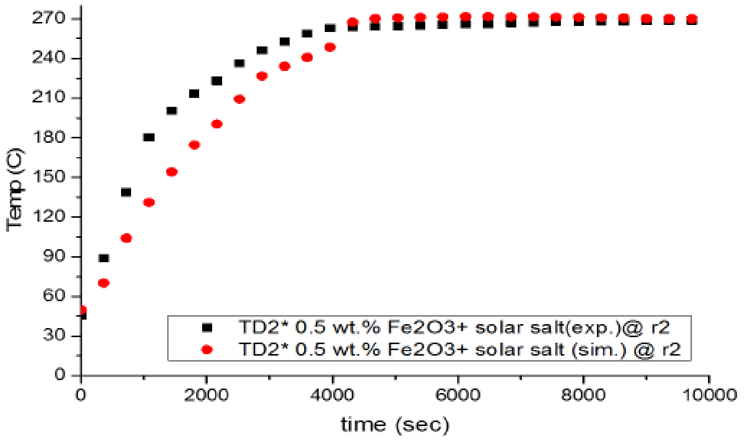

Figure 5-31 shows the transient temperature distribution (experiment vs simulation work) of nanosalt (0.5 wt. % Fe_2O_3+ binary solar salt). At the axial direction of z1 (z1=150 mm) and radial direction of TD2* (locates at r2).

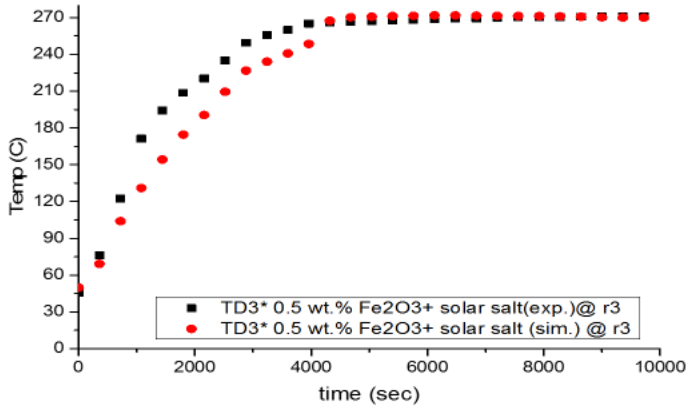

Figure 5-32 shows the transient temperature distribution (experiment vs simulation work) of nanosalt (0.5 wt. % Fe_2O_3+ binary solar salt). At the axial direction of z1 (z1=150 mm) and radial direction of TD3* (locates at r3).

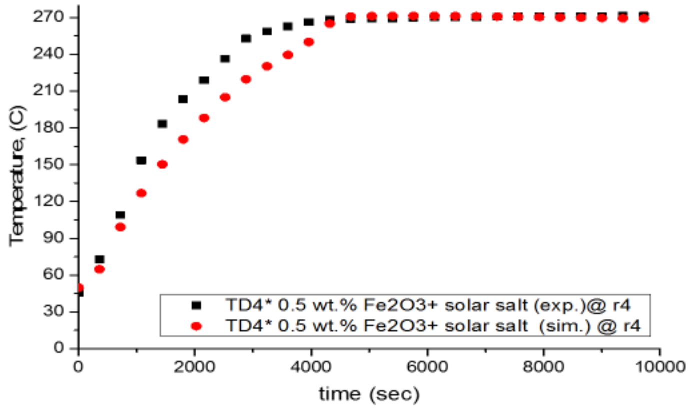

Figure 5-33 shows the transient temperature distribution (experiment vs simulation work) of nanosalt (0.5 wt. % Fe_2O_3+ binary solar salt). At the axial direction of z1 (z1=150 mm) and radial direction of TD4* (locates at r4).

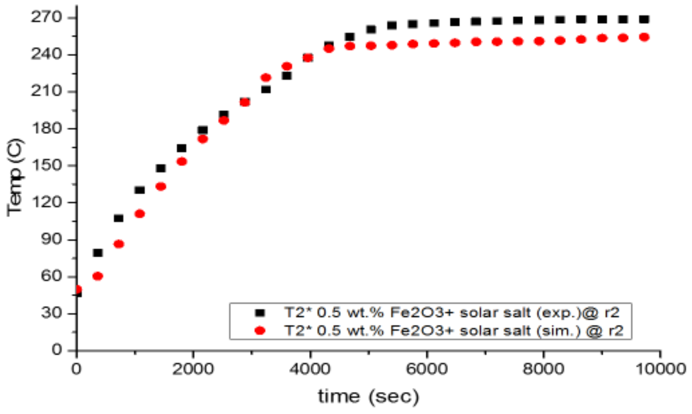

Figure 5-34 shows the transient temperature distribution (experiment vs simulation work) of nanosalt (0.5 wt. % Fe_2O_3+ binary solar salt). At the axial direction of z2 (z2=200 mm) and radial direction of T2* (locates at r2).

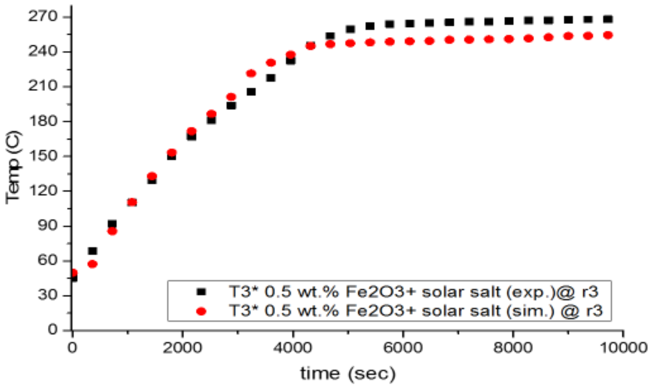

Figure 5-35 shows the transient temperature distribution (experiment vs simulation work) of nanosalt (0.5 wt. % Fe_2O_3+ binary solar salt). At the axial direction of z2 (z2=200 mm) and radial direction of T3* (locates at r3).

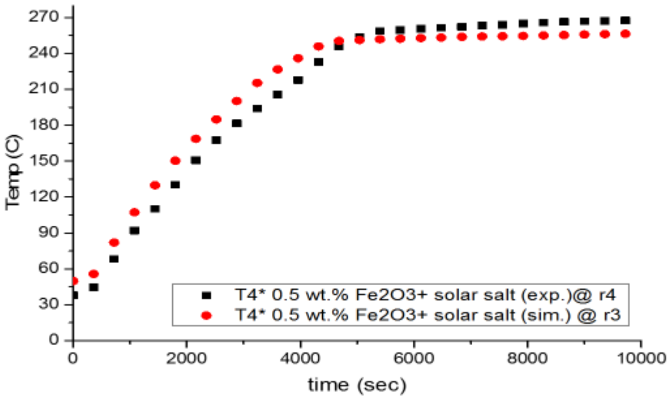

Figure 5-36 shows the transient temperature distribution (experiment vs simulation work) of nanosalt (0.5 wt. % Fe_2O_3+ binary solar salt). At the axial direction of z2 (z2=200 mm) and radial direction of T4* (locates at r4).

Figure (5-37) indicates that nanosalt is better than binary solar salt for both of the experimental and simulation data. At same radial and axial locations, nanosalt (0.5 wt. % Fe_2O_3 + binary solar salt) is melting faster than binary solar salt and this could be due to the higher thermophysical properties of nanosalt material.

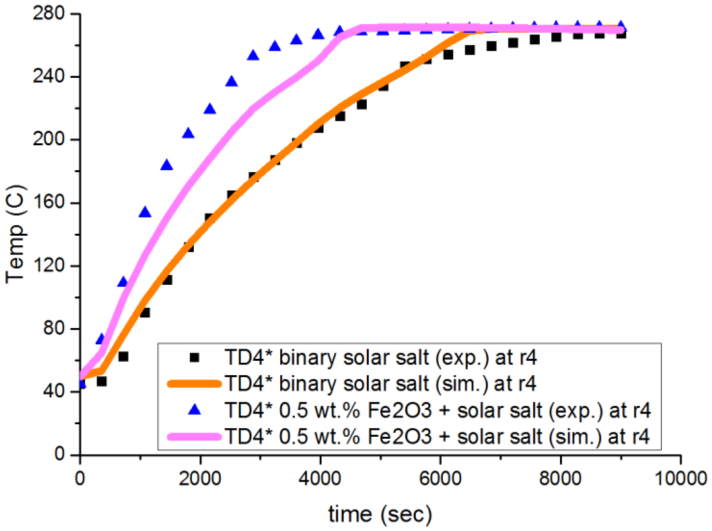

Figure 5-37 shows the experimental and simulation data of temperatures distributions vs time at the axial location of z1=150 mm. The materials are binary solar salt material and nanosalt (0.5 wt. % Fe_2O_3 + binary solar salt).

Furthermore, the thermocouple labelled T5* measures the temperature at a location far from the heater and deepest in the PCM material. This thermocouple (T5*) demonstrates the finishing of the melting process. As soon as the T5* temperature measurement reaches the melting temperature, the melting process is complete. Both of the experimental and simulation data show an acceptable match, as shown in Figure (5-38). However, the simulation data shows a faster increase in temperature than the experimental data and this could be due to the similar reasons mentioned above for the differences between the simulation and experimental work. Additionally, the simulation setup is more idealised than the experimental. During experiments, the material could be more or less sensitive to the heat transfer. Additionally, the mushy zone could be affected by the amount of heat transferred from the hot medium towards the PCM medium. Similarly, the nanosalt material shows a similar behaviour for both cases (experimental and simulation) and there is a little difference which is same as the case when the material is binary solar salt without any additives.

However, the nanosalt shows faster melting process than binary solar salt. Figure (5-38) indicates the big positive effect of nanosalt compared to base solar salt. The nanosalt has less melting time than the binary solar salt in both the experiment and simulation. This means that nanosalt has faster charging time, therefore, higher increments in the temperatures with a shorter time than the case of salt as the PCM.

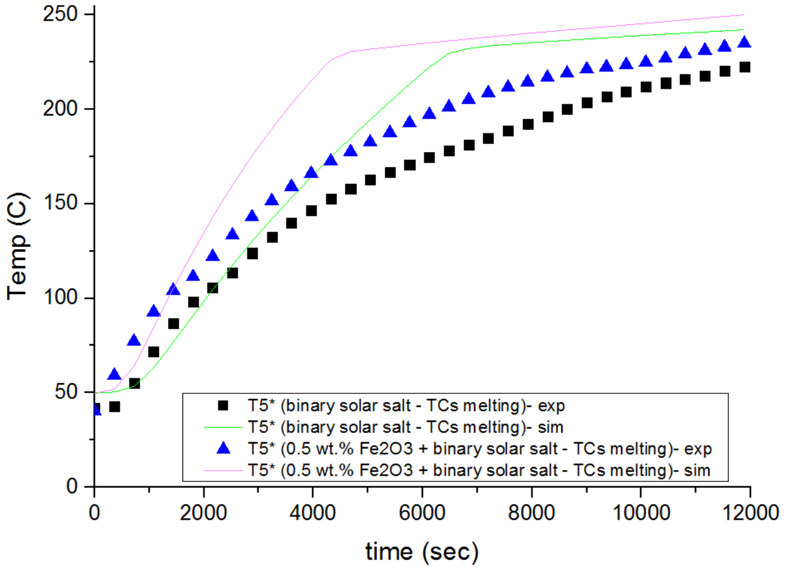

Figure 5-38 shows transient temperature for the experimental and simulation data of binary salt vs nanosalt (0.5 wt. % Fe_2O_3 + binary solar salt material).

Figure (5-39) demonstrates the liquid fraction comparison between binary solar salt and nanosalt (0.5 wt. % Fe_2O_3 + binary solar salt). From Figure (5-39), it can be observed in the liquid layer movement and the melting behaviour during the charging process. It is clearly shown that liquid layers moved faster in nanosalt than binary salt at the same time. For instance, the liquid layer of binary solar salt at 90 min is similar to the one by nanosalt at 60 min. In addition, nanosalt finished the charging earlier than the binary salt. This indicates a faster melting of nanosalt where higher thermophysical properties are possessed by this material.

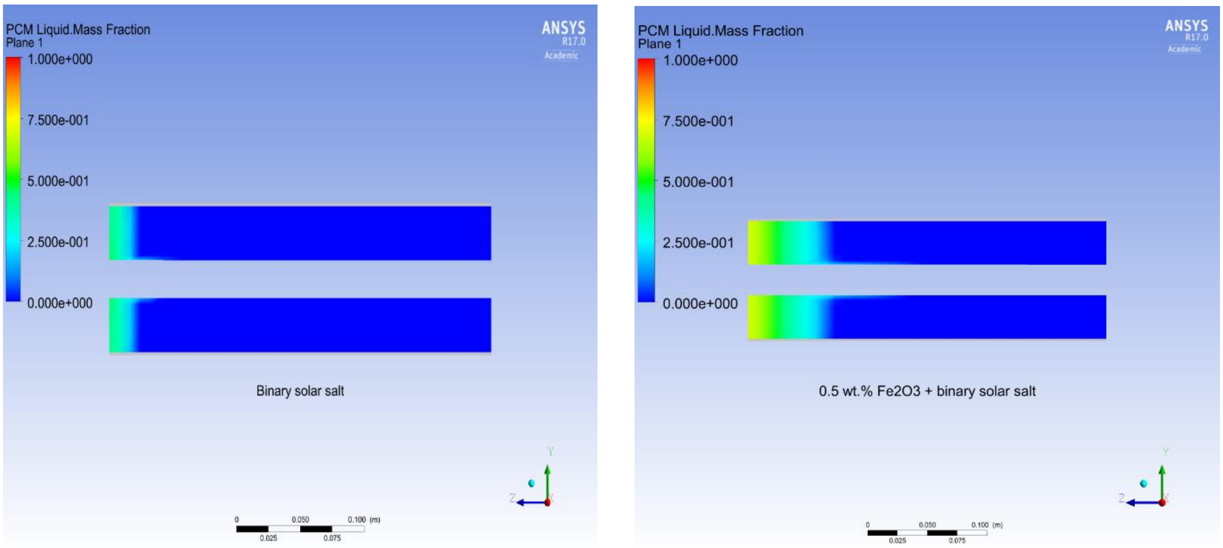

at 30 min.

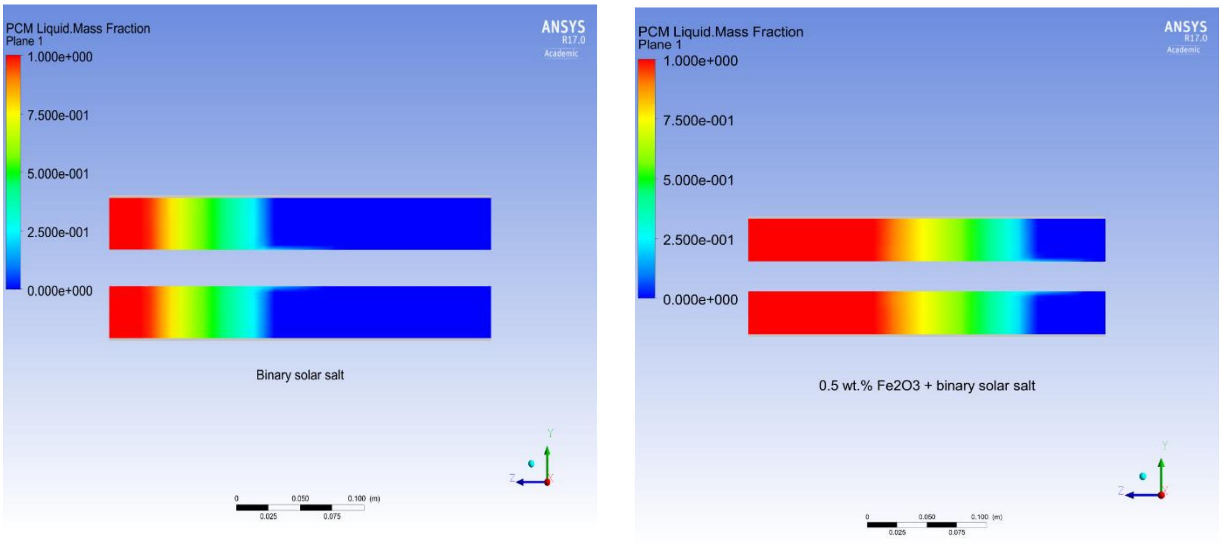

at 60 min.

(a) Liquid mass fraction contours of binary salt and nanosalt at 30 min. and 60 min

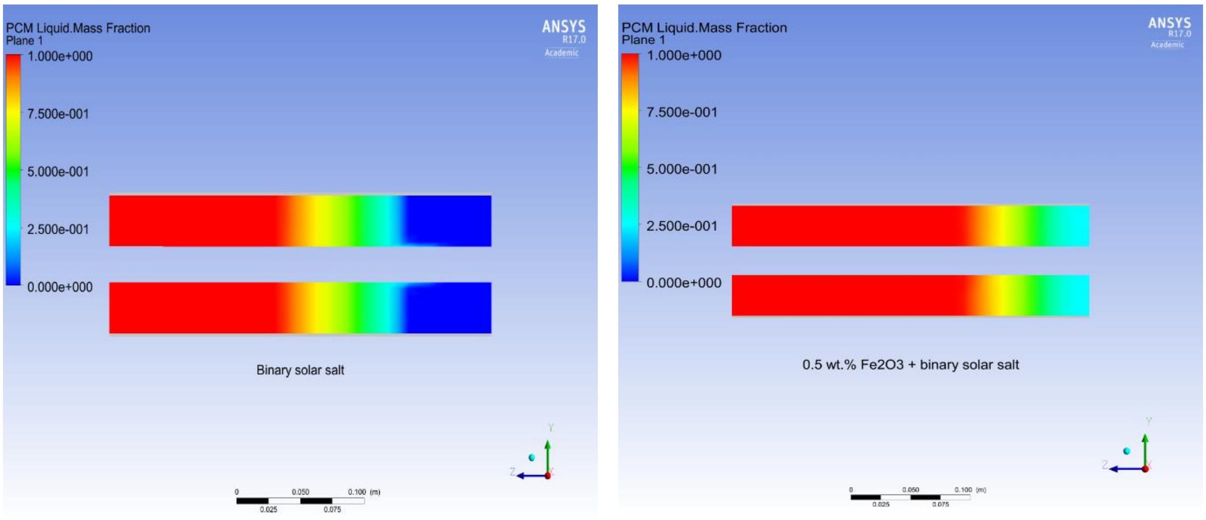

at 90 min.

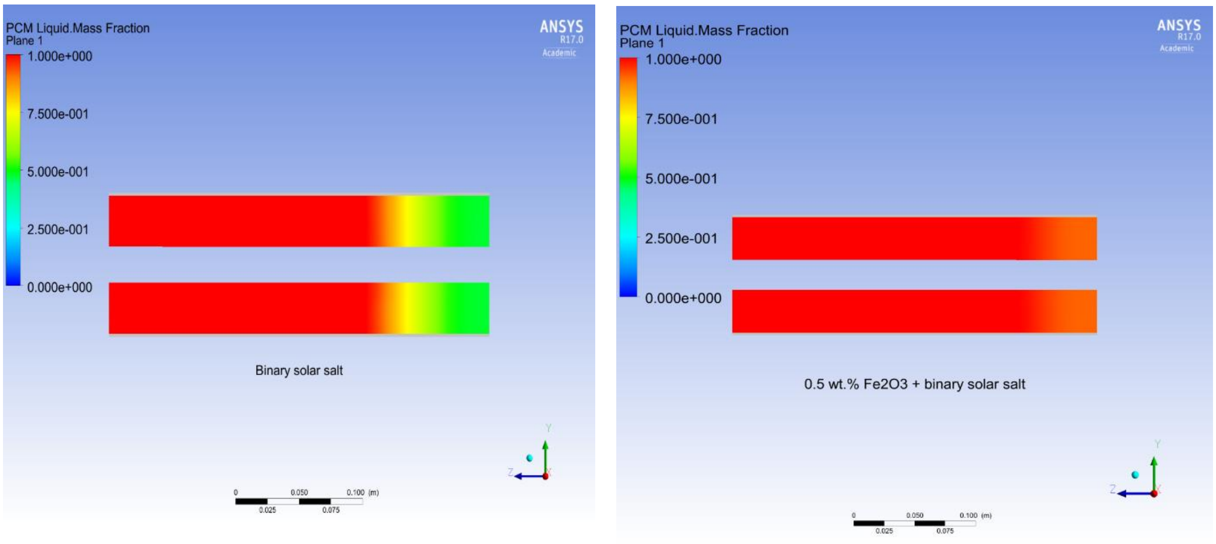

at 198 min.

(b) Liquid mass fraction contours of binary salt and nanosalt at 90 min. and 198 min

Figure 5-39 shows the liquid fraction of binary salt vs nanosalt (0.5 wt. % Fe_2O_3 + binary solar salt material) during different times.

On the temperature contour side, the effect of natural convection is very clear in Figure (5-40). The temperature distribution starts from the top and downward. Actually, the geometry is located vertically with gravity in the –z direction and the figures show this distribution of temperature along the z-direction.

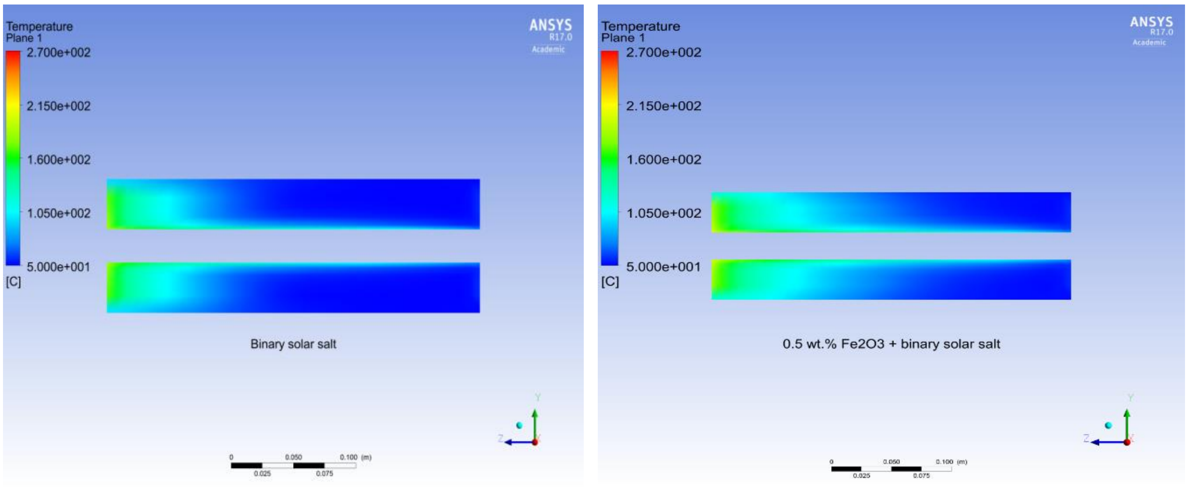

at 6 min.

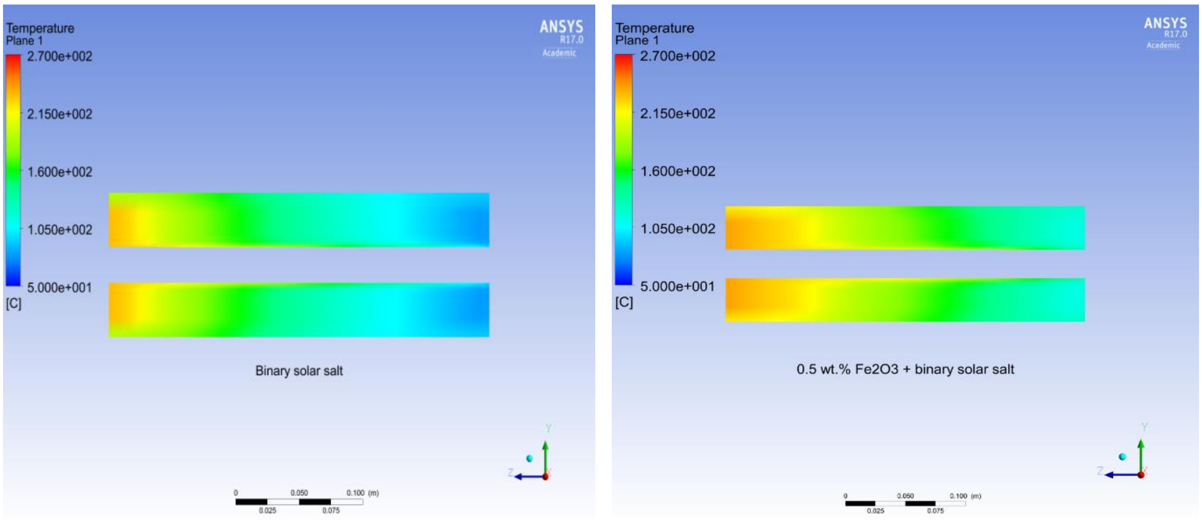

at 30 min.

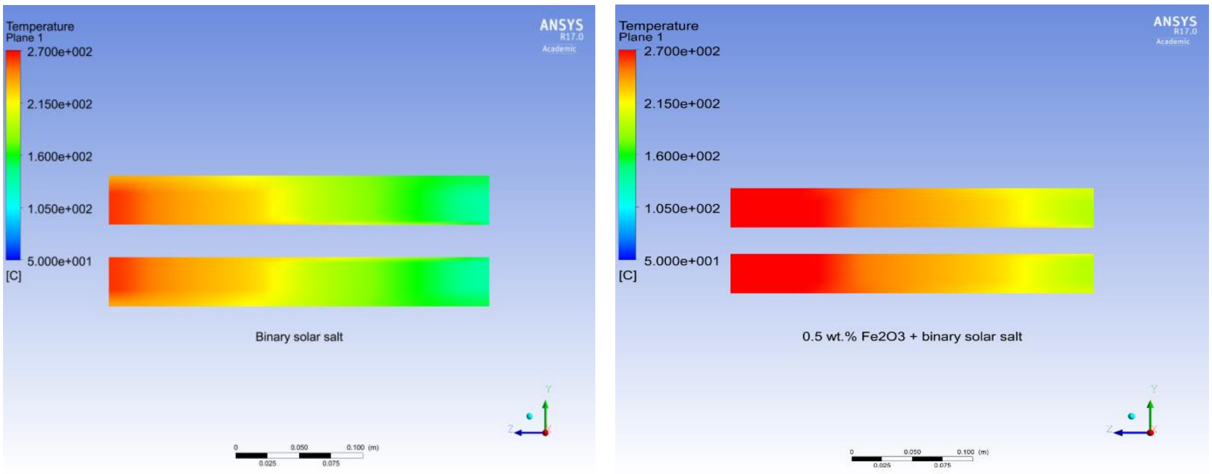

at 60 min.

(a) Temperature contours of binary salt and nanosalt at 6 min., 30 min., and 60 min.

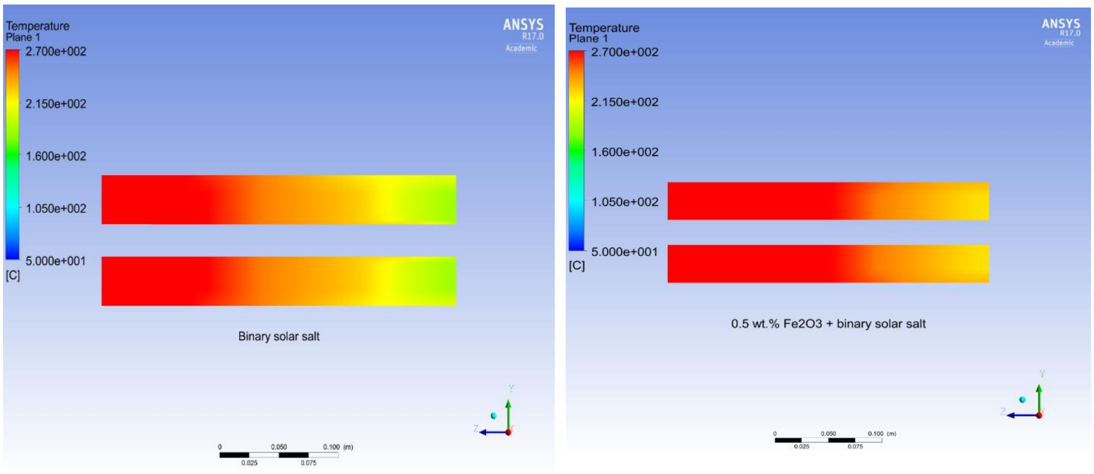

at 90 min.

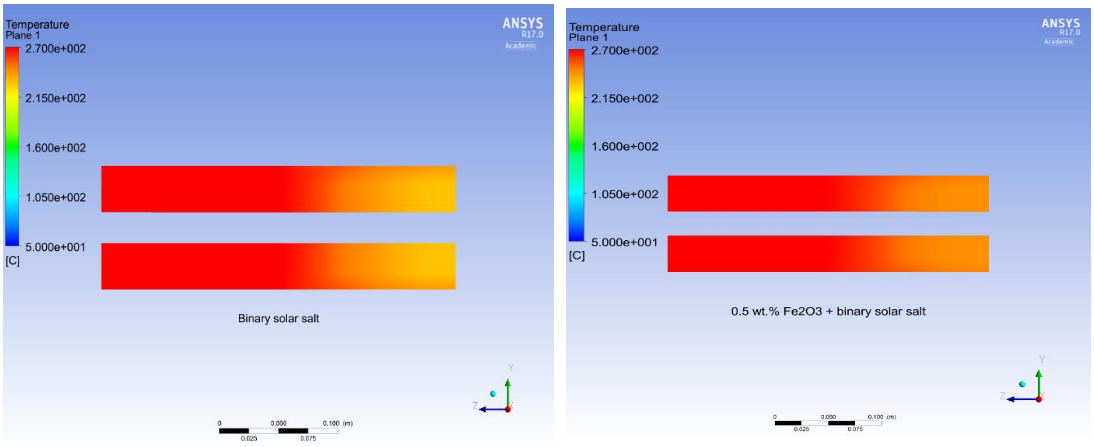

at 180 min.

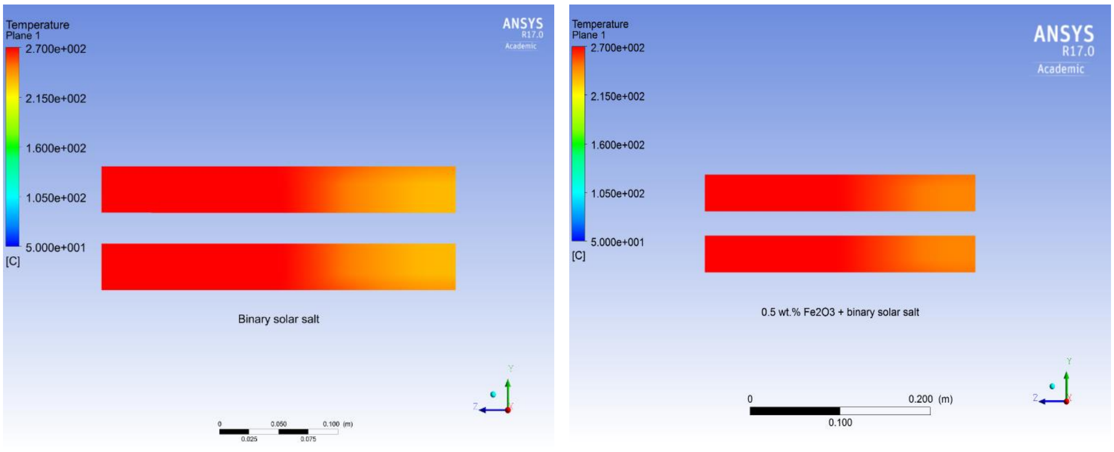

198 min.

(b) Temperature contours of binary salt and nanosalt at 90 min., 180 min., and 198 min.

Figure 5-40 shows temperature contours of binary salt vs nanosalt (0.5 wt. % Fe_2O_3 + binary solar salt material) during different times.

Natural convection in the nanosalt starts earlier due to the density differences between the solid and liquid phases where the lighter phase (liquid phase with low density) would flow up causing heat distribution from the top and downward. Further effect by the gravity is included by our code during the mushy zone which is clearly shown in Figure (5-40). It is observed that as time increases, the temperature will increase until the maximum input temperature is reached. However, nanosalt still has a higher temperature than the salt material. For instance, at time of 90 min, approximately more than half of the nanosalt material has a maximum input value of temperature (270 ^{0}C) while salt still has a lot of mushy zone areas. Muhammad et al. (2015a) showed similar behaviour to ours as demonstrated by Figure (5-41). They used Ansys-Fluent software for their simulation work while we used Ansys-CFX. However, they used different PCM ($NaNO_3$) while in our case it was binary solar salt ($NaNO_3$: KNO_3 with 60:40 molar ratio). Another difference between our work and theirs is the geometrical parameters where the diameter and length are different. All of these difference causes a difference in the results.

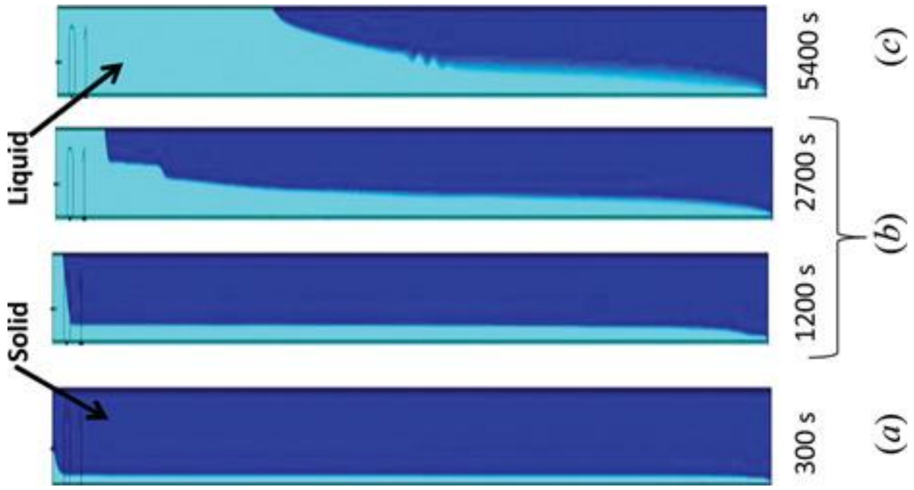

Figure 5-41 shows heat transfer of $NaNO_3$ during different times by (Muhammad et al., 2015a).

Figure (5-42) shows the liquid fraction behaviour for the nearest thermocouple (at radial direction of r1 and the axial direction of z1= 150 mm) to the hot medium for both of the binary solar salt and nanosalt. Figure (5-42) shows a fast conversion from the solid phase to the liquid phase because it near to the hot medium. Although the application of Esapour et al. (2016) is different, Esapour et al. (2016) showed a similar behaviour of liquid fraction vs time to ours, as shown in Figure (5-43).

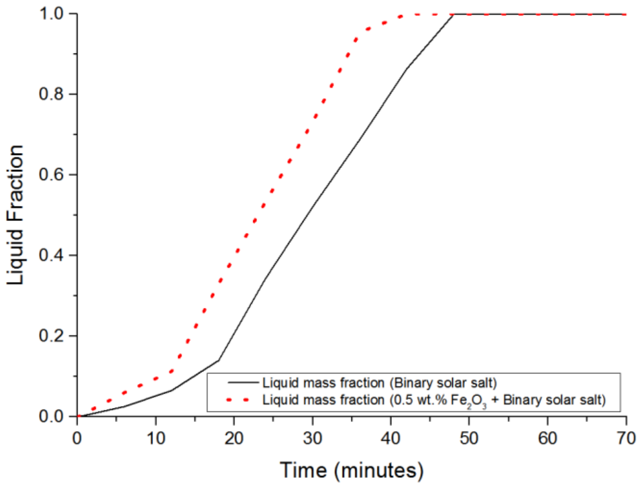

Figure 5-42 shows the liquid fraction of binary salt vs nanosalt (0.5 wt. % Fe_2O_3 + binary solar salt). This is liquid fraction measurement at the radial direction of r1 and an axial direction of z1.

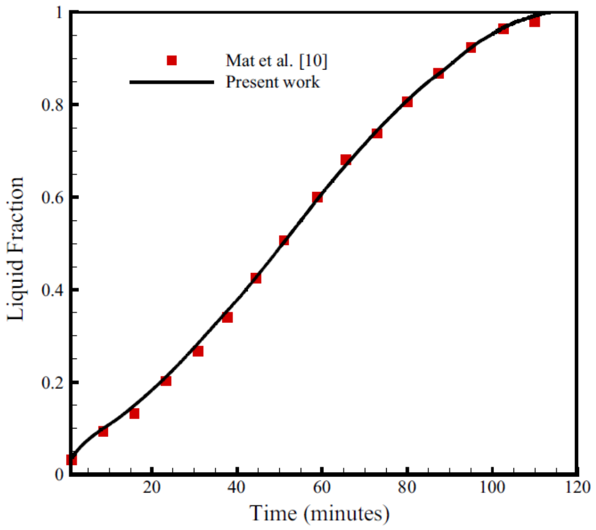

Figure 5-43 shows the liquid fraction vs time of RT35 as the PCM by (Esapour et al., 2016).

In addition, it seems that nanosalt (0.5 wt. % Fe_2O_3 + binary solar salt) shows a melting font in a shorter time than solar salt without any additives. Figure (5-42) confirms the positive effect of adding nanoparticles to the solar salt. An improvement in the liquid fraction of nano-PCM in comparison to PCM observed by (Pahamli et al., 2017), as shown in Figure (5-44). However, Figure (5-44) shows the result for a storage system that is located horizontally, which is not the same as in our case where the storage system was located vertically. Furthermore, Pahamli et al. (2017) studied large weight concentration's (2 wt.% and 4 wt.%), while in our case a small weight concentration of nanoparticles is used (0.5 wt.%).

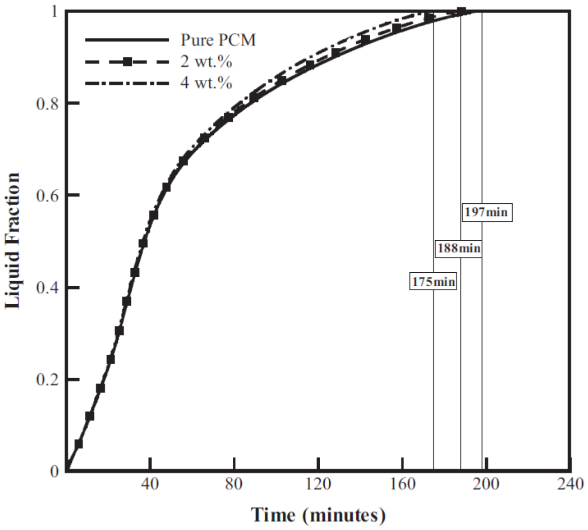

Figure 5-44 shows the liquid fraction of nano-PCM by (Pahamli et al., 2017). The storage system is located horizontally.

On the other hand, Pahamli et al. (2017) considered the effect of the vertical, inclined or horizontal storage system. They reported that the vertical storage system is the best one in term of less charging time, as shown in Figure (5-45). This confirms the benefits for our case where the storage system located vertically.

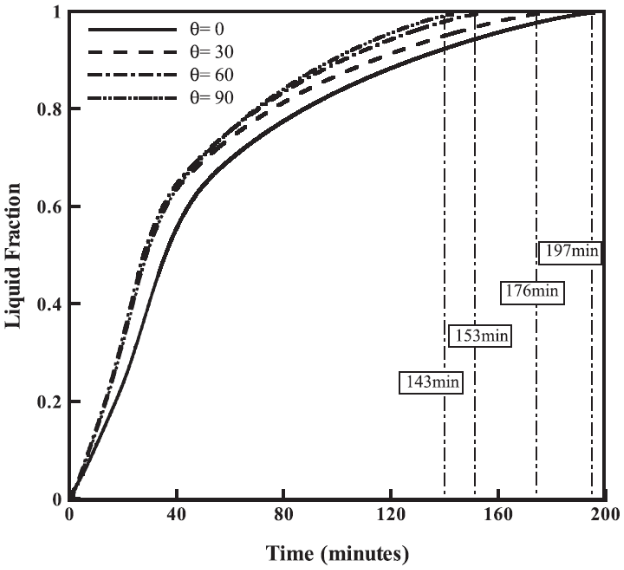

Figure 5-45 shows the liquid fraction of PCM by (Pahamli et al., 2017). The storage system is located horizontally (ϴ=0), inclined by (ϴ=30 or 60) and vertically (ϴ=90).

5.8 Conclusion

For the first time, a validation for an experimental rig, which is designed and built to study heat transfer of salt/nanosalt up to 270 ^{0}C, is conducted using ANSYS CFX software. A melting model is built in the CFX software to meet the similar requirements of our experimental work. The enthalpy porosity method has been implemented in the CFX code to model the melting of the PCM. First of all, the enthalpy porosity model built in CFX was compared with the one in Fluent and a good agreement was obtained. The charging process is simulated for binary nitrate salt ($NaNO_3$: KNO_3 with 60:40 molar ratio) and nanosalt (0.5 wt. % Fe_2O_3 + binary nitrate salt).

The model in CFX has been validated against our experimental data. Temperature measurements at similar locations in the experimental rig and in the CFX model geometry are compared including a different radial or axial locations.

The differences between the experimental data and the simulation have been reduced by a sensitivity study which is considered for different parameters. The effect of many parameters is considered during this study such as the mushy zone constant values (K*), thermophysical properties parameters, mesh study and different time steps. For instance, a sensitivity study has been conducted over cp, ρ, k, latent heat, and K*. It is important to use the correct measured physical properties in order to get a good prediction and the cp time's ρ seems to be the most effective parameter. Where changing the cp value and keeping ρ constant would show a similar effect of changing ρ and leave cp constant. This is more likely to the accuracy of the ρ value which was not measured by us and it was calculated from a reference. It is more likely that ρ is highly affected by the temperatures during the experiments. Additionally, the effects of k or latent heat did not show big change on the results.

Furthermore, three different values of K* have been studied which are 10^4 kg/ m^3.sec, 10^5 kg/ m^3.sec, and 10^6 kg/ m^3.sec. The results of K* showed that it is difficult to get very good quantities agreement. However, trends appear to be correctly predicted and K* of 10^4 kg/ m^3.sec is the best value.

Nanosalt has been simulated in ANSYS CFX and validated with the experimental results of nanosalt. Good agreement is obtained between the experimental and simulated data of nanosalt at different thermocouples locations at axial locations (z1 and z2) and radial locations.

In the simulation data, nanosalt displayed a faster charging time than salt alone due to the higher thermophysical properties of the nanosalt material in comparison to salt alone. A similar conclusion is obtained experimentally for nanosalt in comparison to salt alone. The improvement in the charging process is calculated by the melting time where nanosalt requires less time to finish the melting process both experimentally and in the simulation.

In summary, a good match is observed between the experiments and the simulation data.

Chapter 6 Computational Fluid Dynamics Simulations for Storage Systems Design

6.1 Introduction

This chapter includes the full details of the simulation work using the computational fluid dynamics software (CFD) to optimize the storage system. The details of the geometry setup and mesh are investigated in this chapter. Furthermore, the problem setup is solved using the enthalpy-porosity method by the Ansys-CFX software (version 17.0). The main objective of this chapter is to optimize the storage system tank and the material together by combinations of finned nanoPCM for high temperature applications for the first time. Here in the text, salt is represented by PCM and the nanosalt is represented by nanoPCM.

6.2 Problem Setup (melting of phase change material)

The solution of the melting process in the CFX software depends on the enthalpy porosity method. The full details of this method have been explained in the previous chapter (Chapter 5). In this chapter, the same validated code is used for charging process of PCM/nanoPCM (salt or nanosalt) with different storage system designs. In addition, the viscosity is assumed to be constant for salt (PCM) or nanosalt (nanoPCM) because the concentration of nanoparticles is very low 0.5 wt.%, therefore the difference in viscosity will not be large as shown in Equation (6-1) (Tasnim et al., 2015)

$$\mu_{\mathrm{nanosalt}} = \frac{\mu_{\mathrm{salt}}}{(1-\theta)^{2.5}}$$ **Equation 6-1**

Where μ_{nanosalt} and μ_{salt} represent the viscosity of nanosalt (nanoPCM), and salt (PCM) respectively. θ is the concentration of nanoparticles.

The inner pipe includes fin structures with different structures and comparison among these different designs of a storage system is explained in the next section of results and discussion section. The different cases of storage system design are listed and summarized in Table (6-1).

Table 6-1 shows cases (1 to 12) of storage system design with fins parameters (fins' length and fins' numbers).

Case	Description	Fin length, mm	Number of fins
Case 1 Base case	Concentric cylinder with PCM in middle between the inner and outer pipes and the hot fluid in the inner pipe. Only PCM, neither nanoparticles nor fins.	-	-
Case 2 nanosalt	Same as case 1 with nanoPCM (0.5 wt. % Fe_2O_3+ nitrate solar salt) instead of PCM alone.	-	-
Case 3	salt with fins structure 1	26 mm	4
Case 4	Nanosalt with fins structure 1	26 mm	4
Case 5 – similar to case 3 with same surface area	Salt with fins structure 2	17.2 mm	6
Case 6 - similar to case 4 with same surface area	Nanosalt with fins structure 2	17.2 mm	6
Case 7	Salt with fins structure 3	26 mm	6
Case 8	Nanosalt with fins structure 3	26 mm	6
Case 9	Salt with fins structure 4	32 mm	4
Case 10	Nanosalt with fins structure 4	32 mm	4
Case 11	Salt with fins structure 5	32 mm	6
Case 12	Nanosalt with fins structure 5	32 mm	6

6.3 Geometry and mesh study

Firstly, AutoCAD software (version 2018) was used to build the 3-Dimensional geometry model of different fins-storage systems and these were imported as geometries in the Ansys-workbench software, particularly Ansys workbench-design module (version 17.0). Several different geometries were studied in this chapter depending on each case as shown in Table (6-1). In all of these cases, there are three domains where two of them are solid domains and one is a fluid domain. The large solid domain represents the outer wall with a finite thickness made from stainless steel. The small solid domain represents the hollow un-finned or finned pipe in the centre of the geometry. The PCM is represented in the fluid domain which fills the gap between these two solid domains.

Furthermore, the dimensions are estimated to be similar to our experimental rig. The dimensions of the large solid pipe are outer diameter 101.4 mm and thickness of 2 mm. The dimensions of the fluid domain pipe are diameter 97.4 mm and at the centre is a hollow un-finned or finned solid pipe with a diameter of 25 mm. The small solid domain has an outer diameter of 25 mm with a thickness of 1.5 mm without and with different fin structures. The lengths of all pipes are 300 mm with the z-direction as the axial direction. The material of the pipe is stainless steel for all walls such as the inner hot pipe wall, finned inner pipe, the outer pipe, thickness of both solid domains, top and bottom, and fins materials. The material of the fins is chosen to be stainless steel because of the corrosion effect of nitrate salt (the PCM). The fluid domain contains the PCM which is nitrate salt or nanosalt. There is no inlet nor outlet for this problem. Therefore, the top and bottom covers are assumed as walls boundary condition with certain values of heat losses depending on the measurement of film temperature in the experiments and the full calculations for the values of heat transfer coefficient are discussed previously in chapter 5. Figures (6-1 to 6-6) show the different geometry structures studied for different cases.

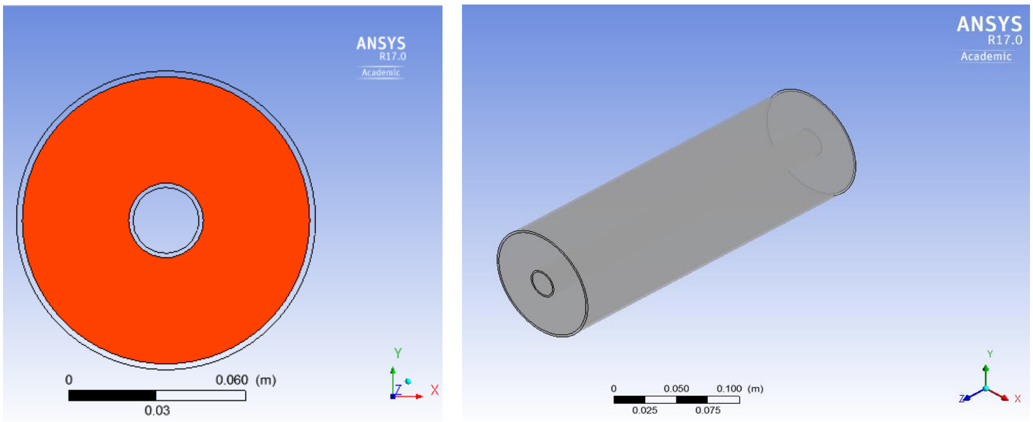

Top view **Side view**

Figure 6-1 shows the geometry of cases 1 and 2.

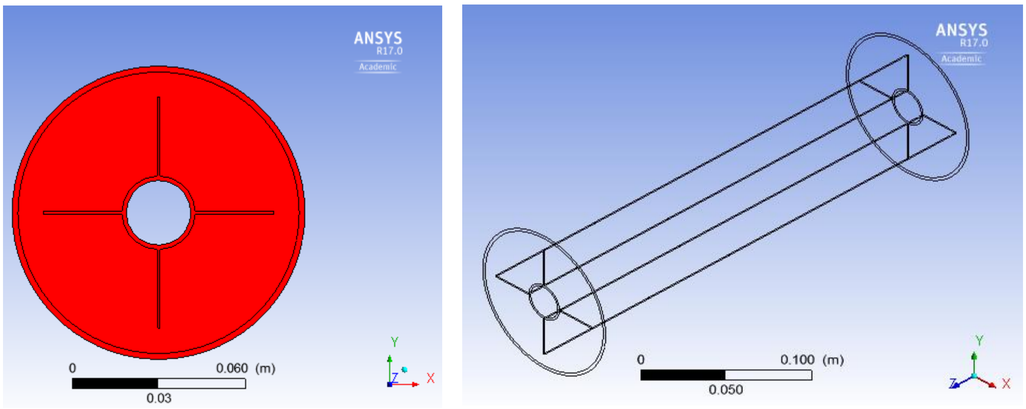

Top view **Side view**

Figure 6-2 shows the geometry of cases 3 and 4.

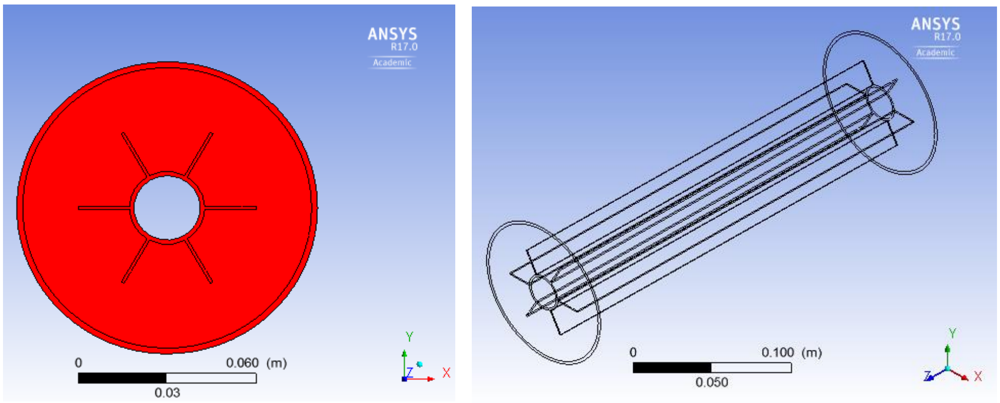

Top view **Side view**

Figure 6-3 shows the geometry of cases 5 and 6.

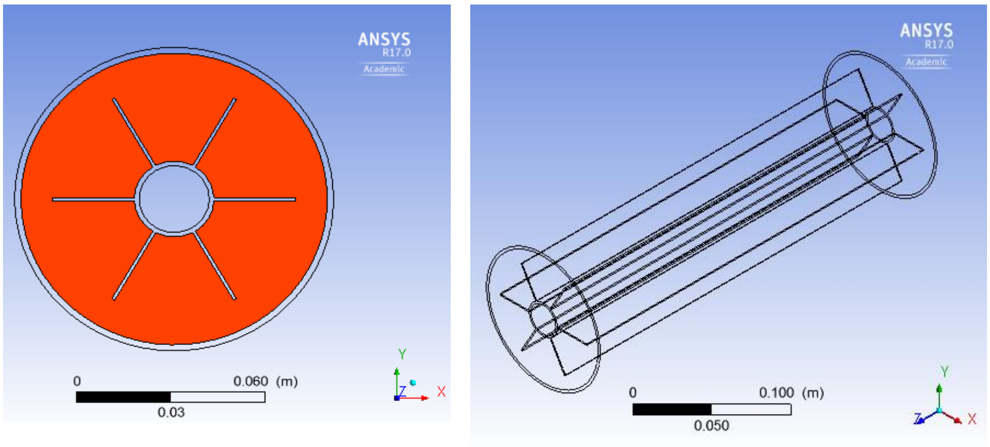

Top view **Side view**

Figure 6-4 shows the geometry of cases 7 and 8.

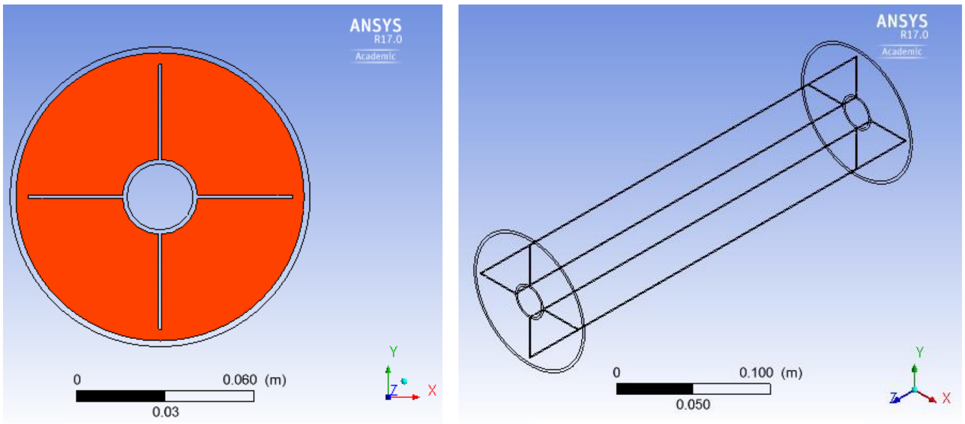

Top view **Side view**

Figure 6-5 shows the geometry of cases 9 and 10.

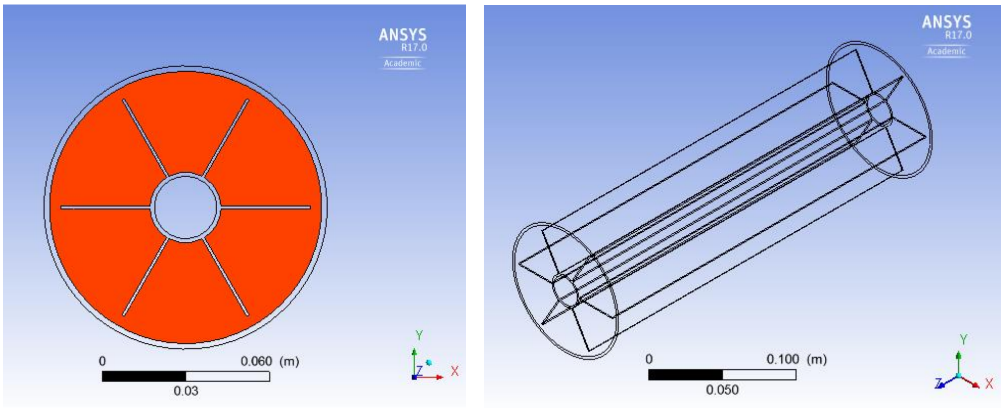

Top view **Side view**

Figure 6-6 shows the geometry of cases 11 and 12.

Secondly, the 3-D rig is meshed by Ansys workbench (version 17.0), as shown in Figure (6-7). For most cases, the type of the mesh used is a combination of both tetrahedral and hexahedral elements. Table (6-2) shows the number of elements used for each case of the storage system design.

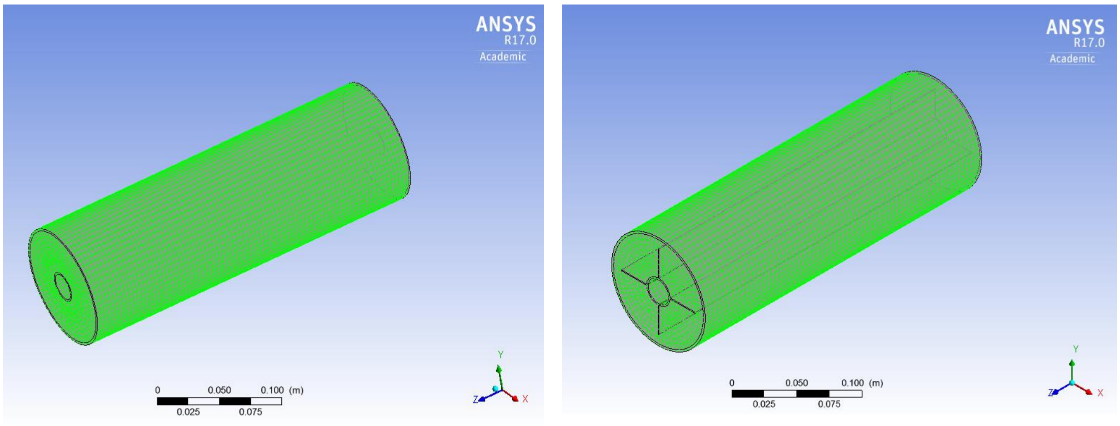

Figure 6-7 shows the mesh used.

Table 6-2 shows the number of elements used for each case.

Case	Number of elements	Case	Number of elements
Cases 1 and 2	52920	Cases 7 and 8	35845
Cases 3 and 4	37252	Cases 9 and 10	37128
Cases 5 and 6	37051	Cases 11 and 12	35443

Furthermore, the effect of elements number has been studied such as mesh 1 (27442), mesh 2 (37128) and mesh 3 (364436). Computations on these three different meshes were conducted and compared as shown in Figure (6-8). Figure (6-8) indicates that increasing element number more than 37128 doesn't show differences. Therefore, the element number of 37128 was selected.

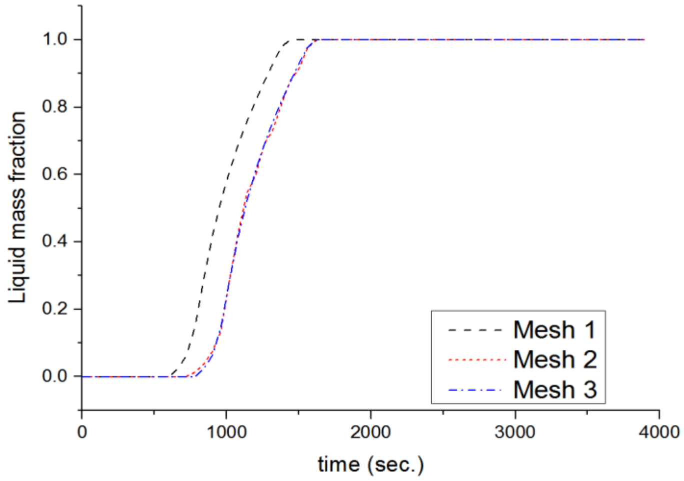

Figure 6-8 Shows liquid mass fraction of different mesh used.

6.4 Boundary condition

The boundary conditions were kept the same for the different cases. For all cases (1 to 12), there is no inlet or outlet, therefore, the top (inlet) and bottom (outlet) covers were simulated as walls with specified heat losses. The values of heat losses were calculated as in the previous chapter (Chapter 5). Additionally, the interface boundary condition of a conservative heat flux boundary condition was employed between the finned/un-finned HTF wall (the inner solid domain) and the surrounded PCM. Another interface boundary condition was used between the inner wall of the large solid domain and the surrounded PCM, as shown in Figure (6-9). The boundary condition of the outer wall (in the large solid domain) was adiabatic with no heat losses to the surrounding environment. Moreover, the hot wall of the HTF (in the inner solid domain) has a boundary condition of constant wall temperature.

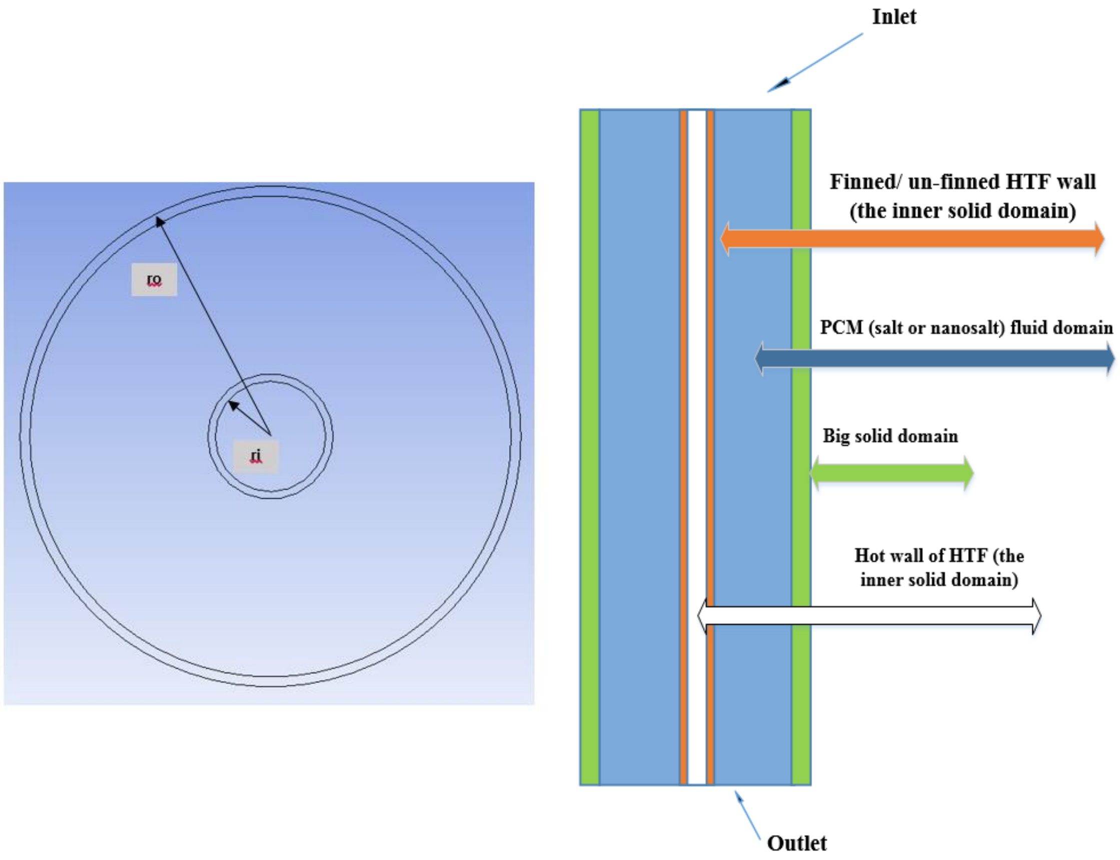

Top view **Side view**

Figure 6-9 shows the layout of the finned and un-finned storage system.

In other words, the temperature condition inside the PCM domain were controlled by the following boundary conditions shown in Equations (6-2 and 6-3) and initial condition shown in Equation (6-4):

$\mathrm{r = r_i}$ $\quad$ $\text{constant wall temperature.}$ **Equation 6-2**

$\mathrm{r = r_o}$ $\quad$ $\mathrm{dT/dr = \ 0 \quad (adiabatic\ wall)}$ **Equation 6-3**

$\mathrm{t = t_{ini}}$ $\quad$ $\mathrm{T\ constant\ at\ r_i < \ r \ < r_o}$ **Equation 6-4**

where r, $\mathrm{r_i}$, $\mathrm{r_o}$ represent the radius (mm), the inner radius of the HTF pipe (mm), and outer radius of the outer pipe (mm), respectively, as shown in Figure (6-9 the top view). Time in seconds represented by t and t_{ini} is the initial time (sec) at the starting of the melting process. The initial temperature of the setup was lower than the melting point and in all cases was 200 ^{0}C while the maximum temperature of the inner HTF pipe was higher than the melting temperature to allow charging process studies for solid phase,

phase change, and liquid phase. For all cases, the maximum temperature studied is 270 ^{0}C. Additionally, for all cases, the temperature and liquid mass fraction have been detected numerically by CFD-POST at different locations (radial, axial and around fins) as shown in Figures (6-10, 6-11 and 6-12). These certain points allow us to compare the different cases and to find the optimal design of the storage system in term of the minimal melting time to finish the charging process.

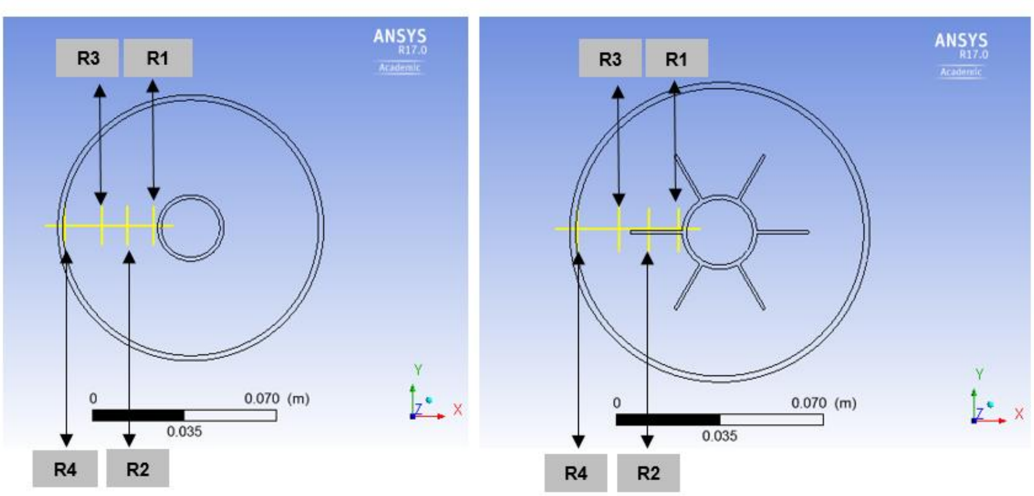

Figure 6-10 shows thermocouples locations in different radial directions (R1, R2, R3 and R4 from the nearest to the hot pipe to the farthest) at the same axial direction for all cases.

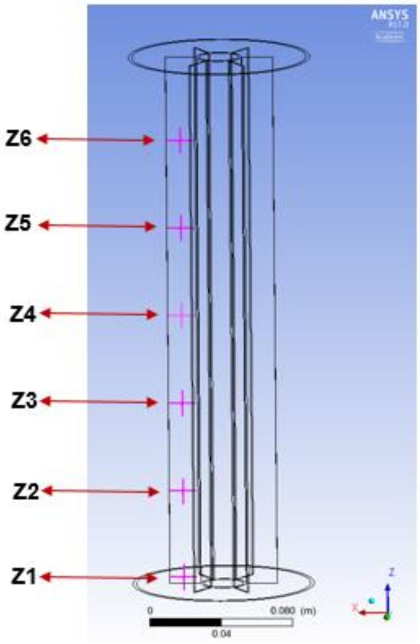

Figure 6-11 shows thermocouples locations in different axial directions (Z1, Z2, Z3, Z4, Z5 and Z6 from the bottom and forward) at the same radial direction for all cases.

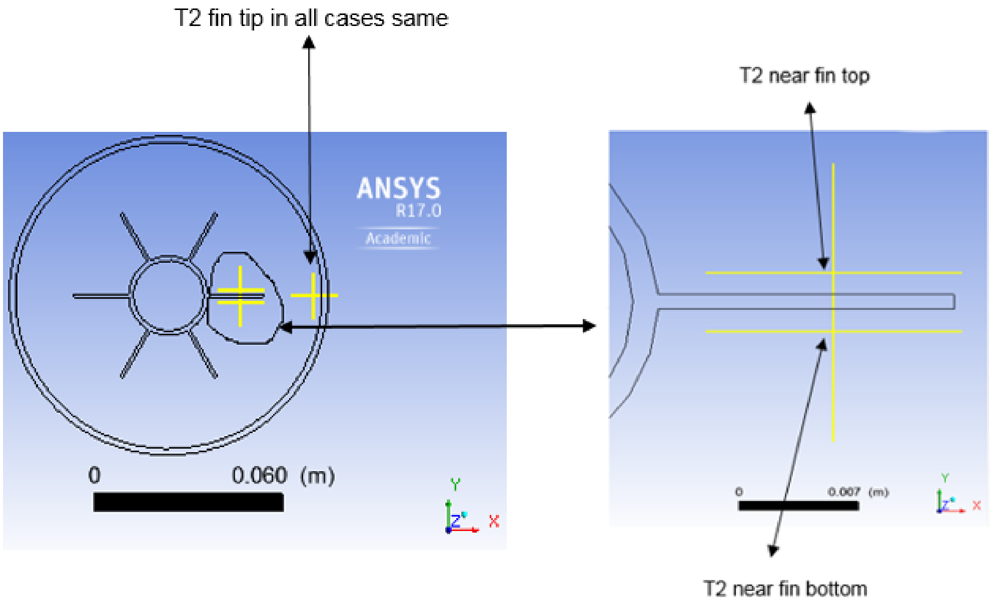

Figure 6-12 shows thermocouples locations above, below and away from the fin tip for all cases.

6.5 Results and discussion

There are many researchers who modelled the fin storage system such as (Castell et al. (2006), Gharebaghi and Sezai (2007), Tay et al. (2013), Lv et al. (2008), Varol and Okcu (2013),Chaitanya et al. (2014), Agyenim et al. (2009), Hossain et al. (2015), Yang et al. (2015), and Kamkari and Shokouhmand (2014)). However, most of them used Fluent software, not the CFX software. As stated above, most of these simulation papers used paraffin or another material such as water, Naphthalene, and RT82 that have a low melting temperature.

Further work needs to be carried out on materials with high melting temperature such as molten salt inside a finned PCM, i.e. eutectic nitrate salt of potassium and sodium mixture with 40:60 by molar ratio. Ansys-CFX would be able to detect the melting front which is not easy during the experiments. Due to the high temperature, it is not safe to use a transparent pipe to watch the phase change and the high temperature difference easily leads to higher heat losses. Therefore, melting front detection for different cases are examined and compared for different storage system designed using Ansys-CFX software. The effect of different fin structures is compared in terms of the same or different surface areas of fins structures, as shown in Table (6-3).

Table 6-3 shows the surface areas of fins and the reduction in the volume of salt for different cases of storage system design

Case	Surface area of fins structures, mm^2	Volume of salt, mm^3	Reduction in volume of salt %
Case 1 Base case	-	2082197	-
Case 2 nanosalt	-	2071786	0.5 %
Case 3	63600	2050997	1.498 %
Case 4		2040586	1.998 %
Case 5 – similar to case 3 with same surface area	63720	2051057	1.496 %
Case 6 - similar to case 4 with same surface area		2040645	1.996 %
Case 7	95400	2035397	2.248 %
Case 8		2024986	2.748 %
Case 9	78000	2043797	1.844 %
Case 10		2033386	2.344 %
Case 11	117000	2024597	2.766 %
Case 12		2014186	3.266 %

6.5.1 Same surface area of the fin structure

There are different cases used to optimize the fin structures inside a storage system using different arrangements of fins with similar surface areas, around 63600 mm^2, as shown in Table (6-3).

One of them consists of four fins with 26 mm in length to represent case 3 using nitrate salt as the PCM, or case 4 using nanosalt as PCM instead of nitrate salt. This is a new combination of nanosalt and fins. For both cases 5 and 6, the length of fins was 17.2 mm and six number of fins are used by keeping a similar fin surface area as cases 3 and 4, respectively. Table (6-3) shows the surface area of different storage system designs. Additionally, the packed volume of PCM is the actual volume of the salt divided by the volume of the storage system, and in the case of the presence of fins, there is a reduction in the volume of the salt, as shown in Table (6-3). The higher volume of fins leads to less volume of the storage medium resulting with less storage density. However, this reduction in storage medium volume is low, less than 2% in cases 3 to 6. The effect of reducing the mass of a storage medium can be negligible in comparison with the higher improvement of the charging process in cases of fins and nanoparticles compared to the case of salt alone.

Figures (6-13 a and b) show the liquid fraction at different selected times (6 min. and 24 min.) of cases 1 to 6. First of all, the effect of nanoparticles on the PCM is studied here in case 2 showing a positive approach with faster melting than case 1 of the only salt. This could be due to higher thermophysical properties than the base materials (salt) which means faster conduction of heat from the hot pipe than case 1 of salt alone. This improvement is noticeable from the first 6 min. On the other hand, it is clearly noticed a higher number of fins (case 5) shows faster charging than a fewer number of fins (case 3). This is due to the higher improvement in the conduction process from the inner hot pipe towards the PCM, due to higher thermal conductivity value of the fins materials compared to the PCM conductivity. This is especially notable at the beginning of the charging process because at the beginning of the melting process, the conduction heat transfer is the dominant mode. The increasing of the melted layer around the inner hot pipe would increase the effect of convection after a while from the beginning of the charging process, because of density differences and the buoyancy effect. The presence of the finned structure could block the flow of the melted PCM, leading to a limitation of natural convection. However, this limitation of natural convection is highly dependent on the fin shapes. In the case of circular fins, higher decreasing of natural convection can be observed, while in the case of longitudinal fins (which is the shape used in this study), the effect on natural convection is not so big (Agyenim et al., 2009). Agyenim et al. (2009) concluded that longitudinal fin structures improve the charging process better than other types of fins. The overall improvements in charging process are noticeable in cases 3 and 5 in comparison to cases 1 or 2.

In Figure (6-13), it is shown that case 5 better than case 3 in term of faster charging. This could be due to the fact that case 3 has only four fins which transfer the heat from the inner hot pipe towards the PCM in the radial direction. This could require a longer time to finish the charging process than case 5 which has six fins at different angular and radial directions. Furthermore, the heat transferred from a dense finned pipe (case 5) could be higher than a less dense finned pipe (case 3), as shown in temperature contours in Figures (6-14 a and b). Figures (6-14 a and b) shows the temperature distributions at different times of different cases where the PCM starts melting in the immediate vicinity of the fin surfaces and the hot surface of the inner pipe. This behaviour happens because of the higher temperature differences between the PCM fluid domain and the hot finned pipe. These could be the reasons behind this improvement in case 5 compared to case 3. Furthermore, at the time of 36 min in Figures (6-14 a and b), almost 2/3 of the PCM approaches the maximum input temperature in case 5, while in case 1 there are some areas where the salt is still in the solid phase. In other cases, particularly cases 2 and 3, almost all the PCM is in the mushy zone area with no solid phase presented. This demonstrates the effect of fins or nanoparticles on the melting rate compared to case 1. However, the cases with finned structures showed better improvement in the charging process than the nanosalt case. For instance, cases 1 and 2 showed melting layers from the top and downward while in the finned cases the heat conducted in different directions due to the conductive solid fins. This is due to the fact that the fins disperse the heat to salt in the wider zone inside the storage system because of their higher thermal conductivity leading to improve the conduction from inner pipe to the PCM domain especially at the beginning of the melting.

Additionally, cases 4 and 6 show the same fins structure design of case 3 and 5, respectively, with nanosalt as the PCM instead of salt alone. The new study of the combined effect of both nanoparticles and fin structures on the storage system shows a powerful effect on the charging process compared with case of the only salt inside the storage system, or only finned-storage system, or nanosalt storage system as shown in Figures (6-13 a and b, and 6-14 a and b). For instance, all PCM was melted in case 6 after only 24 minutes from the charging process starting, while there is around ¼ of PCM still not melted in case 4, as shown in Figures (6-13 a and b). This is due to the arrangement of fins in case 6 with six fins while in case 4 only four fins were used. Although case 6 has shorter fins of 17.2 mm than case 4 with 26 mm, case 6 finished the charging process faster than case 4 though both of them have similar surface area. Furthermore, Figures (6-14 a and b) indicate that in case 6 all nanosalt approaches the maximum input temperature after only 36 min. while case 4 around ¼ of nanosalt approaches the maximum input temperature. This indicates that case 6 is a more optimum design than case 4.

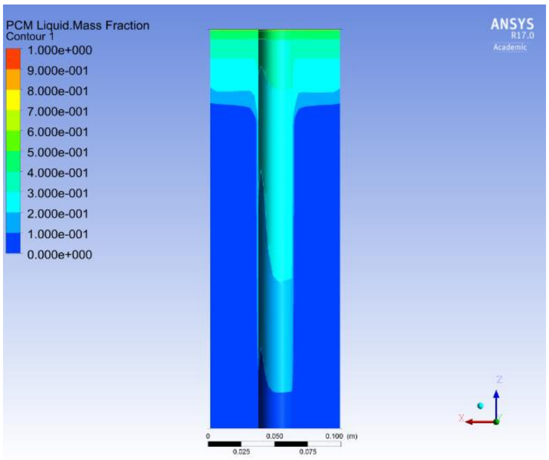

Case 1

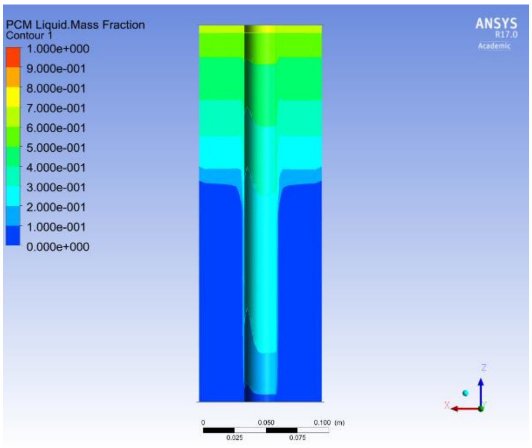

Case 2

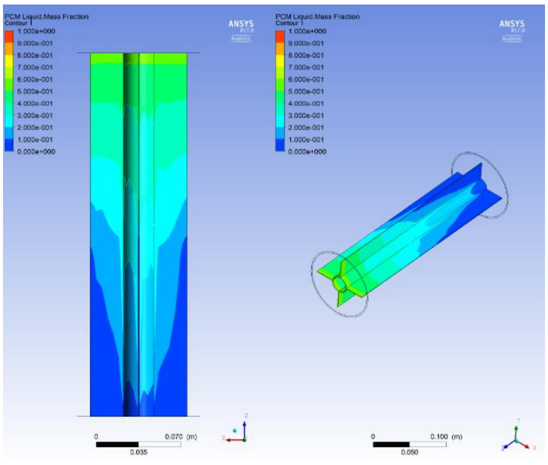

Case 3

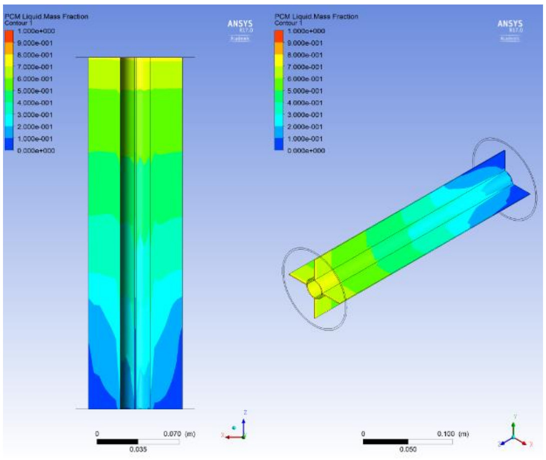

Case 4

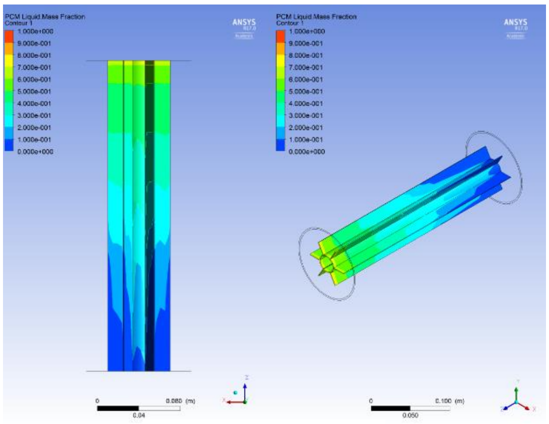

Case 5

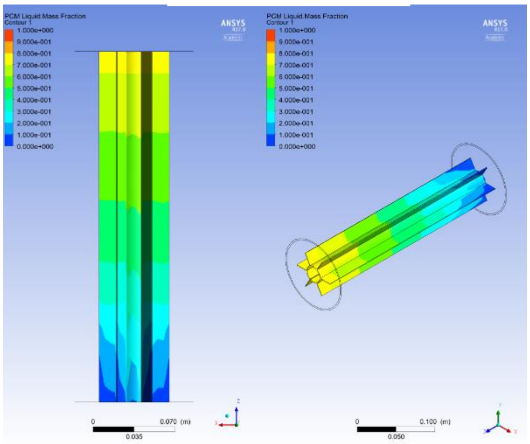

Case 6

(a) The liquid fraction contours for cases (1 to 6) at 6 minutes.

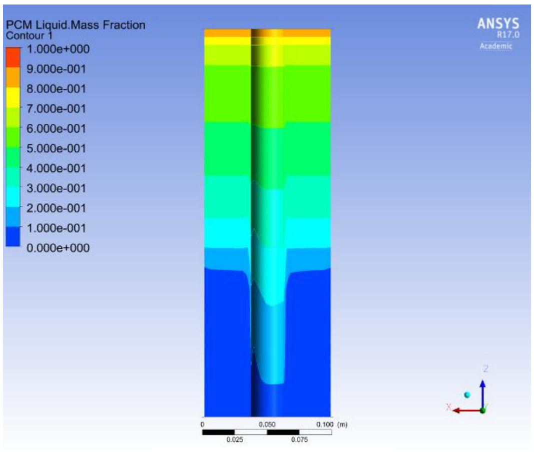

Case 1

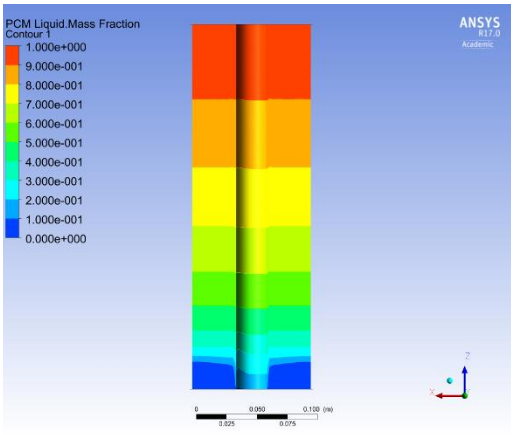

Case 2

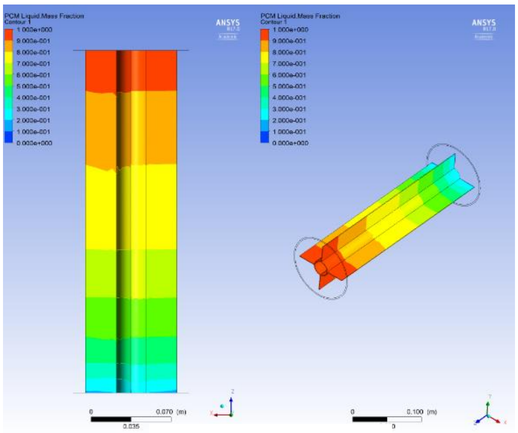

Case 3

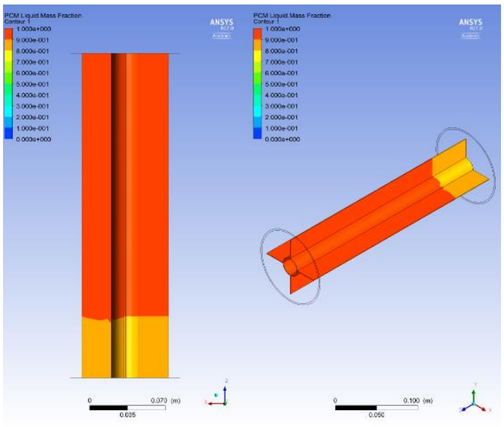

Case 4

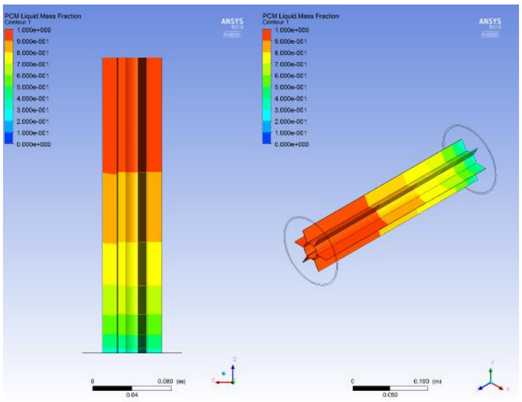

Case 5

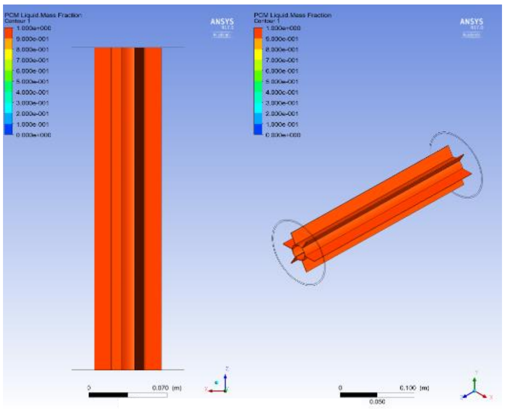

Case 6

(b) The liquid fraction contours for cases (1 to 6) at 24 minutes.

Figure 6-13 shows the liquid fraction contours for cases (1 to 6) at (a) 6 minutes and (b) 24 minutes.

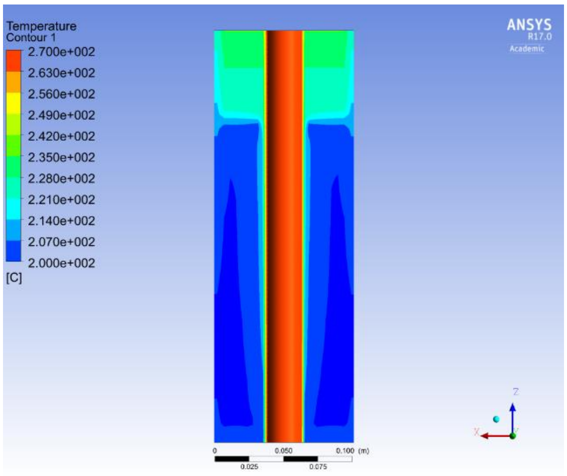

Case 1

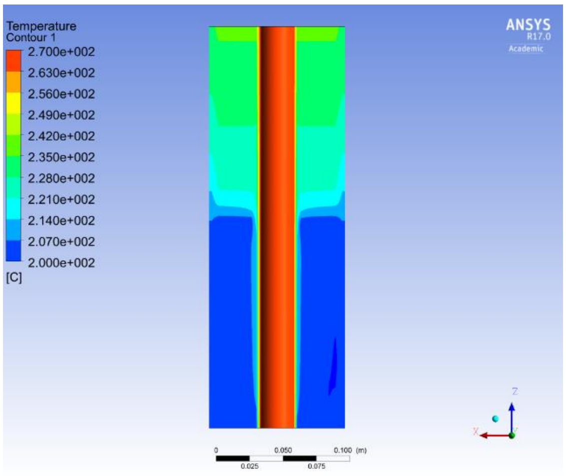

Case 2

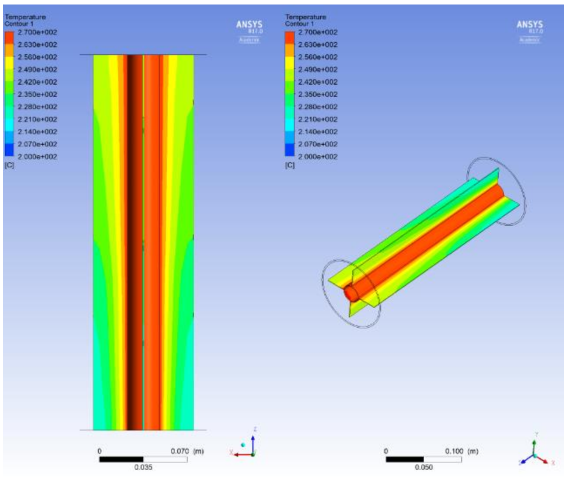

Case 3

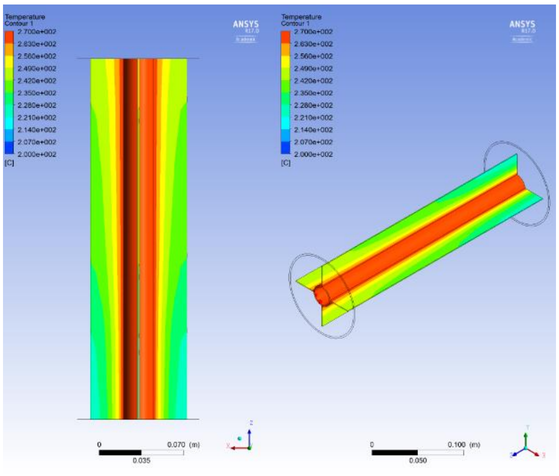

Case 4

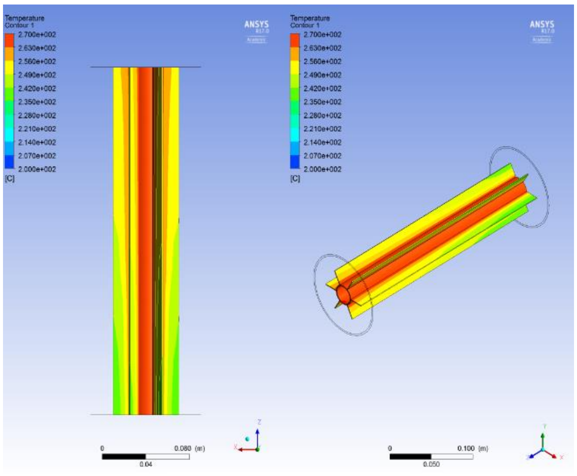

Case 5

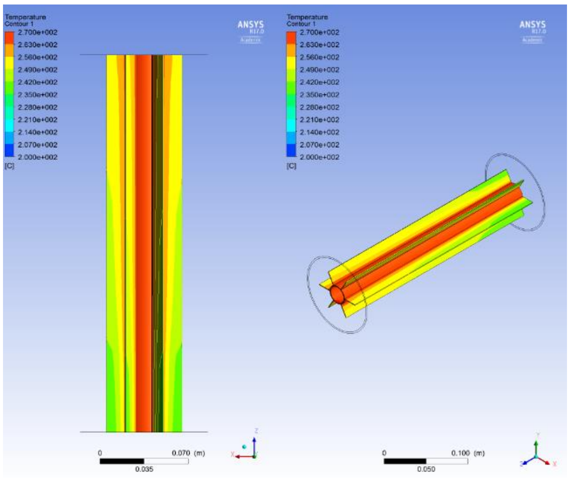

Case 6

(a) The temperature contours for cases (1 to 6) at 6 minutes.

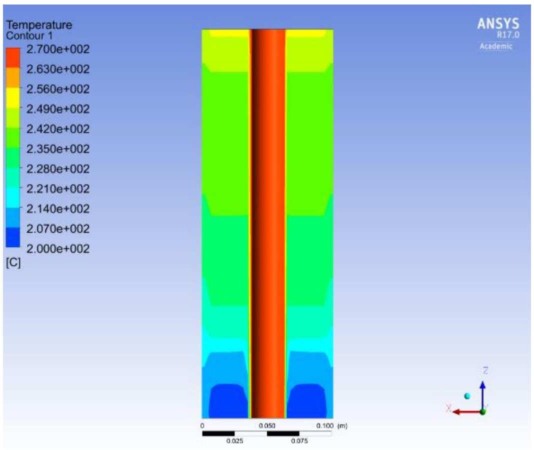

Case 1

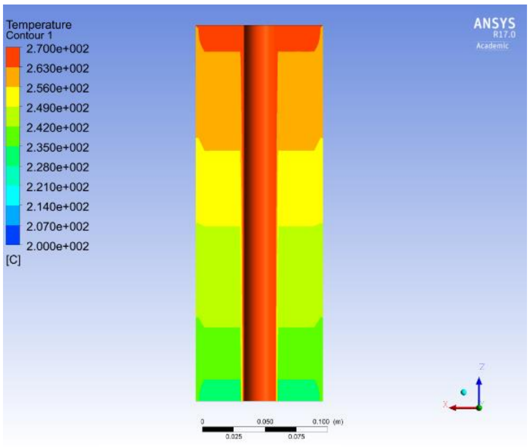

Case 2

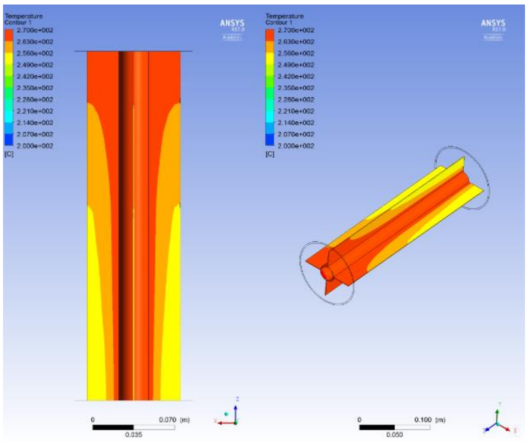

Case 3

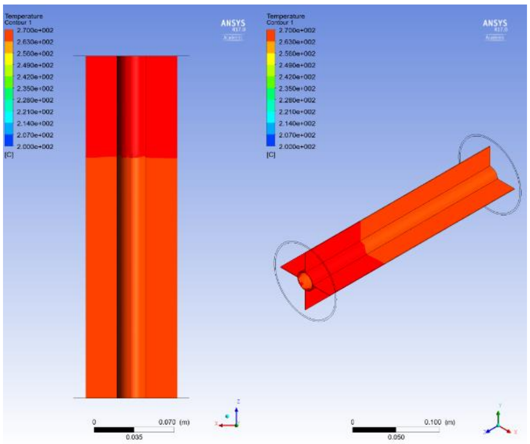

Case 4

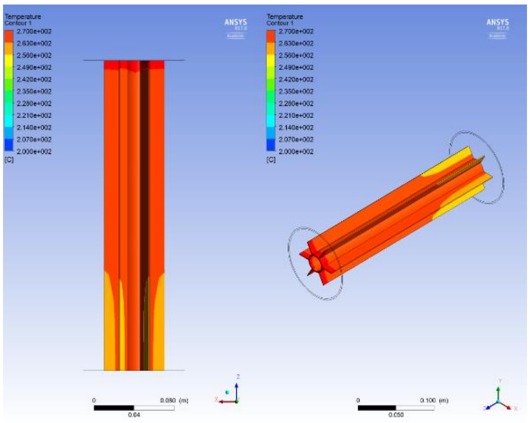

Case 5

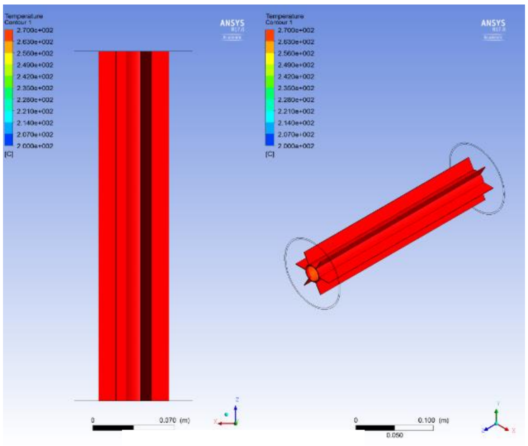

Case 6

(b) The temperature contours for cases (1 to 6) at 36 minutes.

Figure 6-14 shows the temperature contours for cases (1 to 6) at (a) 6 minutes, and (b) 36 minutes.

The distribution of temperature against time for different cases is measured numerically using CFD-post (version 17.0) as shown in Figure (6-15).

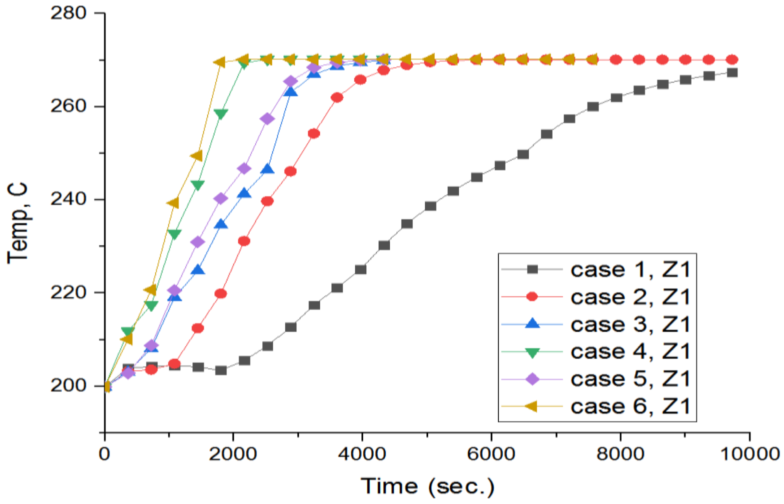

Figure 6-15 Shows transient temperature distributions for different cases (1 to 6) at the axial direction of Z1 with same radial direction.

At a fixed radial, and axial direction of Z1, case 6 is the best one in terms of faster increase in temperature than other cases. Similar to Figure (6-15), Figure (6-16) shows the liquid mass fraction with the same conclusion.

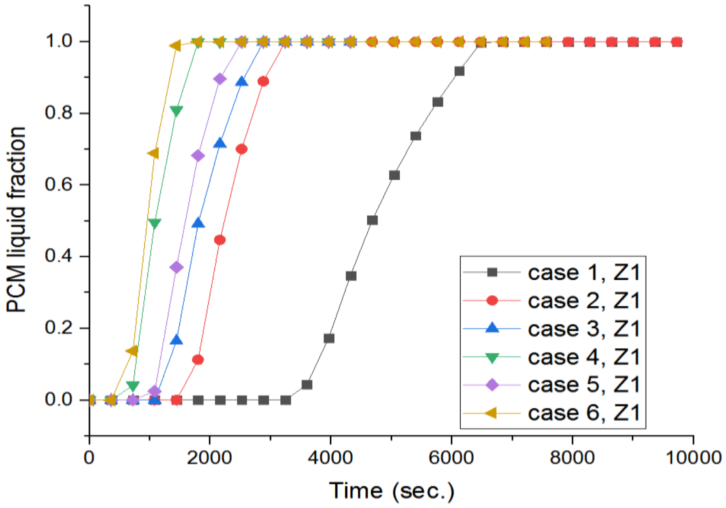

Figure 6-16 Shows liquid mass fraction of different cases (1 to 6) at the axial direction of Z1 with same radial direction.

At another location of different radial directions (R4) and the axial direction of (Z3), liquid mass fraction shows there is little difference between cases 2 and 3, Figure (6-17). This could be due to the measured thermophysical properties used for case 2 (nanosalt) were high enough to improve the charging process with close improvements obtained by the four 26 mm fins (case 3).

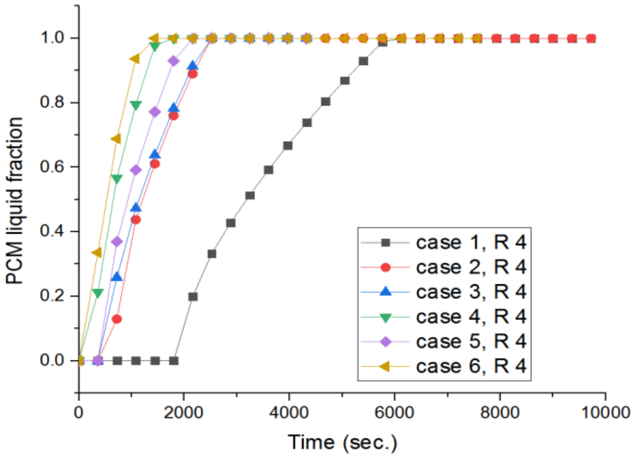

Figure 6-17 Shows liquid mass fraction for different cases (1 to 6) at the radial direction of R4 with same axial direction.

Figure (6-18) shows the transient temperature distributions in term of axial directions (Z1 to Z6) of cases 4 and 6. Case 6 shows a faster charging process at less than 2000 seconds while case 4 approximately reaches the maximum input temperature (270 ^{0}C) after 2000 seconds. This behaviour could be due to the natural convection effect alongside with conduction effect because of fins arrangements such as fins' numbers or fins' length.

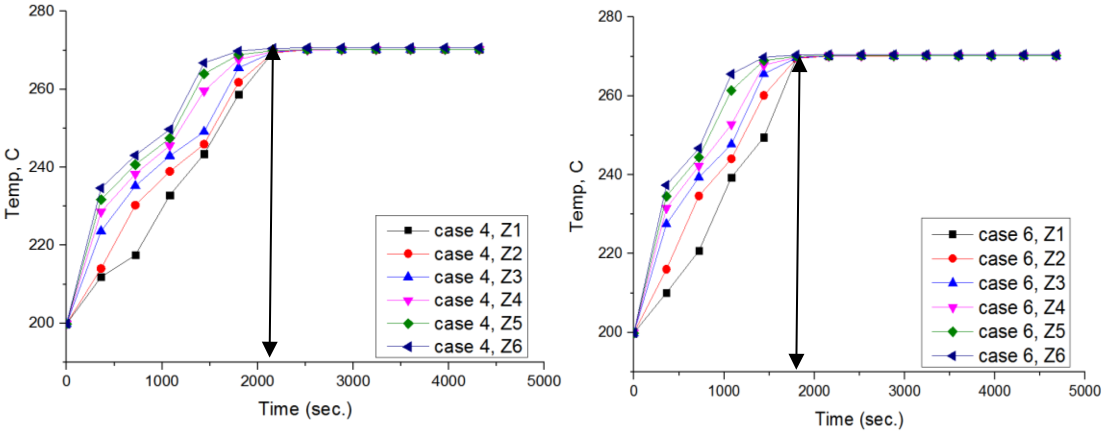

Figure 6-18 shows transient temperature distributions for nanosalt and Fins structure together in the storage system of cases 4 and 6 at different axial direction (Z1 to Z6) with same radial direction.

Similar behaviour has been obtained for temperature distribution at different radial directions as shown in Figure (6-19). The temperature at radial R1 shows faster increment in temperature than others because it is the nearest thermocouple to the hot wall. Additionally, the combined effect of nanoparticles and finned structures implies a combination advantage of thermophysical properties of PCM due to nanoparticles presence and higher conductivity due to fin structures. Case 6 is better than case 5 because of the finned structure arrangement, as the same material properties have been used in both cases.

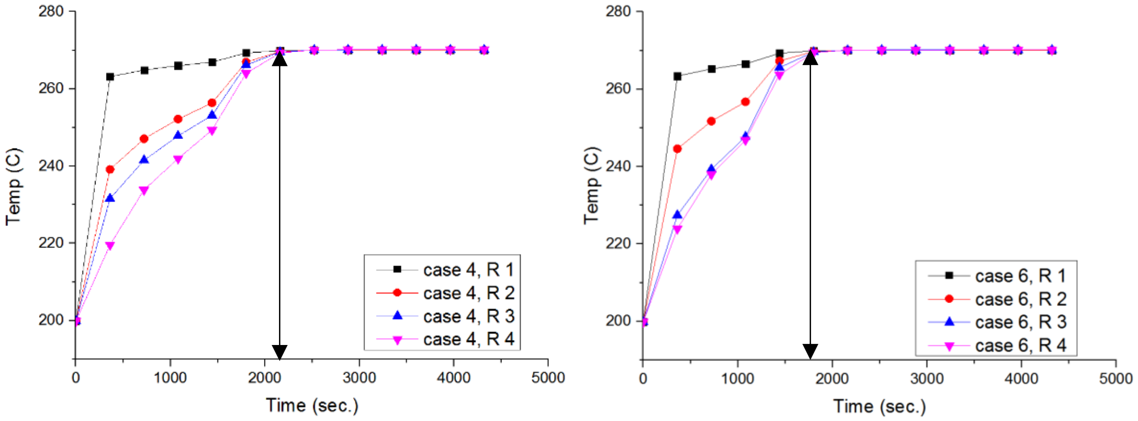

Figure 6-19 shows transient temperature distributions for nanosalt and Fins structure together in the storage system of cases 4 and 6 at different radial direction (R1 to R4) with the same axial direction.

Calculating the liquid mass fraction at the farthest and deepest point indicates the full charging process time for all cases as shown in Figure (6-20). It can be seen that case 4 is better than case 3, and case 6 is better than case 5, similar to the above behaviours discussed earlier in Figure (6-16).

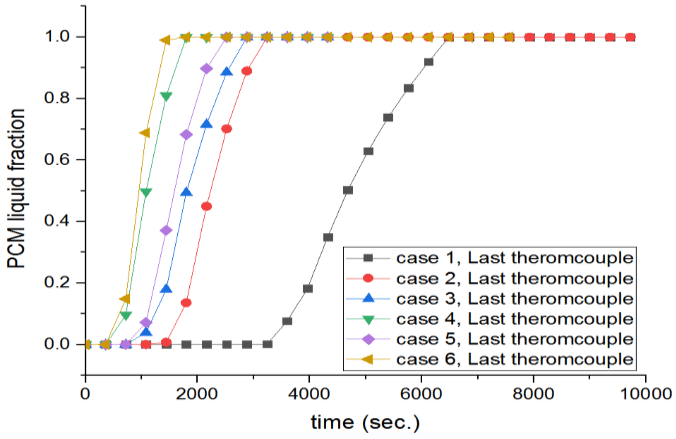

Figure 6-20 shows liquid mass fraction for all cases at a deepest point in the storage system and far away from the hot inner pipe.

Both of Figures (6-21 and 6-22) show the transient temperature distributions around the fins for all cases. It is clearly shown that, at the beginning of the melting process where conduction is dominant, all cases of fins (cases 3 to 6) show a faster increase in temperature and then slow down due to the suppression of convection by the fins presence.

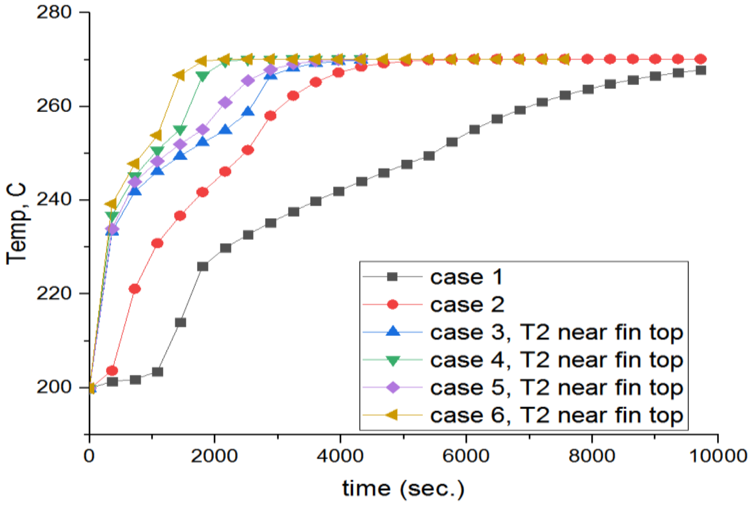

Figure 6-21 shows the transient temperature distributions for the same location of thermocouples among the cases 1 to 6.

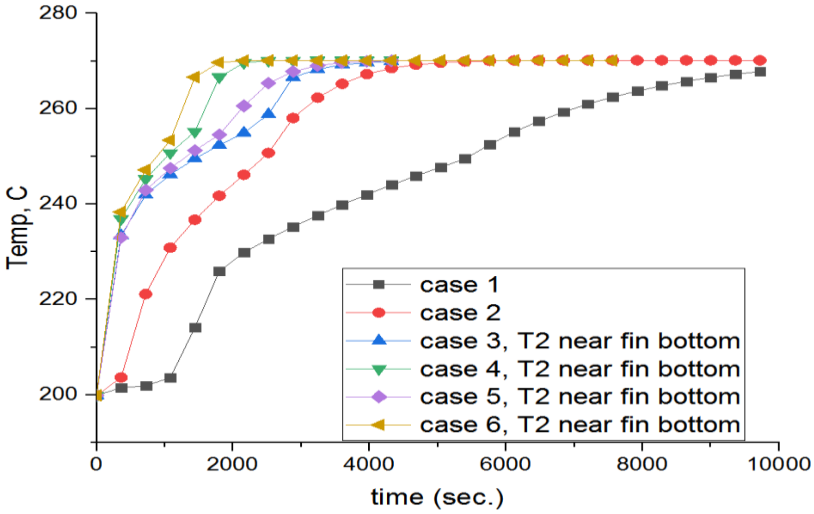

Figure 6-22 shows the transient temperature distributions for the same location of thermocouples among the cases 1 to 6.

Far from the fins, Figure (6-23) demonstrates that no big differences exist between cases 2 and 3. However, case 3 is still better than case 2.

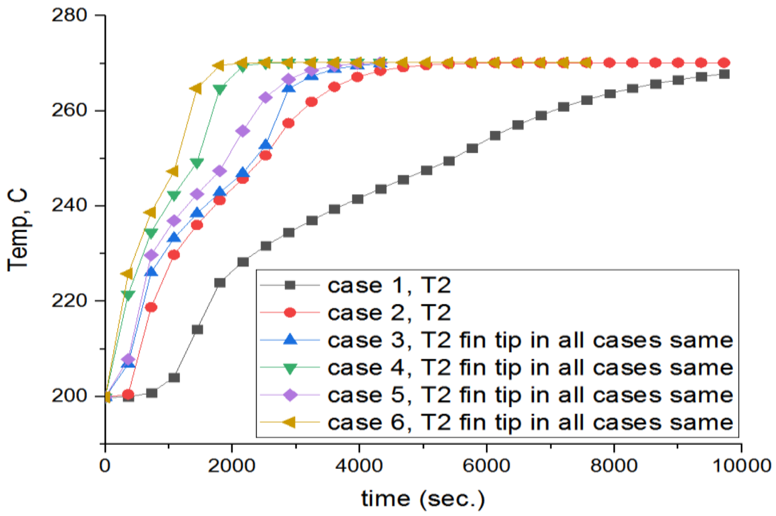

Figure 6-23 shows the transient temperature distributions for the same location of thermocouples among the cases 1 to 6.

Furthermore, a similar trend was observed for a liquid mass fraction in Figure (6-24). In Figure (6-25), cases 3 and 4 showed there are no differences in temperature around fins from top and bottom while in cases 5 and 6 there is little difference. This could be due to the effect of the fins length where longer fins showed a homogenous distribution around the fins while in the shorter fins the temperature was not fully homogenous.

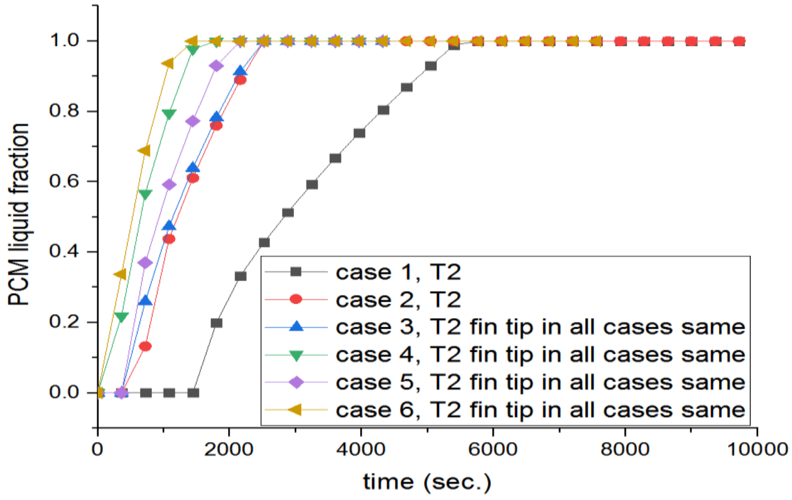

Figure 6-24 shows the liquid mass fraction for the same location of thermocouples among the cases 1 to 6.

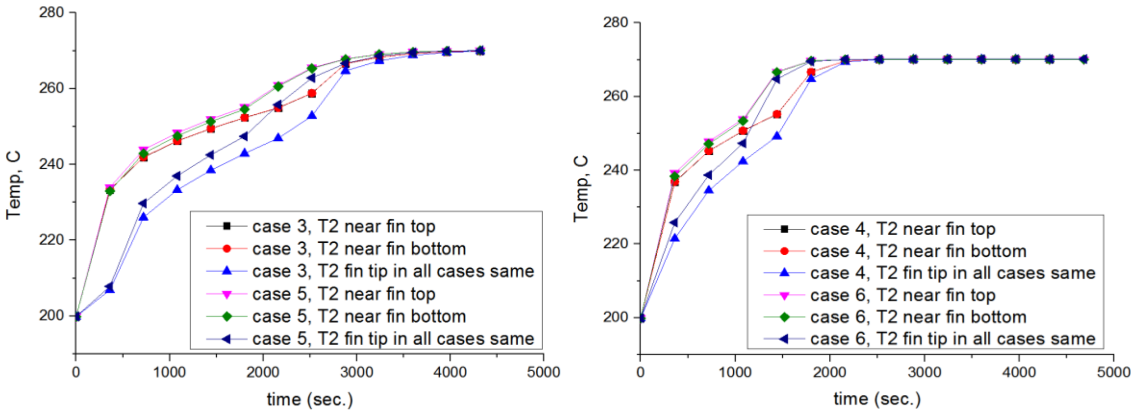

(a) Salt with different fins structures

(b) Nanosalt with different fins structures

Figure 6-25 shows the transient temperature distributions for (a) cases 3 and 5 of salt with different fins structures, and (b) cases 4 and 6 of nanosalt with different fins structures.

It can be concluded from above that keeping similar surface area when changing the arrangements of the fins is better than using longer fins in one direction. Moreover, the combined effect of both nanoparticles and fins improves the heat transfer better than one factor alone by reducing the charging time up to 76.471 % as shown in Table (6-4).

Table 6-4 shows the reduction in melting time for different cases (case 1 to 6)

Case	Melting time, sec.	Reduction in melting time, sec.	Reduction in melting time, %
Case 1 Base case	6120	-	-
Case 2 nanosalt	3600	2520	41.176 %
Case 3	3240	2880	47.059 %
Case 4	1800	4320	70.588%
Case 5	2520	3600	58.824 %
Case 6	1440	4680	76.471 %

6.5.2 Different surface area of the fin structure

The effect of increasing surface area of the finned structures has a remarkable effect on the charging process. The increasing of fins' length or fins' number are studied as shown in Table (6-1). The effect of fin structures on decreasing the packed volume of salt is listed in Table (6-3) with maximum reduction in salt volume by 3.266 % for case 12.

Figures (6-26 a and b) show the liquid fraction at different selected time for cases 7 to 12. It can be seen that the number of fins has a greater effect on the charging process than the length of fins. After 6 min only, there are no huge differences among cases 7, 9 and 11 of salt as the PCM or cases 8, 10 and 12 of nanosalt as the PCM. However, when time passes and after 24 min. from the starting of charging process, both cases 8 and 12 finished the charging process while case 10 showed some volume less than ¼ of PCM (nanosalt) still in the mushy zone. This clarifies the effect of fins number over the fins length specifically between case 8 (26 mm with 6 number of fins) and case 10 (32 mm with 4 number of fins). On the other hand, using salt as the PCM instead of nanosalt would require a longer time to finish the charging process as indicated in Figures (6-26 a and b). After 24 min, liquid mass fraction contours showed that in both cases 7 and 11, half of the PCM is still in the mushy zone area and only less than ¼ of PCM completes the melting process for case 9. This could be due to the effect of fins length or numbers on the melting behaviour. A similar trend is observed for temperature contours in Figure (6-27 a and b). It is observed that similar improvements can be concluded in both cases 7 and 11, and cases 8 and 12. Additionally, the melting started from the top and moved downwards with simultaneous melting around the fins structure forming a melting front with shapes as shown in contours in Figures (6-26 a and b, and 6-27 a and b).

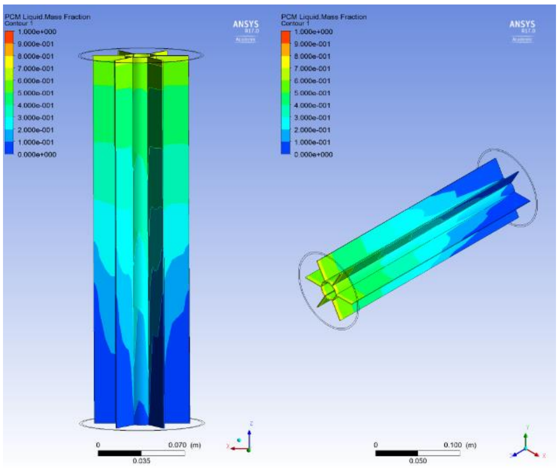

Case 7

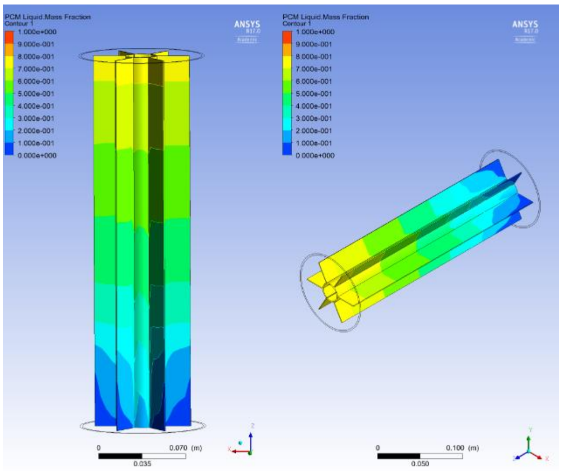

Case 8

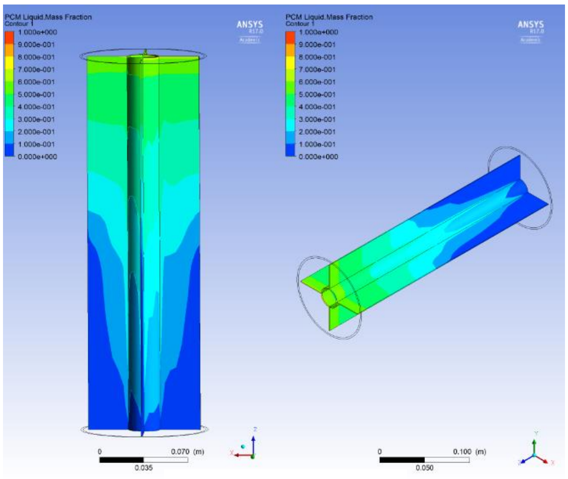

Case 9

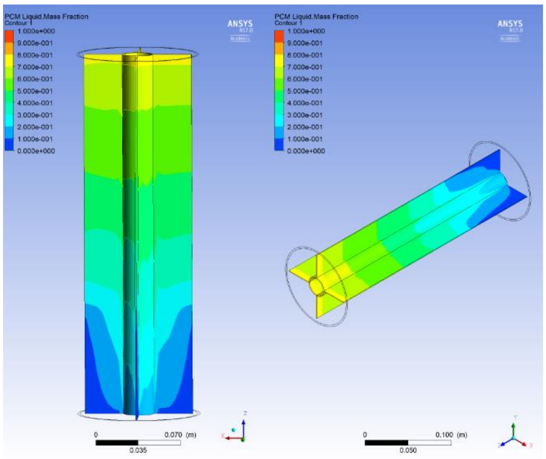

Case 10

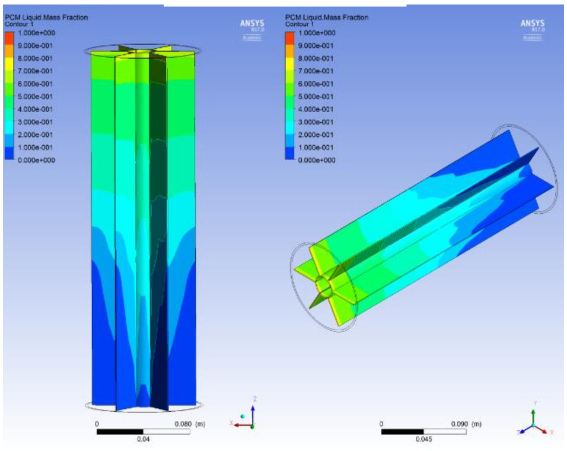

Case 11

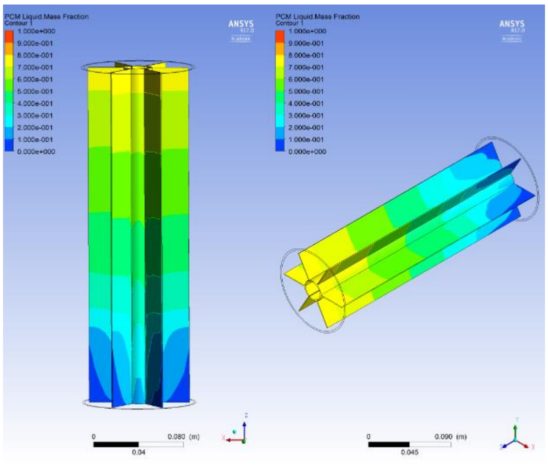

Case 12

(a) Liquid fraction contours for cases (7 to 12) at 6 min.

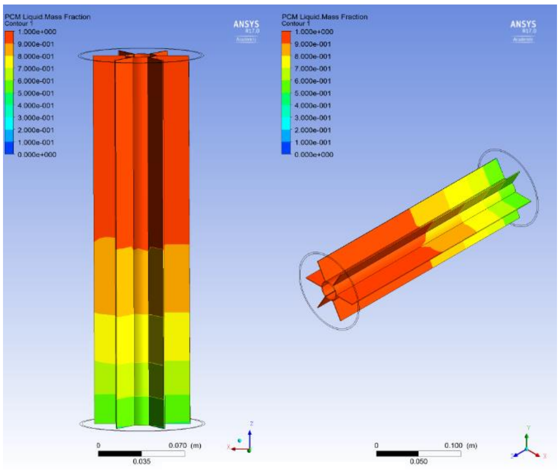

Case 7

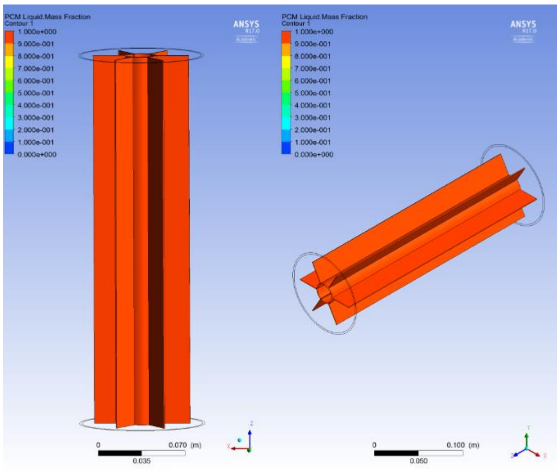

Case 8

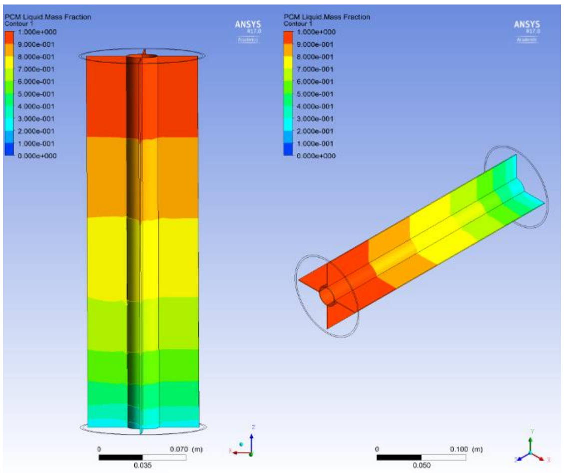

Case 9

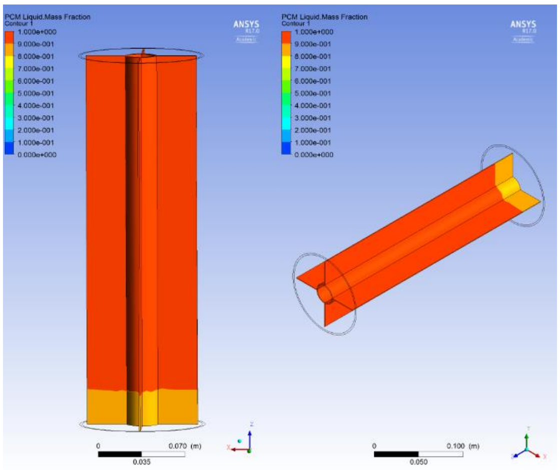

Case 10

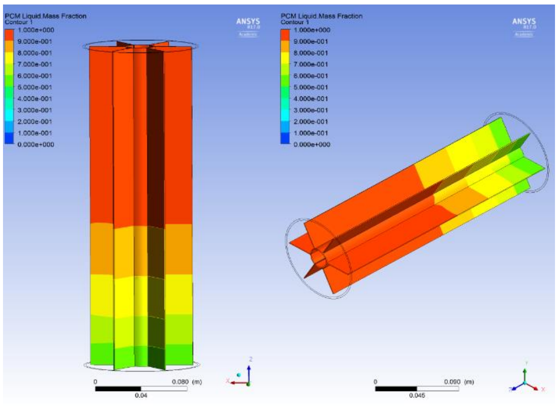

Case 11

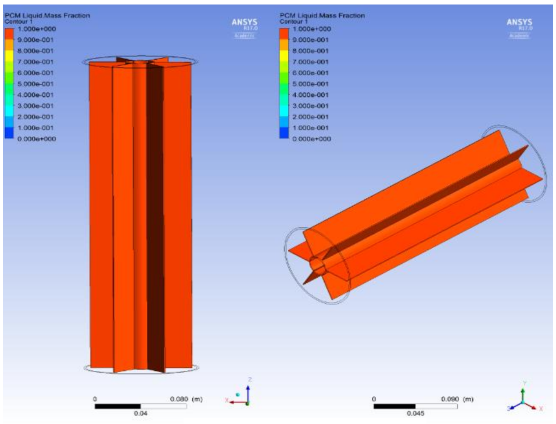

Case 12

(b) Liquid fraction contours for cases (7 to 12) at 24 min.

Figure 6-26 shows the liquid mass fraction contours for cases (7 to 12) at (a) 6 min., (b) at 24 min.

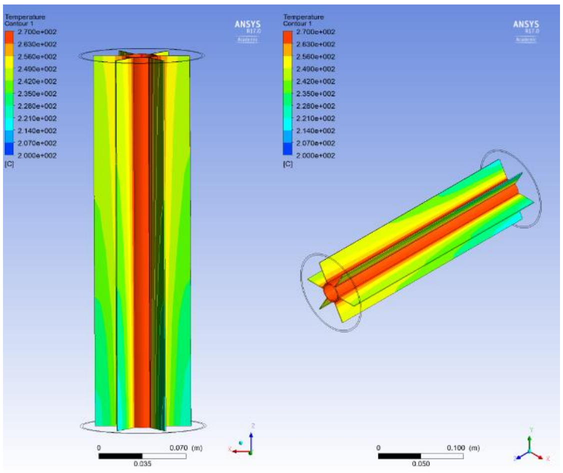

Case 7

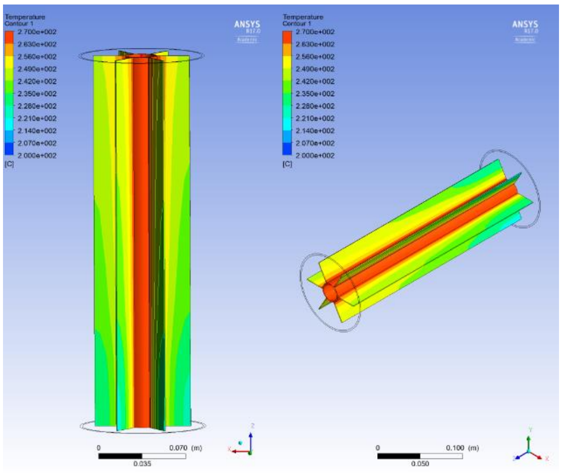

Case 8

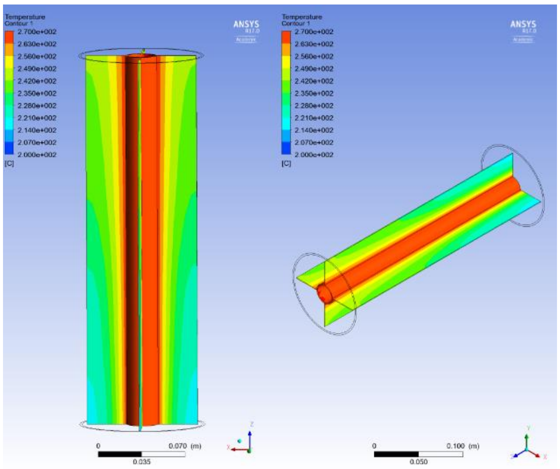

Case 9

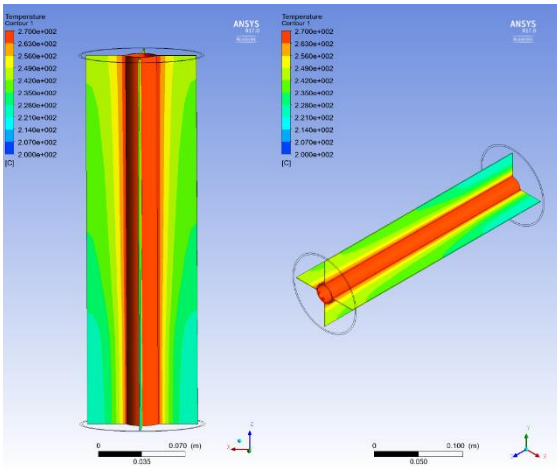

Case 10

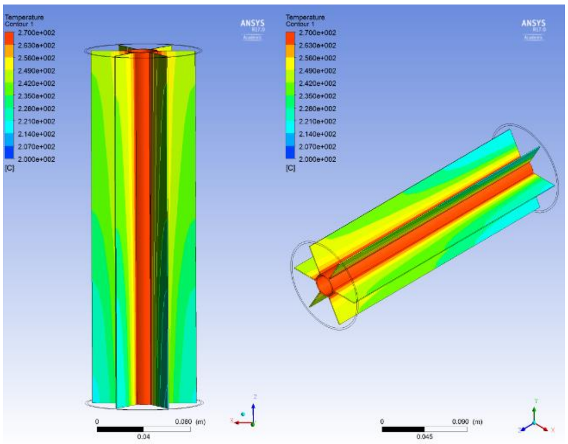

Case 11

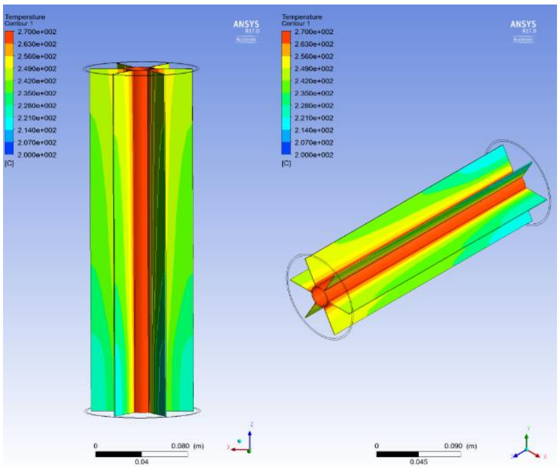

Case 12

(a) Temperature contours for cases (7 to 12) at 6 min.

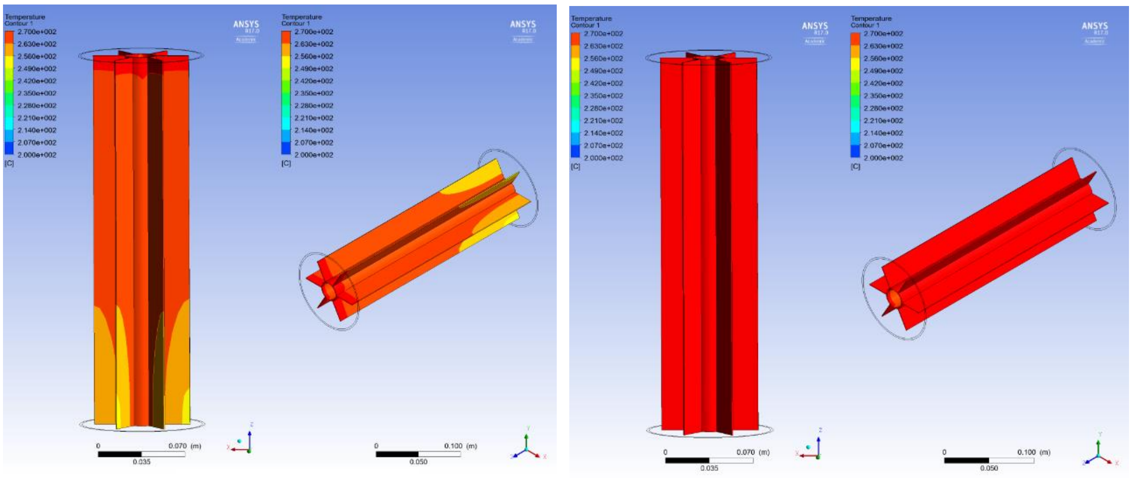

Case 7

Case 8

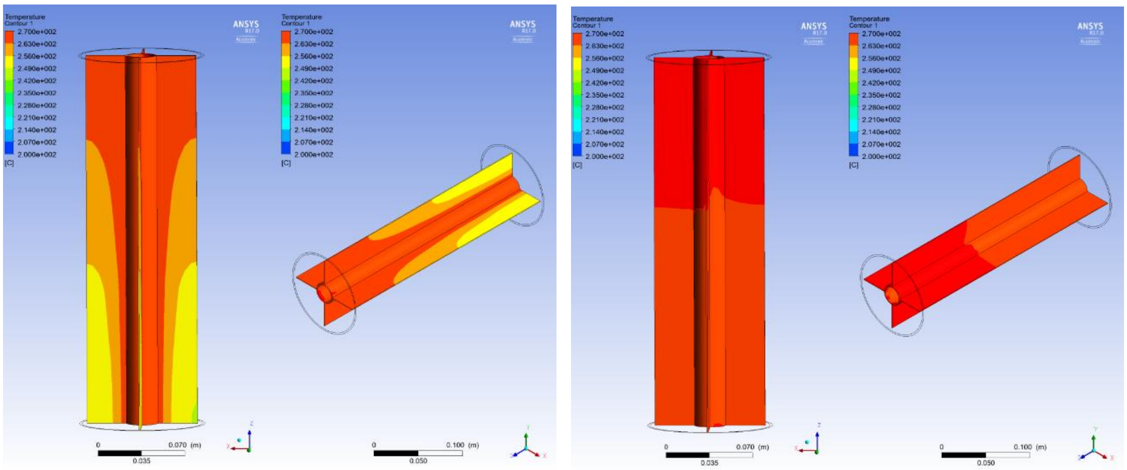

Case 9

Case 10

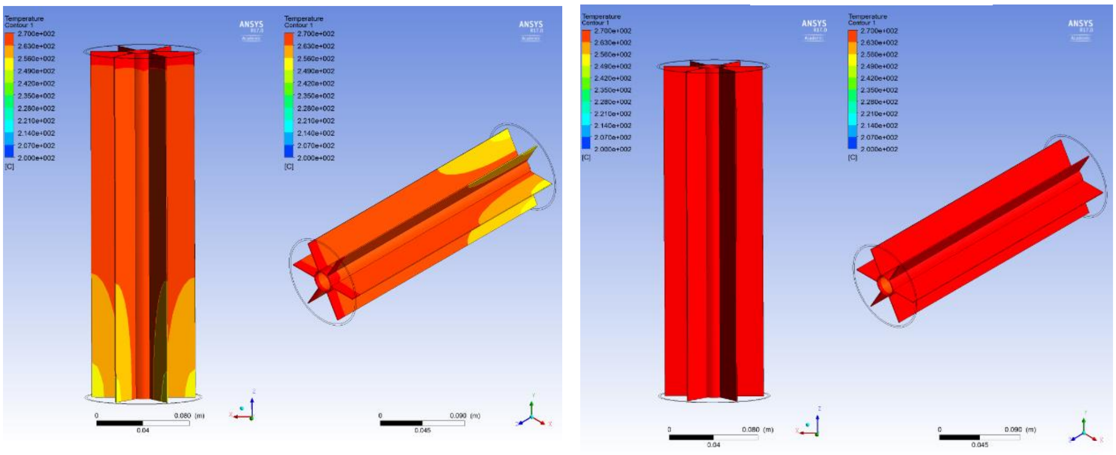

Case 11

Case 12

(b) Temperature contours for cases (7 to 12) at 36 min.

Figure 6-27 shows temperature contours for cases (7 to 12) at (a) 6 min, (b) 36 min.

The temperature distribution at the axial direction of Z1 is shown in Figure (6-28). It can be concluded that the higher increase of fins length to 32 mm does not show higher improvements in the charging process than the other cases of 26 mm. For instance, similar temperature distributions are observed between cases 7 and 11, 8 and 12 while there are some differences between cases 3 and 9, 4 and 10.

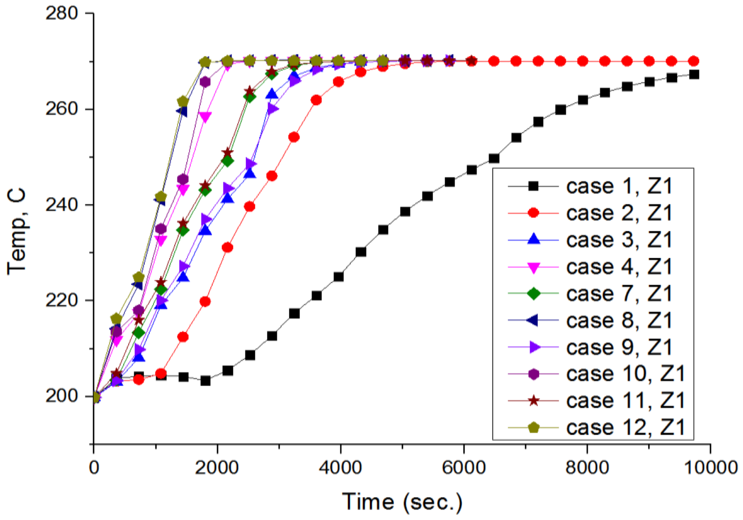

Figure 6-28 shows the transient temperature distributions at the axial direction of Z1, for cases 1 to 4 and 7 to 12.

Figure (6-29) shows similar behaviour to that of Figure (6-28) but for the liquid fraction. For examples, Figure (6-30) shows a comparison between cases 7 and 8 that have been conducted showing little or no differences between cases 7 and 11 over the different temperatures measurements at different axial directions (Z1 to Z6).

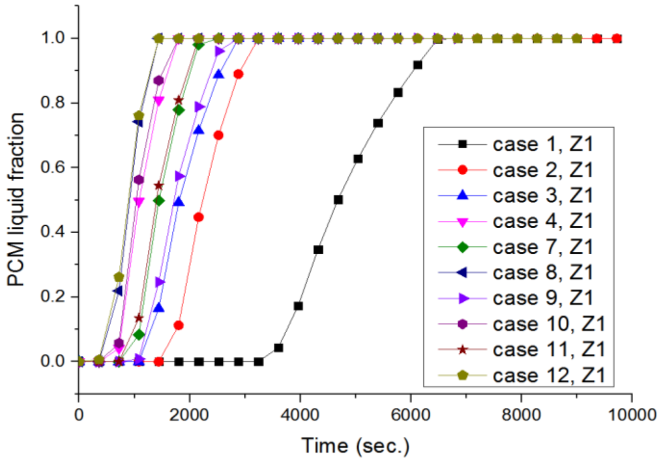

Figure 6-29 shows the liquid mass fraction at the axial direction of Z1, for cases 1 to 4 and 7 to 12.

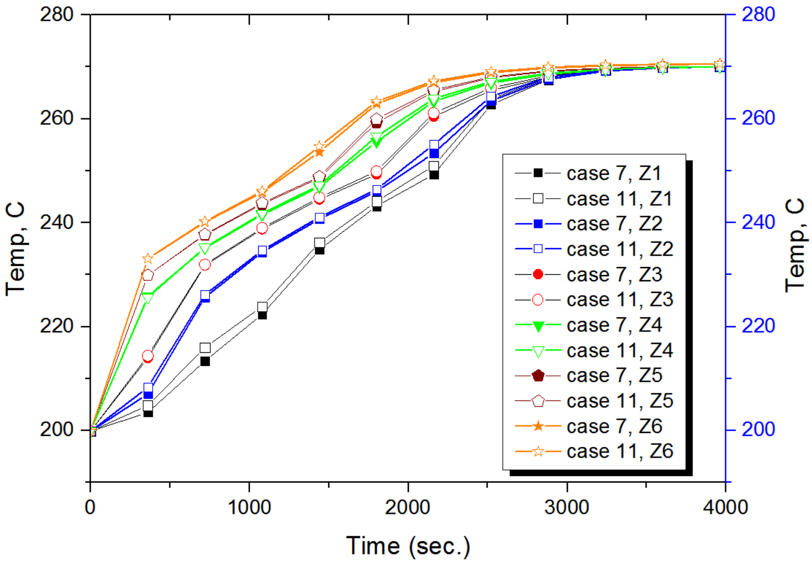

Figure 6-30 shows the transient temperature distributions at the different axial direction for two different cases 7 and 11.

Similarly to Figure (6-30), Figure (6-31) demonstrates the difference between cases 8 and 12 where little or no differences are concluded. This suggests that increasing the fins' length could lead to a longer charging process because the longer fins would highly suppress the natural convection, and hence affect negatively on the heat transfer. The effect of fins on natural convection is related to the fins shapes, dimensions or numbers. The case of thin fins does not have a large effect on natural convection, where the fins used in this study in this chapter were thin fins with 1 mm thickness.

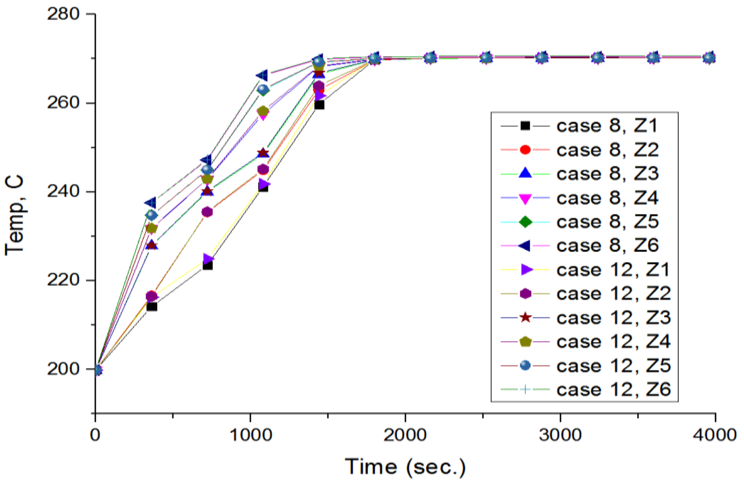

Figure 6-31 shows the transient temperature distributions at the different axial direction for two different cases 8 and 12. Similar behaviour between cases (10 and 4) and (3 and 9)

On the other hand, a comparison between case 7 of finned PCM and case 8 of finned nanoPCM is conducted in Figure (6-32). It is clearly noticeable that the nanosalt-finned system far better than the salt-finned system where in case 8 PCM reaches the maximum input temperature (270 ^{0}C) less than 2000 seconds while around 3000 seconds is needed to reach the maximum input temperature in case 7, as shown in Figure (6-32). This clarifies the powerful effect of both nanoparticles and finned structures in the storage system where a shorter time is required to complete the charging process due to higher conductivity of both nanosalt and fins structure, and the higher thermophysical properties such as latent heat and cp of nanosalt.

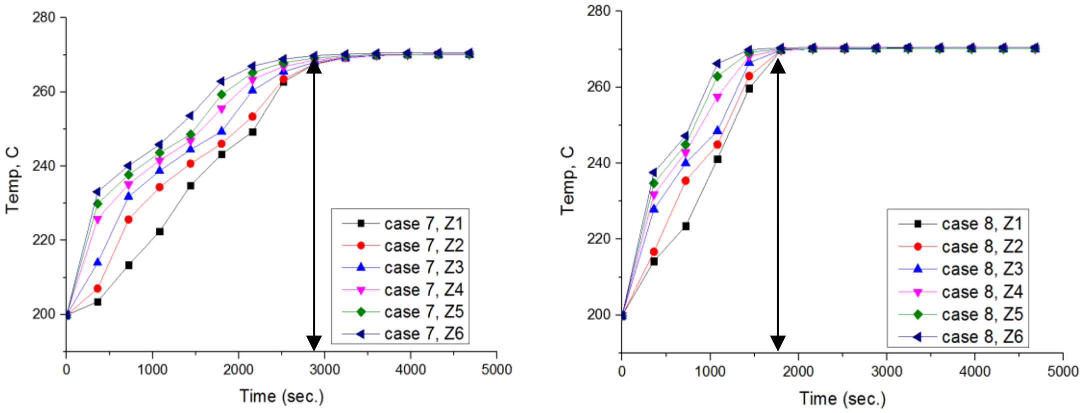

Figure 6-32 shows transient temperature distributions for salt and fins, and nanosalt and Fins structure together in the storage system of cases 7 and 8 at different axial direction (Z1 to Z6) at same radial direction.

Liquid mass fraction profiles of different cases are shown in Figure (6-33) which indicates no differences between cases 8 and 12 as explained earlier in Figures (6-28 and 6-29).

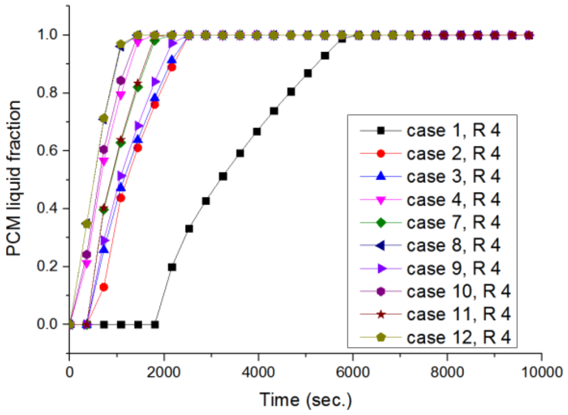

Figure 6-33 Shows liquid mass fraction for different cases (1 to 4 and 7 to 12) at the radial direction of R4 with same axial direction.

At different radial directions, Figure (6-34) indicates that there are no or little differences in temperature distributions in cases 7 and 11. This clarifies the effect of optimum fins structure design where the length of fins affects the melting process.

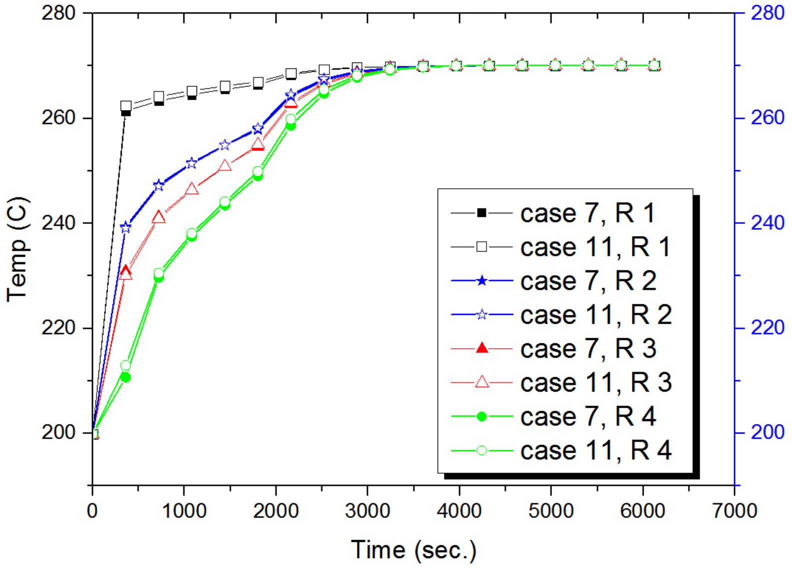

Figure 6-34 shows the transient temperature distributions at different radial directions for two different cases 7 and 11.

Figure (6-35) shows a comparison between case 7 (PCM in finned system) and case 8 (nanoPCM in finned system). Case 8 is far better than case 7 in conducting heat at different radial directions in a shorter time. This is because case 8 has higher thermophysical properties of nanoPCM than case 7.

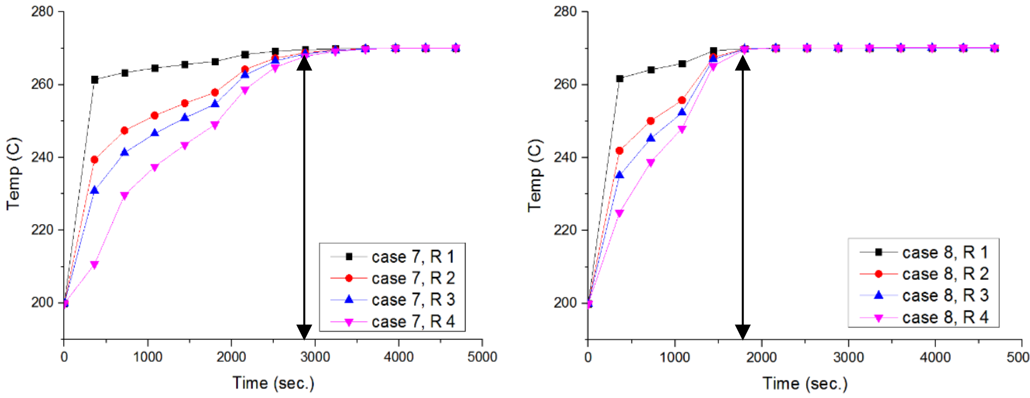

Figure 6-35 shows transient temperature distributions for salt and fins or nanosalt and Fins structure together in the storage system of cases 7 and 8 at different radial direction (R1 to R4) with same axial direction.

Moreover, Figure (6-36) shows liquid mass fraction measurements in CFD-post at the deepest point. As explained above both of cases 8 and 12 show very little differences due to the effect of fins length.

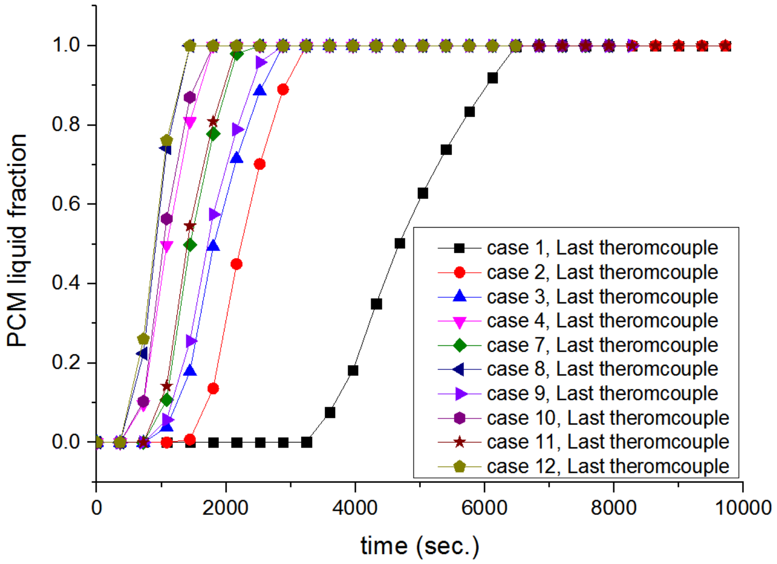

Figure 6-36 shows liquid mass fraction for cases (1 to 4 and 7 to 12) at the deepest point in the storage system and far away from the hot inner pipe.

Temperature measurements around the fins structure using points near to the fin top and bottom are shown in Figures (6-37 and 6-38). It can be concluded that there are no differences between cases 7 and 11, and cases 8 and 12. In the beginning, the temperature increases very fast then the rate of increase starts to be gradual. This is because at the beginning conduction dominates the melting process and as soon as the PCM starts melting a thick layer of melted PCM is formed. Due to density differences the solid PCM sinks while liquid PCM flows to the top. Fins improve the charging process far better than case 1 or 2. These improvements depend on the length and number of fins.

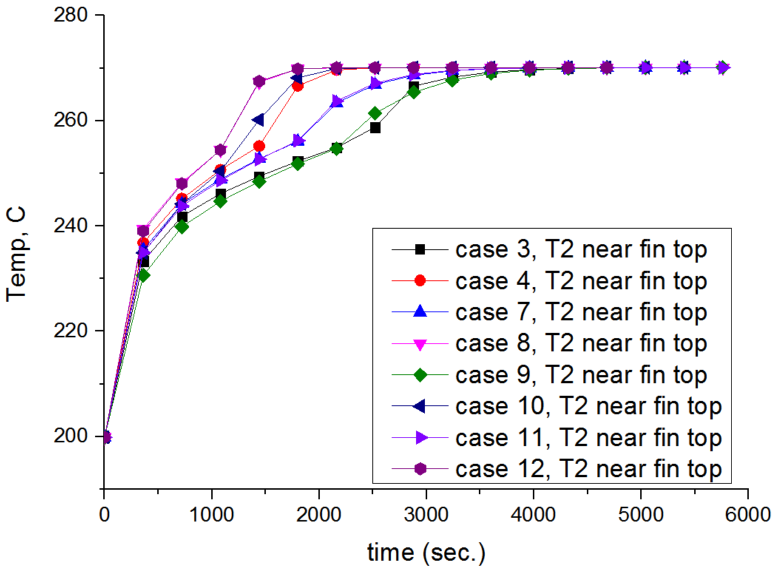

Figure 6-37 shows the transient temperature distributions for the same location of thermocouples among the cases 3, 4 and 7 to 12.

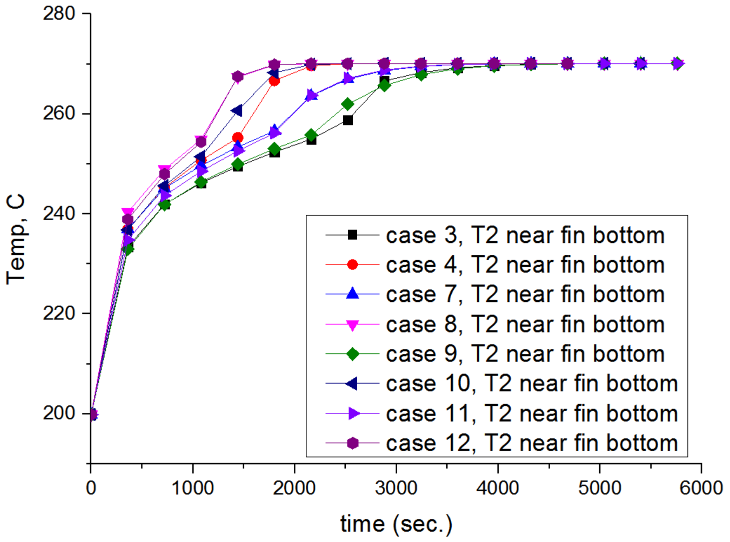

Figure 6-38 shows the transient temperature distributions for the same location of thermocouples among the cases 3, 4 and 7 to 12.

Figure (6-39) shows a comparison among the different cases of fins structure showing that cases 8 and 12 are the best in term of improving the melting process of PCM.

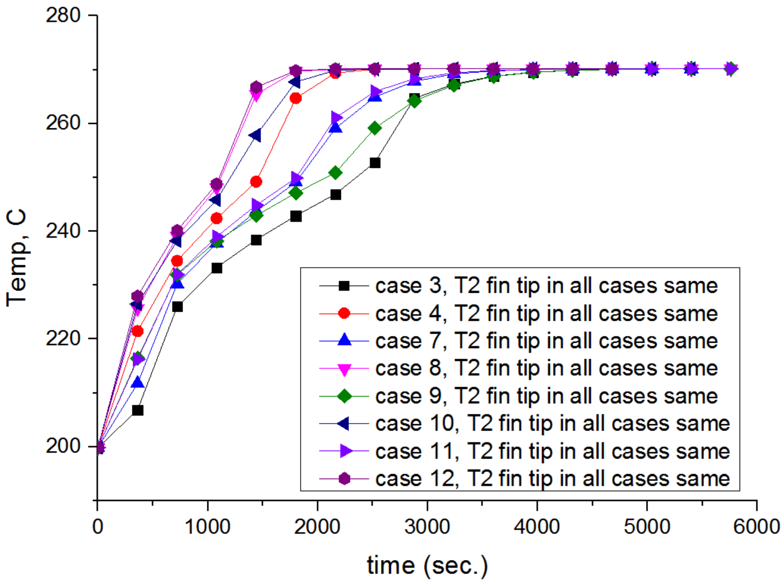

Figure 6-39 shows the transient temperature distributions for the same location of thermocouples among the cases 3, 4 and 7 to 12.

Figure (6-40) shows similar behaviour obtained by Figure (6-39) for a liquid mass fraction. Figure (6-41) shows a comparison of the same fins structure but the different base material (salt or nanosalt) using cases 7 and 11 and 8 and 12 for this comparison. In case of salt as the base material, a longer time is required to disturb the heat from the hot medium toward the salt while faster in case of nanosalt. This is due to the combined effect of the fin structure and nanosalt which in turn improves the melting process by reducing the charging time up to 79.412 %, as shown in Table (6-5).

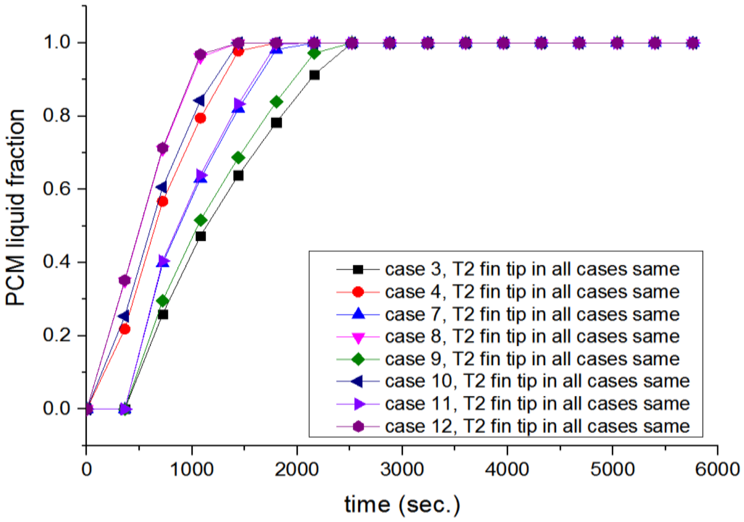

Figure 6-40 shows the liquid mass fraction for the same location of thermocouples among the cases 3, 4 and 7 to 12.

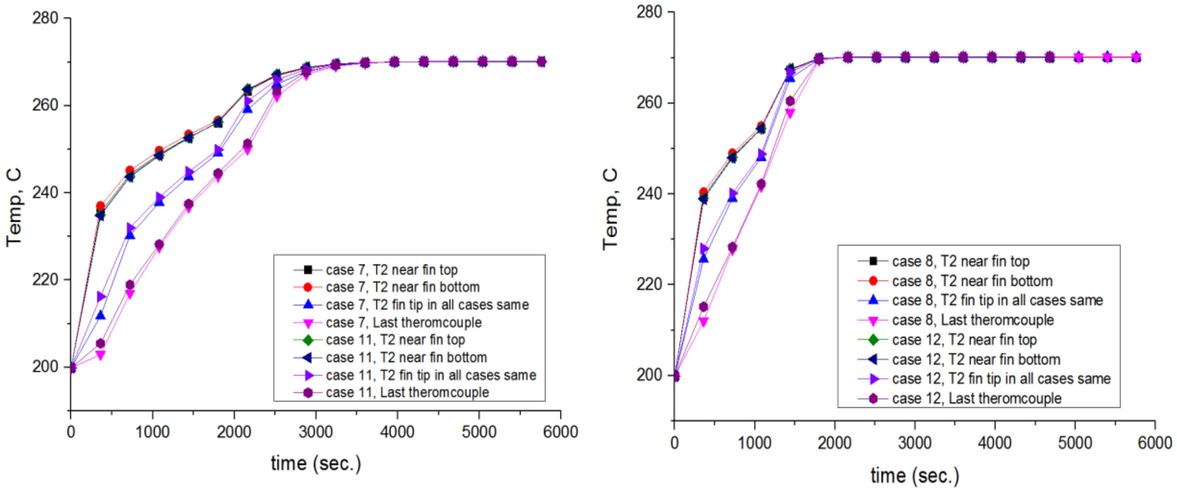

Figure 6-41 shows the transient temperature distributions for cases of salt and fins structure (cases 7 and 11) and nanosalt and fins structure together (cases 8 and 12).

Table 6-5 shows the reduction in melting time for different cases (cases 1 to 4 and 7 to 12)

Case	Melting time, sec.	Reduction in melting time, sec.	Reduction in melting time, %
Case 1 Base case	6120	-	-
Case 2 nanosalt	3600	2520	41.176 %
Case 3	3240	2880	47.059 %
Case 4	1800	4320	70.588%
Case 7	2040	4080	66.67 %
Case 8	1260	4860	79.412 %
Case 9	2400	3720	60.78 %
Case 10	1500	4620	75.49 %
Case 11	1980	4140	67.647 %
Case 12	1260	4860	79.412%

In all cases, fins are more promising in decreasing the charging time than un-finned storage systems. Furthermore, nanosalts inside a finned pipe are even more promising where a shorter period of time is required to finish the melting process. The length of fins showed an effect on the melting process of salt/nanosalt where 26 mm is the optimum fins length.

Equations (6-5, 6-6, and 6-7), which are discussed in Chapter 4, demonstrate that any increase in Rayleigh number would result in an increase in the heat transfer coefficient causing an improvement in convection heat transfer mode during the charging process of salt/nanosalt. However, this increment is dependent on thermophysical values such as density, temperature difference, characteristic length, specific heat capacity, thermal conductivity and viscosity. It is clear that both thermophysical properties and geometrical parameters (characteristic length) have an impact on the natural convection mode and they are changed depending on the geometry of each case studied without (case 1 or 2) or with different fins arrangements (cases 3 to 12).

$$\mathrm{Ra} = \frac{\mathrm{g}\rho^2\beta\,\Delta\mathrm{T}\,\mathrm{L_c}}{\mu}\frac{\mathrm{cp}}{\mathrm{k_{avg}}}$$ **Equation 6-5**

$$\mathrm{Nu} = 0.304\,\mathrm{Ra}^{0.27}$$ **Equation 6-6**

$$\mathrm{h} = \mathrm{Nu} * \mathrm{k}/\mathrm{L}$$ **Equation 6-7**

In all cases of fins structure, the effect of conduction is high enough to overcome any suppression of natural convection and this is why the fins cases (case 3 to 12) show improvements in charging process over case 1.

6.6 Conclusions

The effect of nanoparticles or fin structures or the combined effect of fins and nanoparticles on the charging process of PCM are studied. Different fins arrangements with the same surface area or different surface area with different fin lengths and fins numbers were conducted.

Two different sections where studied. The first section employed the same surface area of fins structure with different arrangements. The arrangements of fins depend on the length and number of fins. It is concluded that shorter fins with higher number show faster charging than longer fins with less number of fins. Particularly, case 3 was 26 mm in length and 4 fins were used while in case 5 of 17.2 mm in length and 6 number of fins were used. Additionally, case 3 improved the charging process by 47.059 % while case 5 gives better improvements by 58.824 %.

Further improvements were obtained with the nanosalt-finned system in comparison to nanosalt system or salt-finned system. For instance, case 6 delivered an improvement in charging process by 76.471 % while in case 5 of the salt-finned system was 58.824 %. Although the surface area is same in cases 3 and 5 (or cases 4 and 6), the improvements in charging process were better in case 5 than case 3 (and case 6 than case 4). This demonstrates the effect of arrangements of fins structure on the melting process especially the number of fins which deliver heat from the hot medium towards the PCM medium in many directions in comparison to less number of fins. Additionally, the improvement of conduction process at the early stage of the melting process was noticeable.

The second section was about the different surface area of fins structure. This section studies optimization in term of fins length and numbers on the charging process of salt or nanosalt. Cases (3, 7, 9 and 11) studied different numbers and length of fins structure on the salt-finned system. It can be concluded that case 11 is the best case in term of the faster charging process. The melting time improved by 67.647 %. However, there is no big difference between cases 7 and 11. This is due to the effect of fins length. Where longer fins could be work as an insulator and the optimized length is required. Therefore, case 7 was approximately similar to case 11 in term of improvement of the charging process of the salt-finned system. Further improvements can be obtained when nanoparticles effects are included in the nanosalt-finned system particularly cases (4, 8, 10, and 12). The optimization study showed that case 8 is the best one in term of improving melting time by 79.412 %.

Overall, the best cases were nanosalt- finned storage systems. In particular case 8 showed the highest improvement in the charging process by decreasing the melting time by 79.412%. The fin length was 26 mm and the number of fins was 6 in case 8. Actually, there is only a small difference in the improvement of melting time between case 8 and case 6, which was around 3%.

It can be concluded that nanosalt is better than salt in term of faster melting time. The finned system shows a promising improvement in the charging process of PCM than PCM alone or nanoPCM (nanosalt). Finned nanosalt storage systems should show a remarkable improvement in the solar energy storage system design.

Chapter 7 Conclusions and Recommendations

7.1 Conclusion

Due to the importance of solar energy storage, this research project has focused on the storage medium and the solar energy storage design for high temperature applications. Both thermal conductivity and specific heat capacity of salt need to be improved. There are many highlighted conclusions achieved by this research such as:

1. Different methods to prepare nanosalt were studied. The first method was the conventional 2-step method using water dispersion with purchased nanoparticles. The 2-step method was used to disperse Fe_2O_3, or CuO, or TiO_2 nanoparticles (0.5 wt. %, 1 wt. % and 1.5 wt. %) in single salt (KNO_3) or nitrate binary salt ($NaNO_3$: KNO_3 with 60:40 molar ratio) to achieve good properties for nanosalt samples. The second method was the novel 1-step method which directly prepared CuO nanoparticles inside the molten salt. Different factors for the preparations such as time and temperature were studied in the 1-step method to study the effect of them on the prepared nanoparticles and then on the thermophysical properties of the nanosalt samples. The comparison between these two methods studied and illustrated the energy storage properties in terms of sensible heat, latent heat and the melting temperature. The 1- step method showed a higher increment in case of sensible heat and latent heat than the 2-step method especially with the preparation of CuO-nanosalt at 450 ^{0}C for 1 hour. Furthermore, in most cases, nanoparticles show a good effect on the nanosalt samples and this will lead to improving the energy storage medium. As a result, an improvement in the thermal solar power plant is expected. In summary, the use of nanosalt to store thermal energy in term of charging/discharging processes will be very helpful due to their positive effects on both thermal conductivity and heat capacity.
2. All of cp, $T_{melting}$, latent heat and thermal conductivity of nitrate salts or nanosalts were studied using differential scanning calorimetry and laser flash analysis, respectively. Using Fe_2O_3 nanoparticles, we got a higher improvement of cp up to 11% and thermal conductivity up to 60%. In particular, the latent heat was increased up to 15% with 1 wt. % CuO-binary salt. The storage energy was improved up to 6% with Fe_2O_3

nanoparticles in comparison to solar salt only, which means an increase in the efficiency of the TES system. Moreover, an increase in the sensible energy of nano-KNO_3 by 7.88% was observed.

3. An experimental device was designed and manufactured for the purpose of the heat transfer study of nitrate salt or nano-nitrate salt up to 350 ^{0}C for the first time. A novel study of heat transfer of salt ($NaNO_3$ or binary solar salt) vs nanosalt (0.1 wt. % Fe_2O_3 + salt, 0.5 wt. % Fe_2O_3 + salt, 1 wt. % Fe_2O_3 + salt, 0.5 wt. % CuO + salt) is conducted in an experimental rig for the first time. Temperature profiles at different radial, theta and axial locations are observed. Furthermore, at a fixed radius, a uniform temperature distribution was observed for both salt and nanosalts, as measured at four theta locations (0^0, 90^0, 180^0, and 270^0). The charging time was found to be reduced by nanosalt. Heat conduction is also faster in the nanosalt due to its improved thermal conductivity. Additionally, the cooling time of nanosalt was also reduced due to nanoparticles' presence in comparison to salt alone. All of these results show the advantages of nanosalt as a storage medium for future applications in solar thermal power plants.
4. For the first time, a validation for an experimental rig, which is mentioned in the above point 3, is conducted using CFD software. A melting model was built in the ANSYS CFX software to meet the similar requirements of our experimental work. The enthalpy porosity method has been implemented in the CFX code to model the melting of the PCM. A sensitivity study has been conducted by studying the effect of many parameters such as the mushy zone constant values, thermophysical properties parameters, mesh independence and different time steps. For instance, a sensitivity study was conducted over cp, k, latent heat and K*. It is important to use the correctly measured physical properties in order to get a good prediction and the specific heat per unit volume (ρ * cp) seems to be the most sensitive parameter. Furthermore, the results of K* showed that it is difficult to get a very good quantitative agreement. However, trends appear to be correctly predicted. In summary, a good matching is observed between the experiments and the simulation data.
5. The effect of nanoparticles or fins structure or the combined effect of fins and nanoparticles on the charging process of PCM were studied in Chapter 6. Different fins arrangements with the same surface area or different surface area with different fins length or different fins number were conducted. It can be concluded that nanosalt is better than salt in term of faster melting time. The finned system showed a promising improvement in the charging process of PCM than PCM alone or nanoPCM

(nanosalt). The best case was for the finned nanosalt storage system particularly case 8 showed the highest improvement in the charging process by decreasing the melting time by 79.412 %. Where fin length was 26 mm and the number of fins was 6 in case 8. The same surface area used in cases 3, 4, 5 and 6 shows that case 6 reduced the charging time by 76.471 % with number of fin 6 and fin length was 17.2 mm. Actually, there are no big differences between case 8 and case 6 around 3%. Finned nanosalt storage systems should show a remarkable improvement in the solar energy storage system design.

The general conclusion can be summarized as improving the storage materials' thermophysical properties (using nanoparticles with the nitrate salt) and the optimization of the storage system design (using nanoparticles, fins structure or both of them in the nitrate salt-storage system).

7.2 Recommendations

There are more aspects that can be looked for in order to enhance the solar energy storage system either experimentally or numerically.

1. Consider the effects of hybrid nanoparticles on the nitrate salt using Fe_2O_3 with CuO or any other types of nanoparticles. Then measure thermophysical properties to find whether the hybrid nanoparticles show any improvements or not.
2. Other types or concentrations of nanoparticles could be tested using this experimental rig with other types of salt such as ternary nitrate salt, carbonate salt, etc.
3. Thermal conductivity could be measured over wider ranges of concentration of nanoparticles in the nanosalt sample. This would help to find an optimum concentration value.
4. Find good types of stabilizers that withstand the higher temperature conditions of nanosalts. The stabilizer would help to stabilize nanoparticles in nanosalt sample for a longer period.
5. For the 1-step method, nanoparticles could be prepared in larger amounts by designing furnaces where all fumes produced by the reactions can be disposed of safely. This would produce higher amounts of nanosalt, especially for the large scale applications.

6. For the rig design, change the heat source to a liquid flow rate instead of the heater element. This could be compared with this thesis.
7. The combination of fins and nanosalt can be studied experimentally using this experimental rig.
8. The combination of metal foams and nanosalt can be studied experimentally using this experimental rig.
9. The geometrical parameters, such as length, diameter and orientations of the annular cylinders, could be studied both experimentally and numerically using the ANSYS CFX code which is validated by this thesis.

APPENDIX CFX Program codes for PCM

```
# State file created:  2018/06/26
20:04:34
# Build 17.0 2015.11.13-23.37-135321

LIBRARY:
  CEL:
    EXPRESSIONS:
      Density Mixture = (PCMSol Mass
Fraction / Density solid + PCMLiq Mass
\
        Fraction / Density liquid)^(-1)
      Density Mixture Grav = Density
Mixture * (1-(PCM thermal expansion \
        coefficient*(T-Tref )))
      Equation of Cp liquid = ((c4 is
constant of cp liquid \
        *Temperature)+c5 is constant of
cp liquid)
      Equation of Cp solid = ((c2 is
constant of cp solid \
        *Temperature)-c3 is constant of cp
solid)
      Gravity Force z = (Density Mixture
Grav - Density ref) * -g
      Kperm = Kstar *(1-LiqVolFrac )^2
/(1e-3+(LiqVolFrac) ^3)
      PCMLiq Mass Fraction = min(max(
(Temperature - Tsolidus) / (Tliquidus - \
        Tsolidus), 0),1)
      PCMSol Mass Fraction = 1 -
PCMLiq Mass Fraction
      T outer = 543 [K]
            c2 is constant of cp solid = 6.2
[J kg^-1 K^-2]
      c3 is constant of cp solid = 1410.5
[J kg^-1 K^-1]
      c4 is constant of cp liquid = 1 [J
kg^-1 K^-2]
      c5 is constant of cp liquid = 784.4 [J
kg^-1 K^-1]
          END
  END
  MATERIAL: PCM Liquid
    Material Group = User
    Option = Pure Substance
    PROPERTIES:
      Option = General Material
      EQUATION OF STATE:
        Density = Density liquid
        Molar Mass = 1.0 [kg kmol^-1]
        Option = Value
      END
      SPECIFIC HEAT CAPACITY:
        Option = Value
        Specific Heat Capacity = Equation
of Cp liquid
        Specific Heat Type = Constant
Pressure
      END
      REFERENCE STATE:
        Option = Specified Point
        Reference Pressure = 1 [atm]
        Reference Specific Enthalpy =
PCM Latent Heat
        Reference Temperature = Tref
      END
      TABLE GENERATION:
        Maximum Temperature = 600 [K]
        Minimum Temperature = 300 [K]
      END
      DYNAMIC VISCOSITY:
        Dynamic Viscosity = PCMLiq
viscosity
        Option = Value
      END
      THERMAL CONDUCTIVITY:
        Option = Value
        Thermal Conductivity = PCMLiq
conductivity
      END
      THERMAL EXPANSIVITY:
        Option = Value
        Thermal Expansivity = PCMLiq
thermal expansion coefficient
      END
    END
  END
  MATERIAL: PCM Material
    Constitutive Relation Under
Relaxation = 1.0
    Material Group = User
    Materials List = PCM Liquid,PCM
Solid
    Option = Variable Composition
Mixture
  END
  MATERIAL: PCM Solid
    Material Group = User
```

```
  Option = Pure Substance
  PROPERTIES:
   Option = General Material
   EQUATION OF STATE:
    Density = Density liquid
    Molar Mass = 1.0 [kg kmol^-1]
    Option = Value
   END
   SPECIFIC HEAT CAPACITY:
    Option = Value
    Specific Heat Capacity = Equation
of Cp solid
    Specific Heat Type = Constant
Pressure
   END
   REFERENCE STATE:
    Option = Specified Point
    Reference Pressure = 1 [atm]
    Reference Specific Enthalpy = 0 [J
kg^-1]
    Reference Temperature = Tref
   END
   TABLE GENERATION:
    Maximum Temperature = 600 [K]
    Minimum Temperature = 300 [K]
   END
   DYNAMIC VISCOSITY:
    Dynamic Viscosity = PCMSol
viscosity
    Option = Value
   END
   THERMAL CONDUCTIVITY:
    Option = Value
    Thermal Conductivity = PCMSol
conductivity
   END
   THERMAL EXPANSIVITY:
    Option = Value
    Thermal Expansivity = 0 [K^-1]
   END
  END
 END
 MATERIAL: Steel
  Material Group = CHT Solids,
Particle Solids
  Option = Pure Substance
  Thermodynamic State = Solid
  PROPERTIES:
   Option = General Material
   EQUATION OF STATE:
    Density = 7854 [kg m^-3]
    Molar Mass = 55.85 [kg kmol^-1]
    Option = Value
   END
```

```
   SPECIFIC HEAT CAPACITY:
    Option = Value
    Specific Heat Capacity =
4.34E+02 [J kg^-1 K^-1]
   END
   REFERENCE STATE:
    Option = Specified Point
    Reference Specific Enthalpy = 0
[J/kg]
    Reference Specific Entropy = 0
[J/kg/K]
    Reference Temperature = 25 [C]
   END
   THERMAL CONDUCTIVITY:
    Option = Value
    Thermal Conductivity = 60.5 [W
m^-1 K^-1]
   END
  END
 END
FLOW: Flow Analysis 1
 SOLUTION UNITS:
  Angle Units = [rad]
  Length Units = [m]
  Mass Units = [kg]
  Solid Angle Units = [sr]
  Temperature Units = [K]
  Time Units = [s]
 END
 ANALYSIS TYPE:
  Option = Transient
  EXTERNAL SOLVER COUPLING:
   Option = None
  END
  INITIAL TIME:
   Option = Automatic with Value
   Time = 0 [s]
  END
  TIME DURATION:
   Option = Time per Run
   Time per Run = 10 [h]
  END
  TIME STEPS:
   Option = Timesteps
   Timesteps = 0.05 [s]
  END
 END
 DOMAIN: HTF solid
  Domain Type = Solid
   END
  END
 DOMAIN: PCM
  Domain Type = Fluid
    MASS AND MOMENTUM:
```

```
          Option = No Slip Wall
        END
    FLUID DEFINITION: Fluid 1
      Material = PCM Material
      Option = Material Library
      MORPHOLOGY:
        Option = Continuous Fluid
      END
    END
      COMPONENT: PCM Liquid
        Mass Fraction = PCMLiq Mass
Fraction
        Option = Algebraic Equation
      END
      COMPONENT: PCM Solid
        Mass Fraction = PCMSol Mass
Fraction
        Option = Algebraic Equation
      END
      HEAT TRANSFER MODEL:
        Option = Thermal Energy
      END
      TURBULENCE MODEL:
        Option = Laminar
      END
    END
    SUBDOMAIN: Subdomain 1
      SOURCES:
        MOMENTUM SOURCE:
          GENERAL MOMENTUM
SOURCE:
            Include Coefficient in Rhie
Chow = On
            Momentum Source Coefficient =
-Kperm
            Momentum Source X
Component = -Kperm *u
            Momentum Source Y
Component = -Kperm *v
            Momentum Source Z
Component = -Kperm *w+ Gravity
Force z
            Option = Cartesian Components
            Redistribute in Rhie Chow = On
          END
        END
      END
    END
  END
  DOMAIN: PCM solid
        Domain Type = Solid
    END
      Material = Steel
    RESULTS:
    TRANSIENT RESULTS: Transient
Results 1
      File Compression Level = Default
      Option = Standard
      OUTPUT FREQUENCY:
        Option = Time Interval
        Time Interval = 6 [min]
      END
  SOLVER CONTROL:
    ADVECTION SCHEME:
      Option = High Resolution
    END
    CONVERGENCE CONTROL:
      Maximum Number of Coefficient
Loops = 10
      Minimum Number of Coefficient
Loops = 1
      Timescale Control = Coefficient
Loops
    END
    CONVERGENCE CRITERIA:
      Residual Target = 1.E-4
      Residual Type = RMS
    END
    ELAPSED WALL CLOCK TIME:
      Elapsed Time = 47 [h]
      Option = Maximum Run Time
    END
    TRANSIENT SCHEME:
      Option = Second Order Backward
Euler
      TIMESTEP INITIALISATION:
        Option = Automatic
      END
    END
  END
 COMMAND FILE:
  Version = 17.0
END
```

References

aalborgcsp. 2015. *History of Concentrated Solar Power (CSP).* [Online]. [Accessed 31/05/2018]. Available from: https://www.aalborgcsp.com/business-areas/solar-district-heating/csp-parabolic-troughs/history-of-csp/.

Abdulateef, A.M. et al. 2017. Experimental and computational study of melting phase-change material in a triplex tube heat exchanger with longitudinal/triangular fins. *Solar Energy.* **155**, pp.142-153.

Abedin, A.H. and Rosen, M.A. 2011. A critical review of thermochemical energy storage systems. *Open Renewable Energy J.* **4**, pp.42-46.

Agyenim, F. et al. 2009. A comparison of heat transfer enhancement in a medium temperature thermal energy storage heat exchanger using fins. *Solar Energy.* **83**(9), pp.1509-1520.

Al-Abidi, A. et al. 2016. Heat Transfer Enhancement for PCM Thermal Energy Storage in Triplex Tube Heat Exchanger. *Heat Transfer Engineering.* **37**(7-8), pp.705-712.

Al-Abidi, A.A. et al. 2013a. Numerical study of PCM solidification in a triplex tube heat exchanger with internal and external fins. *International journal of heat and mass transfer.* **61**, pp.684-695.

Al-Abidi, A.A. et al. 2013b. Experimental study of PCM melting in triplex tube thermal energy storage for liquid desiccant air conditioning system. *Energy and Buildings.* **60**, pp.270-279.

Al-Abidi, A.A. et al. 2014. Experimental study of melting and solidification of PCM in a triplex tube heat exchanger with fins. *Energy and Buildings.* **68**, pp.33-41.

Andreu-Cabedo, P. et al. 2014a. Increment of specific heat capacity of solar salt with SiO2 nanoparticles. *Nanoscale research letters.* **9**(1), pp.1-11.

Andreu-Cabedo, P. et al. 2014b. Increment of specific heat capacity of solar salt with SiO 2 nanoparticles. *Nanoscale research letters.* **9**(1), p582.

ANSYS, I. 2009. *ANSYS FLUENT 12.0, Theory Guide.* [Online]. Available from: http://users.ugent.be/~mvbelleg/flth-12-0.pdf.

Arasu, A.V. and Mujumdar, A.S. 2012. Numerical study on melting of paraffin wax with Al2O3 in a square enclosure. *International Communications in Heat and Mass Transfer.* **39**(1), pp.8-16.

Arıcı, M. et al. 2017. Melting of nanoparticle-enhanced paraffin wax in a rectangular enclosure with partially active walls. *International Journal of Heat and Mass Transfer.* **104**, pp.7-17.

Assael, M. et al. 2005. Thermal conductivity enhancement in aqueous suspensions of carbon multi-walled and double-walled nanotubes in the presence of two different dispersants. *International Journal of Thermophysics.* **26**(3), pp.647-664.

Awad, A. et al. 2018a. Latent and sensible energy storage enhancement of nano-nitrate molten salt. *Solar Energy.*

Awad, A. et al. 2018b. Thermal-physical properties of nanoparticle-seeded nitrate molten salts. *Renewable Energy.* **120**, pp.275-288.

Bakker, A. 2002. Lecture 7 – Meshing, Applied Computational Fluid Dynamics, .

Banerjee, D. 2011. Enhancement of heat capacity of molten salt eutectics using inorganic nanoparticles for solar thermal energy applications. *Developments in Strategic Materials and Computational Design II: Ceramic Engineering and Science Proceedings, Volume 32.* (10), p119.

Bhaumik, M. 2012. CFD simulation of SDHW Storage Tank with and without Heater. *International Journal of Advancements in Research & Technology.* **1**(2), pp.124-134.

Bradshaw, R.W. and Siegel, N.P. 2008. Molten nitrate salt development for thermal energy storage in parabolic trough solar power systems. In: *ASME 2008 2nd International Conference on Energy Sustainability collocated with the Heat Transfer, Fluids Engineering, and 3rd Energy Nanotechnology Conferences*: American Society of Mechanical Engineers, pp.631-637.

Cao, X. et al. 2018. Effect of natural convection on melting performance of eccentric horizontal shell and tube latent heat storage unit. *Sustainable Cities and Society.* **38**, pp.571-581.

Castell, A. et al. 2008. Natural convection heat transfer coefficients in phase change material (PCM) modules with external vertical fins. *Applied Thermal Engineering.* **28**(13), pp.1676-1686.

Castell, A. et al. 2006. Effect of using external vertical fins in phase change material modules for domestic hot water tanks. In: *International conference on renewable energies and power quality (ICREPQ'06), Palma de Mallorca*.

Chaitanya, P.S. et al. 2014. Thermal Analysis of Engine Cylinder Fin by Varying Its Geometry and Material. *IOSR Journal of Mechanical and Civil Engineering (IOSR-JMCE) e-ISSN.* pp.2278-1684.

Chen, X. et al. 2016. Numerical simulation of mixed convection heat transfer of molten salt in horizontal square tube with single surface heating. *Applied Thermal Engineering.* **104**, pp.282-293.

Chen, X. et al. 2018. Experimental study on the specific heat and stability of molten salt nanofluids prepared by high-temperature melting. *Solar Energy Materials and Solar Cells.* **176**, pp.42-48.

Chieruzzi, M. et al. 2013a. Effect of nanoparticles on heat capacity of nanofluids based on molten salts as PCM for thermal energy storage. *Nanoscale research letters.* **8**(1), p448.

Chieruzzi, M. et al. 2013b. Effect of nanoparticles on heat capacity of nanofluids based on molten salts as PCM for thermal energy storage. *Nanoscale research letters.* **8**(1), pp.1-9.

Chieruzzi, M. et al. 2017. Heat capacity of nanofluids for solar energy storage produced by dispersing oxide nanoparticles in nitrate salt mixture directly at high temperature. *Solar Energy Materials and Solar Cells.* **167**, pp.60-69.

Chieruzzi, M. et al. 2015a. A new phase change material based on potassium nitrate with silica and alumina nanoparticles for thermal energy storage. *Nanoscale research letters.* **10**(1), p273.

Chieruzzi, M. et al. 2015b. A New Phase Change Material Based on Potassium Nitrate with Silica and Alumina Nanoparticles for Thermal Energy Storage. *Nanoscale research letters.* **10**(1), pp.1-10.

Chieruzzi, M. et al. 2015c. A new phase change material based on potassium nitrate with silica and alumina nanoparticles for thermal energy storage. *Nanoscale research letters.* **10**(1), p1.

Chol, S. 1995. Enhancing thermal conductivity of fluids with nanoparticles. *ASME-Publications-Fed.* **231**, pp.99-106.

Dasgupta, T. and Umarji, A. 2005. Apparatus to measure high-temperature thermal conductivity and thermoelectric power of small specimens. *Review of scientific instruments.* **76**(9), p094901.

Devaradjane, R. and Shin, D. 2012. Enhanced Heat Capacity of Molten Salt Nano-Materials for Concentrated Solar Power Application. In: *ASME 2012 International Mechanical Engineering Congress and Exposition*: American Society of Mechanical Engineers, pp.269-273.

Dhaidan, N.S. et al. 2013a. Experimental and numerical investigation of melting of phase change material/nanoparticle suspensions in a square container subjected to a constant heat flux. *International Journal of Heat and Mass Transfer.* **66**, pp.672-683.

Dhaidan, N.S. et al. 2013b. Experimental and numerical study of constrained melting of n-octadecane with CuO nanoparticle dispersions in a horizontal cylindrical capsule subjected to a constant heat flux. *International Journal of Heat and Mass Transfer.* **67**, pp.523-534.

Dhaidan, N.S. et al. 2013c. Experimental and numerical investigation of melting of NePCM inside an annular container under a constant heat flux including the effect of eccentricity. *International Journal of Heat and Mass Transfer.* **67**, pp.455-468.

Dudda, B. and Shin, D. 2013. Effect of nanoparticle dispersion on specific heat capacity of a binary nitrate salt eutectic for concentrated solar power applications. *International Journal of Thermal Sciences.* **69**, pp.37-42.

Eck, M. et al. 2008b. The potential of direct steam generation in parabolic troughs – Results of the German Project DIVA. In: Proceedings of the 14th Biennial CSP SolarPACES Symposium, Las Vegas, USA.

Einarsrud, M.-A. and Grande, T. 2014. 1D oxide nanostructures from chemical solutions. *Chemical Society Reviews.* **43**(7), pp.2187-2199.

Elgafy, A. and Lafdi, K. 2005. Effect of carbon nanofiber additives on thermal behavior of phase change materials. *Carbon.* **43**(15), pp.3067-3074.

Ercole, D. et al. 2017. An investigation of thermal characteristics of eutectic molten salt-based nanofluids. *International Communications in Heat and Mass Transfer.* **87**, pp.98-104.

Esapour, M. et al. 2016. Numerical study on geometrical specifications and operational parameters of multi-tube heat storage systems. *Applied Thermal Engineering.* **109**, pp.351-363.

Esen, M. and Ayhan, T. 1996. Development of a model compatible with solar assisted cylindrical energy storage tank and variation of stored energy with time for different phase change materials. *Energy Conversion and Management.* **37**(12), pp.1775-1785.

Faghri, A.Z., Yuwen; Howell,John 2010. *Advanced Heat and Mass Transfer.*

Fan, L.-W. et al. 2014. Heat transfer during melting of graphene-based composite phase change materials heated from below. *International Journal of Heat and Mass Transfer.* **79**, pp.94-104.

Fang, Y. et al. 2017. Experimental study of the thermal characteristics of microencapsulated phase change composite cylinders. *Applied Thermal Engineering.* **114**, pp.1256-1264.

Farid, M. et al. 1989. The role of natural convection during melting and solidification of PCM in a vertical cylinder. *Chemical Engineering Communications.* **84**(1), pp.43-60.

Feldhoff, J.F. et al. 2010. Economic potential of solar thermal power plants with direct steam generation compared with HTF plants. *Journal of Solar Energy Engineering.* **132**(4), p041001.

Feldhoff, J.F. et al. 2012. Comparative system analysis of direct steam generation and synthetic oil parabolic trough power plants with integrated thermal storage. *Solar Energy.* **86**(1), pp.520-530.

Fleischer, A.S. 2015. *Thermal Energy Storage Using Phase Change Materials: Fundamentals and Applications.* Springer.

Fox, E.B. et al. 2013. Thermophysical properties of nanoparticle-enhanced ionic liquids (NEILs) heat-transfer fluids. *Energy & Fuels.* **27**(6), pp.3385-3393.

Gechuanqi, P. et al. 2014. The Simulation of the Steady-state Concentric Cylinder Method for Determining Thermal Conductivity of Sodium Nitrate. *Energy Procedia.* **61**, pp.459-462.

Gharebaghi, M. and Sezai, I. 2007. Numerical investigation of a phase change material (PCM) module with internal fins. In: *ASME/JSME 2007 Thermal Engineering Heat Transfer Summer Conference collocated with the ASME 2007 InterPACK Conference*: American Society of Mechanical Engineers, pp.115-120.

Gibout, S. et al. 2018. Challenges of the Usual Graphical Methods Used to Characterize Phase Change Materials by Differential Scanning Calorimetry. *Applied Sciences.* **8**(1), p66.

Gimenez-Gavarrell, P. et al. 2015. Latent Heat of Fusion and Melting Temperature of Molten Salt Based Carbon Nanotube Suspensions Used as Phase Change Materials. In: *ASME 2015 9th International Conference on Energy Sustainability collocated with the ASME 2015 Power Conference, the ASME 2015 13th International Conference on Fuel Cell Science, Engineering and Technology, and the ASME 2015 Nuclear Forum*: American Society of Mechanical Engineers, pp.V001T10A005-V001T10A005.

Gin, B. et al. 2011. Modeling of phase change material implemented into cold storage application. *HVAC&R Research.* **17**(3), pp.257-267.

Gowreesunker, B. et al. 2012. Improved simulation of phase change processes in applications where conduction is the dominant heat transfer mode. *Energy and Buildings.* **47**, pp.353-359.

Ho, C. and Gao, J. 2013. An experimental study on melting heat transfer of paraffin dispersed with Al2O3 nanoparticles in a vertical enclosure. *International Journal of Heat and Mass Transfer.* **62**, pp.2-8.

Ho, C.J. et al. 2010. Natural convection heat transfer of alumina-water nanofluid in vertical square enclosures: An experimental study. *International Journal of Thermal Sciences.* **49**(8), pp.1345-1353.

Ho, M.X. and Pan, C. 2014. Optimal concentration of alumina nanoparticles in molten Hitec salt to maximize its specific heat capacity. *International Journal of Heat and Mass Transfer.* **70**, pp.174-184.

Hossain, M.S. et al. 2015. Analysis of Thermal Characteristics of Flared and Rectangular Fin Profiles by Using Finite Element Method.

Hosseini, M.J. et al. 2014. Experimental and computational evolution of a shell and tube heat exchanger as a PCM thermal storage system. *International Communications in Heat and Mass Transfer.* **50**, pp.128-136.

Hosseini, M.J. et al. 2015. Experimental and numerical evaluation of longitudinally finned latent heat thermal storage systems. *Energy and Buildings.* **99**, pp.263-272.

Hosseini, S.M.J. et al. 2013. Melting of nanoprticle-enhanced phase change material inside shell and tube heat exchanger. *Journal of Engineering.* **2013**.

Hosseinizadeh, S. et al. 2012. Numerical investigations of unconstrained melting of nano-enhanced phase change material (NEPCM) inside a spherical container. *International Journal of Thermal Sciences.* **51**, pp.77-83.

Hu, Y. et al. 2017. Effect of Al2O3 nanoparticle dispersion on the specific heat capacity of a eutectic binary nitrate salt for solar power applications. *Energy Conversion and Management.* **142**, pp.366-373.

Hwang, Y. et al. 2006. Investigation on characteristics of thermal conductivity enhancement of nanofluids. *Current Applied Physics.* **6**(6), pp.1068-1071.

Ismail, K.A.R. et al. 2001. Numerical and experimental study on the solidification of PCM around a vertical axially finned isothermal cylinder. *Applied Thermal Engineering.* **21**(1), pp.53-77.

Janz, G. et al. 1972. Molten salts: Volume 3 nitrates, nitrites, and mixtures: Electrical conductance, density, viscosity, and surface tension data. *Journal of Physical and Chemical Reference Data.* **1**(3), pp.581-746.

Janz, G.J. et al. 1979. *Physical properties data compilations relevant to energy storage. II. Molten salts: data on single and multi-component salt systems.* NATIONAL STANDARD REFERENCE DATA SYSTEM.

Jesumathy, S. et al. 2012. Experimental study of enhanced heat transfer by addition of CuO nanoparticle. *Heat and Mass Transfer.* **48**(6), pp.965-978.

Jo, B. and Banerjee, D. 2011. Interfacial thermal resistance between a carbon nanoparticle and molten salt eutectic: effect of material properties, particle shapes and sizes. In: *ASME/JSME 2011 8th Thermal Engineering Joint Conference*: American Society of Mechanical Engineers, pp.T30084-T30084-7.

Jo, B. and Banerjee, D. 2014. Enhanced specific heat capacity of molten salt-based nanomaterials: Effects of nanoparticle dispersion and solvent material. *Acta Materialia.* **75**, pp.80-91.

Jo, B. and Banerjee, D. 2015. Enhanced Specific Heat Capacity of Molten Salt-based Carbon Nanotubes Nanomaterials. *Journal of Heat Transfer.* **137**(9), p091013.

Jung, S. and Banerjee, D. 2011. Enhancement of heat capacity of nitrate salts using mica nanoparticles. *Dev Strateg Mater Comput Des II: Ceram Eng Sci Proc.* **32**, pp.127-137.

Kamkari, B. and Shokouhmand, H. 2014. Experimental investigation of phase change material melting in rectangular enclosures with horizontal partial fins. *International Journal of Heat and Mass Transfer.* **78**, pp.839-851.

Kheirabadi, A.C. and Groulx, D. 2015. The effect of the mushy-zone constant on simulated phase change heat transfer. In: *ICHMT DIGITAL LIBRARY ONLINE*: Begel House Inc.

Khodadadi, J. and Hosseinizadeh, S. 2007. Nanoparticle-enhanced phase change materials (NEPCM) with great potential for improved thermal energy storage. *International communications in heat and mass transfer.* **34**(5), pp.534-543.

Kong, L.B. et al. 2014. *Waste Energy Harvesting.* Springer.

Kramer, C.M. and Wilson, C.J. 1980. The phase diagram of NaNO3—KNO3. *Thermochimica Acta.* **42**(3), pp.253-264.

Laing, D. et al. 2009. Advanced high temperature latent heat storage system–design and test results. In: *The 11th International Conference on Thermal Energy Storage–Effstock*, pp.14-17.

Lasfargues, M. 2014. *Nitrate based high temperature nano-heat-transfer-fluids: formulation & characterisation*. thesis, University of Leeds.

Lasfargues, M. et al. 2016. In situ production of titanium dioxide nanoparticles in molten salt phase for thermal energy storage and heat-transfer fluid applications. *Journal of Nanoparticle Research.* **18**(6), p150.

Lasfargues, M. et al. 2015. Mechanical dispersion of nanoparticles and its effect on the specific heat capacity of impure binary nitrate salt mixtures. *Nanomaterials.* **5**(3), pp.1136-1146.

Lasfargues, M. et al. 2017. In Situ Production of Copper Oxide Nanoparticles in a Binary Molten Salt for Concentrated Solar Power Plant Applications. *Materials.* **10**(5), p537.

Lee, S. et al. 1999. Measuring thermal conductivity of fluids containing oxide nanoparticles. *Journal of Heat Transfer.* **121**(2), pp.280-289.

Li, W. et al. 2012. Experimental and numerical studies on melting phase change heat transfer in open-cell metallic foams filled with paraffin. *Applied Thermal Engineering.* **37**, pp.1-9.

Liu, M. et al. 2012. Review on storage materials and thermal performance enhancement techniques for high temperature phase change thermal storage systems. *Renewable and Sustainable Energy Reviews.* **16**(4), pp.2118-2132.

Liu, M. et al. 2016. Review on concentrating solar power plants and new developments in high temperature thermal energy storage technologies. *Renewable and Sustainable Energy Reviews.* **53**, pp.1411-1432.

Liu, S. et al. 2013. Development of a novel molten-salt filled with nanoparticles for concentration solar plants.

Liu, Y.-D. et al. 2009. Experimental study of thermal conductivity and phase change performance of nanofluids PCMs. *Microfluidics and Nanofluidics.* **7**(4), pp.579-584.

Liu, Z. et al. 2005. Experimental study of the characteristics of solidification of stearic acid in an annulus and its thermal conductivity enhancement. *Energy Conversion and Management.* **46**(6), pp.971-984.

Longeon, M. et al. 2013. Experimental and numerical study of annular PCM storage in the presence of natural convection. *Applied Energy.* **112**, pp.175-184.

Louie, B.M. 2011. Design of a steady state thermal conductivity measurement device for CNT RET polymer composites.

Lu, M.-C. and Huang, C.-H. 2013. Specific heat capacity of molten salt-based alumina nanofluid. *Nanoscale research letters.* **8**(1), pp.1-7.

Luo, Y. et al. 2017. Thermal energy storage enhancement of a binary molten salt via in-situ produced nanoparticles. *International Journal of Heat and Mass Transfer.* **104**, pp.658-664.

Lv, M. et al. 2008. Numerical Simulation on Melting and Solidification of a Phase-Change Material in an Aluminum Plate-Fin Thermal Storage. In: *ASME 2008 Heat Transfer Summer Conference collocated with the Fluids Engineering, Energy Sustainability, and 3rd Energy Nanotechnology Conferences*: American Society of Mechanical Engineers, pp.479-484.

Mahdi, J.M. and Nsofor, E.C. 2016. Solidification of a PCM with nanoparticles in triplex-tube thermal energy storage system. *Applied Thermal Engineering.* **108**, pp.596-604.

MALIK, D.R. 2010. *Evaluation of composite alumina nanoparticle and nitrate eutectic materials for use in concentrating solar power plants*. thesis, Texas A&M University.

Manzano-Agugliaro, F. et al. 2013. Scientific production of renewable energies worldwide: An overview. *Renewable and Sustainable Energy Reviews.* **18**, pp.134-143.

Mao, Q. 2016. Recent developments in geometrical configurations of thermal energy storage for concentrating solar power plant. *Renewable and Sustainable Energy Reviews.* **59**, pp.320-327.

Mat, S. et al. 2013. Enhance heat transfer for PCM melting in triplex tube with internal–external fins. *Energy Conversion and Management.* **74**, pp.223-236.

McDonald, J. and Davis, H.T. 1971. Determination of the Thermal Conductivities of Several Molten Alkali Halides by Means of a Sheathed Hot-Wire Technique. *Physics and Chemistry of Liquids.* **2**(3), pp.119-134.

Mehling, H. and Cabeza, L.F. 2008. *Heat and cold storage with PCM.* Springer.

Mintsa, H.A. et al. 2009. New temperature dependent thermal conductivity data for water-based nanofluids. *International Journal of Thermal Sciences.* **48**(2), pp.363-371.

Mondal, S. 2008. Phase change materials for smart textiles–an overview. *Applied Thermal Engineering.* **28**(11), pp.1536-1550.

Muhammad, M. et al. 2015a. CFD modeling of the charging and discharging of a shell-and-tube latent heat storage system for high-temperature applications. *Numerical Heat Transfer, Part A: Applications.* **68**(8), pp.813-826.

Muhammad, M. et al. 2015b. Validation of a CFD melting and solidification model for phase change in vertical cylinders. *Numerical Heat Transfer, Part A: Applications.* **68**(5), pp.501-511.

Muñoz-Sánchez, B. et al. 2017. A precise method to measure the specific heat of solar salt-based nanofluids. *Journal of Thermal Analysis and Calorimetry.* **129**(2), pp.905-914.

Murali, G. and Mayilsamy, K. 2015. Effect of Circular Fins on Latent Heat Storage to Enhance Solar Water Heater, an Experimental Study. In: *Applied Mechanics and Materials*: Trans Tech Publ, pp.13-17.

Myers Jr, P.D. et al. 2016. Nitrate salts doped with CuO nanoparticles for thermal energy storage with improved heat transfer. *Applied Energy.* **165**, pp.225-233.

Nagasaka, Y. and Nagashima, A. 1981. Absolute measurement of the thermal conductivity of electrically conducting liquids by the transient hot-wire method. *Journal of Physics E: Scientific Instruments.* **14**(12), p1435.

nanoscience. 2018. *Scanning Electron Microscopy.* [Online]. [Accessed 01/05/2018]. Available from: https://www.nanoscience.com/technology/sem-technology/.

NETZSCH. 2017. PART A - Theoretical background, LFA 427, Operating Instructions, 09.93. pp.1-32.

Niu, D. et al. 2014. Development of a novel thermal storage molten-salt filled with nanoparticles for concentration solar plants. *BULGARIAN CHEMICAL COMMUNICATIONS.* **46**(4), pp.873-881.

Omotani, T. et al. 1982. Measurement of the thermal conductivity of KNO3-NaNO3 mixtures using a transient hot-wire method with a liquid metal in a capillary probe. *International Journal of Thermophysics.* **3**(1), pp.17-26.

Omotani, T. and Nagashima, A. 1984. Thermal conductivity of molten salts, HTS and the lithium nitrate-sodium nitrate system, using a modified transient hot-wire method. *Journal of Chemical and Engineering Data.* **29**(1), pp.1-3.

Pahamli, Y. et al. 2017. Effect of nanoparticle dispersion and inclination angle on melting of PCM in a shell and tube heat exchanger. *Journal of the Taiwan Institute of Chemical Engineers.* **81**, pp.316-334.

Peng, Q. et al. 2008. High-temperature thermal stability of molten salt materials. *International Journal of Energy Research.* **32**(12), pp.1164-1174.

Pfleger, N. et al. 2015a. Thermal energy storage–overview and specific insight into nitrate salts for sensible and latent heat storage. *Beilstein journal of nanotechnology.* **6**(1), pp.1487-1497.

Pfleger, N. et al. 2015b. Thermal energy storage–overview and specific insight into nitrate salts for sensible and latent heat storage. *Beilstein journal of nanotechnology.* **6**, p1487.

Prakash, C. 1990a. Two-phase model for binary solid-liquid phase change, Part I: Governing equations. *Numerical Heat Transfer, Part B Fundamentals.* **18**(2), pp.131-145.

Prakash, C. 1990b. Two-phase model for binary solid-liquid phase change, part II: Some illustrative examples. *Numerical Heat Transfer, Part B Fundamentals.* **18**(2), pp.147-167.

Price, H. et al. 2002. Advances in parabolic trough solar power technology. *Journal of solar energy engineering.* **124**(2), pp.109-125.

Qi, W. and Shiming, Y. 1999. Experimental study of natural convection heat transfer of air layers in vertical annuli under high Rayleigh number conditions. *Heat Transfer—Asian Research.* **28**(1), pp.50-57.

Rahimi, M. et al. 2014. Experimental Investigation of Phase Change inside a Finned-Tube Heat Exchanger. *Journal of Engineering.* **2014**.

Riazi, H. et al. 2016. The effect of nanoparticle morphology on the specific heat of nanosalts. *International Journal of Heat and Mass Transfer.* **94**, pp.254-261.

Rohit, A.K. et al. 2017. An overview of energy storage and its importance in Indian renewable energy sector: Part I – Technologies and Comparison. *Journal of Energy Storage.* **13**, pp.10-23.

Rousse, D.R. et al. 2009. An overview of phase change materials and their implication on power demand. In: *Electrical Power & Energy Conference (EPEC), 2009 IEEE*: IEEE, pp.1-6.

Saidur, R. et al. 2011. A review on applications and challenges of nanofluids. *Renewable and Sustainable Energy Reviews.* **15**(3), pp.1646-1668.

Sambasivam, S. 2015. Development Of Alkali Chlorides As Heat Transfer Fluids With Addition Of Nanoparticles.

Santini, R. et al. 1984. Measurement of thermal conductivity of molten salts in the range 100–500° C. *International journal of heat and mass transfer.* **27**(4), pp.623-626.

Sarı, A. 2003. Thermal characteristics of a eutectic mixture of myristic and palmitic acids as phase change material for heating applications. *Applied Thermal Engineering.* **23**(8), pp.1005-1017.

Sari, A. and Kaygusuz, K. 2001. Thermal energy storage system using stearic acid as a phase change material. *Solar Energy.* **71**(6), pp.365-376.

Schmidt, P. 2011. On the design of a reactor for high temperature heat storage by means of reversible chemical reactions.

Schuller, M. et al. 2012. *Molten Salt-Carbon Nanotube Thermal Energy Storage for Concentrating Solar Power Systems Final Report.* Texas Engineering Experiment Station.

Schuller, M. et al. 2015. Experimental investigation of the specific heat of a nitrate–alumina nanofluid for solar thermal energy storage systems. *International Journal of Thermal Sciences.* **91**, pp.142-145.

Sciacovelli, A. et al. 2013. Melting of PCM in a thermal energy storage unit: Numerical investigation and effect of nanoparticle enhancement. *International Journal of Energy Research.* **37**(13), pp.1610-1623.

Sciacovelli, A. et al. 2015. Maximization of performance of a PCM latent heat storage system with innovative fins. *Applied Energy.* **137**, pp.707-715.

Sebti, S. et al. 2011. A numerical investigation of solidification in horizontal concentric annuli filled with nano-enhanced phase change material (NEPCM). *World Applied Sciences Journal.* **13**(1), pp.09-15.

Seo, J. and Shin, D. 2014. Enhancement of specific heat of ternary nitrate (LiNO3-NaNO3-KNO3) salt by doping with SiO2 nanoparticles for solar thermal energy storage. *Micro & Nano Letters.* **9**(11), pp.817-820.

Serrano-López, R. et al. 2013. Molten salts database for energy applications. *Chemical Engineering and Processing: Process Intensification.* **73**, pp.87-102.

Sharma, A. et al. 2009. Review on thermal energy storage with phase change materials and applications. *Renewable and Sustainable energy reviews.* **13**(2), pp.318-345.

Sharma, R. et al. 2014. Numerical study for enhancement of solidification of phase change materials using trapezoidal cavity. *Powder Technology.* **268**, pp.38-47.

Shin, D. 2011. *Molten salt nanomaterials for thermal energy storage and concentrated solar power applications*. thesis, Texas A&M University.

Shin, D. and Banerjee, D. 2010. Effects of silica nanoparticles on enhancing the specific heat capacity of carbonate salt eutectic (work in progress). *The International Journal of Structural Changes in Solids.* **2**(2), pp.25-31.

Shin, D. and Banerjee, D. 2011a. Enhanced specific heat of silica nanofluid. *Journal of heat transfer.* **133**(2), p024501.

Shin, D. and Banerjee, D. 2011b. Enhancement of specific heat capacity of high-temperature silica-nanofluids synthesized in alkali chloride salt eutectics for solar thermal-energy storage applications. *International Journal of Heat and Mass Transfer.* **54**(5–6), pp.1064-1070.

Shin, D. and Banerjee, D. 2014. Specific heat of nanofluids synthesized by dispersing alumina nanoparticles in alkali salt eutectic. *International Journal of Heat and Mass Transfer.* **74**, pp.210-214.

Shin, D. and Banerjee, D. 2015. Enhanced thermal properties of SiO2 nanocomposite for solar thermal energy storage applications. *International Journal of Heat and Mass Transfer.* **84**, pp.898-902.

Shmueli, H. et al. 2010. Melting in a vertical cylindrical tube: numerical investigation and comparison with experiments. *International Journal of Heat and Mass Transfer.* **53**(19), pp.4082-4091.

Siva, K. et al. 2010. Experimental and numerical investigation of phase change materials with finned encapsulation for energy-efficient buildings. *Journal of Building Performance Simulation.* **3**(4), pp.245-254.

Smirnov, M. et al. 1987. Thermal conductivity of molten alkali halides and their mixtures. *Electrochimica acta.* **32**(7), pp.1019-1026.

Snow, C.L. et al. 2010. Size-dependence of the heat capacity and thermodynamic properties of hematite (α-Fe 2 O 3). *The Journal of Chemical Thermodynamics.* **42**(9), pp.1142-1151.

Song, W. et al. 2018. Effect of SiO2 nanoparticles on specific heat capacity of low-melting-point eutectic quaternary nitrate salt. *Solar Energy Materials and Solar Cells.* **179**, pp.66-71.

Sparrow, E. and Broadbent, J. 1982. Inward melting in a vertical tube which allows free expansion of the phase-change medium. *Journal of Heat Transfer.* **104**(2), pp.309-315.

Suárez, C. et al. 2015. Transient analysis of the cooling process of molten salt thermal storage tanks due to standby heat loss. *Applied Energy.* **142**, pp.56-65.

Tao, Y.B. et al. 2015a. Effect of surface active agent on thermal properties of carbonate salt/carbon nanomaterial composite phase change material. *Applied Energy.* **156**, pp.478-489.

Tao, Y.B. et al. 2015b. Preparation and thermal properties characterization of carbonate salt/carbon nanomaterial composite phase change material. *Energy Conversion and Management.* **97**, pp.103-110.

Tasnim, S.H. et al. 2015. Convection effect on the melting process of nano-PCM inside porous enclosure. *International Journal of Heat and Mass Transfer.* **85**, pp.206-220.

Tay, N. et al. 2015. Investigation of the effect of dynamic melting in a tube-in-tank PCM system using a CFD model. *Applied Energy.* **137**, pp.738-747.

Tay, N. et al. 2013. Comparison of pinned and finned tubes in a phase change thermal energy storage system using CFD. *Applied energy.* **104**, pp.79-86.

Thirugnanasambandam, M. et al. 2010. A review of solar thermal technologies. *Renewable and sustainable energy reviews.* **14**(1), pp.312-322.

Thirumaleshwar, M. 2009. *Fundamentals of heat and mass transfer.* Pearson Education India.

Tian, H. et al. 2017. Enhanced thermal conductivity of ternary carbonate salt phase change material with Mg particles for solar thermal energy storage. *Applied Energy.* **204**, pp.525-530.

Tiznobaik, H. et al. 2015. Effect of formation of “long range” secondary dendritic nanostructures in molten salt nanofluids on the values of specific heat capacity. *International Journal of Heat and Mass Transfer.* **91**, pp.342-346.

Tiznobaik, H. and Shin, D. 2012. Investigation of Molten Salt Nanomaterials for Solar Thermal Energy Storage Application. In: *ASME 2012 Heat Transfer Summer Conference collocated with the ASME 2012 Fluids Engineering Division Summer Meeting and the ASME 2012 10th International Conference on Nanochannels, Microchannels, and Minichannels*: American Society of Mechanical Engineers, pp.51-54.

Tiznobaik, H. and Shin, D. 2013a. Enhanced specific heat capacity of high-temperature molten salt-based nanofluids. *International Journal of Heat and Mass Transfer.* **57**(2), pp.542-548.

Tiznobaik, H. and Shin, D. 2013b. Experimental validation of enhanced heat capacity of ionic liquid-based nanomaterial. *Applied Physics Letters.* **102**(17), p173906.

TOPLOTE, S.H.L. and STRUKTURAH, I.V.S. 2012. Simulation of latent-heat thermal storage integrated with room structures. *Materiali in tehnologije.* **46**(3), pp.239-242.

Trp, A. 2005. An experimental and numerical investigation of heat transfer during technical grade paraffin melting and solidification in a shell-and-tube latent thermal energy storage unit. *Solar Energy.* **79**(6), pp.648-660.

Tufeu, R. et al. 1985. Experimental determination of the thermal conductivity of molten pure salts and salt mixtures. *International journal of thermophysics.* **6**(4), pp.315-330.

Vaivudh, S. et al. 2008. Heat transfer of high thermal energy storage with heat exchanger for solar trough power plant. *Energy Conversion and Management.* **49**(11), pp.3311-3317.

Vajjha, R. et al. 2009. Density measurement of different nanofluids and their comparison with theory. *Petroleum Science and Technology.* **27**(6), pp.612-624.

Valan, A.A. et al. 2013. Numerical performance study of paraffin wax dispersed with alumina in a concentric pipe latent heat storage system. *Thermal science.* **17**(2), pp.419-430.

Varol, Y. and Okcu, M. 2013. Numerical Investigation of Fins Effect for Melting Process of Phase Change Materials. In: *ASME 2013 International Mechanical Engineering Congress and Exposition*: American Society of Mechanical Engineers, pp.V08AT09A035-V08AT09A035.

Vasquez Padilla, R. 2011. Simplified methodology for designing parabolic trough solar power plants.

Velraj, R. et al. 1997. Experimental analysis and numerical modelling of inward solidification on a finned vertical tube for a latent heat storage unit. *Solar Energy.* **60**(5), pp.281-290.

Voller, V.R. and Prakash, C. 1987. A fixed grid numerical modlling methodology for convection-diffusion mushy region phase-change problems *International Journal Heat Mass Transfer.* **30**(8), pp.1709-1719.

Vyshak, N.R. and Jilani, G. 2007. Numerical analysis of latent heat thermal energy storage system. *Energy Conversion and Management.* **48**(7), pp.2161-2168.

Wang, S. et al. 2012. Melting in cylindrical enclosures: numerical modeling and heat transfer correlations. *Numerical Heat Transfer, Part A: Applications.* **61**(11), pp.837-859.

Warzoha, R.J. and Fleischer, A.S. 2014. Determining the thermal conductivity of liquids using the transient hot disk method. Part I: Establishing transient thermal-fluid constraints. *International Journal of Heat and Mass Transfer.* **71**, pp.779-789.

Wen, D. and Ding, Y. 2006. Heat transfer of gas flow through a packed bed. *Chemical Engineering Science.* **61**(11), pp.3532-3542.

White, L.R. and Davis, H.T. 1967. Thermal conductivity of molten alkali nitrates. *The Journal of Chemical Physics.* **47**(12), pp.5433-5439.

Wiberg, E. et al. 2001. *Inorganic chemistry.* San Diego; Berlin; New York: Academic Press ; De Gruyter.

Wu, S. et al. 2012. Numerical simulation on thermal energy storage behavior of Cu/paraffin nanofluids PCMs. *Procedia Engineering.* **31**, pp.240-244.

Wu, S. et al. 2010. Preparation and melting/freezing characteristics of Cu/paraffin nanofluid as phase-change material (PCM). *Energy & Fuels.* **24**(3), pp.1894-1898.

Xie, Q. et al. 2016. Thermal Storage Properties of Molten Nitrate Salt-Based Nanofluids with Graphene Nanoplatelets. *Nanoscale Research Letters.* **11**(1), pp.1-7.

Yang, H. and Banerjee, D. 2012. Study of Specific Heat Capacity Enhancement of Molten Salt Nanomaterials for Solar Thermal Energy Storage (TES). In: *ASME 2012 Third International Conference on Micro/Nanoscale Heat and Mass Transfer*: American Society of Mechanical Engineers, pp.639-644.

Yang, L. et al. 2015. Numerical analysis on performance of naphthalene phase change thermal storage system in aluminum plate-fin unit. *Heat and Mass Transfer.* **51**(2), pp.195-207.

Ye, W.-B. et al. 2011. Numerical simulation on phase-change thermal storage/release in a plate-fin unit. *Applied Thermal Engineering.* **31**(17), pp.3871-3884.

Yoo, D.-H. et al. 2007. Study of thermal conductivity of nanofluids for the application of heat transfer fluids. *Thermochimica Acta.* **455**(1), pp.66-69.

Zeng, Y. et al. 2013. An experimental investigation of melting of nanoparticle-enhanced phase change materials (NePCMs) in a bottom-heated vertical cylindrical cavity. *International Journal of Heat and Mass Transfer.* **66**, pp.111-117.

Zhang, P. et al. 2015. Heat transfer characteristics of a molten-salt thermal energy storage unit with and without heat transfer enhancement. *Applied Energy.* **137**, pp.758-772.

Zhang, Y. et al. 1993. Melting in an enclosure with discrete heating at a constant rate. *Experimental thermal and fluid science.* **6**(2), pp.196-201.